Very high energy gamma ray astronomy and non pulsating low mass x-ray binaries

Carraminana, Alberto

VERY HIGH ENERGY GAMMA RAY ASTRONOMY AND NON PULSATING LOW MASS X-RAY BINARIES

BY

Alberto Carramiñana, M. Sc.

A thesis submitted to the University of Durham
in accordance with the regulations for admittance
to the degree of Doctor of Philosophy

DEPARTMENT OF PHYSICS
UNIVERSITY OF DURHAM

FEBRUARY 1991

ABSTRACT

This thesis is concerned with non pulsating Low Mass X-Ray Binaries as Very High Energy γ-ray sources, in particular Scorpius X-1, the brightest of these objects in X-rays, and the most likely to be detectable at energies above 250 GeV.

After a first introductory chapter, experimental techniques presently used in Very High Energy γ-ray Astronomy are reviewed.

In the third chapter statistical techniques used to quantify count rate excesses and orbital modulations are described and applied to data from Scorpius X-1. Data taken in 1988 and 1989 showing a 3σ count excess, reported previously elsewhere, are found to show orbital modulation at the 3% statistical level. The analysis of data taken on 1990 shows no signal. Periodicity tests, in particular the Rayleigh test, are also described.

The principles of a segmented fast algorithm for period searches in Cerenkov data using memory limited, but relatively fast, micro-computers are shown in the fourth chapter. Various of these machines can be used simultaneously in order to achieve a large efficiency. A method to perform various trials per independent frequency is also presented.

The results of period searches in data from three selected objects (Scorpius X-1, GX 5-1 and Supernova 1987A) are presented. No periodicity is found at significant level in these data. The complete power spectrum of four segments of data from Cygnus X-3 showing a signal near to 12.59 ms are also shown.

The final chapter considers theoretical models developed

previously for more massive systems accounting for the different physical scenario of these low mass systems. The process of pair production between high energy photons and the radiation field of the accretion disc appears as the tightest constraint on how close to the neutron star high energy photons can be produced.

For Nigel and Catherine

VERY HIGH ENERGY GAMMA RAY ASTRONOMY AND NON PULSATING LOW MASS X-RAY BINARIES

Contents

PREFACE

Since October 1987 the author has been working with the very high energy γ-ray group at Durham University. He was involved in seven dark Moon periods of observation with Cerenkov telescopes: five with the Mark III telescope at Narrabri, between April 1988 and February 1990, and two with the Mark IV telescope at La Palma, on June/July and August/September 1989. During these periods he was involved in observations of all the objects studied in this thesis with the exception of GX 5-1.

The author was involved in the development of data analysis programs: he was responsible for a period search program using fast algorithms on Acorn Cambridge workstations. This program is described in Chapter IV and used in Chapter V. He also wrote a program for event binning, count rate fitting and burst searching.

He was involved in pre-processing of data from both telescopes and responsible for period searches in data of various objects primarily Scorpius X-1, but also SN1987A, GX 5-1, 1E2259+586, 4U1830-20, and SS433.

The author wrote several programs related to the modelling of high energy emission from binary sources. These programs were designed to investigate particular aspects of this emission such as the production of very high energy γ-rays by the interaction of beams of particles with matter either from companion stars or accretion discs; the motion of charged particles in magnetic fields related to these systems and its consequences for orbital light curves; the absorption of high energy photons by pair

production in magnetic fields and in the radiation fields of accretion discs.

None of the material contained in this thesis has been submitted previously for admittance to a degree in this or any other university.

ACKNOWLEDGEMENTS

I would like to thank all the people at U.N.A.M. who have been involved in giving me the support that made this work possible: scientific and moral support from the I.A.U.N.A.M.; financial support from all the people at D.G.A.P.A.

My supervisor Keith Orford is thanked for his guidance and ideas throughout this work. His advice and company during long observing nights down under were well appreciated.

Vince Mannings is thanked for keeping the interest high with late night chats about binary systems, gamma ray astronomy, astrophysics in general and many other conversations more related to non scientific topics. His merciless corrections of my writing in the last chapter were appreciated.

Pete Edwards is thanked in particular for translating a large part of this work from a non defined language into english and in general for his warm character.

I would like to thank also friends and colleagues at the observatory: Lowry McComb, Karen Brazier, Stella Bradbury, Chris Bowden, Steve Rayner, Susan Hilton, Ken Tindale, Ted Turver, Eric Lincoln, Paula Chadwick; and at the physics department: Nobuo, Rafael, Alfonso, Carlos, Richard B., Ian, Richard E., ...

Professor Arnold Wolfendale and Professor Alan Martin are thanked for the provision of the facilities in the Department of Physics.

And ... of course! Esperanza.

I. INTRODUCTION

In recent years the Cerenkov ground based technique has led to interesting results concerning the emission of very high energy photons from Galactic objects. Most of these objects are related to systems containing a neutron star, intrinsically the most promising candidates. Nevertheless, quite distinct physical scenarios can be identified: on one hand, there is the Crab, know to be an isolated rotating neutron star; on the other side, accreting X-ray pulsars have been reported as sources of high energy photons: binary systems like Centaurus X-3 and Vela X-1, containing a massive early-type star, or Hercules X-1, which has an A star, and is therefore classified as a low mass system. In these objects, the neutron star is known to possess a strong magnetic field, $B_* = \{2.9 \pm 0.3\} \times 10^{12}$ Gauss in the case of Hercules X-1 (Mihara *et al.*, 1990), and the source of energy is the accretion of matter from the companion. In these young systems, with ages of a few times 10^7 years, the existence of a pulse period for the X-ray emission gives a powerful way to test the data.

More recently, there have been some hints that, at the other end of the evolutionary sequence, some of the millisecond pulsars, very low mass and old (age $\sim 10^{10}$ years) compact binary systems, might also be sources of very high energy (VHE) γ-rays. In these objects accretion has ceased, the magnetic field of the neutron star has decayed to a value of $\sim 10^7$ Gauss, and it is mainly the fast rotation, related to the accretion history, that

can provide the required energy. It is again the knowledge of a pulse period that allows the measurement of extremely weak signals, all at marginal levels of statistical significance.

Between the X-ray pulsars, objects like Centaurus X-3 or Vela X-1, high mass systems ($M_c \geq 10 M_\odot$), and Hercules X-1, less massive ($M_c \approx 2\ M_\odot$), but still young, and the very low mass binary millisecond pulsars ($M_c \leq 0.4\ M_\odot$), there is a large number of (X-ray) bright low mass X-ray binaries (hereafter LMXRB), like Scorpius X-1, the first non solar X-ray source discovered. With the except of Cygnus X-3, there has been no reports of high energy emission from this class of LMXRB. This might well be related to the absence of coherent pulsations in these systems, which frequently show a more complex sort of oscillations, known as quasi periodic oscillations (or QPOs). These QPOs are detected as broad features in the power spectrum. The lack of a pulse period to test makes the detection of a weak signal more difficult, relying either on count excesses relative to the background, or in orbital modulation effects, like the 4.8 hour period observed in Cygnus X-3. These two methods demand much more stable atmospheric conditions than testing for short term periodicities, as tens of hours of data under clear skies are required. A high energy pulsar without a counterpart in other observed regions of the energy spectrum might well be hidden in the Cerenkov data without any hint of its presence. The report of a 12.6 ms pulsed signal from Cyg X-3 (Chadwick *et al.*, 1985) can well be one of such examples. Period searches in γ-ray emitting LMXRB can be of considerable interest.

In spite of the absence of a period to test, LMXRB are interesting candidates for high energy emission. Table 1.1, adapted from van der Klis (1989a), shows the low mass X-ray sources from the 3A catalogue not identified with an early type star (with the exception of Cygnus X-3), and an average flux in the (2-11 keV) band above 100 μJy. Cyg X-2, GX 9+9, and 4U1820-30 do show X-ray modulation, which for 4U1820-30 is related to an orbital period of 685 seconds (and an implied semi-major axis of only 0.43 light.seconds). Three objects that might be related to this kind of X-ray sources are SS433, Cir X-1 and 1E2259+286. In the hypothetical case of these systems being as bright above 300 GeV as in X-rays (2-11 keV band), eight of them would be detectable at the 3σ level after one observation with the Mark III telescope, and most of them with 40 hours of data. As a reference, the same extrapolation for Cygnus X-3 implies a detection time of 5.5 hours. Although these figures are most likely to be optimistic, if these objects show the same sort of high energy activity as Cygnus X-3 appears to have, at least the eight brightest should be detectable. The main deterrent for this is the lack of a testable period. Three steps that can be followed to analyse these objects are:

- first, to search for a count excess,
- second, the data can be tested for orbital modulations,
- third, data showing an excess can be used for period searches.

In the following chapters, some methods of analysis that can be applied to these sources will be described.

Object	Mean X-Ray Flux (10^{-10} erg$cm^{-2}s^{-1}keV^{-1}$)	<X-Ray Flux> / Cosmic Back. (%)	Time for 3σ Detection (hours)	Q
Sco X-1	300	60.0	6×10^{-3}	Y
GX 5-1	29	5.8	0.65	Y
GX 349+2	19	3.8	1.5	Y
GX 17+2	16	3.3	2.0	Y
GX 9+1	16	3.1	2.2	
GX 340+0	12	2.4	3.9	Y
GX 3+1	10	2.1	5.1	Y
Cyg X-2	10	2.1	5.1	Y
GX 13+1	8.2	1.6	8.1	
GX 9+9	7.0	1.4	11.1	
4U1820-30	6.3	1.3	13.8	Y
4U1705-44	6.3	1.3	13.8	Y
4U1636-53	5.3	1.1	19.3	
Ser X-1	4.8	0.97	23.3	
GC X-1	4.1	0.82	32.4	
4U1728-33	4.1	0.82	32.4	
GX 339-40	3.9	0.77	36.5	Y
4U1735-44	3.9	0.77	36.5	

TABLE 1.1

Bright LMXRB as Very High Energy γ-Ray Sources

Cosmic ray background ≡ 5×10^{-8} erg.cm^{-2}.s^{-1} at 300 GeV
=> a count rate of 68.6 events.min^{-1} ;

Q ≡ QPOs observed in X-Rays? (Y = yes).

II. VHE OBSERVATIONAL METHOD

2.1 GAMMA RAY ASTRONOMY ABOVE AND BELOW 0.5 TeV

2.1.1 Introduction

γ-ray photons are the most energetic form of electromagnetic radiation ("The End of the Rainbow") and probably also the one spanning on a widest range; it covers at least six orders of magnitude in energy, from the rest mass of the electron (0.511 MeV) up to PeV (Peta electron-volt or 10^{15} eV), and possibly EeV (Exa electron-volt or 10^{18} eV) energies. It is not surprising that very different methods of detection are required for different energy intervals.

It is interesting to note that the column density of the atmosphere of the Earth, in contrast with that of most of the bodies of the solar system, is a few times the bremsstrahlung mean free path for a relativistic electron (or positron) and the pair production length for a highly energetic gamma ray. As a consequence, photons and nucleons with energies above 10^{11} eV have the property of interacting in a detectable way with the atmosphere, giving us the opportunity of studying from ground level the most energetic regions of the spectrum, not accessible to satellites.

2.1.2 Detection of γ-rays at energies below 10 GeV

Gamma rays in this energy range are detected with instruments carried outside the atmosphere by either satellites (Table 2.1) or balloons. These energies are below the values of interest to us and only a summarised mention of the techniques used to detect them will be made here. The interested reader is referred to Longair (1981), Hillier (1984) and Ramana Murthy and Wolfendale (1986).

Explorer XI	1961	First to detect γ-rays
Vela	1967	First to detect γ-ray bursts
OSO 3	1968	First successful γ-ray telescope Detection of Galactic γ-ray emission and discovery of γ-ray Background
OSO 7	1972	Discovery of solar γ-ray lines
SAS 2	1972	First γ-ray map of the Galaxy
COS B	1975	Most detailed map of the γ-ray sky
HEAO 1	1977	First low energy gamma ray survey
HEAO 3	1979	γ ray lines from Al 26 in the Galaxy
Solar Max	1980	Discovers Co 56 lines from SN1987A
Gamma I	1990	Only γ-ray observatory working with Coded mask system
GRO	1991	Successfully launched in April 1991

TABLE 2.1

Gamma Ray Satellites

(i) Low energy telescopes: from 0.5 to 3 MeV

Gamma Rays in this energy range interact mainly through Compton scattering:

$$\gamma + e^- \longrightarrow \gamma + e^- \qquad \text{(II.1)}$$

The two main detectors in this energy range are the scintillation counter and solid state detectors. In the first kind of device an electron is ejected from an atom by the incident γ-ray through Compton scattering; the scintillator converts part of the energy of the electron into light through ionisation with a phototube finally detecting this light. Scintillation counters can be relatively large while solid state detectors have better spectral resolution but smaller active area. The requirements of the observation, either energy resolution or flux measurements, dictate the choice of detector.

At these energies the direction in which electrons are ejected by Compton scattering is weakly correlated with the direction of the incoming γ-ray. As a consequence, detectors suffer from very poor angular resolution (of some degrees) and consequently they have a high background; shielding of the detector is used to improve the angular resolution. Designs for telescopes with resolution of about one arc minute at 1 MeV have been proposed (Dipper, 1980).

(ii) Compton telescopes: from 3 to 10 MeV

At energies above 3 MeV the angular dependence of the

Compton cross section $d\sigma/d\Omega$ becomes important, and the secondary electrons and photons begin to retain the direction of the incoming γ-ray. Compton telescopes, relying on the detection of either the scattered photon or the secondary electron, are more sensitive to the direction of the source than scintillation counters or solid state devices.

(iii) Spark chambers: from 5 MeV to 1 GeV

At energies above a few MeV the production of electron - positron pairs ($\gamma \rightarrow e^+e^-$) takes over from Compton scattering as the dominant absorption process for energetic photons. Spark chambers are composed of several parallel metal plates alternatively connected to earth and a high voltage (voltages of consecutive plates would read: high - earth - high - earth - etc...); these plates are embedded in an inert gas, like neon or argon. The pair of energetic charged particles produced by the incoming γ-ray passing through the plates triggers a spark in the gas along its path. As the high voltage cannot be permanently maintained, a triggering system is required, imposing a lower limit to the energy range of around 10 MeV.

Spark chambers suffer from frequent cosmic ray background events due to either charged particles or neutrons. Both the SAS-II and COS-B satellite relied on spark chamber detectors. At energies in the GeV range the area of the instrument limits its sensitivity as fluxes become too low.

Two recent examples of the use of these techniques in satellites are Gamma I and GRO (Ramana Murthy & Wolfendale, 1986,

Bertsch *et al.*, 1988 and Kniffen *et al.*, 1988).

(iv) GAMMA I,

This Soviet French collaboration, launched last July, is a high energy gamma ray telescope designed primarily for energies between 50 and 500 MeV. Although similar in concept to its predecessors SAS-II and COS-B, this satellite, consisting of two spark chamber systems separated by a gas Cerenkov counter, is expected to improve upon previous results. The instrument has a relatively poor energy resolution (70% at 100 MeV down to 40% at 400 MeV), but a novel system of a coded aperture mask collimator is expected to improve its angular resolution from one degree down to 20 arc minutes (Hartman, 1988).

(v) The "Gamma Ray Observatory",

This is one of the four satellites of the Great Observatories program of NASA, the other three being the Hubble Space Telescope, the Advanced X-ray Astrophysics Facility and the Space Infrared Telescope Facility. GRO is to carry four instruments:

- BATSE: Burst and Transient Source Experiment,

This experiment consists of eight scintillator counters and is designed in particular to study the puzzling γ-ray bursts, and in general as a wide field of view monitor. Its aperture is to cover all the sky not shadowed by our planet (two thirds of the sky) with a resolution of one degree. These γ-ray bursts are

more intense in the low energy region of the spectrum; as a consequence the optimal response of the instruments is for energies between 20 keV and 600 keV with 30% resolution at 90 keV (7.3% at 660 keV); nevertheless photons up to 100 MeV can be detected. As these bursts are sudden and variable on a short timescale high time resolution is required (down to 2 μs).

- OSSE : Oriented Source Spectrometer Experiment

The OSSE is made up of four actively shielded and passively collimated NaI scintillators designed to measure spectra and time variability (time resolution down to 125 μs) from a large variety of celestial bodies. OSSE is planned to work in the energy range between 0.1 and 10 MeV, where lines from radioactive elements are common, with a high resolution (8% at 0.7 MeV and 3% at 6 MeV). The field of view is 3.8° x 11.4° FWHM

- COMPTEL: Imaging Compton Telescope

In the Compton telescope COMPTEL an incoming photon is to undergo scattering in a first stage of liquid scintillators and absorption in a NaI crystal located below. It is to be 20 times more sensitive than any other instrument before in the energy range between 1 and 30 MeV . By monitoring the energy losses of the γ-ray ("how much" and "where") on each of the two stages, Comptel will deduce both the energy (with $\Delta E/E \approx 5\%$) and direction of the original photon (with an angular resolution of 1.7° to 4.4°). The combined arrival information of several events will allow to locate the source within 7.5 arc minutes.

- EGRET : Energetic Gamma Ray Experiment Telescope

EGRET is basically a spark chamber system operating at energies from 20 MeV up to 30 GeV; the latter are in the neighbourhood of the present thresholds of ground level detectors (around 200 GeV). Its source resolution, between five and ten arc minutes, is to be the highest among the instruments inside GRO. The energy resolution is 15% in the centre of its energy range. Timing measurements are to be made with an accuracy of 0.1 ms.

2.1.3 Atmospheric detection of γ-rays above 0.1 TeV

For energies in the MeV range, the atmospheric absorption of γ-rays restricts their observation to balloons and satellites; but once these energies reach a few GeV the flux of photons becomes too low and detectors with the area required are not feasible in the practice. On the other hand, their interaction with the atmosphere becomes more intense, and the number of sub-products increases up to the point that the effect of a single photon can be detected. Three methods of observing the interaction of cosmic rays and γ-rays are presently used, each one covering a different range of energies: the Cerenkov technique is used around and below the TeV (10^{12} eV) region of the spectrum; the detection of secondary particles covers energies above 0.1 or 1 PeV (10^{15} eV) together with the recent method of reconstructing the particle cascades triggered by primary particles or photons of energies up to the order of 1 EeV (10^{18} eV) using nitrogen fluorescence.

(i) Particle cascades,

High energy γ-rays interact with matter, or other photons, producing a particle pair; but an "isolated" photon cannot decay into a pair by itself keeping the energy - momentum four vector invariant. Once it has been emitted by an astronomical source, a γ-ray travels in a straight path until it meets another photon like starlight, or matter like our atmosphere. When the γ-ray penetrates a column depth of $\kappa_o \approx 37$ g.cm^{-2} in the atmosphere of the Earth (which has a total column depth ≈ 1033 g.cm^{-2}), it interacts with an atmospheric atomic nucleus and creates an electron-positron pair which has most of the original energy. These particles travel a similar length before producing a high energy photon through bremsstrahlung. These electromagnetic interactions enter a loop as shown in Diagram 2.1.

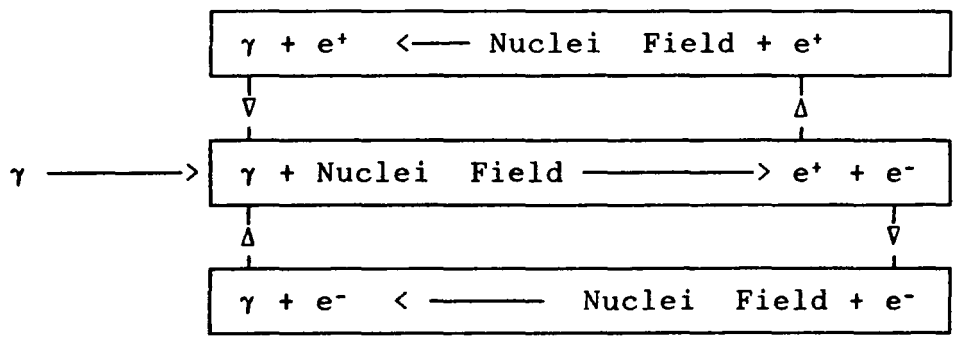

DIAGRAM 2.1

An Electromagnetic Cascade

The cascade ceases when either the photons begin to interact through Compton scattering rather than pair production, or bremsstrahlung ceases to be the dominant process of energy loss for the electrons. Compton process predominates over pair production for photon energies below 10 MeV, while ionisation takes over bremsstrahlung at 84 MeV, the latter turnover indicating the end of the development of the cascade. As these processes happen at energies well above $m_e c^2 \approx 0.5$ MeV electrons, positrons and photons are emitted in a narrow beam. The overall cascade occurs within a thin cone, whose aperture is in fact determined by processes other than Cerenkov emission, pair production or bremsstrahlung; mainly Coulomb scattering of particles by air nuclei.

This electromagnetic cascade process is a simplified version of what happens when a high energy nucleus, protons been the most common cosmic nuclei, enters the atmosphere. A more complex shower of particles, schematically shown in Diagram 2.2, is triggered by the strong interaction between the incoming proton and an atmospheric nuclei, producing charged and neutral pions.

Each neutral pion decays into two γ-rays which undergo pair production in the field of a nuclei, starting the "electromagnetic component" of the cascade, a replica of a γ-ray initiated shower. On the other hand, the production of muons by the charged pions results in the "muon component" of the cascade. The respective rest mean lifetimes of neutral pions, charged pions and muons are 0.84×10^{-16} s, 2.6×10^{-8} s, 2.2×10^{-6} s. The respective energies required for these three particles to

travel some 10 km down in the atmosphere and reach sea level are 5.3×10^{19} eV, 1.8×10^{11} eV and 1.6×10^{9} eV; one can see that no neutral pion will reach ground level in contrast to muons which are commonly detected underground. A third component, the "nucleonic component" characteristic of a proton shower, is generated by the still energetic proton, and nuclei fragments left after the first collision, undergoing further interactions. Differences between a cascade initiated by a proton or by a photon derive from the first interaction producing charged pions and consequentially muons and neutrinos which reach the ground.

The study of these muons and the weakly interacting neutrinos using underground and underwater detectors, like the NUSEX experiment (Battistoni *et al.* 1986) and DUMAND project (Matsuno *et al.* 1989) respectively, is a relevant topic in cosmic ray physics. It is important to note that the production of particle pairs by photons is not restricted to e^+e^- and other pairs (like muon - antimuon) can also be produced. As it is easier to produce light particles (the electron having the lowest rest mass) muon pairs, although observed in cascades, are rare.

(ii) Particle arrays: the extensive air shower technique,

The column density of the atmosphere of the Earth at sea level, 1033 $g.cm^{-2}$, is sometimes quoted as equivalent to a column of Mercury with a height of 76 cm. This is also equivalent to 28 times the absorption path for bremsstrahlung and pair production, which means that the energy $E(\gamma)$ of a cosmic γ-ray will divide itself in a 28 fold process. Rossi & Geisen (1941) found that the

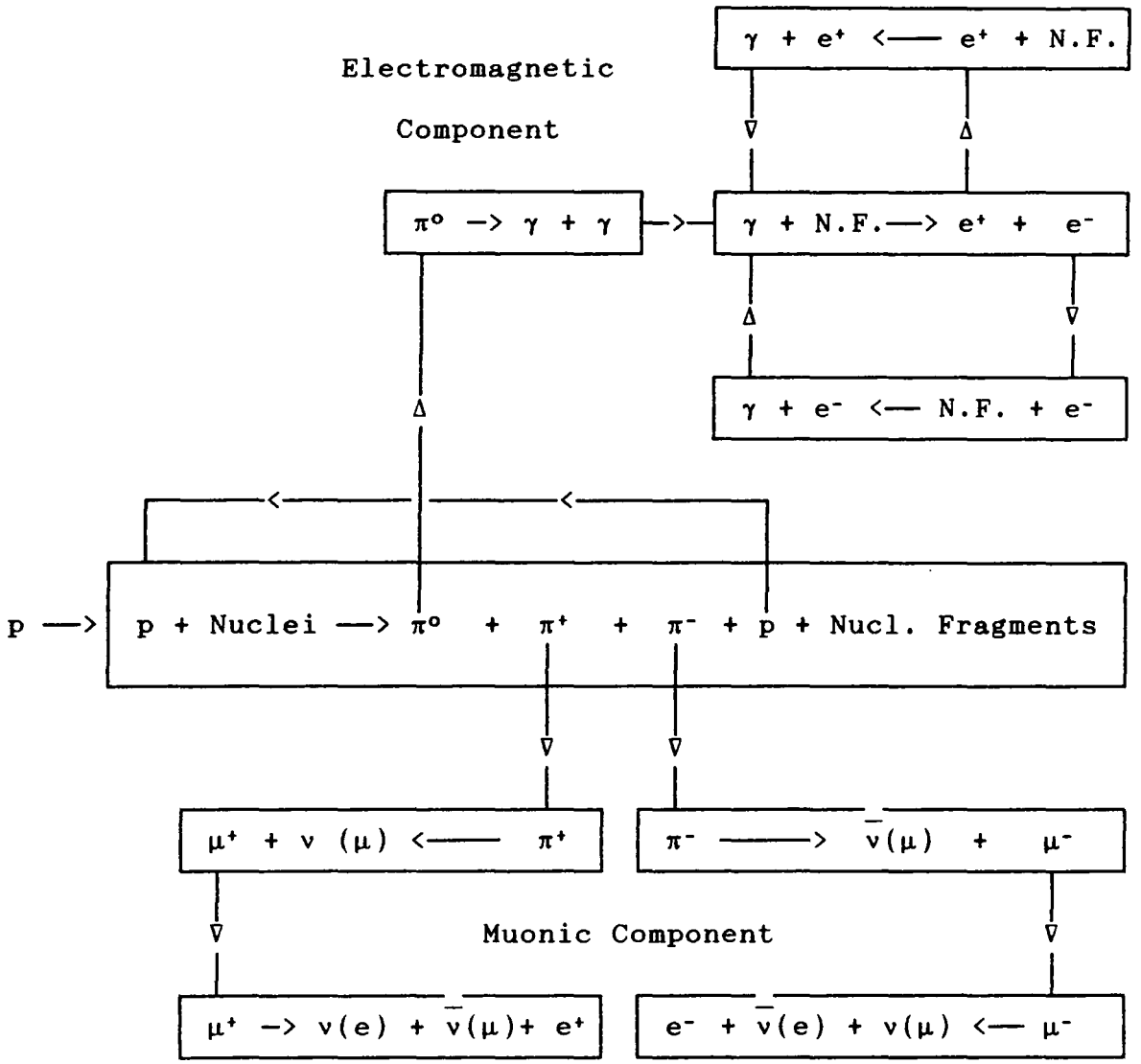

DIAGRAM 2.2

A schematic Proton Cascade

N.F. = Nuclei (electromagnetic) Field.

Although only three pions are shown, several are typically produced, their actual number been of the order of $(E_{cr}/1GeV)^{1/4}$ i.e. up to 30 at 10^{15} eV

primary must have an energy in the 10^{14} eV range in order to have a detectable number of particles reaching the ground. In their model the cascade grows by this combined process of pair production and bremsstrahlung and stops when particles begin to interact through ionisation. Arrays of scintillator counters, located at a moderate altitude (like 2000 metres), can detect the particles (about a million electrons and positrons) of a cascade initiated by a 10^{14} eV gamma ray and distributed in an area of some 10^8 cm^2. Analysis of the arrival times at different detectors is used to obtain the direction of the primary in the sky. These arrays can work normally during day time and the experiments run almost continuously for years. A recent example is the SPASE array (Smith *et al.*, 1989) located at the South Pole, where the zenith angle of celestial objects does not vary.

(iii) Shower reconstruction using Nitrogen fluorescence in the air,

The Fly's Eye detector in Utah (Baltrusaitis *et al.*, 1985; Loh *et al.*, 1990) studies the highest energy cosmic rays, in the range from 10^{17} eV (0.1 EeV) up to 10^{20} eV. The method consists of observing the N_2^+ emission from air fluorescence in the atmosphere ($3300A \leq \lambda \leq 4000A$) caused by the particles of the cascade in order to determine the track and energy deposition of the shower; it requires clear and moonless nights. The effective area of this detector varies with energy from 63 km^2 at 10^{18} eV up to 790 km^2 at 10^{20} eV. "Neutral EeV emission" from the direction of Cyg X-3 has been reported using data recorded over

six and a half years with this detector (Cassiday *et al.*, 1989).

An alternative instrument which exploits the same principle and has a much lower cost, the "side-looking air-fluorescence detector" or SLD, has recently been designed and preliminary tested by Bowen & Halverson (1990). This detector is design to cover areas of the order of 500 km^2, required to get an appreciable flux of cosmic rays above 10^{19} eV. It requires of the order of ten photomultiplier tubes rather than a thousand as required by the Fly's Eye.

2.2 THE ATMOSPHERIC CERENKOV TECHNIQUE

2.2.1 Cerenkov radiation

When a charged particle moves trough a medium of refraction index n with a speed $v = \beta c$ larger than the speed of light (c/n) radiation is emitted. Renowned physicists are associated with this phenomenon, known as Cerenkov emission (sometimes Vavilov - Cerenkov), either anticipating it (Heaviside, 1890), discovering it (Cerenkov 1934) or describing it in theoretical terms (Frank & Tamm, 1937; Jackson 1975). A simplified description of the process in relation to air showers is given by Jelley (1982).

A particular feature of Cerenkov radiation is that the emission does not come from the particle but from the medium itself, as the dipoles of its particles change orientation in late response to the passage of the (supraluminical) charge. This

change in the dipole vectors results in an emission of photons symmetric to the axis of motion of the charge and with characteristic angular aperture $\psi \approx \cos^{-1}(1/\beta n)$. The total energy radiated per unit length and frequency ν is (Lang, 1986):

$$I(\nu) = \frac{d^2E}{dl\ dt} = \frac{2\pi\ e^2\ \nu}{c^2}\left[1 - \frac{1}{\beta^2 n(\nu)^2}\right] \qquad (II.2)$$

In general the criteria $n(\nu)\beta \geq 1$ restricts the emission to bands in the spectrum where $n(\nu)$ abruptly increases above $1/\beta$ (anomalous dispersion). But if β is very close to one, and the condition $n(\nu)\beta \geq 1$ is therefore satisfied (which is the case for electron in cascades), this point loses its relevance and the emission occurs in a large region of the electromagnetic spectrum. For frequency ranges where $n(\nu)$ can be approximated by a constant the emission increases linearly with ν ; Cerenkov radiation is therefore more intense in the UV and blue than in the low energy part of the spectrum.

2.2.2 Cerenkov radiation in the air

The refraction index of the air at sea level is constant, in a first approximation, its value been $n_{mean} \approx 1 + 2.9 \times 10^{-4}$. In a more accurate approach, n decreases monotonically with wavelength, varying from $n_{red} \approx 1 + 2.7 \times 10^{-4}$ at 7000Å, to $n_{UV} \approx 1 + 3.2 \times 10^{-4}$ in the near ultraviolet (3000Å). The threshold energy above which Cerenkov radiation is emitted by

electrons (and positrons) moving through the air at sea level (using n_{mean}) is $E_{ch} \approx 21.8$ MeV, corresponding to a Lorentz factor $\gamma_{ch} \approx 43$.

Cascades start at a mean altitude of the order 30 km, which corresponds to the stratosphere, although statistical deviations from this number are large. The conditions of pressure and temperature in the atmosphere vary with altitude; for example, while in the stratosphere (above some 20 km) the temperature gradient is positive ($dT/dz > 0$), in the lowest layer, the troposphere, the air temperature is larger nearer to the ground ($dT/dz < 0$). The refraction index of the air varies with the temperature T, in degrees Kelvin, and the pressure P, in millibars, according to (Lena, 1988):

$$n = 1 + 0.8 \times 10^{-4} \, P(mb)/T(^{\circ}K) \quad . \qquad (II.3)$$

As mentioned above, the Cerenkov emission given by (II.2) is more intense in the blue and UV regions of the electromagnetic spectrum. Absorption of these photons by ozone is important at wavelengths below 3000A, and practically complete below 2000A. The maximum in the concentration of O_3 occurs at about 16 km, where cascades are developing. Molecular oxygen O_2 also contributes to the absorption of UV photons.

2.2.3 Cerenkov radiation from electromagnetic cascades

From expression (II.2) an approximate estimation of the number of Cerenkov photons emitted by a γ-ray shower can be made. The cascade stops growing when the energy of electrons and positrons falls below the ionisation threshold of $E_i \approx 83$ MeV (or a Lorentz factor $\gamma \approx 165$); therefore electrons in the developing shower will have $\gamma \geq 4\gamma_{ch}$. This allows to approximate expression II.2 by $I(\nu) \approx 2\pi\nu\,(e/c)^2\,(1/\gamma_{ch}^2 - 1/\gamma^2)$, and with a simplistic model for the cascade, where the total number of electrons and positrons at a given atmospheric depth κ is given by $n(\kappa) = 2/3\,\exp(\kappa/\kappa_o)$, the total number of Cerenkov photons can be estimated. The relation between the atmospheric depth κ and physical height z, given by $\kappa(z) = \kappa_{atm}\,e^{-z/H}$, where H is the characteristic scale of the atmosphere (around 7950 metres), κ_{atm} is its column density, is also used. With this ingredients, and as the cascade triggered by a primary photon of energy E_p develops from $\kappa = \kappa_o$ to $\kappa_o\,Ln(E_p/E_i)$:

$$N_{phot} \approx \int \frac{I(\nu)}{h\nu}\, n\{\kappa(z)\}\cdot dz\cdot d\nu$$

$$N_{phot} \approx \frac{2\,\alpha\,\Delta\nu\,H}{3\,\gamma_o^2\,c} \int_1^{Ln(Ep/Ei)} \frac{(1 - A\,e^{2x})\,e^x}{x}\,dx \approx 9.58 \times 10^6\ g(E_{ch}/TeV)$$

(II.4)

where $\alpha = 2\pi\ e^2/hc$ is the fine structure constant, the window in the spectrum is $\Delta\nu \approx 10^{14}$ Hz (i.e. $4000 \leq \lambda \leq 4500$ A) and the energy is scaled using $A = (21.77\text{MeV} / E_p)^2$. The dimensionless function $g(\xi)$ is the integral in II.4, normalised to its value at $E_p = 1$ TeV (normalisation factor is 1464.29); it behaves linearly as shown in Figure 2.1. Considering 10^8 cm^2 as the typical area covered by the flash at ground level, the surface density of incoming photons is of the order of 0.1 cm^{-2} at TeV energies. This value is likely to be an upper limit as the absorption of photons by the atmosphere in the range $\Delta\nu$ has been neglected.

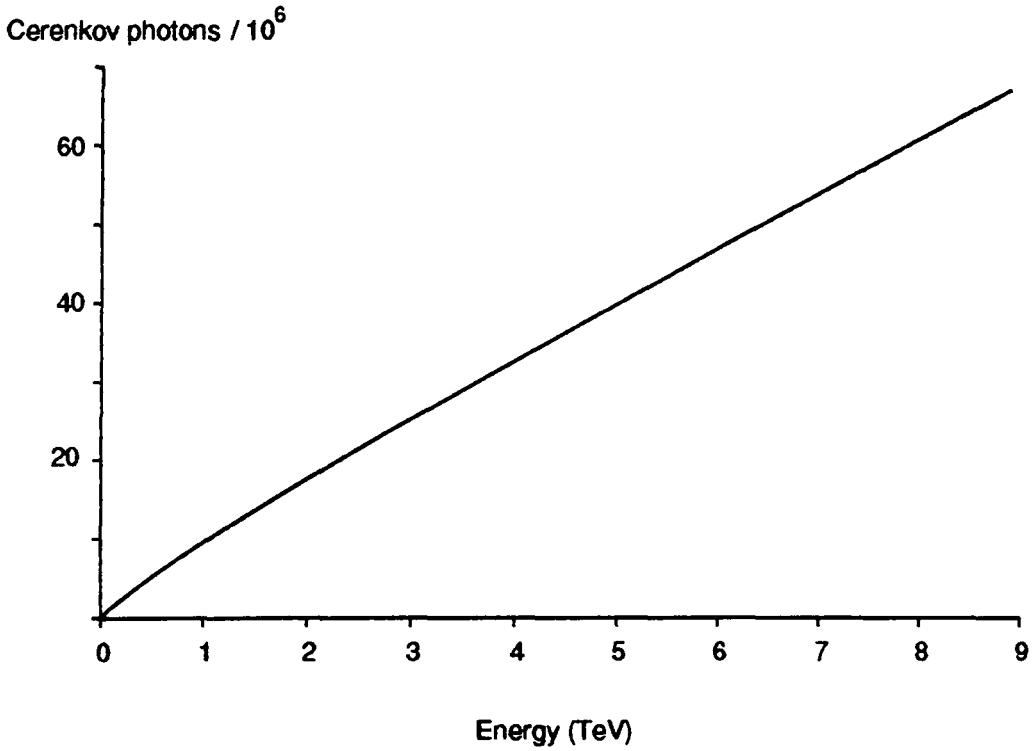

Figure 2.1

Number of Cerenkov photons as function of the energy of the primary

2.2.4 The distribution of Cerenkov photons at ground level

The emission of all three processes considered here, pair production, bremsstrahlung and Cerenkov, involve narrow beams at high energies. Nevertheless the actual cone occupied by the particle and light pool is larger than suggested by these processes. Multiple Coulomb scattering causes the shower cone to widen and cover an area with typical radius of the order of 100 metres. Browing & Turver (1977) estimated the maximum radius of the shower pool to be between 400 and 450 metres, quoting 100 to 200 metres as a more useful - measurable - radius; more recently Macrae (1985) estimated the typical radius of the light pool to be in the range 45 to 110 metres. The angular (lateral) distribution of light is itself determined by that of the particles. The shape of the Cerenkov flash varies with the impact parameter b, the distance between the telescopes axis and the showers axis. The Cerenkov flash is roughly circular for small impact parameters and acquires an elliptical shape as b increases (Macrae, 1985; Browing & Turver, 1977). The number of Cerenkov photons along the axis of the ellipse peaks at distances of the order of 100 metres, the exact value depending on primary energy, impact parameter and zenith angle.

More recently, Hillas (1985) and Hillas & Patterson (1986a) studied the differences between the Cerenkov images produced by γ-ray and proton showers. They conclude that nucleon images should be broader (due to the emission angles of pions in nuclear collisions), longer (since the nucleonic shower penetrates deeper

into the atmosphere) and with their axis rarely aligned with the point source (alignment occurring only by chance). As a conclusion of their simulations, Hillas & Patterson (1986b) gave the following suggestions to optimize Cerenkov detectors:

(i) to reduce the threshold energy, as the cosmic proton background spectrum is expected to be harder than the source photon spectrum, due to the increase of the multiplicity of π^o production with proton energy. The ratio of photons to protons should therefore be larger at lower energies.

(ii) to select an aperture for which the relative ratio of γ-shower to p-shower and background sky photons is optimised. They quote an optimum value for the aperture of 1.4° (2.4° in the absence of sky noise),

(iii) to increase the mirror area, so that Cerenkov photons become easier to distinguish from fluctuations in the UV and optical emission of the night sky,

(iv) to use UV or blue filters, although the choice of filters is dependent on the response of the phototubes used,

(v) to work at low altitude where showers are more developed and their differences are more marked,

(vi) to use more mirrors, either (a) independently, (b) in coincidence, (c) testing relative responses, or (d) concentration tests to identify the smaller images,

(vii) to use fast timing either to try to reconstruct the shape of the light pulse or to improve the arrival times (the latter point does not seem so relevant as UTtime is normally known at the μs level; relative timing between telescopes in

Dugway was ‹ 1 ns),

(viii) to select images based on parameters like their width, length and orientation.

As Cerenkov telescopes are still on the stage of optimising the signal (γ showers) to noise (p showers) ratio, the search for measurable distinctions between the two kinds of cascades is a very active topic in VHE astronomy. Different methods to enhance the signal to noise ratio result in distinct classes of TeV telescopes.

2.3 CERENKOV TELESCOPES FOR TeV ASTRONOMY

An interesting review about the early work on Cerenkov emission from the sky is given by Jelley (1982 and 1986), one of the scientists involved in the first detection of this radiation from EAS. In 1953 Galbraith and Jelley mounted an ex World War II signalling mirror with a photomultiplier in a dustbin and succeeded in making the first observations of Cerenkov pulses from the sky (Galbraith & Jelley, 1953). The following year Jelley and Gold, then the Assistant to the Astronomer Royal, pointed a six inch refractor at the Crab Nebula with the hope of detecting cosmic rays from it. The actual use of the Cerenkov technique to observe γ-rays was first suggested in 1961 by Zatsepin & Chudakov (1961); the sixties were the first decade of VHE astronomy, with a boost given in 1968 by the discovery of pulsars. Since those early days the number of telescopes has been

growing, in particular during the eighties. A list of some Cerenkov telescopes appears in Table 2.2. Present Cerenkov detectors are based on two main concepts:

(1) the first one is to chose the optimum aperture while keeping the energy threshold as low as possible. An aperture too large gives more background photons than desired, while a too narrow one results in missing Cerenkov photons from a shower on axis. The value derived by the Durham group for the optimum aperture is one degree. An instrument based on aperture rejection is the Mark III telescope of the University of Durham situated in Narrabri, Australia. A brief description of this telescope, and the similar Mark IV which operated at La Palma in the Islas Canarias, will be made as practically all the data used in this work were taken with these instruments (see also Tables 2.3a and 2.3b). A more detailed description of the Mark III telescope is made by Brazier *et al.* (1989a, 1989c).

(2) A second strategy is to try to differentiate between gamma ray and proton (or cosmic ray) showers by studying how the Cerenkov photons are distributed. This requires a complete characterisation of the shower (photon distribution) which cannot be achieved while working at the lowest threshold of the instrument: in other words the detector has to work at higher energies in order to get more information from each event. Construction by the Crimean group lead by Stepanyan of a version of this "imaging" telescope, with 37 tubes covering a circle of one degree diameter, began in 1983. This instrument has recently become operational (Vladimirsky *et al.*, 1989).

GROUP	Site	Operation Dates or Status
LEBEDEV Inst.	Crimea, USSR	1960-64
A.E.R.E, U.K. & DUBLIN	Malta	1964-70
CRIMEA	Crimea, USSR	1965-
SMITHSONIAN I.	M^t Hopkins, USA	1967-76
CRIMEAN A.O.	Crimea, USSR	1969-73
TATA	Ootacamund, India	1969-
SYDNEY & SMITHSONIAN I.	Narrabri, Australia	1972-74
JPL	Edwards A.F., USA	1981 -
DURHAM	Dugway, USA	1982-84
SMITHSONIAN+	M^t Hopkins, USA	1983-
BHABHA	Gulmarg , India	1985-
POTCHESTROOM	Nooitgedacht, SAF	1985-
WISCONSIN+	Haleakala, Hawaii	1985-90
RIVERSIDE+	Albuquerque, USA	1986-
TATA	Patchmarchi, India	1987-
DURHAM	Narrabri, Australia	1986 -
DURHAM	La Palma, Islas Canarias	1987-89
WHIPPLE+	M^t Hopkins, USA (a)	1987-

TABLE 2.2a

Some Cerenkov Telescopes

GROUP	Site	Operation Dates or Status
ACAD. SINICA	Beijing, China	1987-
ADELAIDE	Woomera, Australia	1988-
WHIPPLE+	M^{t} Hopkins, USA (b)	1988-
ASGAT	Pyrenees, France	1989-
C.A.O.	Crimea, USSR	1989-
ACAD. SINICA	Delingha, China	1990-
BEIJING	Xing Long, China	(1990)
WISCONSIN+	South Pole	(1990)
DUBLIN S.PATRICK	----------	Construction
DUMAND	----------	Proposal
"SOLAR ONE"	Barstow, USA	Proposal (10 GeV)

TABLE 2.2b

Some Cerenkov Telescopes (Cont...)

Another instrument of this kind, at M^{t} Hopkins, Arizona, has been under operation for the last four years giving some controversial first results. A description of this instrument can be found in Macrae (1985). An improved version, with a detector package of 109 phototubes covering one degree around the source on the sky, has recently started to operate and is described by Lamb *et al.* (1989).

2.3.1 An Aperture Rejection Telescope: the Mark III

(i) site,

The Mark III telescope is located at Narrabri, New South Wales, Australia. The geographical coordinates of this site are longitude 149° 49' 1" East, and latitude 30° 28' 59" South. The site is at 260 metres of altitude and relatively close to the Anglo Australian Telescope facilities (100 km), and the Australia Telescope at Culgoora (some 20 km).

(ii) Mechanical design,

The telescope consists of three multi-mirror "telescope units" working in parallel and requiring triple coincidence (all three reporting a detection) to accept an event as such. At the focus of each dish (or "telescope unit") is the detector package consisting of seven photomultipliers (hence 21 PMTs in total). The experiment is controlled by seven BBC microcomputers from inside a cabin located a few meters from the telescope.

The telescope is on an Alt-Azimuth mount from an old surplus gun mount . One of the BBC microcomputers is exclusively dedicated to the control of the steering, receiving information of the telescope pointing position (resolution 0.05°) from two shaft encoders every 0.1 s, and sending the desired (computed) values for azimuth and altitude to two DC servomotors. These motors drive the telescope through gears mounted directly on the structure.

(iii) Mirrors and optical design,

The Mark III telescope is composed of a total of 130 mirrors, 44 on the central unit and 43 on each of the lateral dishes. Each mirror has a diameter of 60 cm, so that the total reflective surface is ~ 1.24 x 10^5 cm^2 per dish. The effective aperture FWHM is ($1.4^\circ \pm 0.2^\circ$) when the angular size of a Cerenkov flash is considered, while experimental measurements give ($1.5^\circ \pm 0.2^\circ$).

(iv) Detector package,

At the focus of each dish there is a package of seven phototubes, in which the central channel (designated as CENTRE or channel #1) is used to track the source, while the other six channels (labelled OFF or 23456 respectively as indicated in Figure 2.2) monitor neighbouring regions of the sky. These six Off Axis tubes are arranged in an hexagonal pattern with the remaining (On Axis) phototube at the centre; each tube covers one degree on the sky, the distance between any two PMT corresponding to 2°. The Off Axis tubes form a ring guard working as a control for rejection of events (Chapter III). Events triggering only the CENTRE channel are the most likely to come from the source.

As the spectrum of the Cerenkov flashes peaks around 3000-4000A, the tubes used are sensitive to blue and UV light. The tubes on the Mark III telescope have fast response, as the Cerenkov pulses are of very short duration (10 ns), and have optimum response in the spectral interval 3200 - 4500 A. They

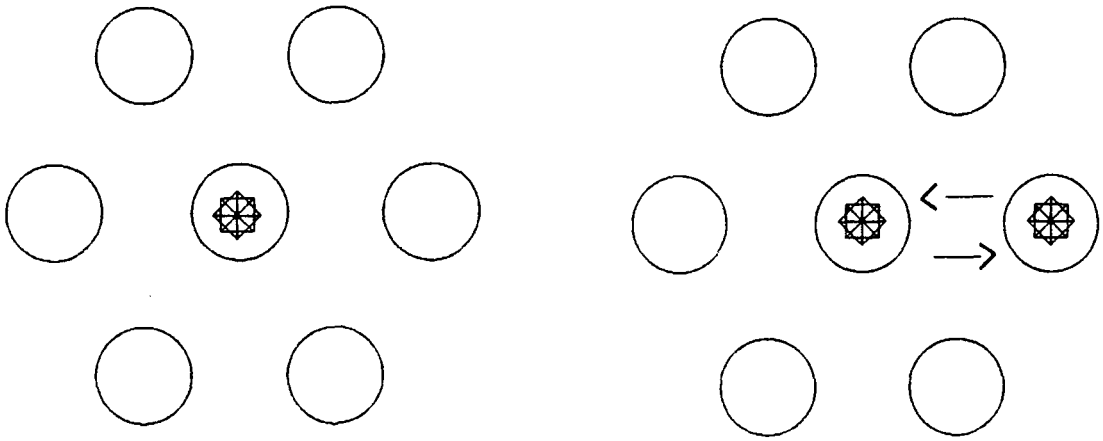

Operating Modes

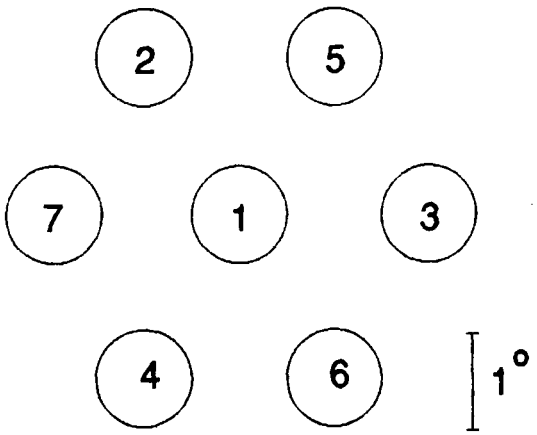

FIGURE 2.2

Nomenclature of PMT channels
and operating modes

are operated at high voltage, typically around 1500 or 1800 Volts, in order to achieve high gain and speed, with the implicit penalty of high noise from sky brightness.

Variations in sky brightness result in changes in the gain of the photomultipliers. A feedback LED system, named Automatic Gain Control (or AGC), is used to keep the gain constant under changing sky conditions due to zenith angle, or related to the comparison of intrinsically different regions in the sky. This AGC system works by keeping the total amount of light incident on the tube constant. Variations in the gain of the PMT using AGC warranty stability fall below 0.1%; this is particularly important in the chopping mode, where differences of a few percent in the counts are relevant.

(v) Modes of operation,

- the "tracking" mode,

In this mode the telescope is directly pointed with the CENTRE channel on source all through the run. This is the easiest operating mode and is used when the candidate source is known to have a periodicity in some region of the spectrum (typically in X-rays or radio frequencies). The presence of clouds, giving an unstable count rate, is not a direct obstacle for testing data for periodicities when these are below the range of weather variability (i.e. some minutes).

- the "chopping" mode,

The candidate source can be alternated between the CENTRE

channel (#1) for two minutes and channel THREE for the next two minutes. Channel #3 is chosen because no change in zenith angle is practically done. In this mode the AGC system is necessary to ensure a constant gain in the PMT; stable sky conditions are indispensable. A source of TeV γ-rays should give an excess in the number of counts On source with respect to Off source when comparing channels #1 and #3. Periodicity tests are less demanding than On/Off tests and as a consequence the chopping mode is used mainly when no period is known, as in the case of Scorpius X-1. It is occasionally used for pulsating sources as a complement: chopped data can be tested for periodicity, whilst the tracking mode does not allow testing for steady count excesses. The use of the tracking mode, rather than the chopping mode, in the case of pulsars is motivated by other reasons, like avoiding the intrinsic differences between phototubes #1 and #3 which could mask enhancements of the count rate in time intervals of the order of a few minutes.

- drift scan mode,

This operating mode was more commonly used in the "old days". The detector is pointed to a specific position on the sky, preferably near the zenith, where a potential source is to pass. Data are recorded before, during, and after the passage of the object, and the behaviour of the counting rate is tested. This mode, less sensitive than the other two, is nowadays mostly considered for the study of extended sources, like the Galactic Centre. Note that this mode can be run with a very primitive telescope as no steering is required.

(vi) Data Logging & Timekeeping, housekeeping

The data logging system is show in Figure 2.3. The system has 1 Mb of random access memory (RAM), which allows 16000 events (64 bytes each) to be buffered for future recording if a sudden increase in the event rate (~ 1 count.s^{-1}.$channel^{-1}$) occurs.

When any of the seven channels detects a strong signal in triple coincidence (all three dishes registering a relatively large amount of light in the same channel) an event is triggered by that channel and recorded. Every event record consists of:

- the arrival time of the event with a resolution of 1μs. A Rubidium clock is used, as accurate timing is needed for long term study of pulsars. The measured slip rate is 1.166 ms per month (or 4.5×10^{-10}), and is known with ± 0.014 ms.$month^{-1}$ accuracy (the error is then 5×10^{-12}).

- a "fire pattern" indicating which channel(s) has been triggered by the event. For example, the pattern "14" describes an event triggered by channels #1 and #4. The fire pattern also indicates which channel is On Source (usually channel #1 in the tracking mode, and either channels #1 and #3 when "chopping"),

- the charge on each of the 21 PMT for each event. For data analysis purposes only events triggering the On Source channel alone are used ("fire pattern" equal to 1 in the tracking mode, "fire pattern" equal to 1 or 3 in the chopping mode depending on the On Source channel). More recently the charges from the PMT have also been used to select events as a sort of variable aperture system (Brazier, 1991 and Chapter III).

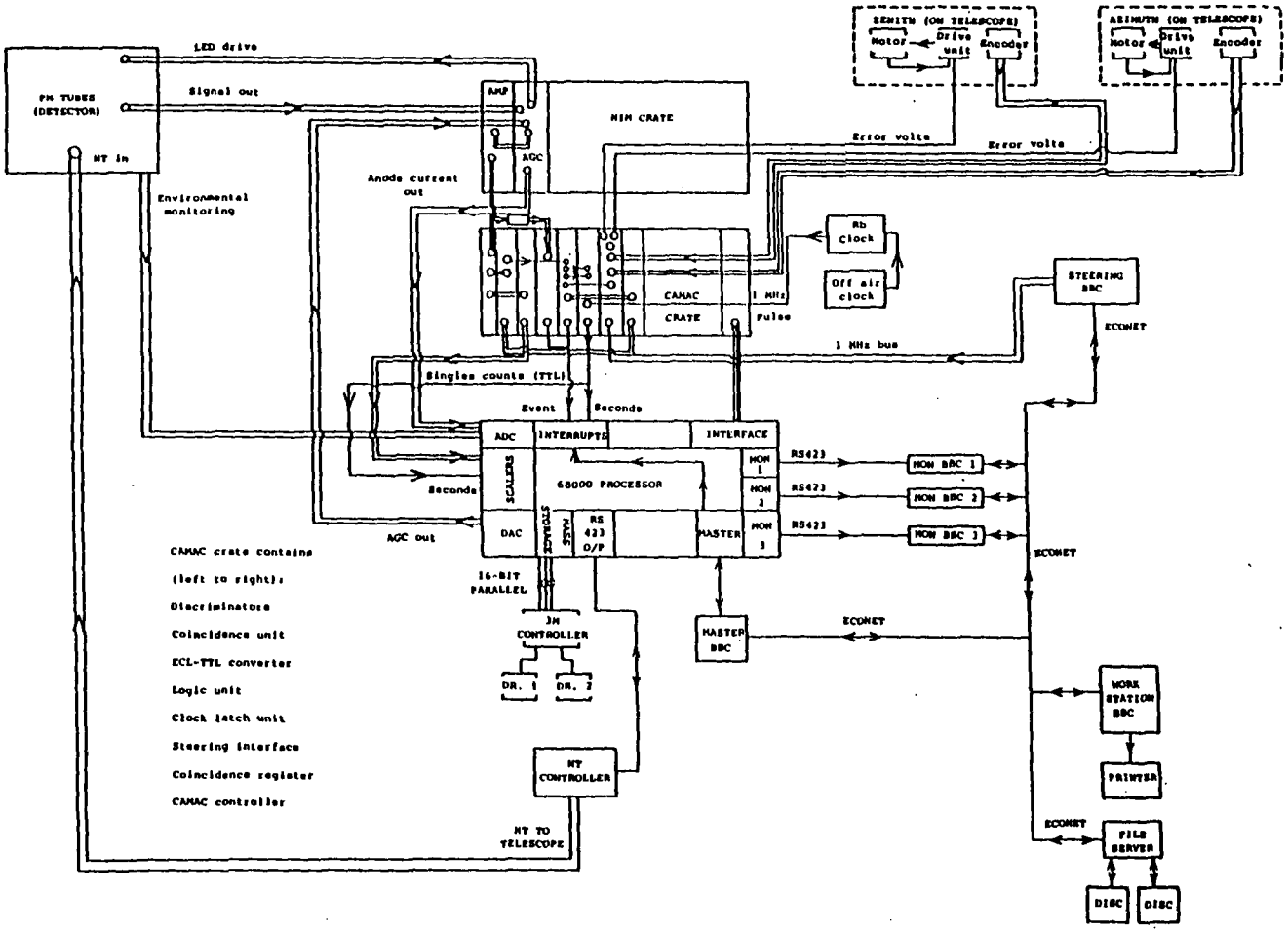

Figure 2.3

Data logging system of the Mark III telescope
(from Brazier et. al., 1989a)

The values of the target and actual coordinates of the object ion the sky, together with the anode currents on channels #1 and #3, are also stored. The dead time to record an event is 640 μs[1], although the system allows for the extra storage of 16 events during this time to be latched with a secondary dead time of 6 μs. At a lower rate, and with lower priority, a continuous monitoring of environmental conditions (like wind speed, humidity, temperature) is done throughout each run, in order to determine the stability of the system.

2.3.2 The Mark IV telescope at La Palma

Data from Sco X-1, GX 5-1 and SN1987A in this work were obtained with the Mark III telescope while data from Cyg X-3 were taken with the Mark IV, a smaller version of the Mark III designed to be easier to operate. Initially installed at La Palma in the Canary Islands (from summer 1988 to autumn 1989), at some 100 metres from the Issac Newton Telescope, it has been relocated recently to the same site as the Mark III at a distance of 100 metres from it. One interesting aspect of this change of site is the comparison between the behaviour of the telescope at high (La Palma) and low (Narrabri) altitude although the most relevant point is the use of both telescopes observing the same object simultaneously, counting most of the events independently (with

[1]Although believed previously to be 350 μs, a recent sample of electronic noise allowed us to measure the dead time of the system giving τ_d = 0.639 ± 0.092 ms.

something like 10% common showers).

The Mark IV telescope has basically the same design as the Mark III. The characteristics of both instruments are summarised in Tables 2.3(a,b).

	MARK III	MARK IV
ENERGY THRESHOLD at Zenith	300 GeV	380 GeV
SITE		
Location	Narrabri, N.S.W.	La Palma, I.C.÷
Latitude	30° 28' 59" S	28° 45' 34" S
Longitude	149° 49' 01" E	17° 52' 34" W
Altitude	260 metres	2400 metres
TELESCOPE DESIGN		
Number of Dishes	3	3
Number of Mirrors	43 + 44 + 43	18 + 18 + 18
Total Area (m^2)	3 x 12.4	3 x 5.4
Aperture (°) Design	1.4° ± 0.2°	
Aperture (°) Measured	1.5° ± 0.2° (0.9?)	

TABLE 2.3a

Some characteristics of the Mark III & Mark IV Telescopes

÷ Transferred to Narrabri

MIRRORS	
Radius	30 cm
Reflectivity (3500 ≤ λ ≤ 7200 A)	0.75 - 0.80
Focal Length (Inner mirrors) Focal Length (Outer mirrors)	240 ± 8 cm 260 ± 8 cm
PMTs	
Model	RCA 4518
Voltage (volts)	1500 - 1800
discrimination threshold	50 mV
Noise rate	30 kHz
Anode Current	25 μA
OPERATING MODES & PURPOSES	
Tracking =>	Period Testing
Chopping =>	Background Comparison
Drift Scan =>	Galactic Centre

TABLE 2.3a

Characteristics shared by the Mark III and Mark IV Telescopes

2.3.3 Imaging Telescopes: the Whipple cameras

The idea of an imaging detector able to resolve Cerenkov showers, and able to reject proton events, was suggested by Weekes & Turver (1977). There has been some scepticism about the plausibility of distinguishing both events (Macrae 1985). The

criticism is based on the premise that fluctuations between showers with the same kind of primary are expected to be larger than the intrinsic differences between p and γ-showers.

Telescopes recording two-dimensional Cerenkov images have been designed and constructed in the last few years (Cawley et al., 1990 and Vladimirsky *et al.*, 1989), the first instrument to become operational being the 37 PMT camera at the Fred Whipple Observatory on Mt Hopkins Arizona (lat. 31° 41', long. 110° 53' and altitude 2320 metres). A second, and more sophisticated version, of this sort of Cerenkov telescopes, the "High Resolution Camera" (HRC), recently started to operate. A complete description of the HRC is given by Cawley *et al.* (1989).

The HRC telescope is a ten metre reflector formed by 248 spherical mirrors each of 61 cm diameter in a nine ring hexagonal pattern. The field of view covers 4° with a resolution of 0.12°. At the focal plane is the detector package composed of 91 phototubes (Hamamatsu R1398), each with a sky projected diameter of 0.25°. These tubes are closely packed in five concentric hexagonal rings ("zones"). Eighteen larger tubes (RCA 6342/IV), covering a circle of diameter 0.50° each, arranged in an external ring, constitute the outer pixels of the detector. Figure 2.4 shows the detector packages of the HRC, the 37 PMT camera and the Mark III telescope at the same scale. Evens are triggered when two (normally, but up to six) of the inner 91 PMT produce a pulse above a threshold normally set at 40 photoelectrons.

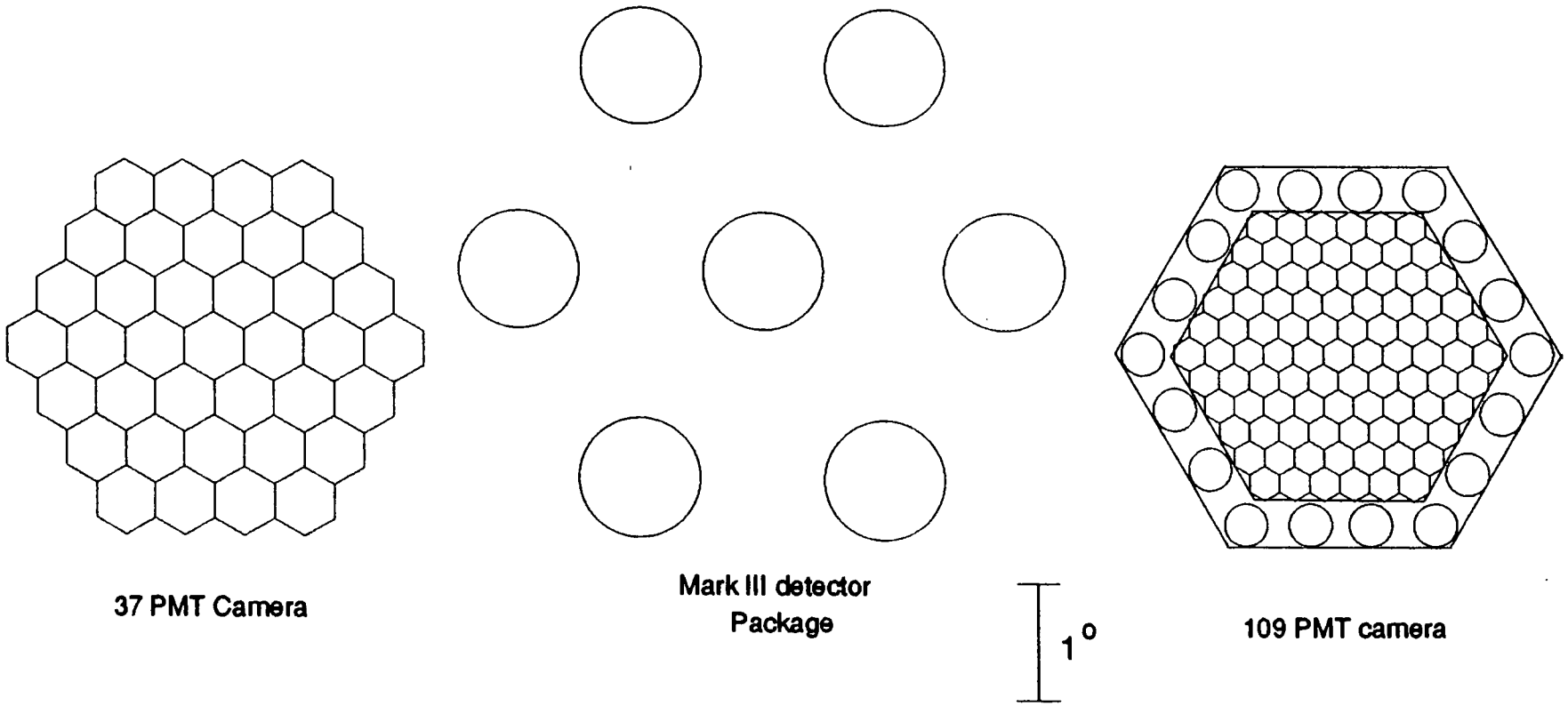

FIGURE 2.4

Relative dimensions of the Mark III
and Whipple detector packages

The imaging technique relies heavily on two points: (i) a prescription of measurable differences between p and γ-showers, and (ii) the measurement of the Cerenkov event with the consequent characterisation of the shower.

The first problem has to be attacked through numerical simulations of cascades, as no experimental measurements are feasible. As mentioned previously, Hillas (1985) and Hillas & Patterson (1986a) reported the results of numerical simulations which include the response of the HRC and defined a set of parameters characterising a shower. These are designated as {DISTANCE, WIDTH, LENGTH, MISS, AZWIDTH, CONC} and are illustrated by Figure 2.5. Hillas simulations predict fairly separate distributions for proton and γ-ray showers for some of the parameters, in particular for AZWIDTH. The predicted distributions for proton showers were found to be in good agreement with background measurements.

Quantifying these parameters relies on the image processing, done by subtracting pedestal values and normalising for the different gains of the tubes. The process is complicated by the distinct response of each phototube and its dependence on external (ambient) conditions, like the background light falling on it. While the background light falling on each phototube of the Mark III is equivalent to a star of magnitude 5.5, this raises to 7.0 and 8.5 for the 37 PMT and 109 PMT cameras respectively. Bright stars ($m_b \leq 5$) can increase the background substantially; fluctuations are not expected to increase at the same level but non linear effects may come into play. The 3rd

magnitude star ζ Tau in the field of the Crab forced the Whipple group to "eliminate" the tube by hardware.

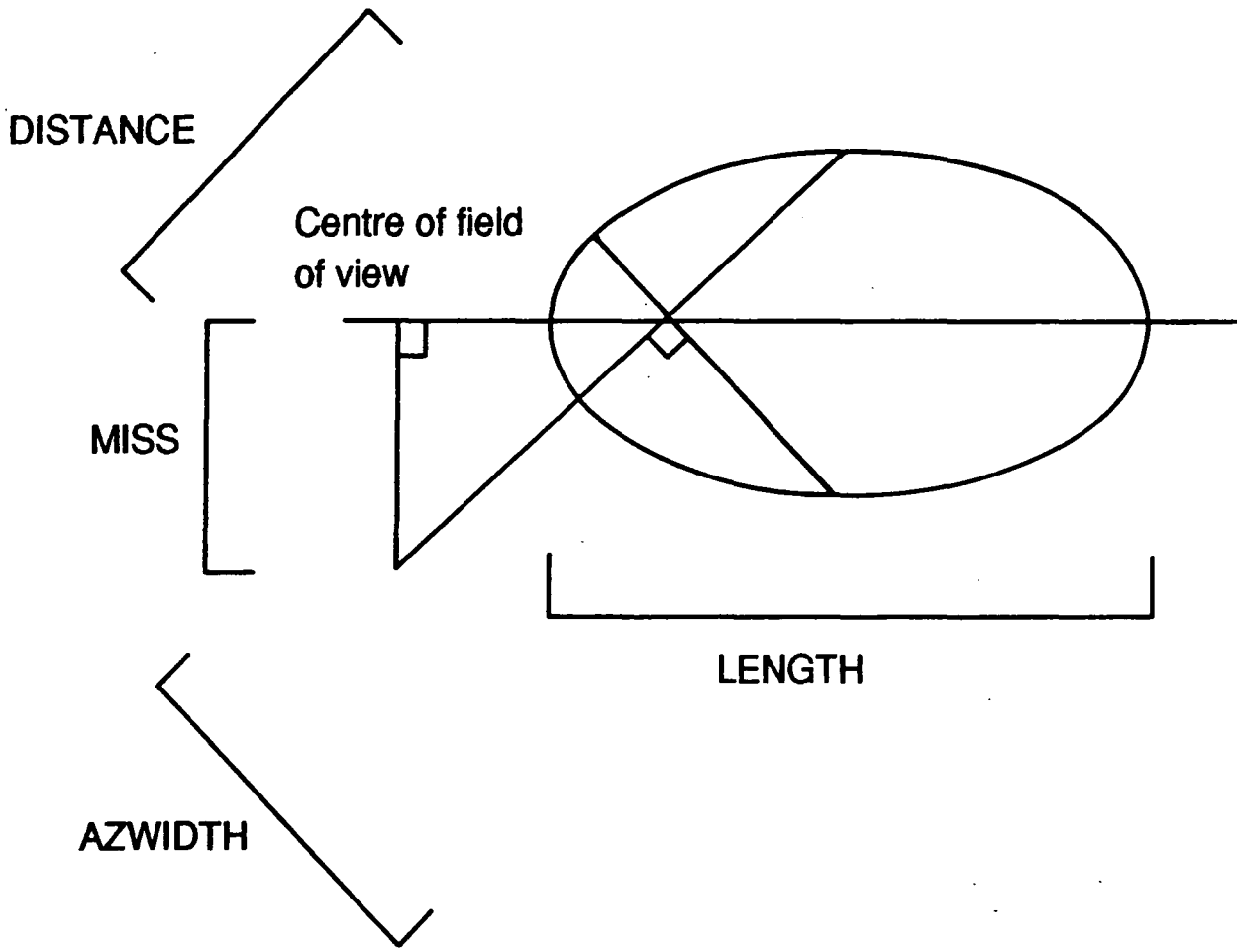

Figure 2.5
Parameter characterisation of a γ-ray image
(from Cawley et al., 1990)

Using the first version of this instrument, the 37 PMT camera, the Whipple group observed the Crab and reported an enhancement of the signal, when the AZWIDTH cut was applied, from a non significant 1σ excess up to a non statistical 8.9σ. Measurements with the new 109 pixel HRC have recently improved this figure to 15σ (Lang *et al.*, 1990), with the AZWIDTH cut being again the most powerful. As the background is efficiently rejected the Whipple camera is working with fluxes an order of magnitude below those of the previous methods.

These first encouraging measurements were soon followed by some puzzling results:

- contrary to all previous results the emission was not found to be pulsed (Ramana Murthy & Wolfendale, 1986, give a list of reports of pulsed emission from the Crab). It is worth remembering that, from COS-B and SAS-II observations, it appears that *all* the emission from the Crab above 0.4 GeV is in the pulsed component (Longair, 1981). Therefore, a cutoff in the pulsar spectrum relative to the Nebula emission has to occur. Also, while the presence of pulsations is evidence for emission from the pulsar, the lack of pulses does not indicate anything about the origin of the excess,

- when the cuts are applied to raw data showing a pulsed signal from Hercules X-1 the peak in the periodogram disappeared. The same occurred with data from 4U0115+63 (Macomb *et al.*, 1991) and 1E2259+586 (Cawley *et al.*, 1991). Upper limits for these sources have been set at levels well below fluxes previously reported as signals, in conflict with evidence accumulated for

more than a decade. Although in principle these differences can be attributed to long term variability, especially for objects like Cygnus X-3 and Hercules X-1 (4U0116+63 had previously been quoted as a steady source), the HRC has not found any indication of activity other than the unpulsed signal from the Crab nebula.

This uncomfortable dilemma points towards uncomfortable solutions:

(i) TeV astronomers have been underestimating the degrees of freedom involved in their statistical analysis and consequentially reporting fluctuations systematically for more than a decade. The conflicting results are based on periodicity tests; most of the statistical methods of these tests are well known and such an impressive chain of mistakes appears unlikely,

(ii) the imaging cuts "fake" a signal from the Crab. The results appear to be genuine and are consistent with those found by the University of Michigan group using rough imaging with only seven phototubes (Akerlof *et al.*, 1990). Systematic effects are far from obvious. It must be said that, while the counts from the two reported observations of the Crab seem to indicate a good rejection of protons, it is not clear what the proportion of γ-rays accepted is (an acceptance of 50% or even 30% is compatible with the two Whipple results; Appendix II),

(iii) something is amiss in our understanding of how cascades occur. This is in fact unlikely as interactions occur at energies accessible with particle accelerators and therefore cross sections are well known. Errors in the simulations would not be expected to result in the present conflict,

(iv) X-ray binaries like Hercules X-1 and Cygnus X-3 emit some unknown kind of long lived neutral radiation. However, it is difficult to understand how this radiation has not been found in particle accelerator experiments,

(v) the imaging cuts do not work in the case of X-ray binaries. If, for example, the imaging cuts worked properly in the energy interval 0.1 to 5.0 TeV but not above the latter value while binaries emit photons mostly above 5 TeV, then a timing or raw DC measurement can give a signal which would disappear under imaging cuts. Although the photon energy spectrum is generally believed to have a power-law dependence with energy, it could well be that some mechanism suppresses photons inside particular parts of the spectrum. In Chapter VI it is shown that absorption of high energy photons by the radiation field of an accretion disc can produce such an effect. Although this argument can be questioned, it seems more reasonable to postulate an unexpected shape for the energy spectrum rather than to invoke "new physics" at energy ranges available to the experimental physicist.

None of these solutions appears to be satisfactory and the answer to the present dilemma is not likely to arrive before measurements at the same flux levels as those reported by the Whipple group are made, preferably with an alternative technique. Although imaging is the most promising tool for TeV astronomers consistency is now much required: different methods should give the same answers.

2.4 FUTURE PROSPECTS: OTHER METHODS & COMMENTS

The sensitivity of present TeV telescopes, with the probable exception of imaging cameras, appears to be below the level required to obtain non statistical results (i.e. well above the 3σ level). The next generation of TeV telescopes has to rely on a more solid basis, either in a significant improvement in the count rate or in background rejection. Two prospects are:

(i) Arrays of independently counting Cerenkov detectors;

The flux from the Crab nebula reported by the Whipple group is 1.8×10^{-11} cm^{-2}s^{-1} above 0.7 TeV (Weekes *et al.*, 1989) or about only 0.2% of the cosmic ray background and more recent measurements give 7×10^{-11} cm^{-2}s^{-1} above 0.4 TeV (Lang *et al.*, 1990). A sufficiently large number of Mark IV type telescopes in an array, each with a count rate of two events per second (a healthy count rate) observing for 50 hours, would be able to detect such a signal. Table 2.4 gives the number of such telescopes required for a detection at the "x" sigma level assuming an aperture of 1° and a flux of 7×10^{-11} cm^{-2}s^{-1} (the inferred γ-ray flux is 0.4% the cosmic ray background).

The values shown in Table 2.4 are likely to be lower bounds as they assume telescopes counting independently (no common showers) and all the observing time is assumed to be useful (no bad weather/data). It is clear that an array of ten "ring guarded" telescopes should have a significant signal ($\geq 8\sigma$) after

50 hours of observing under stable conditions. Although an array of counting telescopes has the advantage of only relying on the isotropic characteristics of the cosmic ray background, its size is ultimately limited by economics. The success of proton rejection techniques is likely to lead to instruments of greater sensitivity.

σ Level	3	6	9	12	15
Total Number of events required x 10^6	0.55	2.21	4.98	8.86	13.8
Total Observing Time with a Counting rate of 2 Hz (in Hours)	77	308	692	1230	1917
Number of Telescopes required for a detection in 50 hrs	2	7	14	25	39

TABLE 2.4

Events, Hours & Number of Telescopes (considering 50 Hours per Telescope) required to detect at a particular Sigma Level the TeV Flux Reported for the Crab Nebula by the Whipple Group using Non Imaging Telescopes

(ii) Rejection of proton-showers and other background,

Differences in the shape of the Cerenkov time pulses have recently been used to reject proton events and from there to

obtain a 4.2σ excess after only 100 *minutes* of ON source data (Tumer *et al.*, 1990). Each event has to be resolved at the nanosecond level. The authors do not mention if their rejection criteria were based on simulations or on quantitative estimations of the differences between proton and γ-ray events (the latter appears to be the case).

Another discrimination criteria proposed is based on spectral differences (UV excess in the p-showers; Stepanian, Fomin & Vladimirsky, 1983). The GT-48 telescope of the Crimean Astrophysical Observatory relies partially on this principle (together with imaging techniques; Vladimirsky *et al.*, 1989).

In order to reject proton events, future detectors are likely to rely on more than one of these aspects: geometrical shape, time profile of the Cerenkov pulse, spectral differences and the construction of arrays of Cerenkov telescopes. It is worth noting that a perfect rejection of protons (and acceptance of γ-rays does not imply a noise free astronomy as cosmic ray electrons are likely to become the ultimate noise and most probably inevitable background. Working at 0.4 TeV and with a field of view of 1.2° diameter (80 min^{-1} proton rate), the electron background has a flux of $\sim 7.7 \times 10^{-11}$ $cm^{-2}s^{-1}$. Using one detector (shower area $\approx 10^8$ cm^2) and fifty hours of observation objects with fluxes below $\sim 6.2 \times 10^{-12}$ $cm^{-2}s^{-1}$ (at $E \geq .4$ TeV) would be undetectable at the 3σ level. This is just one tenth of the value reported from the Crab and twice the upper limit derived for 4U0115+63. Arrays of Cerenkov telescopes would then have a last word.

III. NOISE, DATA PROCESSING & DATA ANALYSIS

3.1 INTRODUCTION: COSMIC RAYS AND NOISE

Well before the birth of γ-ray or X-ray astronomy, cosmic ray physics was already firmly established. Cosmic ray studies gave the first direct estimates of chemical abundances outside the solar system and the Galaxy. Until the recent development of large accelerators, cosmic rays provided the only available sample of high energy particles, with energies up to 10^{20} eV, well above the limits presently conceived for accelerators. Explaining how particles can acquire energies comparable to that required to type a keyboard provides a though challenge to theoreticians. The energy spectrum of cosmic rays for energies between 3×10^{9} eV and 3×10^{15} eV is well fit by a power law of index 1.6 while the most energetic cosmic rays, presumably of extragalactic origin, follow a steeper spectrum of index 2.1. For a total collecting area A and angular aperture Ω the flux of cosmic rays, mainly protons, above a threshold energy E is:

$$J(\geq E) = 1.47\ s^{-1}\ (A/10^{7} cm^{2})\ (\Omega/10^{-3} sr)\ (E/250GeV)^{-1.6}\ , \qquad (III.1)$$

equivalent to a particle flux of $1.6 \times 10^{-8}\ cm^{-2}.s^{-1}\ (E/TeV)^{-1.6}$ for an aperture of diameter one degree. The Mark III has a typical count rate between 50 and 100 events per minute at a threshold energy of around 300 GeV.

In 1954, in the very early days of VHE γ-ray astronomy, Jelley and Gould (Jelley, 1986) made an unsuccessful attempt to detect cosmic rays from the direction of the Crab. Nowadays we known that had they found a signal this would have been due to γ-ray emission; charged particles in our Galaxy are deflected from their force-free straight path by the (3 μG) Galactic magnetic field. The Larmor radius, defined as the radius of the circular motion described by the projection of the movement of a charged particle perpendicularly to the field line, quantifies this deflection. Its value, for a proton of energy E in the magnetic field B of the Galaxy, is well below typical distances between stars (Hillas, 1984a):

$$r_L = 4 \times 10^{-4} \text{ pc } (E/\text{TeV}) \ (1\mu\text{G}/B) \quad , \quad \text{(III.2)}$$

reaching nearly one kpc at EeV (10^{18} eV) energies. Only neutral long lived particles like neutrons, neutrinos and photons, follow straight paths. However, free neutrons have a measured rest mean life of 887.6 ± 3 seconds (Lindley 1989; Mampe *et al.* 1989) and cannot travel more than one parsec without decaying unless their energies are above 10^{16} or 10^{17} eV[1]. Neutrinos, although stable, interact with much smaller cross sections and therefore do not trigger electromagnetic air showers (EAS) in the atmosphere.

---

[1] Recent evidence by Cassiday *et al.* (1989) of an excess of cosmic rays at energies above 10^{18} eV from the direction of Cygnus X-3 might be the first example of a detection of baryons from an astronomical source other than the Sun.

As a consequence cosmic rays, constituted mainly of charged particles like protons, He nuclei and electrons (their relative abundance are in the ratio 1 : 0.14 : 6×10^{-3}), do not travel in straight paths, and lose any information concerning their production sites in transit. They constitute the background noise (events uncorrelated in time or space) from where punctual sources of γ-rays are to be distinguished. For a threshold energy of 250 GeV the luminosity required by a source located at one kiloparsec to have the same flux as the cosmic ray background, (expression III.1) is nearly 10^{37} erg.s^{-1}, or 10^{39} erg.s^{-1} at ten kiloparsecs. Signal to noise ratio is a fundamental problem in VHE γ-ray astronomy, as reported signal strengths are at best a few percent of the cosmic ray background. In general, it is necessary to use statistical methods to search for either temporal or spatial correlations in data samples (peaks in a periodogram or count excesses).

3.2 SEARCH FOR COUNT EXCESSES

3.2.1 Categories of events & chopping mode

Events are classified as ANY, CPLUS, CONLY and CHOP depending on which channel, or channels, are triggered. Triggering thresholds are previously set, and any tube registering a charge above that level is said to have fired. Categories of events are defined as follows (Figure 3.1; see also Appendix I):

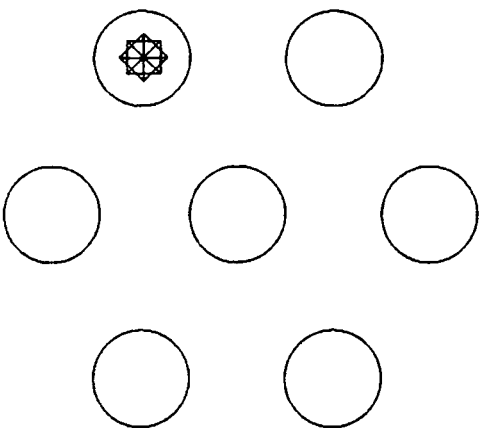

OFFAXIS

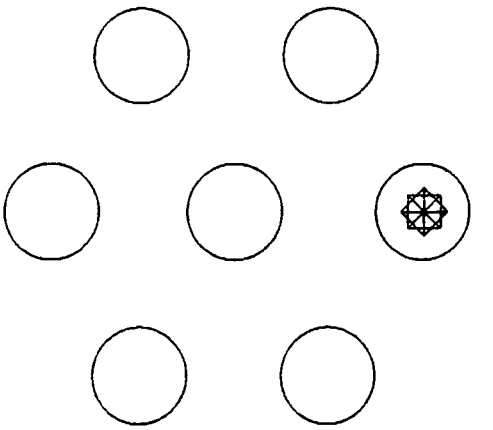

CHOP
(when Channel #3 is ON Source)
OFFAXIS
(when Channel #1 is ON Source)

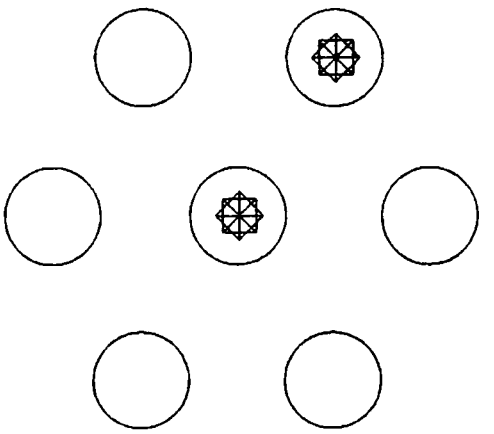

CPLUS

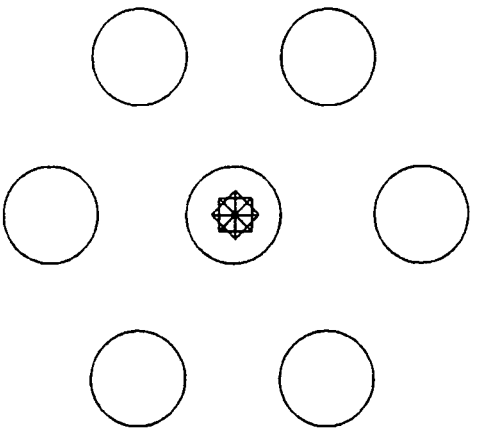

CONLY

Figure 3.1

Categories of events

- ANY events are those that trigger any one of the seven tubes. Obviously those not firing the on source channel are most likely to be cosmic rays and can be rejected as noise;

- CPLUS events trigger the CENTRE (#1) channel;

- a sub-category of these are the CONLY events which only trigger the CENTRE channel. These are the principal candidates for γ-rays;

- when data are recorded in the chopping mode (Chapter II), the source is alternately viewed by channel #1 and one of the lateral channels (#3 usually) in a four minute cycle. CHOP events are those with the ON source channel (either CENTRE or THREE) being the only one fired.

In CONLY events the recorded charge information (photon density), or QT, can be used to reject further events, those with lateral channels "almost" firing. This has an effect similar to reducing the effective aperture of the telescope. Although QT software cuts have proven useful in enhancing signals, for example with Centaurus X-3 (Brazier *et al.*, 1989b and 1989c), the data selection criteria used in this work has only relied on the firing pattern.

3.2.2 Method

As already mentioned in Chapter II, data intended to give an estimation of the direct flux from a candidate object are taken using the "chopping" mode: the telescope is pointed to the candidate source for two minutes (i.e. source on channel #1),

then to the background (source on channel #3) for the next two minutes. A two hour data file would contain thirty of these four minute chopping cycles. Because the count rate is dependent on the zenith angle, the counts of a particular two minute bin on source, ON(j), have to be compared with the sum of half the counts of the previous and following off source bins, that is OFF(j-1)/2 + OFF(j+1)/2, rather than with a complete neighbour. A datafile taken under clear and stable skies, having an odd number of cycles (2n+1), provides three estimators of count excesses, two independent for channels #1 and #3, and their sum:

$$\mathrm{Exc\#1} = \sum_{j=1}^{n} \left[\frac{1}{2}\,\mathrm{ON\#1}(2j-1) - \mathrm{OFF\#1}(2j) + \frac{1}{2}\,\mathrm{ON\#1}(2j+1) \right] ,$$

$$\mathrm{Exc\#3} = \sum_{j=1}^{n} \left[\mathrm{ON\#3}(2j) - \frac{1}{2}\,\mathrm{OFF\#3}(2j-1) - \frac{1}{2}\,\mathrm{OFF\#3}(2j+1) \right] ,$$

$$\mathrm{ExcTOT} = \mathrm{Exc\#1} + \mathrm{Exc\#3} \quad . \qquad \text{(III.3)}$$

It should be noted that channels #1 and #3 are not really equivalent, as the CENTRE channel (#1) is surrounded by six guard channels while channel THREE is only guarded by three channels (CENTRE, #5 and #6; see Figure 3.1); this results in a better background rejection for the CENTRE channel. In fact, before an update was done in 1989, only channels #1 to #4 were used to trigger events and, as a result, channel #3 was only efectively

guarded by #1 (as #5 and #6 would not reject events). Also the gain of each tube, kept constant for channels #1 to #4 by the AGC system described in Chapter II, is different and therefore each PMT has its individual count rate. Under the hypothesis that no γ-ray source is present (the *null hypothesis*) the counts from both channels are expected to have a Poisson distribution and the estimators of excesses, Exc from III.3, should follow:

$$\langle Exc \rangle = 0$$

$$\sigma(Exc) \approx \left[\sum_j \{ ON + OFF \} \right]^{1/2} . \qquad (III.4)$$

When an excess is found in both channels, or at least in the sum of their counts, and no external influence on the count rates is present (like a cloud), it is possible to estimate the (Poissonian $\approx$ Gaussian) probability to observe such an excess. Excesses above three standard deviations have a 1.36×10^{-3} probability of arising by pure chance, and are considered as evidence for the existence of a TeV γ-ray source.

3.2.3 Example: the Scorpius X-1 database

(i) Introduction:

Scorpius X-1 is the brightest non solar X-ray source on the sky. Although it is probably the most studied low mass X-ray binary, the optical (and IR) emission from the companion, presumably a red dwarf, has yet to be detected. The system is dominated by the

flow of matter onto the neutron star via an accretion disc, accompanied by optical and X-ray emission. The study of the time and energy dependence of its power spectrum, where quasi periodic oscillations (QPO) were found some five years ago (Middleditch & Priedhorsky, 1985 and 1986; van der Klis, 1989a), has become a major tool in helping to understand the behaviour of the inner regions of the accretion disc. It was first reported as a TeV source by Jager *et al.* (1986), then by Brazier *et al.*, 1990b.

(ii) The Durham database and results

The Durham group has recorded data on Scorpius X-1 since March 1987. The 1987 database consists of three "good weather" nights, none with an excess above 1σ, giving a global count of 16750 events On source against 16677 events Off source. In contrast both the 1988 and 1989 data did show a positive excess as presented in Brazier *et al.* (1990b).

In 1988 a dozen datafiles were recorded under clear conditions, containing in total more than 270 000 events and showing a 2.5σ count excess. Although all individual excesses were below the 3σ significance level, ten of twelve nights showed excesses between 0.2σ and 1.9σ; only two nights did not have a positive signal (with significances of -0.5σ). The overall count excess translated to a flux of $(1.2 \pm 0.4) \times 10^{-10}$ cm^{-2}s^{-1} for photons of energies above 0.3 TeV (Brazier *et al.*, 1990b).

The following year only three datafiles were recorded, as bad weather in Narrabri prevented useful observations during June and July. These data were recorded on the nights of the 2nd, 6th

and 8th of May, and showed respective excesses of 2.3σ, 2.0σ and 1.3σ. The count rate of the first, and longest, of these nights covering nearly four hours, shown in Figure 3.2, presents fluctuations with respect to a parabolic fit consistent with Poisson statistics ($\sigma/\sigma_{Poisson} \approx 0.907$). This datafile, like the ones of the 12th and 13th of May 1988, has a high and well behaved count rate (sky conditions were described as excellent in all three cases). The 1989 data indicate a flux of photons of $(2.0 \pm 0.6) \times 10^{-10}$ cm^{-2}s^{-1}, for E $\geq$ 0.3 TeV, significant at the 3.1σ level. The luminosity implied by the 1988 and 1989 Durham data, assuming a distance to the system of 1.5 kpc, is about $L(>0.3 \text{ TeV}) \approx 2 \times 10^{34}$ erg.s^{-1}; this is more than three orders of magnitude below the average X-ray energy output of $L(2\text{-}11 \text{ keV}) \approx 7 \times 10^{37}$ erg.s^{-1}. The 1988 data also gave indications of a possible orbital modulation; a careful analysis of these data will be presented in the next section.

After these encouraging indications of high energy γ-ray emission from Sco X-1, during May, June and July 1990 data were taken at the Narrabri site with both the Mark III and Mark IV telescopes. The former detector recorded twelve datafiles under clear skies with more than 22 x 10^4 (ON + OFF) events in total. The Mark IV, running under preliminary conditions after arriving at the Narrabri site from La Palma, only took usable data during five nights (simultaneously with the Mark III), recording nearly 7 x 10^4 (ON + OFF) events in total. While the Mark IV data showed an excess below the 3σ significance level (1.4σ) the larger Mark III database was consistent with no emission. The Mark III data

that were taken simultaneously with the Mark IV showed a very smal excess (0.4σ) well below any statistical significance.

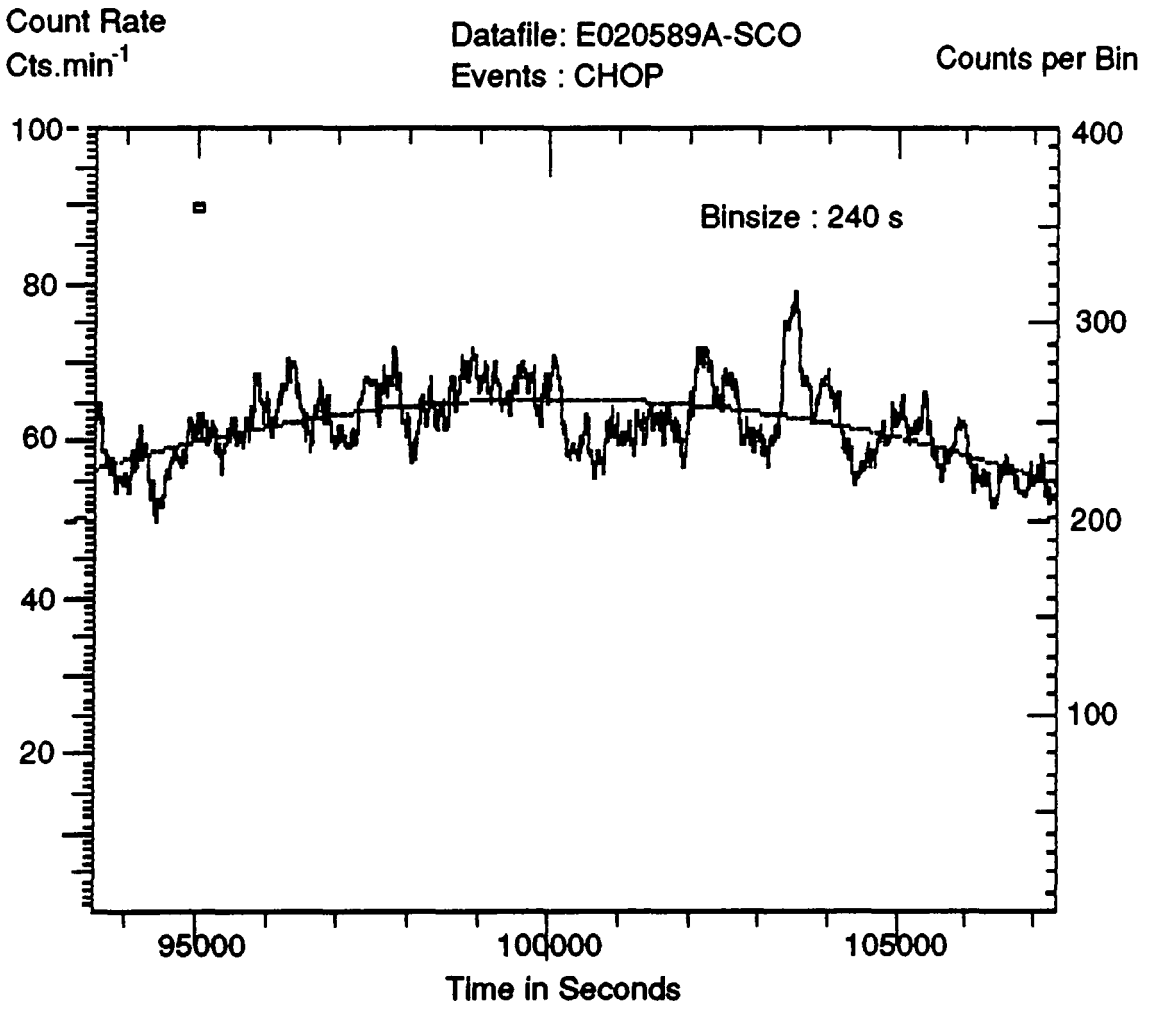

Figure 3.2

Count rate of Scorpius X-1 data taken on May 1989
The broken line is the parabolic fit to count rate
Binsize is equal to chopping cycle
to include both channels equally

3.2.4 Long term behaviour and Orbital modulation in Sco X-1

(i) Previous work,

The Scorpius X-1 database has more than 6 x 10^5 (On+Off) events and spans over four years; how the signal has varied during this time may give an insight on the long term behaviour of the VHE emission. The signal strength, as a percentage of the cosmic ray background, averaged over each observing season is shown in Figure 3.3. The source appears to have passed from a low state in 1987, to a high state during 1988 and 1989, to finally return to a low state in 1990. Both the 1988 and 1989 data gave evidence for a steady source on timescales between days and months.

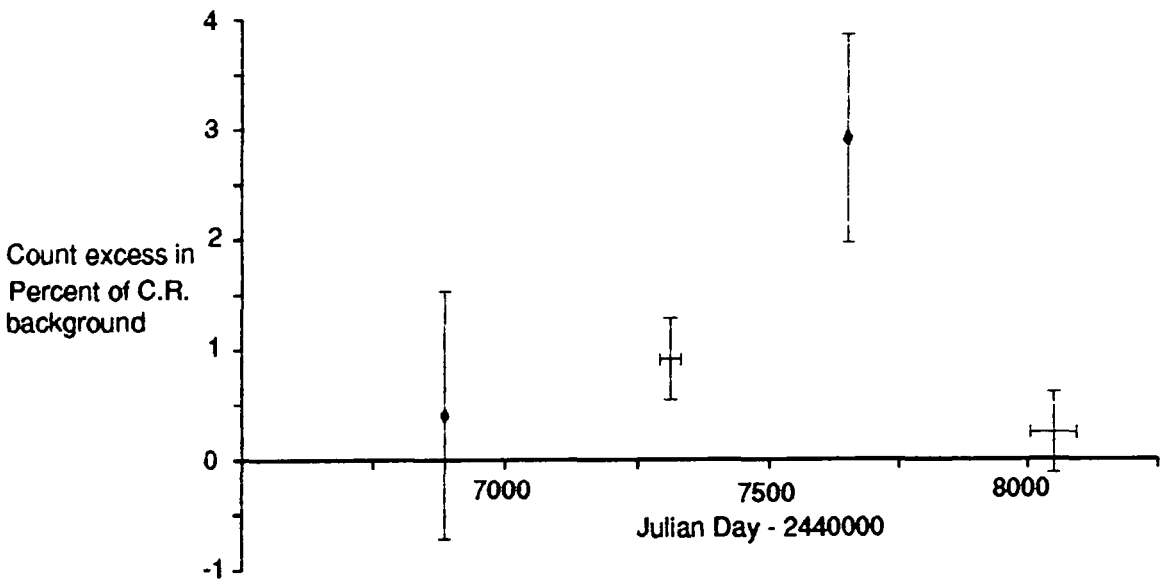

Figure 3.3

Long term behaviour of Scorpius X-1 data
Signal strength averaged over observing seasons
Error bars in signal strength represent 1 sigma
Error bars in Julian day represent the duration
of the observing season

Figure 3.4, from Brazier *et al.* (1990b), shows the variation of the signal strength with orbital phase using the epoch of superior conjunction as determined by Crampton *et al.* (1976). As the excess in the 1988 data was much more significant in the Centre channel, which had a full ring guard while channel #2 did not (guard system was implement for channel #2 in 1989, as mentioned in Section 3.2.2), the points included were exclusively CONLY events (rather than CHOP). Although an enhancement in the signal strength for orbital phases between 0.25 and 0.50 is apparent, the data are clearly far from conclusive, being consistent with either a 100% sinewave modulation or no dependence with orbital phase at all.

(ii) Construction of orbital light curves

Light curves were constructed for the 1988 data and for the entire, 1987-1990, database (one curve for CONLY events and another including all the events). The phase coverage in 1987 and 1989 was not complete, and the 1990 data did not show any effect; therefore no conclusion regarding an orbital modulation can be draw from these data. The method used here is different to the one presented in Brazier *et al.* (1990b), where individual observations were divided in segments, covering approximately two hours each (~ 0.1 phase); the orbital phase associated to each segment was that of the middle of the two hour observation. The differences between the method used in Brazier *et al.* and here are:

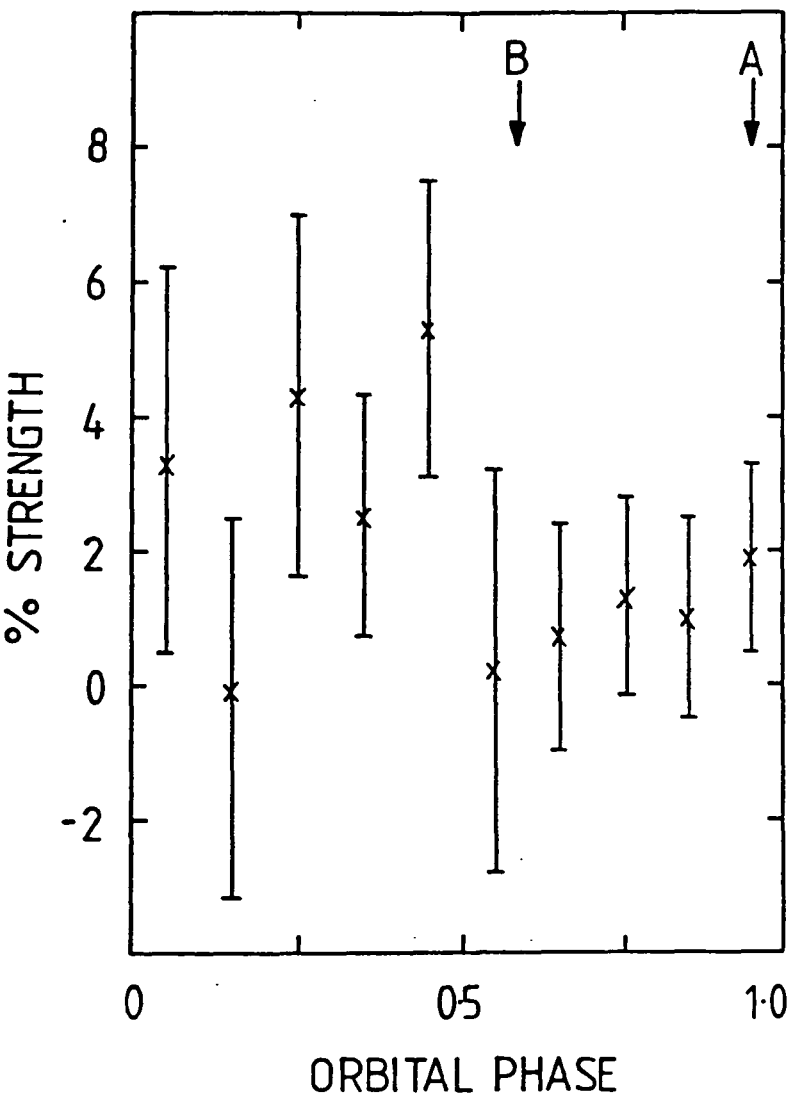

Figure 3.4

Variation of signal strength of VHE γ-ray emission with orbital phase
Phase 0 defined as superior conjunction from Crampton et al. (1976)
A shows the minimum optical emission from LaSala & Thortensen (1985)
B shows the minimum in X-ray emission from Priedhorsky et al. (1987)
Figure from Brazier et al., 1990b

- the epoch of eclipse considered here was from of LaSala & Thorstensen (1985; hereafter LST). This is a more recent update on the orbital parameters of Sco X-1, compared with the original detection of the orbital period by Gottlied *et al.* (1975), and the following paper by Crampton *et al.* (1976). LST considered the motion of both the Hβ and the HeII lines, concluding that they must arise from different parts of the system, as they do not follow exactly the same orbit. In particular, these authors conclude that the Helium line at 4686 angstroms is the most likely to follow the motion of the compact object, which is expected to be the source of high energy emission. The velocity of this line is fitted by the following parameters (a.sini assumes a circular orbit):

$$\text{Orbital period} = 0.787313 \text{ days} \quad ,$$
$$\text{Epoch eclipse} = \text{JD}2445084.53638 \quad ,$$
$$\text{a.sini} = 2.127 \text{ light.seconds} \quad .$$

As the orbital period is well determined ($\pm 10^{-6}$ days; error bar in JD is ~ 0.03 days), this ephemerides only introduces a small shift in phase (≤ 0.1) in relation to Crampton *et al.*, (1976);

- the light curves were computed with twenty bins. The number of bins was chosen prior to analysis;

- the main difference is how orbital phases were related to the data. Each four minute chopping cycle was treated independently; associated to each cycle there is an excess, computed from expression III.3, an error (obviously large for an individual cycle), and a time with an uncertainty of two minutes.

Each four minute cycle was then included in the corresponding orbital phase bin, the uncertainty in phase being 10^{-3} (i.e. two minutes). Therefore the orbital phase was included more accurately than in Brazier *et al.* (1990b).

(iii) Results and statistical significance

The orbital light curve obtained with this method for the 1988 data, using only channel#1 events, is shown in Figure 3.5; this can be compared with Figure 3.4, the data in both plots being the same. A broad feature covering from orbital phase 0.15 to 0.55, almost a third of the orbit, is present in the 1988 CONLY light curve (Figure 3.5).

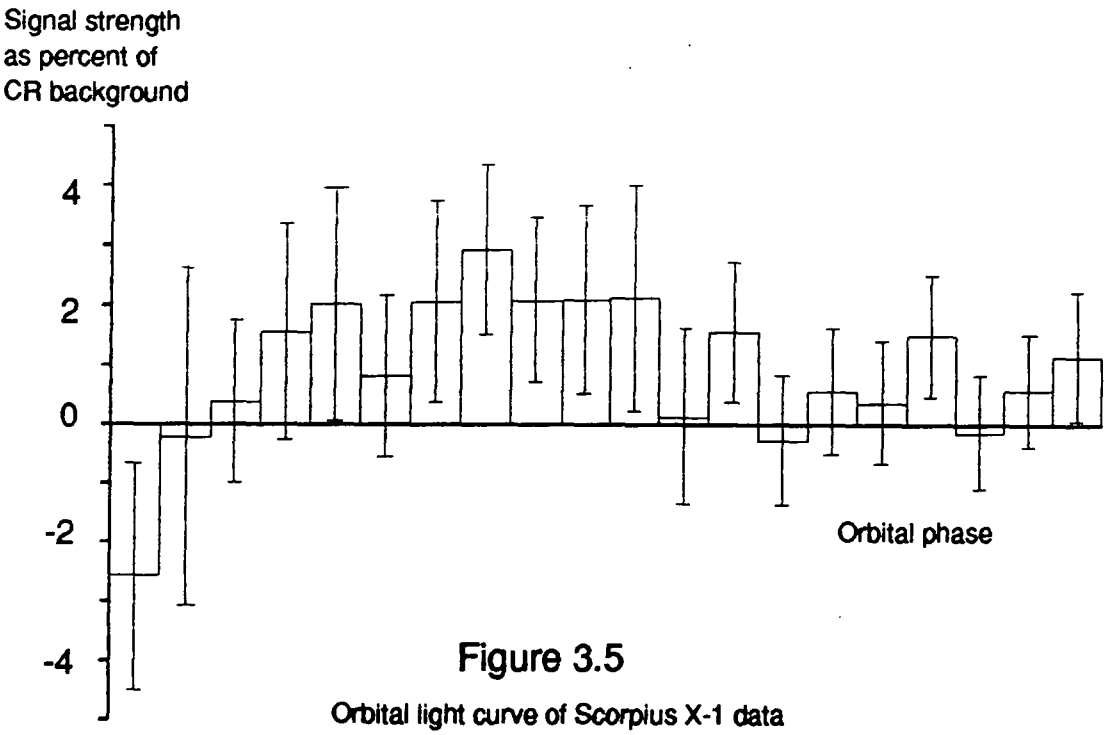

Figure 3.5

Orbital light curve of Scorpius X-1 data
Data are from 1988 and selection is CONLY

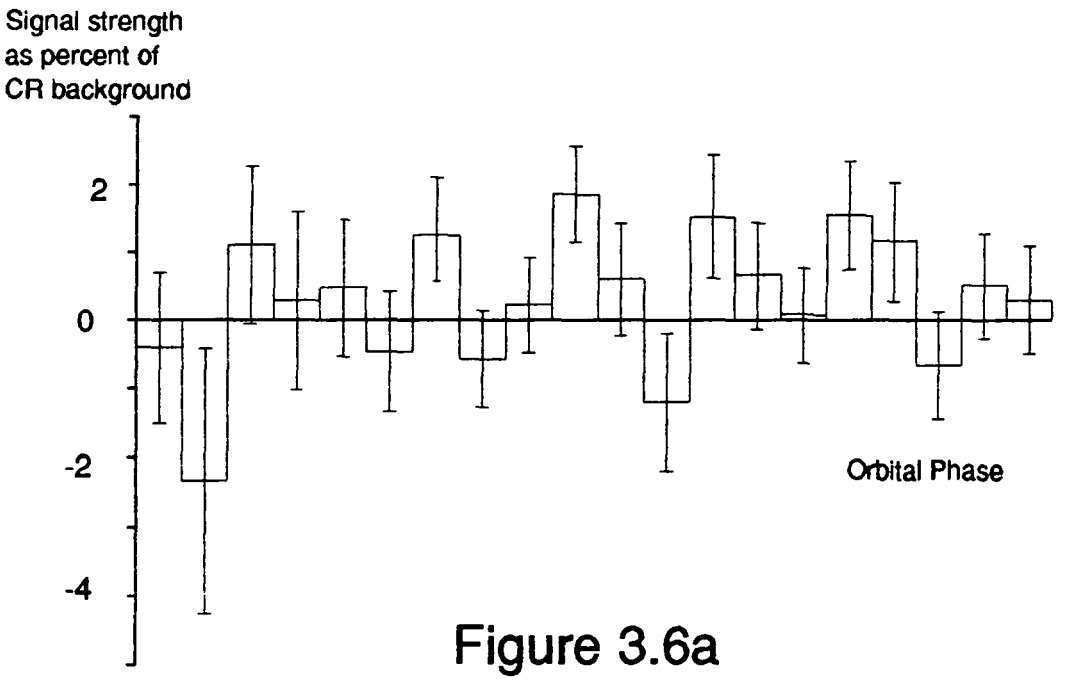

Figure 3.6a

Orbital light curve of Scorpius X-1 data
Data are from 1987 to 1990 and selection is CONLY

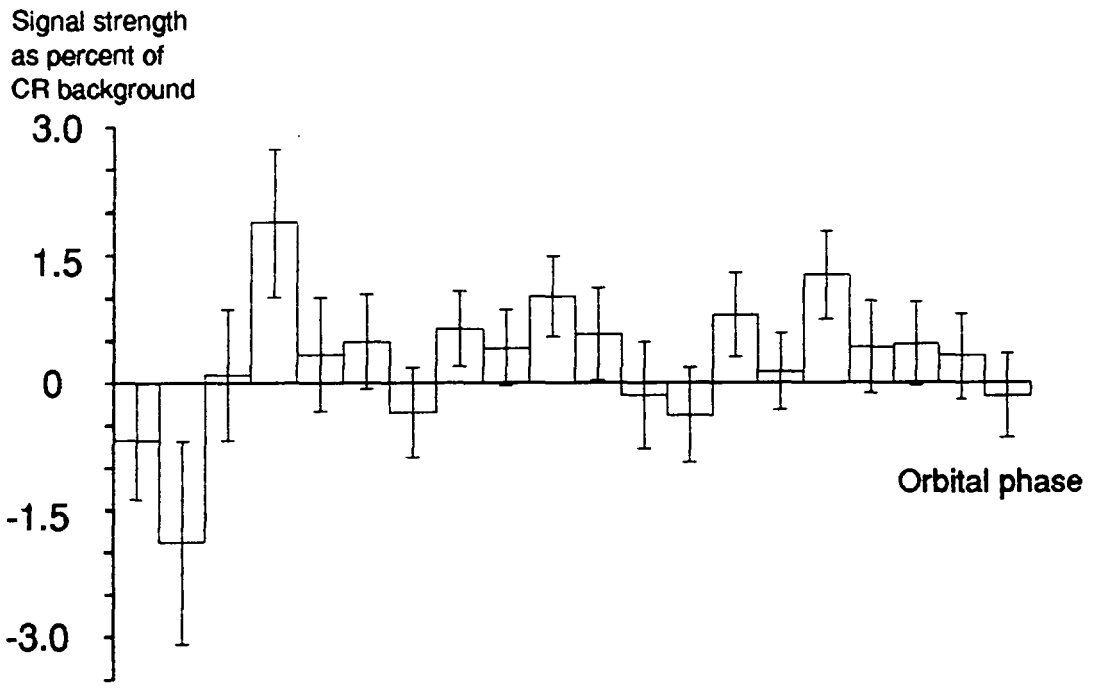

Figure 3.6b

Orbital light curve of Scorpius X-1 data
Data are from 1987 to 1990 and selection is CHOP

Figures 3.6a and 3.6b show the strength *versus* orbital phase for the entire Scorpius X-1 database (1987 to 1990), using channel#1 and both channels respectively. No effect is evident in Figure 3.6a. For the full database (1987-1990; all data), including the data with no signal, the curve is mostly flat, except for three (non consecutive) bins each with an excess above 2σ, the highest being 2.5σ at orbital phases (0.75-0.80). Considering the number of bins (20) and the amplitude of the excess, this has a small statistical significance (~ 12%).

However, the broad feature in Figure 3.5, where eleven consecutive bins have an excess, is more interesting, and it is relevant to estimate its statistical significance. In terms of its harmonic content, the power in the first harmonic is 4.9, and has a probability of 4.6×10^{-3} to arise by pure chance[2]; this peak corresponds to orbital phase 0.394. When accounting for nine trials, one per harmonic (there are nine trials rather than ten because frequency "0" corresponds to the mean of the sample), the final probability is 4.1%. It is arguable if all these trials have to be considered, as a modulation with a weak first and second harmonics would not give a "realistic" light curve

---

[2] Probabilities computed using:

$$\text{Prob}(nR^2 \geq x) \approx e^{-x} \left[1 + \frac{2x - x^2}{4n} - \frac{24x - 132x^2 + 76x^3 - 9x^4}{288\, n^2} \right]$$

appropriate to the number of trials (n=9 as only ten independent harmonics can be estimated)

(incidentally, the second harmonic has the next strongest power; however its value is only 1.51, therefore consistent with chance). Because of the error bars, it is difficult to give a more accurate estimation of the true statistical significance of this result without performing some computer simulations.

In order to take into account our error bars, simulations of the light curve were performed as follows: 20 random numbers were generated, one for each of the bins in the light curve. Each random number was selected from a Gaussian distribution[3] with mean zero and standard deviation the one measured for the particular orbital phase bin. Given that set of 20 values of strength *versus* phase, the harmonic components of the (simulated) light curve were calculated. Note that, as each simulation uses only 20 values, problems due to possible biases in the random number generator were not expected (a review about Monte Carlo theory is given by James, 1980).

A total of 60000 simulations were performed. The first harmonic of the samples generated was found to be above the measured value 2072 times, which corresponds to a 3.45 % chance probability (Figure 3.7a). If the distribution of all nine harmonics is considered, the observed value was surpassed 17741 times out of 5.4×10^5 trials giving practically the same significance (1.85σ). Taking this as a measure of the detected effect, then the orbital modulation is significant at the 95%

---

[3] A random number from an uniform distribution was generated by the computer; then a numerical transformation from uniform to Gaussian-distributed values was used. Other methods to generate Gaussian distributions appear in James (1980)

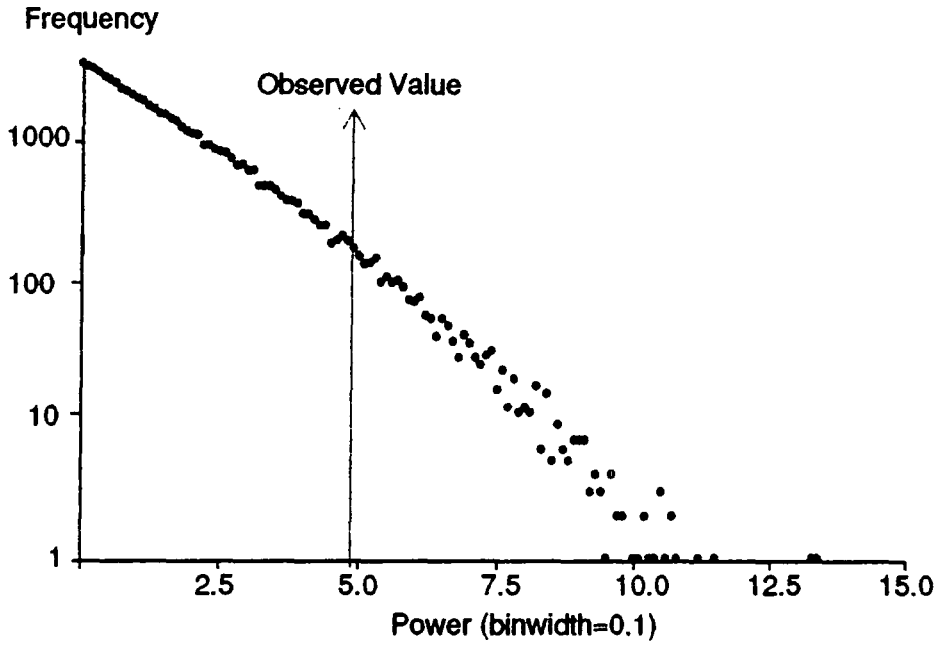

Figure 3.7a

Distribution of the power in the first harmonic
for 60000 simulations of the 1988 Sco X-1 light curve

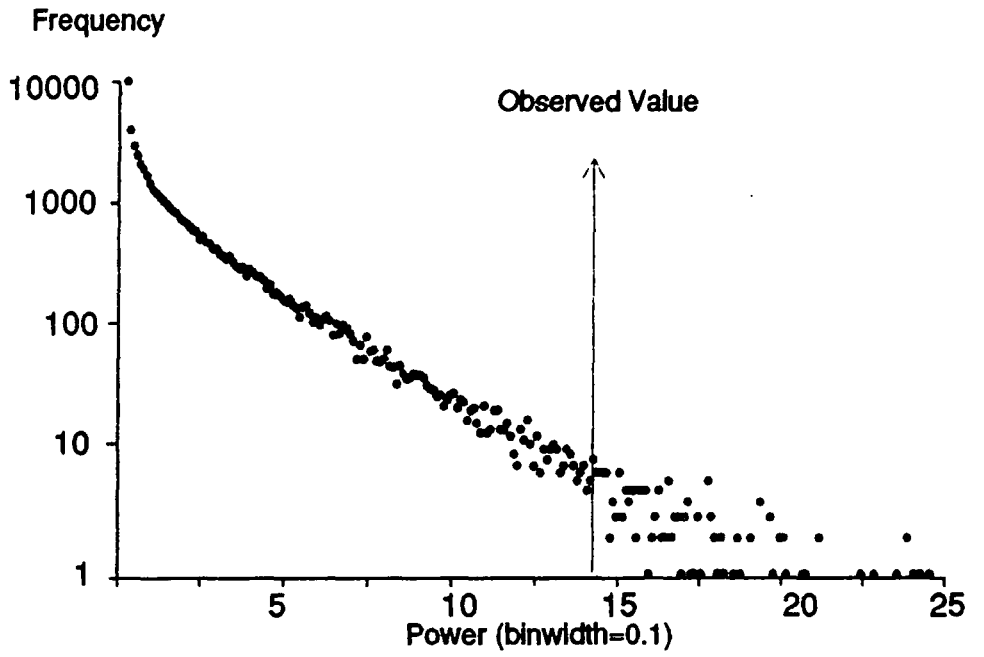

Figure 3.7b

Distribution of the mean squared i.e.
power at harmonic zero
for 60000 simulated samples

confidence level, but a more strict criteria (like 99%) would reject the hypothesis of a strong first harmonic component. Finally, the mean of the sample was above the measured value only 155 times (out of 60000), suggesting a chance probability of 2.58×10^{-3}, equivalent to a 2.8σ deviation (Figure 3.7b) and consistent with the previous conclusion of TeV γ-ray emission from Scorpius X-1 by Brazier *et al.* (1990b).

Other light curves do not show clear signs of orbital modulation. In particular, the 1988 data when the events from channel #3 are also considered, is flat except for the bin at orbital phases (0.35,0.40) which shows a 2.6σ excess, of low significance (~ 10%), given the number of bins. It is clear that the addition of the 1987, 1989 and 1990 data scrambles the relatively weak modulation observed in 1988. Although the 1988 CONLY data give a strong suggestion of an orbital modulation in TeV emission from Scorpius X-1, a definitive claim for such an effect requires future confirmation with more data showing a positive count excess.

3.3 THE ANALYSIS OF PERIODIC DATA: RAYLEIGH & OTHER TESTS

3.3.1 Introduction

A pulsed signal carries precious information about the nature of its source. It tells about rotations and orbital movements, and suggests the size of the emitting region. The presence of a

periodic signals in any region of the electromagnetic spectrum is a valuable key to understand the physical conditions under which the emission is produced. As the pulse period is the signature of the source, the detection of periodicities constitutes a powerful statistical tool when trying to establish the existence of a signal.

A method used to identify the presence of pulsations is to construct a light curve from time events of a datafile, or sometimes using a complete database. This requires precise ephemerides and is done for very few sources, mainly pulsars like the Crab and Vela. A less demanding method to test for periodicity is to search for a correlation between the time series and a sinusoid (Rayleigh test), or more complex harmonic function (Z_n^2 test).

When the period value is known from other regions of the electromagnetic spectrum periodicity tests are statistically more powerful than searching for count excesses: the χ^2 statistics involved are more sensitive than Poisson statistics. Another advantage resides in the much weaker dependence on clear sky conditions. A datafile with gaps in the count rate caused by clouds is useless to test for excesses, but may still be useful for a periodicity test. Finally, note that when a signal is strong, the pulsed strength is expected to be less or equal to the DC strength; but marginal signals can result in a positive pulse detection when no count excess is found, as far as the differences are compatible (i.e. small). Obviously, this is not expected to be the rule, and the stronger the pulsed effect is,

the less likely it is to observe it without a count excess.

3.3.2 Data Processing: Corrections for orbital motions

While an astronomical object is been observed from Earth, it spins on its axis and, if in a binary system, it also describes an orbit. At the same time, the Earth itself spins on its own axis and rotates around the Sun. As a consequence of all these movements, any pulsed signal emitted by the source is Doppler shifted, and its period measured from Earth will be changing continuously. If the relative motion of the source with respect to the observer was constant (i.e. radial motion at a uniform speed, like the Hubble flow) the period would be Doppler shifted, but would remain constant with time. However, these orbital movements result in a constantly changing period, with its variations dependent on the parameters of the orbits involved.

A solution to the problems caused by this time dependence of the period, is to deduce from the observed times the values they would take in an invariant reference frame. Such an invariant frame is defined by the relative position r_{inv} of the solar system centre of mass and the centre of mass of the system under study. Denoting by r_o the vector joining the source to the observer, by a the vector joining the observer to the Solar System barycentre, and by r_{scm} the vector between the source and the centre of mass of its system, the invariant vector is:

$$r_{inv} = a + r_o + r_{scm} \quad , \qquad \text{(III.5)}$$

A time t measured by the observer is equivalent to a time t' in the invariant reference frame given as:

$$t' = t + \frac{|r_{inv}| - |r_o|}{c} \approx t + \frac{a}{c} \cdot \bar{r}_o + \frac{r_{scm}}{c} \cdot \bar{r}_o \quad , \qquad (III.6)$$

(defining unitary vectors as: $\bar{r}_o \equiv r_o / r_o$). Orbital motions in two body systems are well understood since the times of Kepler; their characteristics, including usually negligible relativistic effects, are known. It is fortunate that the corrections are independent on the distance r_o to first order, as this is frequently badly known; second order terms are 10^9 times smaller for a typical distance $r_o \approx 1$ kpc. The two terms on the right hand side of expression III.6 define the required corrections:

(i) barycentric corrections,

It is necessary to account for the movement of the observer on Earth relative to the centre of mass of the solar system. This motion is a combination of an uniform rotation of the observer around the Earths axis, the Keplerian rotation of the Earth around the Sun, perturbations caused by the Moon and planets and, if necessary, relativistic corrections. This process, called barycentring, depends on parameters of the solar system which are fairly well known and can therefore be done accurately.

(ii) Source Corrections,

The second correction takes into account the motion of the

source around the centre of mass of its system. In the case of an isolated pulsar there is no such orbital movement; but if the system is binary, a Keplerian, or even fully relativistic (as in the case of millisecond radio binary pulsars) correction is required. This process, designated as focusing, requires various parameters from the system, like the orbital period, its time derivatives (when not constant), the projected major semiaxis, the epoch of eclipse, the mass function, the eccentricity and the longitude of the ascending node. If the orbit is, or can be assumed circular, the correction can be done with only three parameters: the orbital period P_{orb}, the epoch of eclipse T_o, and the projected major semiaxis $a.\sin(i)$.

As an example, the effect of the source motion in the case of a circular and stable orbit is examined. The instantaneous measured frequency ν is related to the emitted frequency ν_o by:

$$\nu = \nu_o \, \gamma \, (1 + \beta \, \sin(i) \cdot \sin(\psi)) \quad , \qquad \text{(III.7)}$$

where $\psi = \psi_o + \Omega \cdot t$ is the orbital phase, $\Omega = 2\pi / P_{orb}$ is the angular frequency, βc is the orbital velocity, γ the Lorentz factor and i the inclination angle. The time variability of the frequency measured at different initial orbital phases can be estimated quantitatively substituting and expanding this expression (using $\gamma \approx 1$):

$$\begin{aligned} \nu \approx \nu_o \, & (1 + \beta \, \sin(i) \cdot \sin\psi_o) + \cos\psi_o \, \nu_o \, \beta \, \sin(i) \cdot (\Omega t) \\ & - \sin\psi_o \, (1/2) \, \nu_o \beta \, \sin(i) \cdot (\Omega t)^2 + \text{Terms}\{(\Omega t)^3\} \quad ; \end{aligned}$$

(III.8)

τ_1 and τ_2 are defined here as the respective characteristic times for the second and third terms on the right hand side of the expression to contribute in "1" to the overall phase νt (note that the first term on the right hand side corresponds to an apparent period derivative):

$$\tau_1 = (\nu_o \beta \sin(i) \cdot \Omega)^{-1/2}$$
$$\tau_2 = (\nu_o \beta \sin(i) \cdot \Omega^2 / 2)^{-1/3} \quad . \qquad \text{(III.9)}$$

Near eclipse and anti-eclipse, $\psi_o \approx 0$ and $\psi_o \approx \pi$, the term with $\cos\psi_o$ is important, while that multiplying $\sin\psi_o$ becomes negligible. In these positions of the orbit, shifts in the pulse phase will occur in a time τ_1, while near quadrature the situation is reversed: the sinus term dominates and the distortion of the pulse phase occurs in a (longer) time τ_2. Consider as an example values from the Scorpius X-1 system:

$$\Omega = 2\pi/0.787313 \text{ days}^{-1} = 9.24 \times 10^{-5} \text{ s}^{-1}$$
$$\beta \sin(i) \approx 60 \text{ kms}^{-1} / c = 2 \times 10^{-4} \quad ,$$

$\beta c \sin(i)$ been the amplitude fit to the HeII line given by LST (Section 3.2.4). Assuming a pulse period of 2 milliseconds, the times required to produce a unitary shift in pulse phase during eclipse and quadrature by the relevant terms in expression III.8 are $\tau_1 = 329$ s and $\tau_2 \approx 1328$ s. Coherence in pulse phase been essential for a periodicity test, a time t recorded from this system needs to be corrected ("focussed") and replaced by t':

$$t' = \gamma t \, (1 + \beta \sin(i) \sin\psi) \, , \qquad \text{(III.10)}$$

when observations are much longer than 329 seconds near eclipse or 22 minutes at quadrature.

A more precise way to quantify this is defining a "distortion" time, which is a function of the (initial) orbital phase ψ_o. This distortion time is defined as the minimum time τ necessary to cause a unitary shift in pulse phase:

$$\left| \nu\tau - \nu_o \cdot (1+\beta \sin(i) \cdot \sin\psi_o)\tau \right| = 1 \, ,$$

or equivalently:

$$\beta \sin(i) \cdot \nu_o \cdot \tau \left| \sin(\psi_o + \Omega\tau) - \sin\psi_o \right| = 1 \, . \qquad \text{(III.11)}$$

This equation has to be solved numerically; a plot of the "distortion" time as a function of orbital phase for the Scorpius X-1 system is shown in Figure 3.8. Three different pulse periods have been used to illustrate the dependence with pulse period. Note that for a pulse period of 2 milliseconds the "distortion" time ranges between 329 and 1598 seconds, in good agreement with the previous approximate estimations, $\tau_1 \approx 329$ seconds and $\tau_2 \approx 1328$ seconds, given by expression III.9.

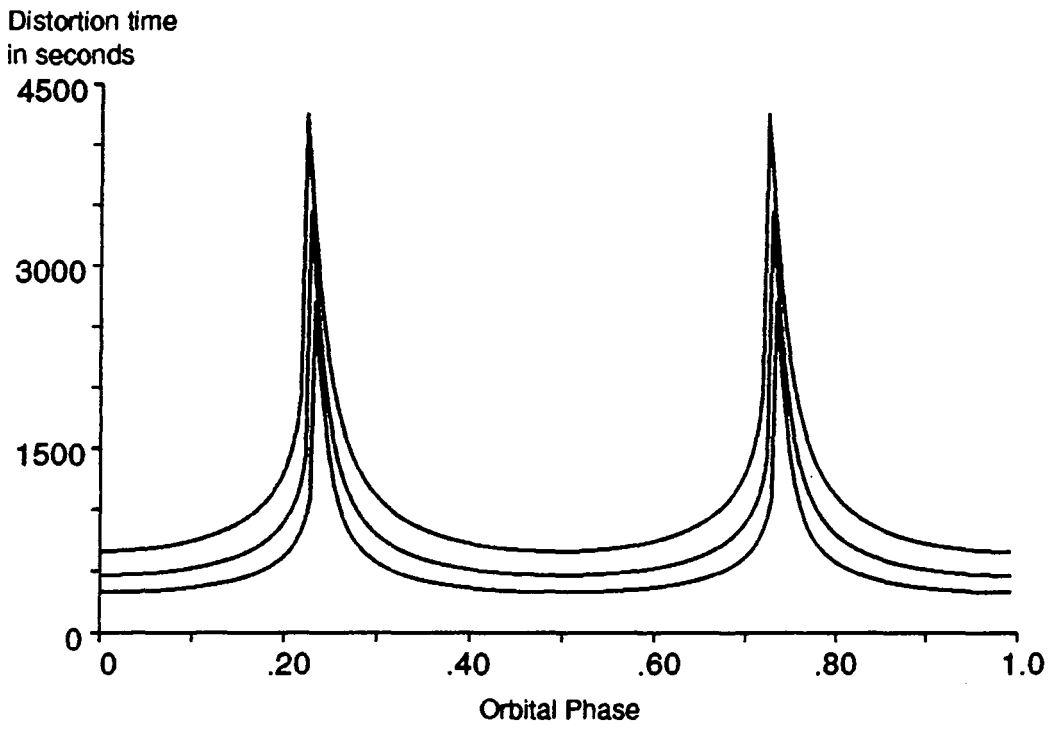

Figure 3.8

Distortion time as a function of orbital phase
the three curves represent from top to bottom
pulse periods of 8.0, 4.0 and 2.0 milliseconds

3.3.3 Independent Frequencies and Fourier Intervals

Once the time series has been corrected to take into account orbital motions a periodicity test can be performed. One of the most fundamental mathematical results of last century states that a function x(t) satisfying the relation:

$$x(t) = x(t+P) \qquad \text{(III.12)}$$

for all t, with P a constant (defined as the period), can be

written as a unique linear superposition of harmonic functions:

$$x(t) = \sum_{k=0}^{+\infty} a_k \cos(2\pi\, kt/P) + \sum_{k=0}^{+\infty} b_k \sin(2\pi\, kt/P)$$

$$= \sum_{k} J_k \exp(2\pi i \cdot kt/P) \qquad ; \qquad \text{(III.13)}$$

the complex notation $e^{ix} = \cos(x) + i\cdot\sin(x)$ is introduced by defining $J_k \equiv a_k - i\cdot b_k$. The mathematical requirements on the function $x(t)$ are not rigid, this result applying also to a discrete time series $x(t) = \Sigma\, \delta(t-t_j) = \{t_j\}$. This result relies on the linear independence of terms with different values of k:

$$\int_0^{+\infty} \exp(-2\pi i \cdot kt/P)\, \exp(2\pi i \cdot k't/P)\, dt = 0 \quad . \qquad \text{(III.14)}$$

Expression (III.13) also applies to a function $x(t)$ defined in the interval $(0;T)$ replacing P by T, so that $x(t)$ can be expressed as an infinite series of harmonic functions with respective argument $2\pi k/T$. Therefore a time series of duration T defines a set of independent periods $\{P_k\}$ by $P_k = T/k$. The corresponding frequencies $\nu_k = 1/P_k$ are known as Nyquist frequencies. A complete periodicity test within a given period range has to cover all the independent periods contained within this interval. The difference between successive periods, known as the Fourier interval (hereafter F.I.), decreases rapidly when the period decreases:

$$P_k - P_{k+1} = \frac{P_k^2/T}{1 + P_k/T} \approx P_k^2/T \left(1 - P_k/T + \cdots \right) . \qquad (III.15)$$

For 10^4 seconds of data (3 hours) and a period P_j around 10 ms the F.I. is 10^{-5} ms.

The intrinsic relationship between periodic and harmonic functions is reflected on the use of the latter in period tests. Given a series of n_e time events $\{t_j\}$, the amplitude of the Fourier coefficient (normalised with respect to the number of events, following van der Klis, 1989b):

$$J_k = 1/n_e \sum_{j=0}^{n_e-1} \exp(-2\pi i \cdot k \cdot t_j/T) \quad , \qquad (III.16)$$

is a measure of the periodic strength of the function at the period $P = T/k$ (or at the frequency $\nu = k/T$).

A common situation, for example in X-ray astronomy, is wanting to calculate J_k for all periods T/k between $T/1$ and T/n, where $n \gg n_e$. In such a case it is convenient usual to "sample" the data in terms of $\Delta \equiv T/n$, that is to count the number x_j of events between $l \cdot \Delta$ and $(l+1) \cdot \Delta$, obtaining a sum with n terms:

$$J_k \approx 1/n_e \sum_{l=0}^{n-1} x_l \exp(-2\pi i \cdot k \cdot l/n) \qquad (III.17) .$$

This expression is only an approximation to (III.16), as the time resolution is restricted to Δ. Expression (III.17) is commonly used in data analysis, although not in TeV astronomy, as the n (imaginary) coefficients J_k can be computed by means of a very

efficient algorithm, known as the Fast Fourier Transform (FFT). This algorithm starts from a time sample of n points x_l and by an iterative process computes its transform J_k in the n Nyquist frequencies with many less computations than the summation and values of k suggest (Chapter 4). On the other hand, the exact expression (III.16) is the one normally used for VHE samples, as the data are sparse (that is $n_e << T/P \sim 10^6\ T_{hours}/P_{ms}$) and the periods to test are generally known; hence the number of frequencies to try is small (well below $n = T/P$).

3.3.4 The Rayleigh test

(i) Definition of the test

This test is the most widely used in TeV γ-ray astronomy. It consists of comparing the data with its best sinusoidal fit for a given trial period P. Given a data sample of time events:

$$x(t) = \sum_j \delta(t-t_j) = a\cos(2\pi t/P) + b\sin(2\pi t/P) \quad , \quad \text{(III.18)}$$

the least squares sinusoidal fit to the data sample x(t) is given by (see Appendix II):

$$a = \frac{\langle x\cdot\cos\omega t\rangle \langle\sin^2\omega t\rangle - \langle x\cdot\sin\omega t\rangle \langle\sin\omega t\cdot\cos\omega t\rangle}{\langle\cos^2\omega t\rangle \langle\sin^2\omega t\rangle - \langle\sin\omega t\cdot\cos\omega t\rangle^2} \quad \text{(III.19)}$$

$$b = \frac{\langle x\cdot\sin\omega t\rangle \langle\cos^2\omega t\rangle - \langle x\cdot\cos\omega t\rangle \langle\sin\omega t\cdot\cos\omega t\rangle}{\langle\cos^2\omega t\rangle \langle\sin^2\omega t\rangle - \langle\sin\omega t\cdot\cos\omega t\rangle^2} \quad ,$$

where $\omega = 2\pi/P$. If the original sample x(t) is a set of random (uncorrelated) time events then the variable:

$$n_e R^2 = \left[\frac{a - E(a)}{\sigma(a)} \right]^2 + \left[\frac{b - E(b)}{\sigma(b)} \right]^2 \quad , \qquad \text{(III.20)}$$

follows a χ^2 distribution with two degrees of freedom. The two expressions in (III.19) can be simplified to:

$$a = 2 \langle x \cdot \cos\omega t \rangle \quad , \quad b = 2 \langle x \cdot \sin\omega t \rangle \quad . \qquad \text{(III.21)}$$

These latter expressions are approximate for $\omega T \gg 1$ (or $P \ll T$), and exact for Nyquist frequencies. For a source with a short period (below T/1000 for example) the χ^2 variable $n_e R^2$ can be simplified to:

$$n_e R^2 = 1/n_e \{ (\Sigma \cos\omega t_j)^2 + (\Sigma \sin\omega t_j)^2 \} \quad , \qquad \text{(III.22)}$$

and follows an (asymptotic) exponential distribution:

$$P(n_e R^2 \geq x) = e^{-x} K(x, n_e) \quad , \qquad \text{(III.23)}$$

with the deviations from an exponential given by the function:

$$K(x,n) \approx 1 + \frac{2x - x^2}{4n} - \frac{24x - 132x^2 + 76x^3 - 9x^4}{288n^2} - \cdots \quad , \qquad \text{(III.24)}$$

When testing for periodic behaviour with a period comparable to the duration of the file, as happens for example in the case of Vela X-1, expression (III.22) is only valid at the Nyquist frequencies and a rigorous analysis requires the use of (III.19).

Scargle (1982) discusses the validity of the standard definition of the periodogram nR^2 given by (III.21) in the case of unevenly sampled data, which is the case when observations taken on different nights are combined; and proposes a new definition of the periodogram which is compatible with the use of expressions (III.19) and (III.20).

For a series of uncorrelated time events ("white noise") after testing m frequencies one would expect to see "one random fluctuation" with chance probability $\approx 1/m$; in other words the maximum value of $n_e R^2$ should tend to Ln(m) when m is large. This imposes a limit on how weak a signal can be if many trials are used. If for example a thousand periods are tested any real signal below $nR^2 \approx \mathrm{Ln}(1000) = 6.91$ would not appear significant. This corresponds to 15% pulsed events in a small ("burst-size") 300 event sample. A typical period search involving 10^6 trial periods would push this detection limit above 20%. As m (independent) tries have been done, the final chance probability of obtaining a value of nR^2 above x is given by Fisher (1954) as:

$$\begin{aligned} P_{adf}(nR^2 \geq x;\ m) &= 1 - \exp\{-m \cdot P(nR^2 \geq x)\} \\ &\approx 1 - \exp\{-m \cdot \exp(-x)\} \quad . \end{aligned} \qquad \text{(III.25)}$$

An intrinsic 10^{-6} probability becomes 10^{-4} if it arrives after 100 trials, and 50% after 7×10^5 trials. When the signal is weak it is important not to waste degrees of freedom; therefore, when the period is known the test is usually restricted to the neighbouring period values; the period error box and some five

extra Fourier intervals on each side been a typical example. Note that for very short periods the F.I., given in expression III.15, becomes very small ($\sim P^2/T$), and therefore the number of trials increases rapidly. Also, in order to be sensitive to periods with values falling in between two independent tries, it is useful to do more than one trial per F.I., i.e. to "oversample". It is shown in the next chapter that testing three periods per F.I. results in an optimum compromise between sensitivity and computer time. Under the ("null") hypothesis that the input data consist of uncorrelated events, or "white noise", the extra terms introduced at $\pm$ 1/3 F.I. have the same (asymptotic) distribution for a large number of events and $P \ll T$. Testing for broad features (of frequency width $\Delta\nu \gg$ one F.I.) requires extra care. For example, adding the nR^2 amplitudes of m neighbouring frequencies, in order to search look for QPO features, alters the number of degrees of freedom of the χ^2 distribution to 2m. As the sensitivity becomes optimum for signals of width $\Delta\nu \approx$ m F.I. a new free parameter is introduced.

(ii) Example: Cygnus X-3, September 1989

In 1985 the Durham group (Chadwick *et al.*, 1985) reported the detection of a seven minute count rate enhacement[1], during an observation of Cygnus X-3 on the 12th of September 1983 at their

[1] A parabolic fit to the count rate from 3:50 hrs UT to 9:17 hrs UT predicts 392 events between 5:15:50 and 5:22:53 hrs UT when 449 events were observed. The deduced number of periodic events was 83 (R=.1846) compared to 57 extra events in relation to the background fit (1.3σ discrepancy).

Dugway site. The time of this enhancement coincided with the phase of X-ray maximum. A period search on this segment of data, done for periods from 50 seconds down to 10 ms, gave a best candidate period of 12.5908 ms with a power of $nR^2 \approx 16.8$, and a final 3.3×10^{-3} chance probability after all the tries were taken into account. Suggestions of confirmation by other groups (like the Whipple group), did not result in corroborating this finding (Fegan *et al.*, 1987; Resvanis *et al.*, 1987). The evidence for a 12.6 ms pulsar in Cygnus X-3 has been treated with major scepticism (see for example Bonnet-Bidaud & Chardin, 1988) and an independent confirmation is necessary. A first detection of the 12.6 ms periodicity by another group, working at 100 TeV, has recently been published by Gregory *et al.* (1990a and 1990b).

The finding of the periodic excess in September 1983, if real, would be expected to be repeated with a similar strength at some stage. In 1984 The Durham group resumed its Dugway campaign and in 1988 the first new observations of Cygnus X-3 were made with the Mark IV telescope at La Palma, Islas Canarias. Although pulsar searches were normally restricted to the 4.8 hour phase of X-ray maximum, preliminary reports by the Adelaide group of a possible detection of the 12.6 ms periodicity *before* X-ray maximum (Gregory *et al.*, 1990a) motivated a more careful search for the pulsed signal. The dataset recorded on the 7th of September 1989 shows a behaviour similar to the one recorded in September 1983. The count rate, shown in Figure 3.9, has three regions which lie significantly above the parabolic fit to the recorded count rate. In the first one, and largest, 218 CONLY events were recorded

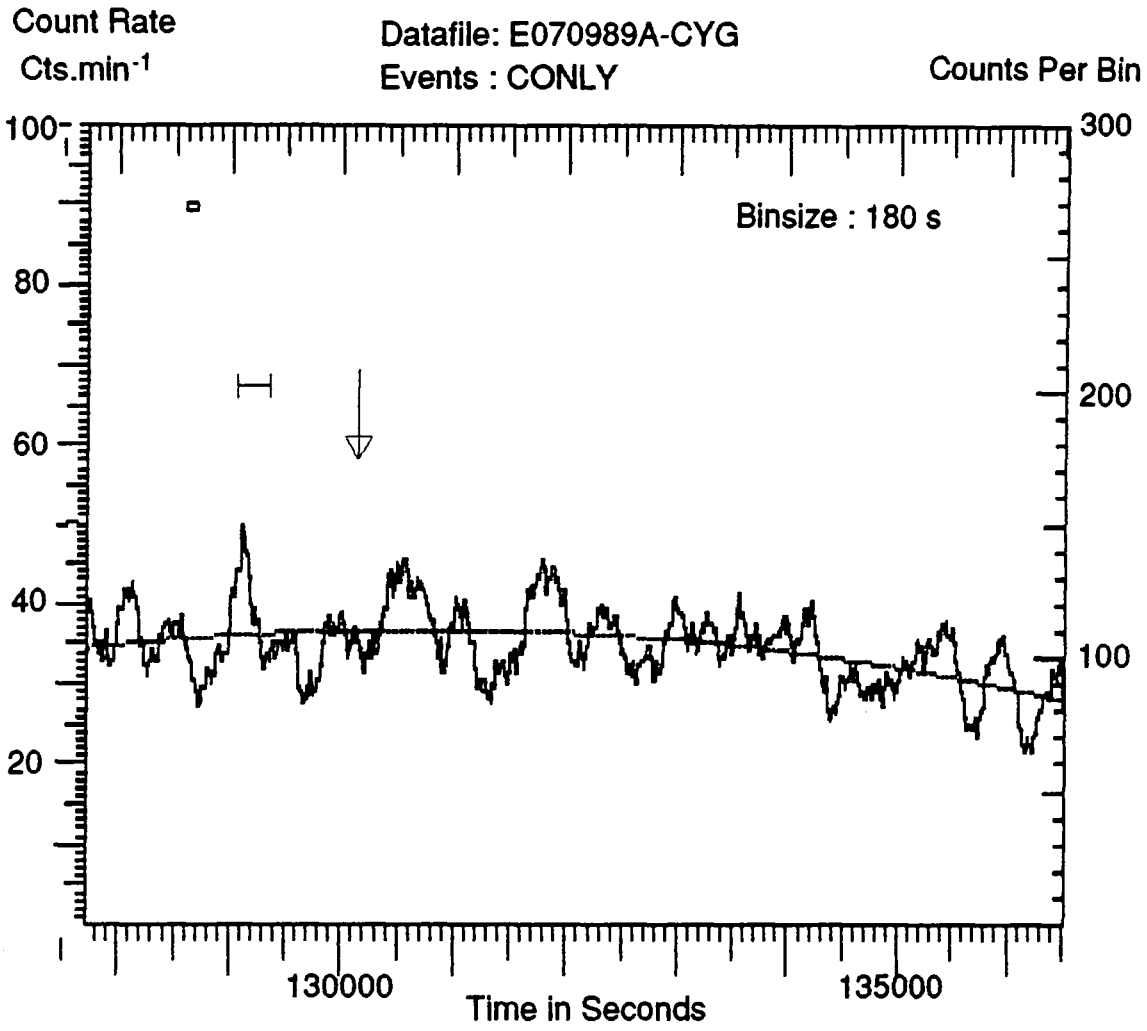

Figure 3.9

Count rate of Cygnus X-3 data taken on September 1989
The arrow indicates the expected time of X-ray maximum
The bar indicates the section of data showing periodic effect
The broken line is the parabolic fit to the count rate

between 23:51:00 and 23:56:05 UT, some 15 minutes before the predicted time of X-ray maximum (00:09:18 UT), while the parabolic fit predicts 184 events (2.5 σ excess). The periodogram for this section of data for periods between 12.59 and 12.60 ms is shown in Figure 3.10. A Rayleigh power $nR^2 \approx 18.1$ is found,

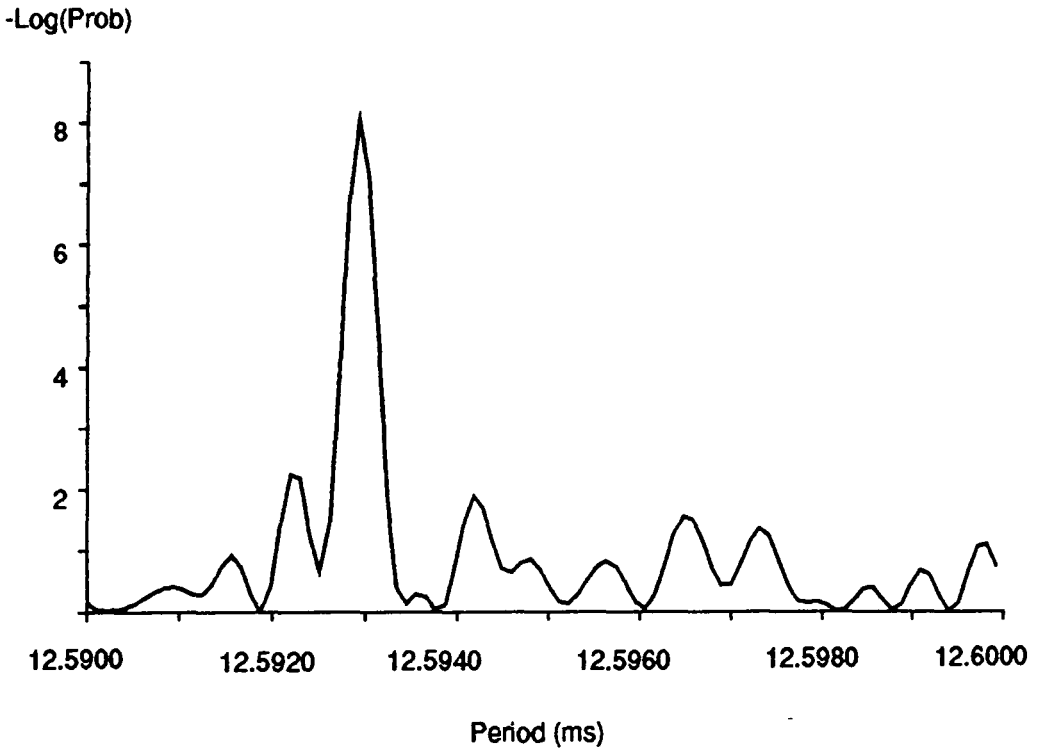

Figure 3.10

Periodogram of Cygnus X-3 data taken the 070989
300 second segment of data indicated in Figure 3.9

implying that 28.8% of the observed events contribute to the periodicity. This gives a number of periodic events (63) which is 2.1σ above the count rate excess (34) suggesting that either (i) the background fluctuated downwards, or (ii) the signal was "pushed" up by background events in phase with the pulsed signal. The actual number of γ-ray events deduced might well lie in between (say 50 events in 300 seconds) and, given the energy threshold of 0.6 TeV, the luminosity implied for a distance of 10 kpc is 2×10^{37} erg.s^{-1}.

This particular segment of data has the strongest pulsed signal detected up to now. If present, a pulsar should eventually appear non statistically (say $nR^2 \geq 50$) either by the use of more powerful observational techniques (a count rate of 1 Hz after rejection with a ring guard or a direct discrimination between protons and γ-rays) during a similar burst, or by the fortunate observation of a more persistent burst (twice as long with the same γ-ray luminosity, for example). Until then the evidence for a 12.6 ms pulsar in Cygnus X-3 will remain controversial.

3.3.5 Other tests

(i) The χ^2 test

For a weak but persistent pulsed signal for which precise ephemerides are available, one can compute the pulse phase of each time event (T_o is the epoch of zero phase, P is the pulse period, dP/dt its time derivative):

$$\phi_j = (t_j - T_o)/P - (1/2)(t_j - T_o)/P^2 \ (dP/dt) + \ldots \qquad \text{(III.26)}$$

and make a histogram of these phases. The light curve obtained folding n_e events into m bins can be tested for uniformity using:

$$\chi^2 = \sum_{j=0}^{m} \left[\frac{n_j - n_e/m}{(n_e/m)^{1/2}} \right]^2 , \qquad \text{(III.27)}$$

(where n_j is the number of events in the j-th bin) and compare its value against its expected value (from a χ^2 distribution with

m degrees of freedom). The light curve itself can be compared with one observed in other regions of the spectrum. An integer number of cycles has to be considered ("Poincare correction") to avoid giving unequal weight to different bins. The test is more sensitive for light curves of width $\approx 1/m$ and therefore the method is optimum for objects with a weak signal, a narrow light curve and good ephemerides (the Crab pulsar is the standard example). Criticisms of this method are based on the fact that the origin and number of bins can be chosen arbitrarily (although because of such criticism researchers tend to use most of the times light curves with twenty bins). A more sophisticated version of this test that avoids this problem is the modified Hodges-Ajne test (testing the individual values of the phases against a von Misses distribution) which relies on circular statistics (Mardia, 1972).

(ii) The Z^2_n test

The Z^2_n statistic is calculated by summing the Rayleigh power (III.22) of the n first harmonics of the test period:

$$Z^2_n = \sum_{k=1}^{n} \{ [\Sigma_j \cos(2\pi k \cdot t_j/P)]^2 + [\Sigma_j \sin(2\pi k \cdot t_j/P)]^2 \} \quad \text{(III.28)}.$$

The distribution of Z_n^2 for a sample of random time events (white noise) is χ^2 with 2n degrees of freedom. The Z^2_n test is a generalisation of the Rayleigh test (which is a Z^2_1 test) which is more sensitive to complicated light curves, like double peaked ones for example.

The choice of a high value of n (say 10) allows the detection of complicated light curves but diminishes the response to a pure sinusoid (where only the fundamental contributes). On the other hand, for a signal with power ξ at its fundamental and 1 at all the other harmonics (average value for white noise) the related probability P_n for the Zn^2 test (Z_1^2 being the Rayleigh test) as a function of n is given by:

$$P_{n+1} = \exp(-n-\xi) \sum_{k=0}^{n} \left[\frac{(n+\xi)^k}{k!} \right] , \qquad (III.29)$$

and shown in the following Figure 3.11. For $n \leq 5$ the probability changes slowly; however, the introduction of more harmonics causes the probability to increase (significance to decrease) more rapidly.

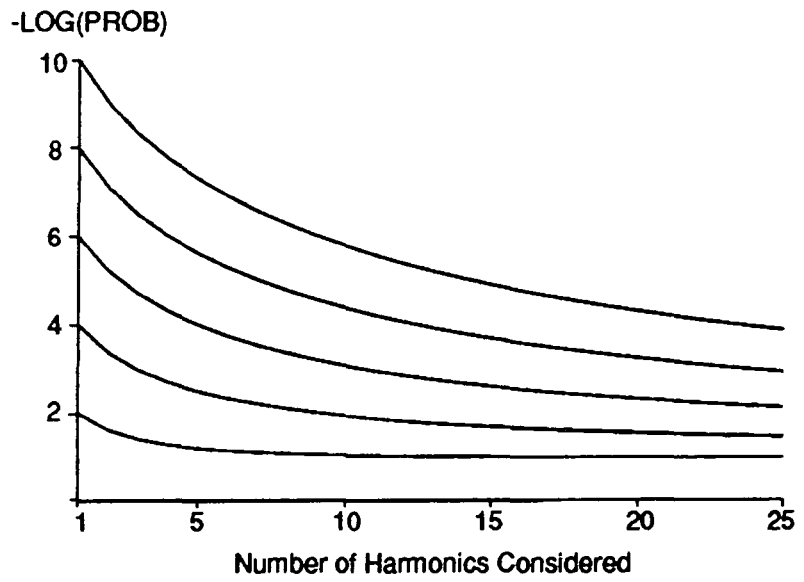

Figure 3.11

Response of the Z_n^2 test to a sinusoidal with noise on its higher harmonics

This case exemplifies how the choice of n influences the significance of the result for a particular light curve. The use of large n increases the sensitivity for narrow light curves while a small n gives a better response for broad light curves. Protheroe (1987b) suggested the use of the Z_2^2 statistic when the shape of the expected light curve is unknown (and alternative is to perform a Rayleigh test on the second and perhaps third harmonics).

(iii) The Protheroe test

Given two time events t_j and t_k, with respective phases φ_j and φ_k, taken from a sample of size m, Protheroe (1985) defined the variable:

$$\Delta_{jk} = 1/2 - \left| \, |\varphi_j - \varphi_k| - 1/2 \, \right| \quad , \qquad \text{(III.30)}$$

and the statistic associated to it:

$$T_n = 2/n(n-1) \sum_{j=1}^{m-1} \sum_{k=j+1}^{m} (\Delta_{jk} + 1/n)^{-1} \quad . \qquad \text{(III.31)}$$

The distribution of T_n for a series of random time events is computed using simulations. This test, sensitive to narrow light curves, has the disadvantage of requiring a considerable amount of computing time; its use is more compatible with PeV energies, where the number of events is smaller. A narrow peaked orbital modulation in the light curve of LMC X-4 at PeV energies was

detected using this test (Protheroe & Clay, 1985).

(iv) The H-test

de Jager *et al.* (1989) proposed this test which is more powerful than the Z^2_n when the shape of the light curve is unknown. The recipe is to find the value m for which Z^2_m is optimised (by minimising the mean square integrated error between fit and observation); the authors suggest truncating the calculation after 20 harmonics. The resulting statistic:

$$H \equiv \text{maximum } (Z^2_m - 4m + 4) \qquad (1 \leq m \leq 20) \ , \qquad \text{(III.32)}$$

does not require the choice of a smoothing parameter like m in the Z^2_m test and is sensitive to both narrow and broad light curves. Although this test is optimum when the shape of the light curve is unknown, de Jager *et al.* suggest the use of the Z^2_m when the light curve is known or when a particular shape is tested.

3.3.6 Causes of non Random Variations on the Count Rate

Finally a brief mention is made of some causes of non random count rates that can be present in the data. Although the presence of this variations in the count rate affects in principle any DC or periodic analysis, in most of the cases they vary on timescales of the order of several minutes or hours and are therefore not expected to have any significant effect when testing the data for a periodic signal below one second.

(i) start & stop observing times,

When various datafiles are added coherently (i.e. in phase) beats in the power spectrum frequently appear. In a typical case four or five datafiles of unequal length, each lasting on average 3 hours and spaced every 24 hours, are linked in phase. The effect on the power spectrum is in fact "case dependent" the relevant points being the actual shape of the observing window (i.e. 3 hrs ON + 20 OFF + 4 ON + ...), the period to be tested and relative strengths and phases of the (Poissonian) noise and signal at, and near to, the trial period.

(ii) chopping mode,

As described in Chapter II, in the chopping mode the telescope alternates the source between channel #1 and channel #3 in a four minute cycle. There is a relatively small "transition" time (four or five seconds) during which the telescope is moving from one channel to the next. This can be modelled as follows: if T is the period of the chopping mode (four minutes), and the centre tube counts c_1 events during its two minutes ON source, while channel #3 counts c_3 events in the next two minutes, the window function w(t) is given by:

$$w(t) = \begin{cases} c_1 & \text{for } 0 \le t \le T/2 \\ c_3 & \text{for } T/2 \le t \le T \end{cases} \quad . \qquad \text{(III.33)}$$

The power on the k-th harmonic (neglecting noise components and

assuming a small sampling rate $\Delta << T$) of the four minutes is:

$$nR^2 = \frac{(c_3 - c_1)^2}{(c_3 + c_1)\, \pi^2\, k^2} \qquad \text{(III.34)}$$

for k odd and $nR^2 = 0$ for k even. One example of a dataset with a strong "chopping signature" was recorded on the night of the 13th May 1988 whilts observing Scorpius X-1. This dataset is almost seven hours long and has a good count rate. The number of ON source counts on the centre channel was 8570 while channel #3 recorded 14085 ON source events. This gives a power $nR^2 \approx 136/k^2$ which gets below the noise level for $k \approx 13$, i.e. for periods below 18 seconds. In the extreme case of evaluating the power spectrum taking CONLY events ($c_1 = 8570$ and $c_3 = 0$) the four minute chopping is above noise down to the 29th harmonic which corresponds to 8 seconds. Any analysis below one second is unaffected by the presence of the chopping components.

(iii) variation with zenith angle,

There is a smooth variation of the count rate with zenith angle noticeable for datasets longer than two hours in duration. Its Fourier components are weak (as this is not a periodic window) and is completely negligible in the power spectrum even at frequencies around (ten seconds)$^{-1}$. The time events $\{t_j\}$ define by themselves a parabolic fit with the deviations from such fit being an indication of the running conditions (Appendix II). The parabolic fit to the count rate can be written as:

$$x(t) = \sum_j \delta(t-t_j) = x_c \left[1 - \frac{1}{2} \left[\frac{t - t_c}{\tau} \right]^2 \right] ,$$

where t_c ≡ the time of culmination, x_c ≡ the count rate at culmination and τ is the characteristic time for count rate variations, which is found to be between two and three hours. This is in agreement with estimations (Appendix II) which predict a timescale of the order of $(2\pi)^{-1}\ k^{-1/2}$ days where $k \approx 2.5$ (which gives $\tau \sim 2.4$ hours). This timescale is dependent on the latitude of the observatory and the declination of the object (the object is assumed to be near to its culmination). An exact ON/OFF analysis would require a correction to account for this count rate variation (the expression III.3 used for the analysis of chopped data accounts for "end effects"). The effect that this count rate variation can have on the periodogram is negligible when searching for periods below few minutes; if desired it can be removed by giving to each event a weight proportional to $w(t_j) = 1 - 1/2\ (t_j - t_c)/\tau^2$ to a time event occurring a $t=t_j$.

(iv) clouds,

Clouds give variable and quasi-random variations (dips) on timescales of few minutes to hours. They have a negligible influence when testing periods in the millisecond range but their presence when searching for count excess is undesirable and may invalidate an ON/OFF analysis.

(v) Dead time of the system,

The dead time is the time required by the system to "digest" an event (Chapter II). When an event is detected the system is "dead" whilts this event is processed and cannot be triggered until this has occured. Dead time corrections become relevant when the event rate is comparable to the dead time. The statistical corrections due to a relatively long dead time can be deduced through simulations as in van der Klis (1989b). Count rates in VHE γ-ray astronomy are of the order of a second, while the dead time for the Mark III telescope is three orders of magnitude below, around half millisecond (Dipper, priv. comm.)[2]. Its influence is therefore negligible.

(vi) incidents and accidents,

Occasionally one might get electronic noise or unusual interruptions of the run (for example, during winter runs mirrors may mist over and the run has to be suspended while demisting). Voluntary interruptions of a run happen under operator control and their effect can normally be taken into account. Other phenomena like electronic noise, lightning, shooting stars in the field of view, etc... cannot in principle fake events as their duration in much longer than the nanosecond timescale of a Cerenkov flash. Very rarely they appear in the data, typically

---

[2] A recent sample of electronic noise allowed us to measure the dead time of the system:

$$\tau_d = 0.639 \pm 0.092 \text{ ms.}$$

giving rise to very narrow spikes in the count rate (as for example tens or hundreds of events in less than one second), normally in more than one channel (they need to happen on the centre channel only if they are to be mistaken as a signal) and are therefore easy to recognise. Data with such noise are either rejected, or have the section with noise removed and are used for period testing only.

3.4 TESTING (SEARCHING) FOR UNKNOWN PERIODICITIES

Periodicity tests are particularly powerful when the pulse period is known. In such a case the number of trial periods is small allowing the detection of weak signals without demanding a large number of calculations. For example, testing ten independent periods with three trials per Fourier interval on a datafile containing 50000 events, about the largest number of events recorded in a single dataset, requires 1.5×10^6 computations. This can be achieved by computers with relative ease.

The situation is more complicated when no test period is available. As mentioned in the last section, a time series of duration T defines a set of independent periods $\{P_k\}$ by $P_k = T/k$. In the case of a unknown period, which might be refered to as a period search, all values down to a minimum period P_{min} are tested. The number of computations implied is:

$$N = n_e \, T/P_{min} = T^2 \, (dn/dt)/P_{min}$$

where dn/dt is the count rate. As most of the systems under study have been related to neutron stars very short term periodicities can be expected; a tentative value for P_{min} may be 10 milliseconds, while P_{min} ~ 1 ms ensures a fairly complete search. For a typical count rate of 1 s^{-1} and considering $N \approx 10^8$ as a practical limit to the number of computations feasible in a reasonable time, the longest a datafile can be is:

$$T_{max} = (N\, P_{min}/(dn/dt))^{1/2}$$

$$\approx 10^3 \text{ s } N_8^{1/2} (P_{min}/10 \text{ ms})^{1/2} (dn/dt/1 \text{ s}^{-1})^{-1/2}$$

$$\approx 316 \text{ s } N_8^{1/2} (P_{min}/1 \text{ ms})^{1/2} (dn/dt/1 \text{ s}^{-1})^{-1/2} .$$

It is clear that only small sections of data can be used for a period search. In the next chapter the use of fast algorithms, which are limited by the size of the computer memory, is described considering the sparse character of the data and practical limitations.

IV. DISCRETE FOURIER ANALYSIS AND PERIOD SEARCHES

4.1 STANDARD FOURIER TECHNIQUES

In Chapter III the definition of the discrete Fourier transform (or DFT) for a series of n_a times t_l (events) ranging between 0 and T was given as:

$$J(\omega_k) = 1/n_a \sum_{l=0}^{n_a-1} \exp(-i\cdot\omega_k t_l) = 1/n_a \sum_{j=0}^{n_a-1} \exp(-2\pi i\cdot k t_l/T) ,$$

(III.16)

where the index k runs from 0 to (n-1) and $\omega_k = 2\pi\cdot k/T$. If the number of events is much larger than that of frequencies, that is $n_a \gg n$, it is convenient to "sample" by defining a time "step" $\Delta \equiv T/n$:

$$J(\omega_k) \approx 1/n_a \sum_{j=0}^{n-1} x_j \exp(-2\pi i\cdot kj/n) \qquad (III.17)$$

where $x_j \equiv$ { number of events between $j\cdot\Delta$ and $(j+1)\cdot\Delta$ }, the $\approx$ sign in (III.17) arising from the restriction of j having only integer values. This is equivalent to use $j\Delta$ as an approximation for the time of each event included in x_j.

Expression (III.17) suggests n (complex) sums to be evaluated at n values of the frequency, requiring in principle n^2

operations (an extra factor of two is implicit in the complex notation). But as the exponential term in expression (III.14) has only n different values, the sums can be group together in order to reduce the number of calculations. Starting from this point, fast algorithms were developed in the sixties (a history of the algorithm in given by Cooley, Lewis & Welch (1967)), which take advantage of a decomposition of time and frequencies (Bloomfield (1976), Good (1958,1971), Cooley & Tuckey (1965), Gentleman & Sande (1966)). The algorithm is most efficient when n is a power of two. It works by performing n rotations starting with the (complex) data array x_j of size n performs $\log_2(n)$ iterations (requiring n operations each time), the final result being the DFT J_k. The relevant point is the ratio of the number of computations required using the two methods: direct computation or fast algorithm. Naming such ratio as "saving factor" s_o, its value when comparing the "fast" and "direct" algorithm is:

$$s_o = n / \log_2(n) = (T/\Delta) / \log_2(T/\Delta) \quad ; \qquad (IV.1)$$

$$\approx 1.46 \times 10^5 \quad , \quad \text{for } T = 1 \text{ hr} \ , \ \Delta = T / 2^{18} \approx 13.7 \text{ ms.}$$

If $n \approx 56863$ one hour of the direct method is equivalent to one second of FFT while $n \approx 1795008$ implies $n/\log_2(n) \approx 1$ day$\cdot$s^{-1} (a Cray supercomputer manages to compute 2^{23} frequencies with a saving ratio of 2.9 days.s^{-1}).

4.2 ANALYSIS OF SPARSE DATA

4.2.1 Software considerations: computer time

TeV gamma ray data are sparse, in the sense that the sample has most of its bins empty when sampled with a rate ~ few millisecond. Typical count rates are of the order of 1 s^{-1}, and even "bursts" do not show a high count rate (~ 2 s^{-1}). TeV data are therefore considered sparse for periods below 500 milliseconds. As a consequence the direct evaluation of Fourier terms (and Rayleigh power) is usually done using (III.16) rather than (III.14), the former expression requiring ($n_a \cdot n$) computations instead of n^2. For sparse data, the "saving" of the fast algorithm is reduced to:

$$S_{sparse} = n_a \; / \; \mathrm{Log}_2(n) \quad ,$$

or in terms of the mean count rate <dn/dt> and sampling time Δ:

$$S_{sparse} = \Delta \langle dn/dt \rangle \cdot s_o = T \langle dn/dt \rangle \; / \; \mathrm{Log}_2(T/\Delta) \quad , \qquad \text{(IV.2)}$$

$$\approx 200 \quad ,$$

for <dn/dt> ≈ 1 Hz, T ≈ 1 Hr and $\Delta = T/2^{18} \approx 13.7$ ms. s_o is the "saving" when data are not sparse. For Cerenkov data, the product of Δ and <dn/dt> can be as small as 10^{-3}, making the "saving" less dramatic although still significant.

4.2.2 Software considerations: computer memory

Unfortunately, there is an intrinsic problem when sampling one hour of data with a sub-millisecond rate: it gives a few millions of numbers (complex for the DFT) to be stored in computer arrays. As a consequence of the low signal to noise ratio, TeV data cannot be cut in small sections, as it is usually done in X-ray astronomy: 1000 seconds of data do not usually have more than 10 or 20 γ-rays except in the strongest bursts (like in Cyg X-3 or Her X-1). The duration of data required for a period search, in the absence of segments showing an increase in the count rate, is usually above 1000 seconds. Typical TeV data files last a few hours ($\sim 10^4$ s) while Δ has to be less than half the minimum period to be tested. For a sampling rate $\Delta \approx 1$ ms, the number of time bins is of the order of $n \approx 10^7 \approx 2^{23}$. A fast Fourier transform (FFT) algorithm requires two real arrays (i.e. one complex array) of size n to be used for both data and transform. If each real takes 4 bytes of memory space, then a microcomputer with 4 Mb is limited to $250000 \approx 2^{18}$ points FFT, the hardest work requiring supercomputers: a 2^{24} points FFT is feasible in a few hours of Cray computer time (Brinklow 1989).

The need of such a large amount of computer memory is a limitation when trying to perform a period search in TeV data, as the whole transform cannot be computed at once without an extremely large computing power. A way to overcome, at least partially, this problem is to perform the FFT in segments. This method, described in detail in Section 4.3.1, has in fact been

considered somewhere else previously in relation to period searches in radio data from pulsars (Ashworth & Lyne, 1987; Brinklow, 1989). The basic idea is the following: in order to perform a search at $n = p \cdot q$ frequencies, with p and q an integer of the same order as the size of the largest (complex) array to be stored in the microcomputer, one can evaluate q (previously selected) values of the transform and retain the relevant information from them. Obviously this has to be repeated p times in order to test all n frequencies. Therefore the "saving" is reduced to:

$$S_{seg} = n_a \,/\, p \; Log_2(q) = \Delta \langle dn/dt \rangle \; q \,/\, log_2(q) \quad , \qquad (IV.3)$$

$$\approx 13.2 \quad ,$$

for $\langle dn/dt \rangle \approx 1\ s^{-1}$, $T \approx 2$ hr, $p = 32$, $q = 2^{17}$ giving $\Delta \approx 1.7$ ms.

The microcomputers used here, Acorn Cambridge Workstations, allow the use of $q = 2^{17}$ for the individual transforms (while retaining 2q each time). The "segmentation index" p was restricted to powers of two (between 1 and 64). For the largest transforms considered the "saving" is of the order of ten, significant but not large.

4.2.3 Even and uneven samples

When data are evenly sampled the Nyquist set of frequencies comes out naturally. For an unevenly spaced sample it is more difficult to define such a "natural" set. Some questions can be asked concerning the data:

- is this an unevenly spaced sample? Although it might first appear that the answer is yes, the time resolution is fixed at 1μs, and the data can be regarded as being (evenly) sampled every microsecond, with the peculiarity of having most of its bins with value zero and the remaining few having weight one. In other words, a sparse but even 1-bit sample.

- although the events do not come at even times (as most or all of them are not pulsed!), in an ideal run the time between successive events is random but quite regular on the long term. It is not expected that the time series would "choose" a particular frequency value (or range) in the power spectrum unless some non random effect is operating.

Scargle (1982) notes that the transform of (random) unevenly spaced data might result in a non exponential distribution. He gives a redefinition of the periodogram (expression III.16) for unevenly spaced data with an exponential distribution. Such a definition is found to give a result very similar to the standard periodogram. His definition was tried in two datafiles with no noticeable difference.

4.3 IMPLEMENTATIONS FOR TeV DATA

4.3.1 Extension of the frequency range: segmented FFT

The extended FFT developed for this work was considered previously elsewhere (Ashworth & Lyne, 1987; Brinklow, 1989). The

main idea resides in the principle of the FFT algorithm which is to expand the (harmonic) exponential of sums into products of exponentials. Considering expression (III.17) for the DFT:

$$J_k = 1/n \sum_{j=0}^{n-1} x_j \exp(-2\pi i \cdot kj/n) \qquad \text{(III.17)} \quad ,$$

with n such that two integers p and q satisfying $n = p \cdot q$ do exist, then the time and frequency indices can be decomposed using an Euclidean division:

$$\begin{aligned} k &= r \cdot q + s \\ j &= \alpha \cdot p + \beta \end{aligned} \qquad \text{(IV.4)}$$

where r,β are integers between 0 and p-1, while s,α are in the interval $\{0,q-1\}$. When k and j are substituted, the harmonic term expanded (using $\exp(-2\pi i \cdot \alpha r) = 1$), (III.17) becomes:

$$(pq) \cdot J(r,s) = \sum_{\beta=0}^{p-1} \left\{ \exp(-2\pi i \cdot \beta(rq+s)/pq) \cdot \sum_{\alpha=0}^{q-1} x(\alpha,\beta) \exp(-2\pi i \cdot \alpha s/q) \right\} .$$

(IV.5)

In the inner summation both indexes α and s go from 0 to (q-1) and it corresponds to a FFT of size q. As this is computed for each value of β, p FFTs of size q are required:

$$\Lambda(s,\beta) = \sum_{\alpha=0}^{q-1} x(\alpha,\beta) \exp(-2\pi i \cdot \alpha s/q) \qquad \text{(IV.6).}$$

this matrix of size q x p is rotated,

$$\Gamma(s,\beta) = \Lambda(s,\beta) \exp(-2\pi i \cdot \beta s/pq) \qquad \text{(IV.7),}$$

and q transforms of size p give the final transform:

$$(pq)\cdot J(r,s) = \sum_{\beta=0}^{p-1} \Gamma(s,\beta)\, \exp(-2\pi i\cdot\beta r/p) \qquad (IV.8).$$

When p is chosen relatively small (values less or equal to 32 and, exceptionally, 64 were considered here) the last two operations can be performed together, without a fast algorithm:

$$(pq)\cdot J(r,s) = \sum_{\beta=0}^{p-1} \Lambda(s,\beta)\, \exp(-2\pi i\cdot\beta(rq+s)/pq) \qquad (IV.9),$$

requiring a total of p computations per value of r. As the main restriction is memory space, fixing the value of r removes the need to store the p x q array $\Lambda(s,\beta)$: $\Lambda(s,0)$ is computed and stored (2q reals) in the space reserved for J(r,s), then $\Lambda(s,1)$ is computed and added to J(r,s) following (IV.9), then $\Lambda(s,2)$, and so on. The total space required then is that of two arrays of size q. The memory size allowed to compute transforms of size q and keep 2q elements. It is nevertheless likely that the storage of $\Lambda(s,\beta)$ would allow a more efficient method.

It is worth mentioning that the segmented method is not an approximation to a larger FFT, as it gives the same result. The freedom gained in memory space (only arrays of size q are required) is balanced by the fact that a complete transform (all values of r and s) should then require $p^2\cdot q\cdot\log_2(q)$ computations rather than $p\cdot q\cdot\log_2(pq)$; varying the sampling rate with r can give a non negligible saving of time with respect to

$p^2 \cdot q \cdot \log_2(q)$. Also, the limitation in memory forces either the selection of some of the information or to find another (passive) memory allocation (like hard discs). An example of how the method was used in practise is shown in the following section for clarification.

4.3.2 Example of a segmented FFT: 210190A-SNA

As an example, the construction of the complete FFT power spectrum of the datafile 210190A will be shown. The results of this analysis are in Chapter V; this section restricts its discussion to the description of the method. On the night between the 21^{st} and 22^{nd} of January 1990, 8597 seconds of data were recorded using the Mark III telescope. The number of events coming from the direction of Supernova 1987A (and not triggering any of the off axis channels i.e. CONLY/CHOP events as described earlier in Chapter III) was 3224 and therefore the count rate was only 22.5 counts per minute or 0.375 Hz. This is a rather poor value, which is not surprising as the zenith angle of the Supernova went from 40 to 48 degrees during the run. The same kind of selection of events on data from Sco X-1 (like in the file from the 020589) gives more than 60 counts per minute.

As already mentioned, the microcomputer used (Acorn Cambridge Workstation) has a 4Mb memory which allows the storage of $3*2^{18}$ real numbers into arrays (4 bytes per real). This space was distributed as follows:

(i) Saving the final product: 2^{18} real part + 2^{18} imaginary ,

(ii) Performing intermediate FFTs: 2^{17} real + 2^{17} imaginary ,

with the total duration of the data file (8597.484 seconds) being equal to 2^{19} times 16.398 ms.

Individual transforms of size 2^{17} were performed although transforms 2^{18} were feasible. FFT size was sacrificed in order to retain as much information as possible. Note that the effective loss of time in doing this is not important as a 2^{17} FFT requires $17*2^{17}$ calculations while a 2^{18} FFT takes $18*2^{18}$ calculations, equivalent to (18/17) two 2^{17} FFTs. Although this might appear to be a saving, a not negligible part of the total computing time (around 25%) is spent unscrambling partial FFTs into the final product using IV.5, and the overall process is slower. The search from 8597.484 seconds down to 4.1 milliseconds is summarised in Table 4.1. The total number of independent periods searched was 2^{21} and its computation by different methods requires the following number of calculations:

Direct evaluation : $3224 \cdot 2^{21}$

FFT of size 2^{21} : $21 \cdot 2^{21}$

Segmented 2^{17} FFTs : $86 \cdot 17 \cdot 2^{17} = 91.375 \cdot 2^{21}$ (minimum)

Segmented 2^{17} FFTs : $132 \cdot 17 \cdot 2^{17} \approx 140.25 \cdot 2^{21}$ (used)

Segmented 2^{17} FFTs : $172 \cdot 17 \cdot 2^{17} \approx 182.75 \cdot 2^{21}$ (optimum)

Here "optimum method" is defined as mean keeping $P_{tried} \geq 4 \cdot \Delta$ (see end of Chapter V) always while the respective minimum values of for P_{tried}/Δ used in this example were (4.0, 4.0, 2.667, 4.0, 3.2, 2.667, 4.746, 4.0). The effective "saving" in calculations

(used/direct method) was a factor of 23.0 although the optimum method gives 17.6. Note that the poor count rate noticeable affects this "saving" as a "healthier" count rate of one hertz would give a saving factor around 50 for the optimum method.

FFT r =	Period Range (in ms)	Δ (ms)	d.o.f. (indep.)	Minimum FFTs	Used FFTs
0 & 1	8597484 - 32.797	16.398	2^{18}	2	4
2 & 3	32.797 - 16.398	8.199	2^{18}	4	8
4 & 5	16.398 - 10.932	4.100	2^{18}	8	8
6 & 7	10.932 - 8.199	2.050	2^{18}	8	16
8 & 9	8.199 - 6.559	2.050	2^{18}	16	16
10 & 11	6.559 - 5.466	2.050	2^{18}	16	16
12 & 13	5.466 - 4.685	1.025	2^{18}	16	32
14 & 15	4.685 - 4.100	1.025	2^{18}	16	32

TABLE 4.1

Steps in Constructing a Segmented FFT for the dataset 220190-SNA

4.3.3 Real data and imaginary samples

The Fourier transform is defined for x_t complex although the data are actually real numbers (events per bin). Leaving the imaginary part of the sample "empty" (zeros) means wasting half of the information available and makes half of the output redundant as (for a real sample) $J_k = J^*_{n-k}$.

A method chosen to avoid this redundancy is mentioned by Bloomfield (1976): this is to use twice the number of real data points, effectively doubling the size of the transform, by defining the variable $z_t = x_{2t} + i \cdot x_{2t+1}$, for t = 0, n/2-1 and transforming it. The n/2 independent terms of the transform of x_t $J_{k=0,n-1}\{x\}$ can be recovered from $J_{k=0,n/2-1}\{z\}$ using:

$$J_k\{x\} = \frac{1}{4} \left(J_k\{z\} + J^*_{n/2-k}\{z\} \right) + \frac{\exp(-\pi i \cdot k/n)}{4i} \left(J_k\{z\} - J^*_{n/2-k}\{z\} \right) \quad . \quad (IV.10)$$

In spite of the extra calculations required there is a gain as a transform of size n/2 is performed rather than one of size n.

4.3.4 Oversampling using a convolution function

Although the series J_k already contains all the information available from the data (and sampling) periodicities can be missed when their power is not contained in one single frequency bin w_k. The sensitivity of the transform to a pure sinusoidal signal with a frequency shift δk_o (where $-1/2 < \delta k_o \leq +1/2$), $x(t) = \exp(2\pi i \cdot \delta k_o \cdot t/n)$ is given by the expression:

$$J(\delta k_o) = \exp\{i\pi\delta k_o(1-1/n)+i\pi k/n\} \frac{\sin(\pi\delta k_o)}{n \sin\{\pi(\delta k_o - k)/n\}} \quad , \quad (IV.11)$$

and by the response at the nearest Nyquist frequency:

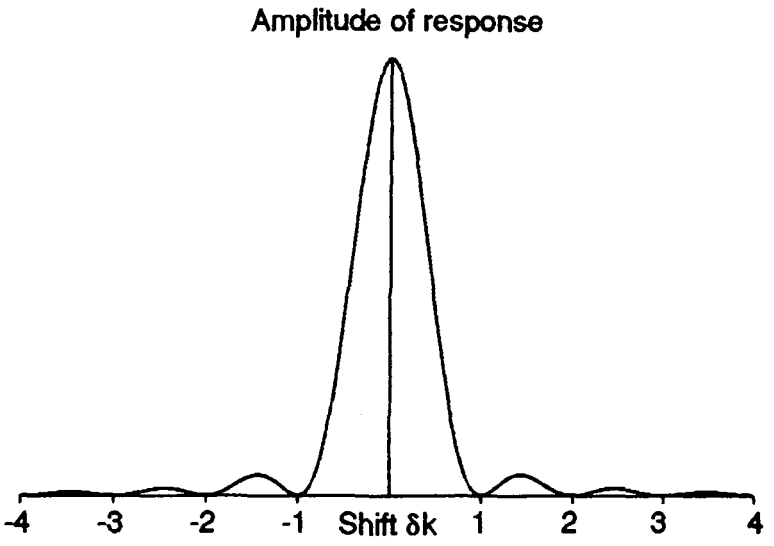

Figure 4.1

Amplitude of the response of a discrete Fourier transform to a sinusoid with a shift δk relative to a Nyquist frequency

Figure 4.2

Same response function as in Figure 4.1
1 trial per Fourier interval
δk between 0 and 1/2

$$J_{k=0}(\delta k_o) = \exp\{i\pi\cdot\delta k_o(1-1/n)\}\cdot\frac{\sin(\pi\delta k_o)}{n\,\sin(\pi\delta k_o/n)} \quad . \qquad (IV.12)$$

Figures 4.1 and 4.2 illustrate these two expressions. The minimum of the response function $J_{k=0}(\delta k_o)$, is at the $\delta k_o = 1/2$ (shifts are hereafter restricted to the interval $-1/2 < \delta k_o \leq 1/2$, as there is always a Nyquist frequency at less than 1/2 Fourier interval of distance); for infinite n this minimum response has the value $J_{k=0}(1/2) \approx (2i/\pi)$; the "measured" value for nR^2 would be $4/\pi^2 \approx 0.4053$ times the input value. The mean response (for infinite n) is $\langle|J(\delta k_o)|^2\rangle \approx 0.7737$. A pure sinusoidal signal with a chance probability 10^{-7} would show on average as a 3.8×10^{-6} but may be degraded as to look like a 1.5×10^{-3} fluctuation. It is obviously desirable not to miss any periodicity located in between Nyquist frequencies. This can be achieved by computing the transform not just at the Nyquist frequencies but also with at frequencies with a shift δk; i.e. by using more than one trial per Fourier interval (F.I.), or oversampling. The use of two trials per F.I. implies shifts with values $\delta k = 0$ and 1/2; three trials per F.I. correspond to $\delta k = 0, \pm 1/3$; five trials to $\delta k = 0, \pm 1/5, \pm 2/5$, and so on ....

The convolution function is deduced by considering the discrete transform at the Nyquist values shifted by δk:

$$J_{k+\delta k} = 1/n \sum_{j=0}^{n-1} x_j \exp\{-2\pi i\cdot(k+\delta k)j/n\} \qquad (III.17) \quad ;$$

the exponential sum is decomposed as a product:

$$J_{k+\delta k} = 1/n \sum_{j=0}^{n-1} x_j \exp\{-2\pi i \cdot \delta k \cdot j/n\} \exp\{-2\pi i \cdot (k+\delta k) j/n\} \ .$$

(IV.13)

The phase shift $\exp\{-2\pi i \cdot \delta k \cdot j/n\}$ is independent of k and can be seen as a function of time (j index). Using the well known result that the transform of the product is the convolution of the transforms (negative sub-indices being understood as modulo n):

$$J_{k+\delta k} = \sum_{l=-k}^{n-k-1} H_l \cdot J_{k-l} \quad , \qquad (IV.14)$$

the function $H_k(\delta k)$, which gives the transform at frequencies in between two Nyquist frequencies, is obtained:

$$H_k(\delta k) = \frac{1}{n} \sum_{j=o}^{n-1} \exp\{-2\pi i \cdot (k+\delta k) j/n\} = \frac{1 - \exp\{-2\pi i \cdot \delta k\}}{n \{1-\exp(-2\pi i \cdot (k+\delta k)/n)\}} \ .$$

(IV.15)

This function is just the response of a DFT to a sinusoid shifted by δk (discussed previously and shown in Figure 4.1) which decays relatively fast. The convolution gives a good approximation using just a few terms on each side. For $n \longrightarrow \infty$, the response to a sinusoid shifted by $\delta k_o = 1/2$ (i.e. the minimum response when an odd number of trials per F.I. are used) can be written as:

$$J(\delta k;1/2) \approx e^{-if} \cdot \frac{2}{\pi} \cdot \frac{\sin(\pi\delta k)}{\pi\delta k} \left\{ 1 + \delta k \sum_{l=0}^{n/2} \frac{l^2 + \delta k/2}{(l^2-1/4)(l^2-\delta k^2)} \right\}$$

(IV.16)

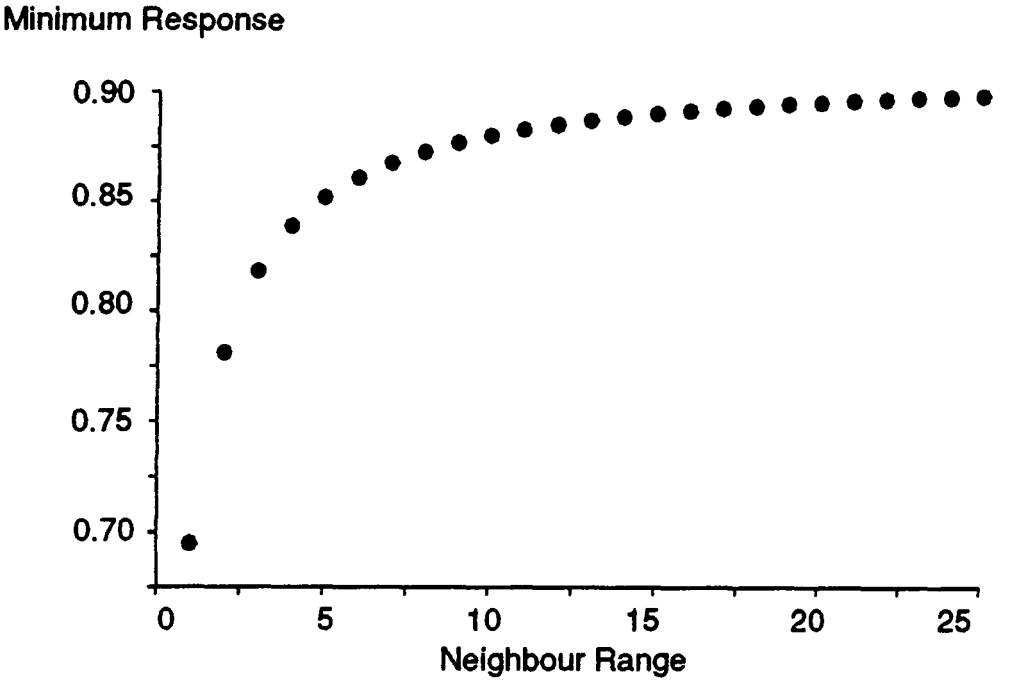

Figure 4.3a

Minimum Response Using 3 trials F.I.
"Neighbour Range" defined in the Text

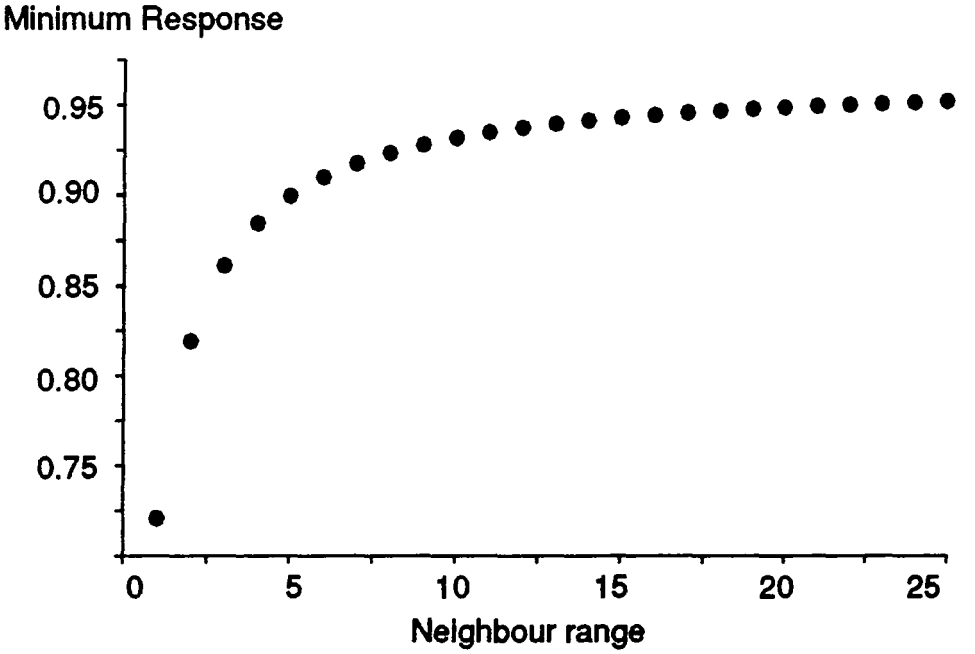

Figure 4.3b

Minimum Response using 5 trials per F.I.

where $f = \pi(\delta k - 1/2)$ denotes pulse phase. Figures 4.3a and 4.3b show how the response increases as a function of the maximum value considered for l (obviously a large l implies an extremely slow process), denoted here as "neighbour range"; considering four "neighbours" on each side increases noticeably the response at a low computing cost. On the other hand, the response, as a function of the signal shift δk_o, improves with the number of trials (Figures 4.4a to 4.4c). van der Klis (1989b) quotes two trials per F.I., $\delta k = 1/2$, and only one adjacent term ($l = 0,1$) as usual practise in X-ray astronomy. The signals considered here are much weaker, and therefore three trials per F.I. (Figure 4.5) with four neighbours considered on each side ($|l| \leq 4$) result in a better compromise between computing time and sensitivity. The cost in computing time turns out to be an extra ten minutes, negligible for a segmented FFT, which takes around four ($p = 16$) or eight hours ($p = 32$), and still worthwhile for a standard FFT (2^{18} points in half an hour) where the machine time is increased by 50%. Oversampling is sometimes done by adding gaps of the same duration as the data before and after the data in order to have three trials per F.I., triplicating the computer time. This can be done when computer time is not a limitation.

It is worth mentioning that no extra information is added, as the shifted terms $\{J_{k+\delta k}\}$ are linear combinations of the transform $\{J_k\}$. The effect of a frequency outside the Nyquist values is already present ("hidden") in the original transform.

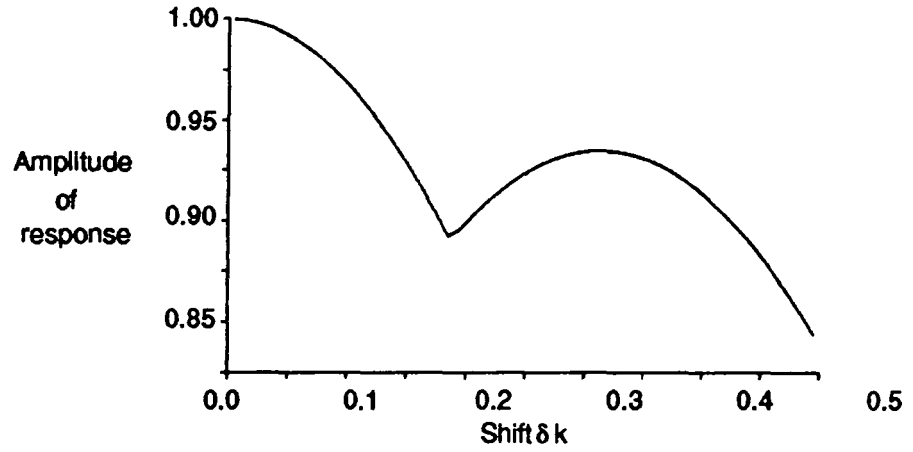

Figure 4.4a

Response function using 3 trials per FI
See Figure 4.2

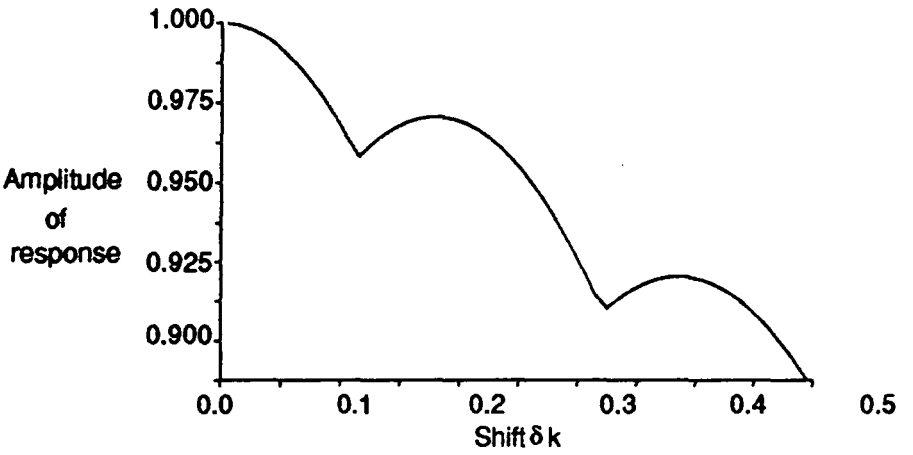

Figure 4.4b

Response function using 5 trials per FI

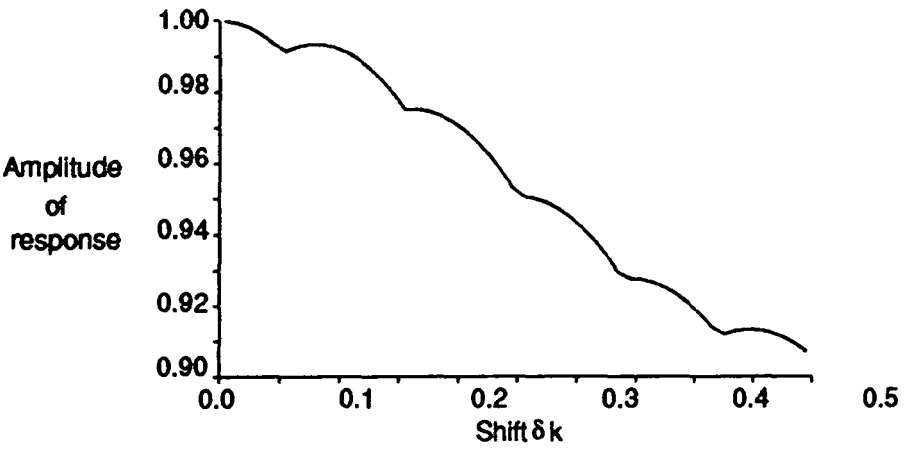

Figure 4.4c

Response function using 11 trials per FI

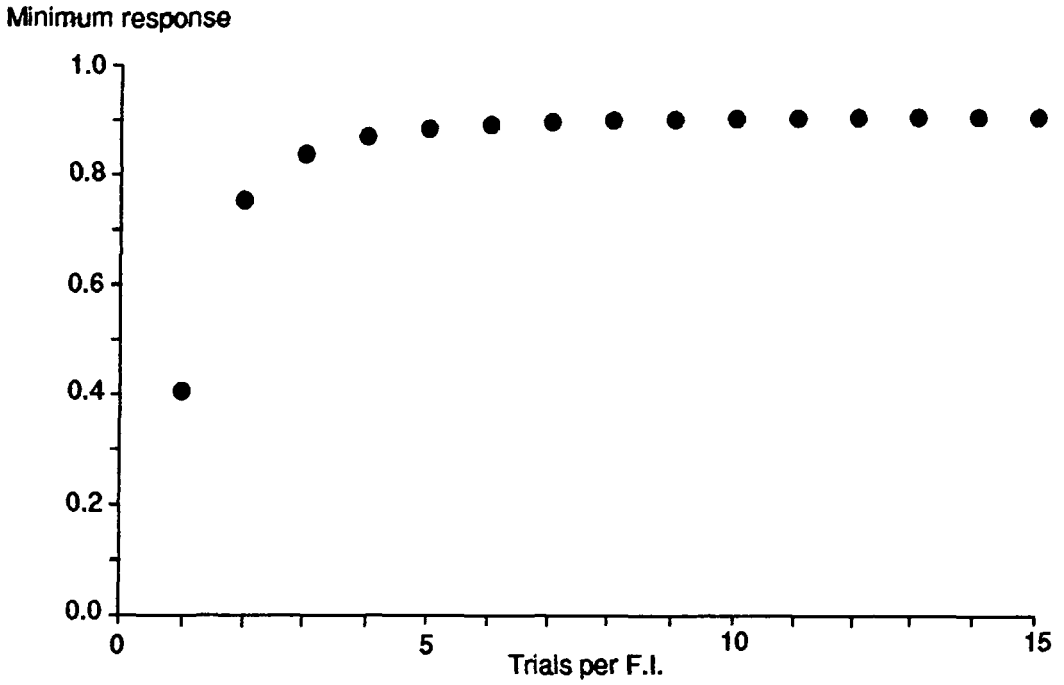

Figure 4.5

Minimum of the response function using
a convolution function over four "neighbours"
Note that 3 trials per F.I. give a very reasonable
accuracy at a low expense.

4.3.5 Accuracy and speed requirements

In the case of segmented FFTs the program was initially designed to work with $4 \cdot \Delta \geq Pmin \geq 2 \cdot \Delta$ (Pmax given by the "order" of the segmentation) giving optimum speed but low sensitivity. The option was afterwards implemented for halving (in principle indefinitely) the sampling rate in order to work in the intervals $(4\Delta, 8\Delta)$, $(8\Delta, 16\Delta)$ and so on. Obviously the computing time was then increased by two (or four or ...).

4.3.6 Use of filters

Possible causes for spurious peaks in the periodogram were mentioned in Chapter III; as they tend to affect the low frequency region of the power spectrum they do not constitute a real problem. It was therefore judged unnecessary to implement any filter. The only relevant case might be when data from various nights are added in phase and strong beats arise. Orbital and secular variations in an unknown periodicity would make this adding in phase pointless for a period search and, therefore, this problem was not envisaged here. The only exception is in Section V.3 where data from SN87A taken in two consecutive nights were used in phase for a period search; because only two consecutive datasets were included no beatings were present at frequencies below 10^{-2} Hz.

4.4 CRITERIA FOR DATA SELECTION AND PERIOD DETECTION CLAIMS

4.4.1 Count excesses and expected Rayleigh power

As direct measurements of fluxes using count excesses, sometimes abbreviated as DC fluxes, are subject to fluctuations it should not be unexpected that Rayleigh powers might appear to be above DC measurements. A 3σ excess in pulsed events is not necessarily in contradiction with no DC excess; if they are both related to a signal one expects to have within fluctuations:

$$(\text{DC flux}) \geq (\text{Pulsed flux}) \quad .$$

By definition 1σ or 2σ fluctuations are common in the background; if a normal distribution is assumed then the relevant probabilities are given by $\text{erf}(1) \approx 0.317$ and $\text{erf}(2) \approx 0.045$. This suggests, for example, that a 3σ pulsed excess on a section of data having a 1σ count excess is compatible with a 2σ DC strength 8% of the times. Obviously an extremely large pulsed strength, like 10σ for example, cannot occur without a similar count excess, like 8σ or 9σ for example, if produced by a source.

4.4.2 Selecting data for a period search

Some criteria have to be used to choose the data which are to be analysed for a period search. Two main requirements are:

(i) count rate excess

Although short term increases in the count rate are expected there is always the possibility that they are related to a source. Either sections or complete sets of data with an excess above two or three times the Poissonian level of fluctuations are considered to be "promising" for a period search;

(ii) particular orbital phase,

When the orbital period and epoch of mid- eclipse are known, data can be selected around a phase where the rate of change of pulse phase with orbital phase is at a minimum (quadrature). Making a

guess of a.sini allows the estimation of how long these pieces of data be (Chapter III).

4.4.3 Selecting period candidates from a period search

Periods appearing above a threshold power were kept. The threshold selected was relatively low as the signals of interest are weak; the level was set at a Rayleigh power of 9.21 which is equivalent to a 10^{-4} chance probability. This value is below expectation and therefore every run gave a list of candidate periods: for every $3 \cdot 2^{18}$ frequencies tested some eighty candidate periods were expected. Transforms were performed for more than one datafile per source in order to search for reappearing frequencies, allowing a small range for possible Doppler shifts due to orbital motion. Reappearances were considered necessary before considering seriously any candidate period found.

4.5 LIMITATIONS IMPOSED BY THE SIGNAL TO NOISE RATIO

TeV signals are generally too weak for a comprehensive period search, considering the number of degrees of freedom involved. If a final probability of 1%, allowing for all degrees of freedom spent, is required after 10^6 tries, then the signal must have a Rayleigh power of $nR^2 = -\mathrm{Ln}(10^{-8}) \approx 18.42$. This is equivalent to a pulsed excess of 8% for 3000 events, or 4.3% for a large 10000 event dataset. In principle a signal below this level is not

expected to show above fluctuations, although the relative phase of signal and noise has a large weight in the actual outcome. For this reason, it was not envisaged that use would be made of extra variables, such as pulse period derivative or plausible orbital parameters, as the number of degrees of freedom increases rapidly. An exception to this will be an attempt to compensate for a circular orbit in Scorpius X-1. This period search analysis, and those of other objects like GX 5-1 and SN1987A, is presented in the next chapter.

V. PERIOD SEARCHES IN TEV γ-RAY DATA

5.1 PERIOD SEARCHES IN SIMULATED DATA

5.1.1 Purpose of simulations

The main purpose of performing these computer simulations was to test the period-search program. Simulated datafiles consisting of a mixture of random and pulsed events, with a duration typical of a real datafile, 5000 seconds, were created. Free parameters were the injected period, the overall count rate and the percentage of pulsed events. Two values for the count rate were used: 1.0 and 5.0 counts per second, the first being a typical count rate for present Cerenkov telescopes while the second count rate should represent that of an array of five or more of such detectors working simultaneously but counting independently. As typical fluxes reported from TeV sources are rarely above 5% of the cosmic ray flux while an object emitting below 2% is not detectable in a single night (at least with the present count rates of the order of one hertz) the percentage of pulsed events injected was between 2 and 6%. Some uncertainty on this figure is present. This is due to noise either suppressing or enhancing depending on the relative phases of signal and noise. Two values were chosen for the period: 64 milliseconds requiring only one direct FFT, and 16 ms which needed a segmented FFT. Both methods, FFT and segmentation, were then checked together.

5.1.2 Results

(i) 1 Hz counting rate

Figures 5.1 and 5.2 show examples of power spectra obtained with the FFT program. The first power spectrum is obtained directly, without segmentation, while the second does require the segmented method. Both datasets had a 6% pulsed excess injected at a period of 64.32 and 16.08 ms respectively, which appears as the strongest power in each plot. As was expected, in the files where a proportion of 4% pulsed events were injected the corresponding peak in the power spectrum appeared about the same level as the highest random fluctuations, while injected signals could not be separated from the noise in the case of a 2% pulsed excess.

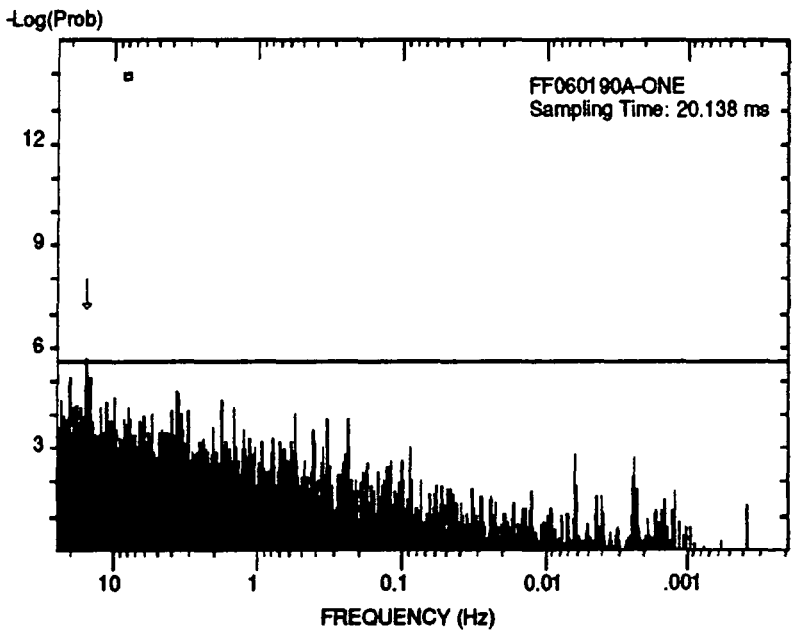

Figure 5.1

FFT power spectrum of simulated data with 6% pulsed excess at 64.32 ms and 1 Hz count rate

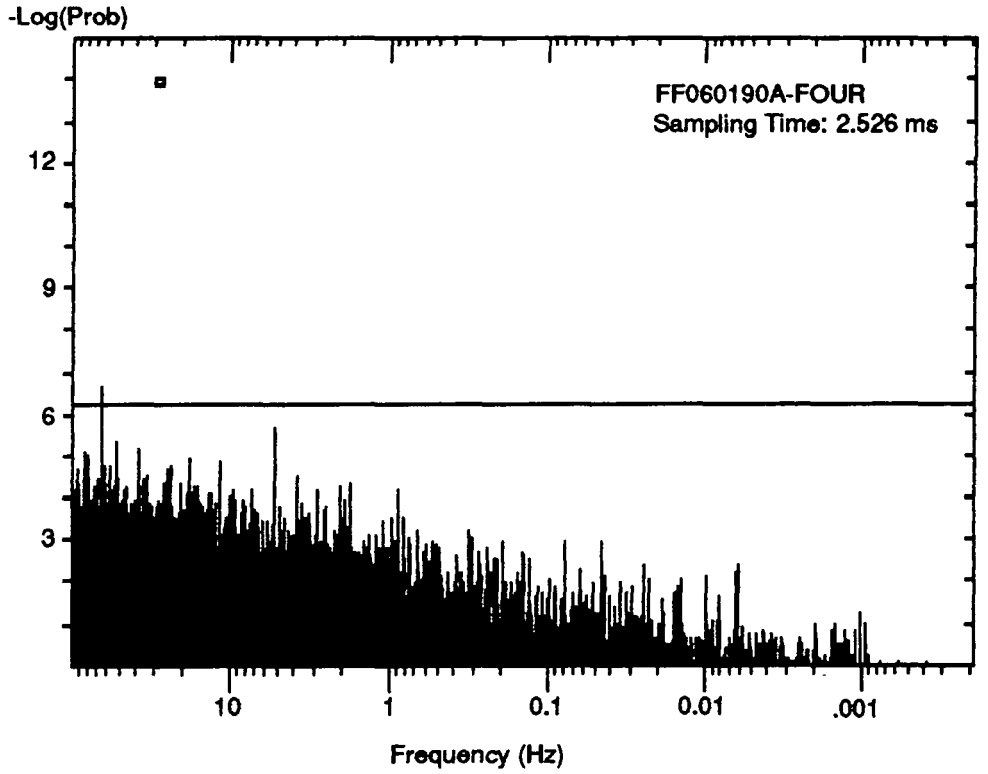

Figure 5.2a

FFT power spectrum constructed using a segmented transform. Dataset has 6% pulsed excess at 16.08 ms and 1 Hz count rate

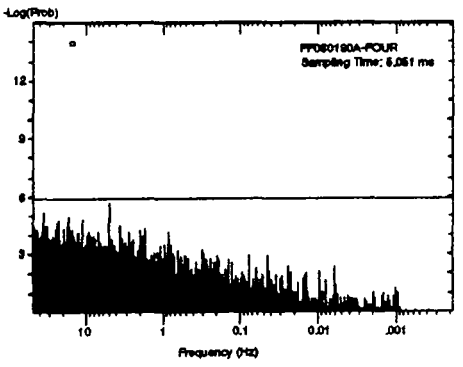

Figure 5.2b

First segment of the transform in Figure 5.2a . Log scale

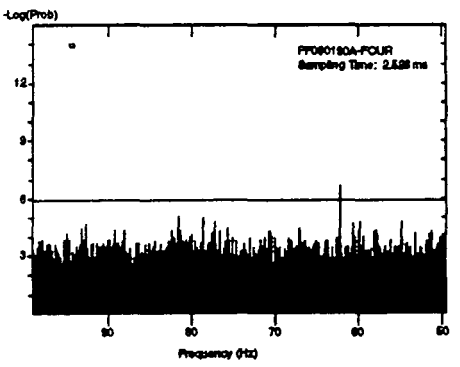

Figure 5.2c

Second segment of the transform in Figure 5.2a . Linear scale

In order to monitor the response of the program to different sampling time, a section of 3929 seconds from the file with 6% excess at 64.32 ms was selected. This duration is such that the ratio of the period to the sampling rate can be chosen to be close to an integer power of two. Figure 5.3a shows the periodogram computed using the exact time of each event; in the following Figures, 5.3b to 5.3d, it can be seen how the power at the injected frequency increases as the sampling time decreases from $P_{inj}/2.146$ to $P_{inj}/8.583$, P_{inj} being the injected period. At the same time the overall section of the periodogram acquires the "exact" profile.

A comparison of the measured and the exact values for the percentage of γ-rays, R, appear in Table 5.1a. Although there may be a slight tendency of the FFT to underestimate the amplitude of the Rayleigh vector, this is far from systematic; as the powers used for comparison were strong, this been the case of interest, a bias might have been introduced. Note that an underestimation of the power can bring a 10^{-6} probability up to 10^{-3} or 10^{-2}, which is obviously not desirable. A factor of two increase in resolution, although also in computer time, gives a noticeable improvement in sensitivity as the calculation of the power becomes more accurate. In these simulations the saving in time (defined in Chapter IV as the ratio between the time required using a direct calculation or a FFT algorithm) was near to 200 when working at near to twice the sampling rate, or around 100 when "double" resolution was used (i.e. sampling rate below a fourth of the minimum period).

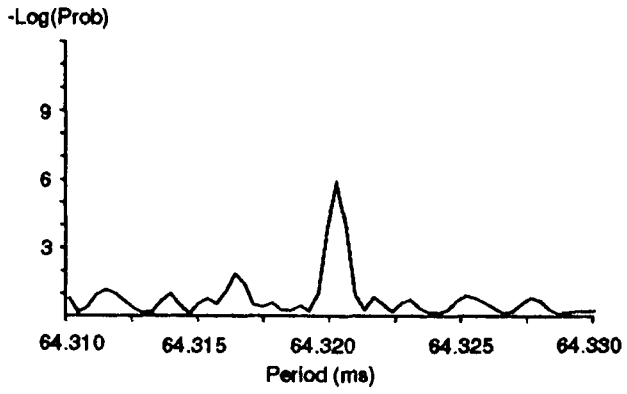

Figure 5.3a

Rayleigh test periodogram of a 3929 second section of the data shown in Figure 5.2 aound the injected period of 64.32 ms

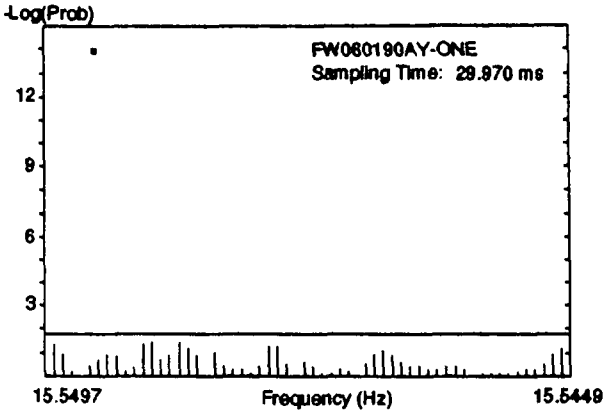

Figure 5.3b

FFT version of Figure 5.3a using period/sampling rate = 2.146

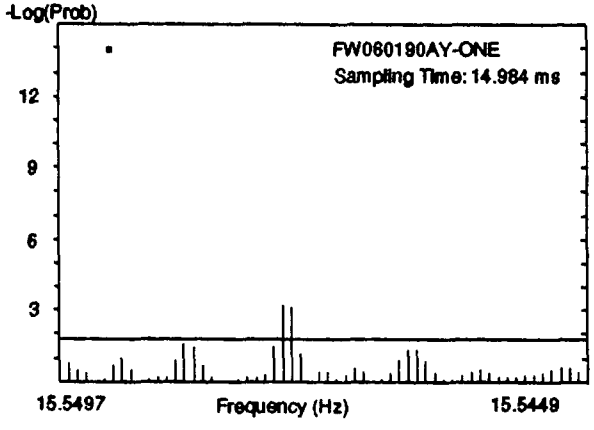

Figure 5.3c

FFT version of Figure 5.3a using period/sampling rate = 4.292

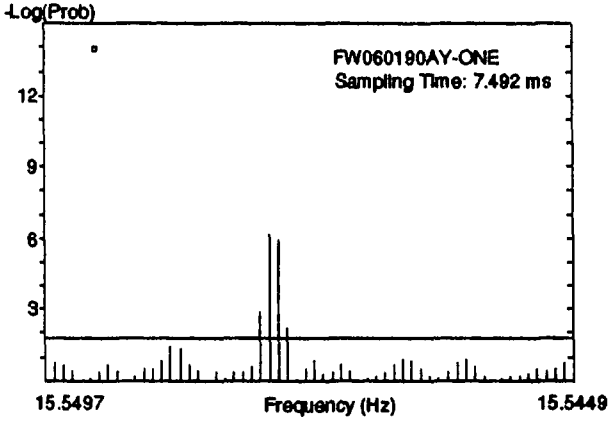

Figure 5.3d

FFT version of Figure 5.3a using period/sampling rate = 8.583

		EXACT		FFT		
Filename	Rate (Hz)	%	Prob .	%	Prob.	P/Rate
C020190A-ONE	1.0	3.32	4×10^{-3}	2.86	2×10^{-2}	3.365
C020190A-FOUR	1.0	3.04	1×10^{-2}	3.54	2×10^{-3}	3.302
C040190A-ONE	1.0	4.27	1×10^{-4}	3.32 3.99	4×10^{-3} 3×10^{-4}	3.446 6.892
		4.40	6×10^{-5}	3.68 4.13 4.69	1×10^{-3} 2×10^{-4} 2×10^{-5}	3.267 6.534 13.068
C040190A-FOUR	1.0	6.33	2×10^{-9}	5.49 6.09	3×10^{-7} 9×10^{-9}	3.404 6.808
		4.51	4×10^{-5}	4.60	3×10^{-5}	6.450
C060190A-ONE	1.0	4.46	5×10^{-5}	2.57 3.88	4×10^{-2} 5×10^{-4}	3.351 6.702
		6.74	1×10^{-10}	5.17 6.03 6.51	2×10^{-6} 1×10^{-8} 6×10^{-10}	3.194 6.388 12.777
C060190AX-ONE	1.0	5.91	3×10^{-6}	3.49 6.25 6.20	1×10^{-2} 5×10^{-7} 6×10^{-10}	2.146 4.292 8.583
C060190A-FOUR	1.0	6.31	2×10^{-9}	4.79 5.97	1×10^{-5} 2×10^{-8}	3.415 6.831
		5.82	4×10^{-8}	5.52	2×10^{-7}	6.366

TABLE 5.1a

Simulations

Comparision of the ratio of pulsed to total events in % between FFT and the exact computation. Files have a 1 Hz count rate
Files ONE : P = 64.32 ms , FOUR: P = 16.08 ms

(ii) 5 Hz count rate

Only one plot is shown (Figure 5.4), corresponding to simulated data with 4% pulsed excess at 16.08 ms. The signal peak is evident due to the higher signal to noise. There is still a tendency to underestimate the Rayleigh power (Table 5.1b) but with these count rates the signal to noise is high enough to give non-statistical peaks in the spectrum and differences become quantitative rather than qualitative. Because of the higher count rate the savings in computer time are considerably larger than with a 1 Hz count rate.

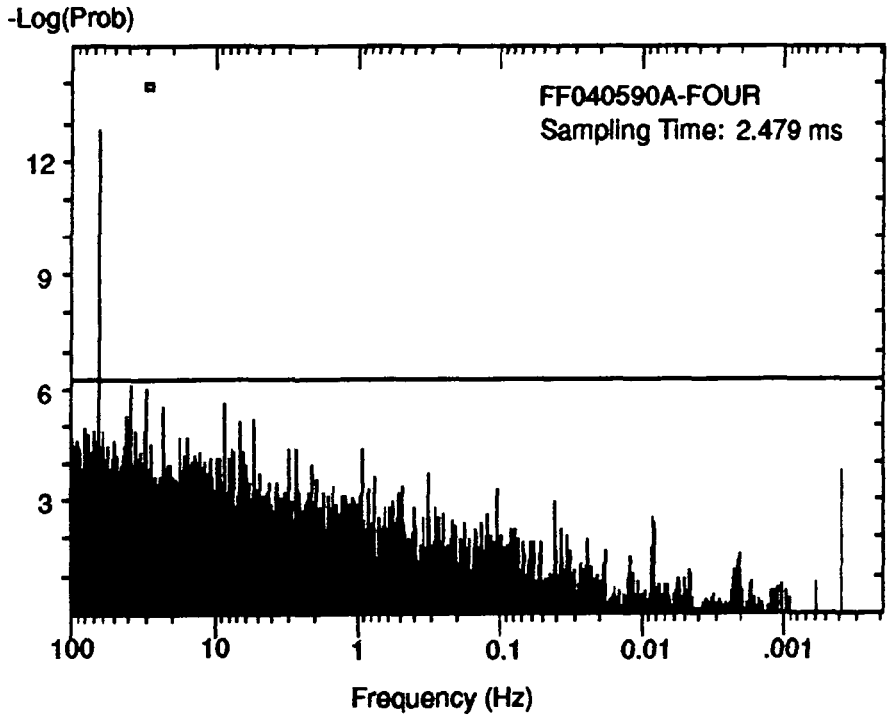

Figure 5.4

Power Spectrum of Simulated Data with a 4% Pulsed Excess at 16.08 ms and 5 Hz Count Rate

		EXACT		FFT		
Filename	Rate (Hz)	%	Prob .	%	Prob.	P/Rate
C020590A-ONE	5.0	4.23	4×10^{-20}	3.69	2×10^{-15}	3.349
C020590A-FOUR	5.0	3.96	9×10^{-18}	2.96	3×10^{-10}	3.348
C040590A-ONE	5.0	4.28	1×10^{-20}	3.54	2×10^{-14}	3.386
C040590A-FOUR	5.0	4.56	3×10^{-23}	4.01	3×10^{-18}	3.368
		3.71	1×10^{-15}	3.44	1×10^{-13}	6.486
C060590A-ONE	5.0	5.95	4×10^{-39}	5.06	2×10^{-28}	3.383
C060590A-FOUR	5.0	6.15	7×10^{-42}	5.77	7×10^{-37}	3.397

TABLE 5.1b

Simulations

Comparis on of the ratio of pulsed to total events in % between FFT and the exact computation. Files have a 5 Hz count rate
Files ONE : P = 64.32 ms , FOUR: P = 16.08 ms

5.1.3 Statistical distributions of power spectra

The distributions of powers were computed and compared with the *expected* asymptotic exponential distribution and the *best* exponential fit. An example is shown in Figure 5.5a, with the following Figures, 5.5b and 5.5c, showing the deviations from the expected and best fit respectively. In Table 5.2 a comparison of the best and expected fits is made for both count rates. In the (absolute) value of the slope of the "best" fit was found to be between 2 % and 5 % above than that of the "expected" fit. Using

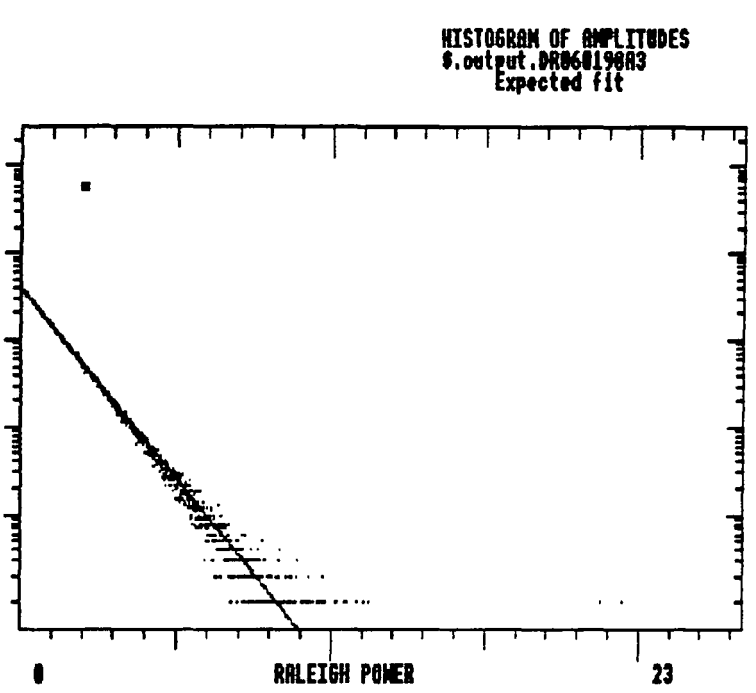

Figure 5.5a

Distribution of powers in simulated data (Fig. 5.1)
Binwidth in power is 0.01. The straight line
represents the expected exponential fit
given by: $n(i)\,di = 3913\ \exp(-0.01\,i)\,di$

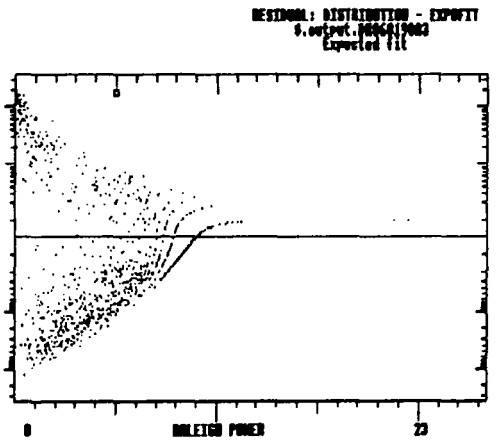

Figure 5.5b

Residuals of the distribution shown in Figure 5.5a
and its expected fit. Depatures at the origin are
$\Delta n(0) \sim 200$, compared to $n(0) \sim 4000$

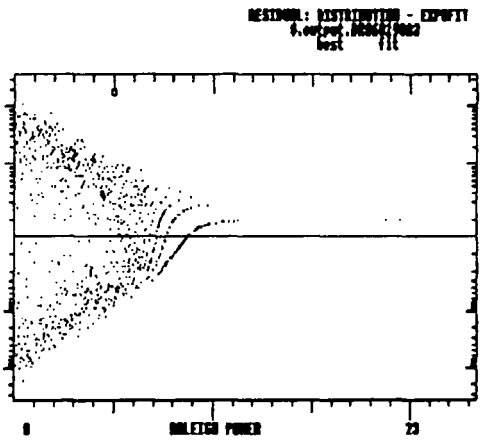

Figure 5.5c

Residuals of the distribution shown in Figure 5.5a
and its best exponential fit.
Departures at the origin are
of the same order as in Figure 5.5b.
Best exponential fit is given by:
$n(i)\,di = 4044.1\ \exp(-0.01035\,i)\,di$

	BEST FIT		EXPECTED FIT		$\frac{\langle R^2 \rangle}{\langle R^2 \rangle_{xptd}}$
Filename	A	β	A	β	
C020190A-ONE	4005.20	.01024	3912.56	0.01	1.00366
C040190A-ONE	4007.54	.01025	3912.56	0.01	0.99686
C060190A-ONE	4023.49	.01030	3912.56	0.01	0.99605
C020590A-ONE	4015.13	.01027	3912.56	0.01	0.99666
C040590A-ONE	4001.92	.01022	3912.56	0.01	0.99801
C060590A-ONE	4021.94	.01029	3912.56	0.01	1.00294

TABLE 5.2a

Comparison between the "best" and the "expected" exponential fit, defined as A EXP(-βi), for the distribution of powers in simulated data.
The step in the distributions is 0.01 of Power.
Count rate is 1 Hz

	BEST FIT		EXPECTED FIT		$\frac{\langle R^2 \rangle}{\langle R^2 \rangle_{xptd}}$
Filename	A	β	A	β	
C020190A-FOUR	8112.94	.01038	7825.13	0.01	1.00348
C020590A-FOUR	8125.56	.01039	7825.13	0.01	0.99949
C040190A-ONE	8048.46	.01029	7825.13	0.01	0.99707
C040190A-FOUR	8093.92	.01035	7825.13	0.01	0.99593
C040190A-FOUR	8171.98	.01044	7825.13	0.01	0.99713
C040590A-FOUR	8118.15	.01039	7825.13	0.01	0.99853
C060190A-ONE	8064.16	.01031	7825.13	0.01	0.99985
C060190A-FOUR	8121.31	.01039	7825.13	0.01	1.00313
C060190A-FOUR	8215.78	.01051	7825.13	0.01	0.99899
C060590A-FOUR	8111.32	.01037	7825.13	0.01	1.00408

TABLE 5.2b

Same as Table 5.2a for a count rate of 5 Hz

real data this "best" slope was usually found to be around 5% or more larger than its expected value. Although these departures are not negligible, correlations with the expected exponential fit were good, mostly above 99%. Further comments will be made at the end of this chapter.

5.2 PERIOD SEARCHES IN THE SCORPIUS X-1 DATABASE

5.2.1 The influence of the unknown orbital parameters

The cyclic Doppler shift to the red and blue of any coherent pulse signal from Scorpius X-1 is a major problem when attempting to find any periodicity present. In this particular case there is an orbital period and even a radial velocity curve for the Doppler shift of the HeII line (with a slightly different orbit for Hβ; Gottlieb *et al.*, 1975; Crampton *et al.*, 1976; LaSala and Thorstensen, 1985) which might be related to the neutron star. On the other hand, the X-ray emission shows no orbital modulation; the upper limit is ~ 0.7% (Priedhorsky & Holt, 1987).

If the Doppler shift of the HeII lines does coincide with the motion of the neutron star, and a pulsar period of two milliseconds is assumed, the values of the time events recorded from the direction of Scorpius X-1 require a correction to account for the orbital motion for datasets with duration above 329 seconds in general, and 22 minutes near orbital phases 0.25

Line	Phase zero (JD - 2440000)	Velocity ($km.s^{-1}$)
HeII 4686 - base	5084.536 ± 0.015	56 ± 6
HeII 4686 - peak	5084.583 ± 0.038	48 ± 13
Hβ - base	5084.628 ± 0.028	42 ± 9
Hβ - peak	5084.599 ± 0.034	57 ± 15

TABLE 5.3

Orbital parameters for Scorpius X-1

from LaSala & Thorstensen (1985)

and 0.75 (as discussed in Chapter III). A periodic signature would only appear if it is strong enough to show itself within this "distortion" time, defined in Chapter III.

The fits to the variations in HeII and Hβ lines from LaSala & Thorstensen (1985) are shown in Table 5.3. As mentioned in Chapter III, one of the conclusions of this authors is that the HeII line should reflect the motion of the compact object, as this line is most probably produced in the outer regions of the accretion disc. This is the case if, for example, the region emitting the line forms a ring centered on the neutron star. The orbital parameters presented in Section 3.2.4 were used to correct (or to "focus") the arrival times for the events from the two

nights which overlap in orbital phase. Crampton *et al.* (1976) suggested an inclination $i \approx 30^{\circ}$ which combined with the value used here for the projected semi-major axis, $a.\sin(i) \approx 2.127$ light seconds, gives a semi-major axis of 4.245 light seconds, a reduced mass for the system of 0.132 $M_{\odot}$ and, assuming a neutron star of 1.44 $M_{\odot}$, a companion with a mass of just 0.146 $M_{\odot}$.

5.2.2 Data selected for period search and its orbital phase

As mentioned in Chapter III, observations of Scorpius X-1 were made from March 1987 to July 1990. The data showing a positive count excess were recorded in May - June 1988 and May 1989; and, as discussed in Chapter III, the 1988 data shows an excess for orbital phases between 0.15 and 0.55. The presence of a signal was the main criteria for selecting data for the period search. The data selected were those recorded on the nights of the 110588, 120588, 130588, and 020589.

Datafiles were divided in (slightly overlapping) subsets of about 1/10 of the orbital period (around 6800 seconds), the chosen sections being named C110588A2, C120588A1, C120588A2, C130588A3, C130588A4, E020589A1 and E020589A2 (see Appendix I for a description of the database, convention on filenames and the correspondence between time events and JD/UT time). The file E020589 overlaps exactly in phase with C120588 and was cut in two files (E020589A1 and E020589A2) covering exactly the same orbital ranges as the corresponding subfiles from 120588 (C120588A1 and C120588A2).

File	Duration (seconds)	Orbital phase range	% DC excess and channel	Background events
C110588A2	7799	.1940 .3087	Side : 0.79 Centre: 4.30 Total : 2.50	2905 2765 5670
C120588A1	9179	.3574 .4924	Side : 1.78 Centre: 5.80 Total : 3.27	5350 3155 8505
C120588A2	6535	.4447 .5408	Side :-.68 Centre: 6.45 Total : 1.90	4278 2420 6698
C130588A3	6238	.8013 .8930	Side : 2.52 Centre: 4.54 Total : 3.28	3644 2183 5827
C130588A4	6836	.8913 .9918	Side : .74 Centre: 6.16 Total : 2.87	2300 1493 3793
E020589A1	9179	.3574 .4924	Side : 7.31 Centre: -.56 Total : 3.32	4656 4512 9168
E020589A2	6535	.4447 .5408	Side : 3.59 Centre: 3.26 Total : 3.42	2980 3007 5987

TABLE 5.4

Orbital phases and count excesses of segments

of data selected for the peiod search

Unfortunately, of these datafiles only the one recorded on the 110588 includes the time of quadrature, as it can be seen in Table 5.4. Period searches were also made in versions of the files C120588A1, C120588A2, E020589A1 and E020589A2 in which arrival times were corrected to account for the motion of the HeII line. Obviously this correction is only useful if the line

does indeed represent the motion of the neutron star (and the TeV source is co-located with the compact object!). As this correction appears necessary in order to find rapid pulsations, the HeII orbital parameters were used in here.

Finally five independent small sections of data showing an increase in the count rate (mostly below significance) from the two datafiles 120588 and 020589 were extracted and analysed. None of the other datafiles showed local increases in the count rate ("bursts") which might give suitable data segments for a period search (Scorpius X-1 appears to be a relatively steady source as indicated by Brazier *et al.*, 1990b). The five segments selected were named as C120588AA, C120588AB, E020589AA, E020589AB and E020589AC and had durations between 480s and 2160s (Appendix I) still large compared to the distortion time (Figure 3.10) as these "burst candidates" were between orbital phases 0.35 and 0.55, where the Doppler effect is not negligible for short periods and a weak pulsed emission.

5.2.3 Period Searches & Results

Segmented FFTs were performed in order to cover the range between two and five milliseconds. For the files extracted from the nights of 120588 and 020589 segmented FFTs were performed to test all periods above 2.0 ms, covering 3×2^{22} and $3^2 \times 2^{20}$ degrees of freedom for the first and second segments respectively (that is 1.26×10^7 d.o.f. for 120588A1 and 0.94×10^7 d.o.f. for 120588A2). Figures 5.6a and 5.6b show some of the power spectra.

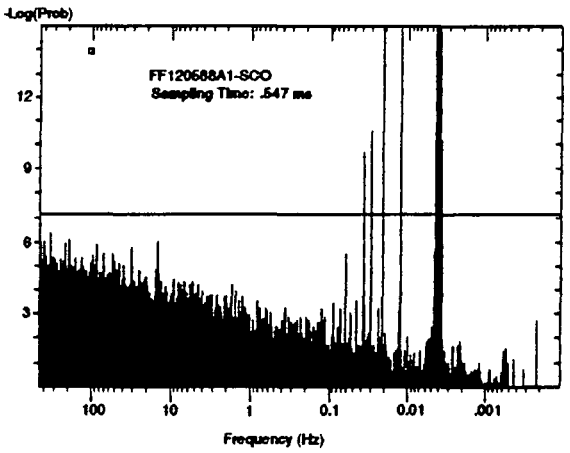

Figure 5.6a

Power spectrum of Scorpius X-1 data
taken the 120588. Event selection is CONLY
Note the powers introduced by the 4 minute
chopping cycle. Minimum period is 2.19 milliseconds

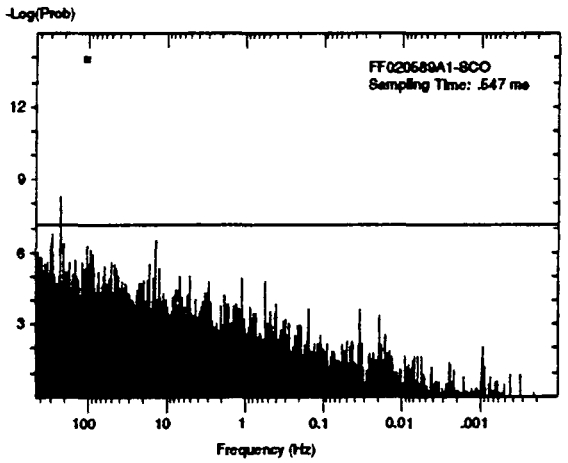

Figure 5.6b

Power spectrum of Scorpius X-1 data
taken the 020589. Event selection is CHOP
This data show the best candidate period
of 4.482 milliseconds

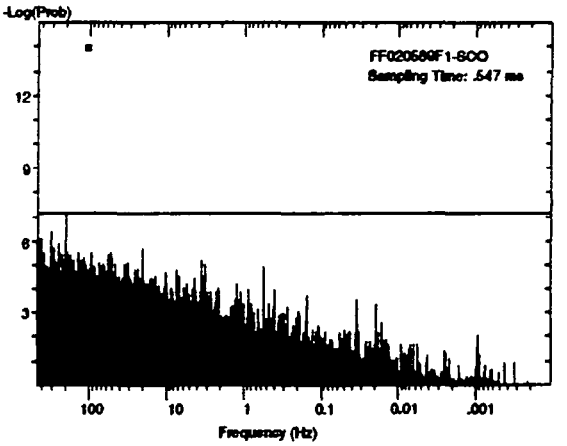

Figure 5.6c

Power spectrum of Scorpius X-1 data
taken the 020589. Event selection is CHOP
Data are the same as in Figure 5.6b with
an attempt to correct for orbital motion

In the case of the short sections the period search covered all the range down to two milliseconds. Anything showing better than a set threshold probability of 10^{-4} (having some 10^6 trials, this represents a few hundred "suspects" per power spectrum computed) was preselected in a first list of candidate periods. Values harmonically related to the four minutes from the chopping mode were discarded. The Rayleigh powers of the candidate periods were recomputed directly from expression (III.16). Afterwards the final lists of periods were compared to see if there was any repetition.

The results for each file and for the three groups, entire files, corrected files and small sections with high count rate, are shown in Tables 5.5a to 5.5e. The best candidate for a period in an individual complete file (either "raw" or "focused") is (4.482007 ± .000002) milliseconds (file E020589A1 in Figure 5.6a), with a chance probability of 2.13×10^{-9}; after allowing for the number of frequencies tried in this particular file the effect has a 2.64% chance probability, and a 19.3% probability of being a fluctuation when accounting for the total number of files. Figure 5.6d shows the statistical distribution of more than 10^7 powers from various files (E020589A1 + E020589A2 + C120588A1 + C120588A2) while the following Figures, 5.6e and 5.6f, show the residuals (departures) from the expected exponential fit.

The search for peaks repeated in different files revealed a period of (2.565765 ± .000005) ms appearing in the two (independent) files E020589AA and E020589AB (non overlapping

File	Period (ms)	Chance Probability	d.o.f. 3×2^{18}	Overall Prob.	
C110588A2	3.5339245	3.43×10^{-8}	9	0.22	*
C120588A1	5.0888200	9.35×10^{-7}	16	$1 - 8 \times 10^{-6}$	
C120588A2	2.9083328	3.58×10^{-7}	12	0.97	
C130588A3	2.7188759	1.55×10^{-6}	9	$1 - 2 \times 10^{-4}$	*
C130588A4	3.0327650	2.76×10^{-8}	8	0.16	*
E020589A1	4.4820074	2.13×10^{-9}	16	0.026	
E020589A2	32.633825	4.26×10^{-8}	12	0.33	
BEST	4.4820074	2.13×10^{-9}	72	0.11	

TABLE 5.5a
Period Search Results for Scorpius X-1
* ≡ Search between 2 and 5 ms. Otherwise search for ≥ 2 ms.
The error in the Period is around $P^2/T \cdot 10^{-6}$ or 10^{-5} ms depending on the Period and Duration of the Datafile

File	Period (ms)	Chance Probability	d.o.f. 3×2^{18}	Overall Prob.	
C120588F1	3.5811753	1.96×10^{-8}	16	0.22	*
C120588F2	4.1810406	1.80×10^{-7}	12	0.82	*
E020589F1	3.2663458	3.03×10^{-8}	16	0.32	
E020589F2	4.1536646	8.23×10^{-8}	12	0.54	*
BEST	3.5811753	1.96×10^{-8}	56	0.58	*

TABLE 5.5b

Period Search Results for Scorpius X-1
Files Corrected for Orbital Motion
* ≡ Search between 2 and 5 ms. Otherwise search for ≥ 2 ms.

File	Period (ms)	Chance Probability	d.o.f. 3×2^{18}	Overall Prob.
C120588AA	2.8510764	8.89×10^{-7}	4	0.94
C120588AB	18.1790103	3.78×10^{-6}	1	0.95
E020589AA	3.6513330	4.67×10^{-8}	4	0.14
E020589AB	2.3115291	3.65×10^{-6}	3	$1 - 2 \times 10^{-4}$
E020589AC	2.1444144	5.22×10^{-8}	2	0.079
BEST	3.6513330	4.67×10^{-8}	14	0.40

TABLE 5.5c

Period Search Results for Scorpius X-1
Segments of Data. $P \geq 2$ ms.

File	Period (ms)	Chance Probability	d.o.f. 3×2^{18}	Overall Prob.
BEST	4.4820074	2.13×10^{-9}	128	0.19

TABLE 5.5d

Period Search Results for Scorpius X-1
Best Overall Candidate Period

File	Period (ms)	Chance Probability	d.o.f. 3×2^{18}	Overall Prob.
E020589AA E020589AB	2.56576471	1.71×10^{-9} (phased)	264.2 $\pm$ 13.1	0.30 ± 0.01

TABLE 5.5e

Period Search Results for Scorpius X-1
Period Repeated with Significance better than 10^{-4}
in more than One Datafile

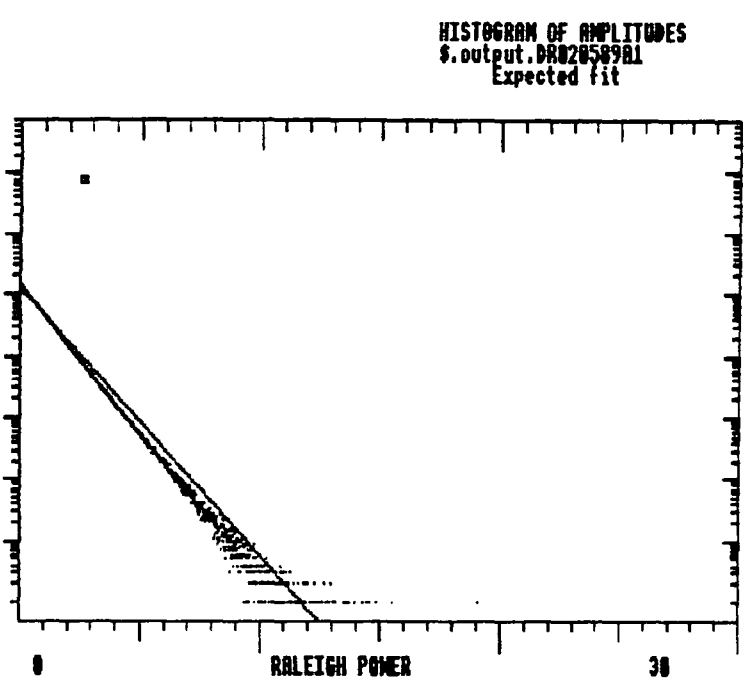

Figure 5.6d

Distribution of powers in Scorpius X-1 data
Datafile 020589A1 as in Figure 5.6b
The straight line represent the expected fit
Expected fit parameters: $a = 1.25 \times 10^5$, $\beta = 0.01$)
Best fit parameters: $a = 1.46 \times 10^5$, $\beta = 0.0117$)

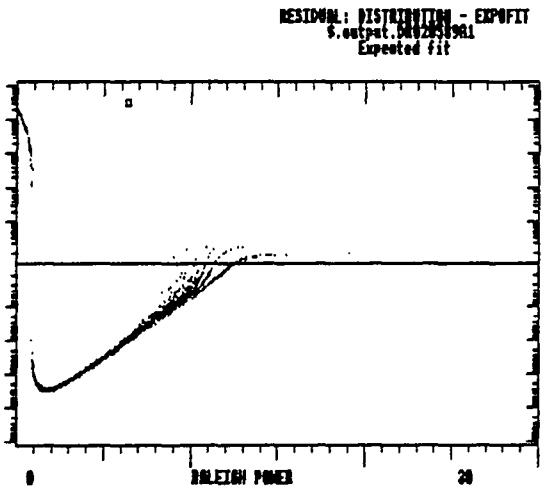

Figure 5.6e

Residuals of the distribution in Figure 5.6c
and its expected exponential fit.
Departure at power origin is around 5.8σ
(σ = sqrt(fit))

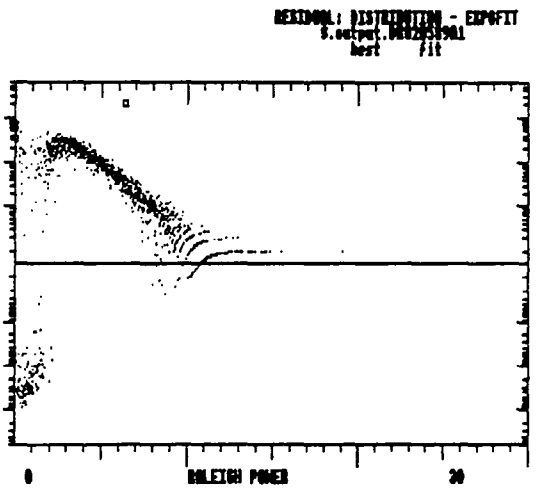

Figure 5.6f

Residuals of the distribution in Figure 5.6c
and its best exponential fit
Departure at power origin is around 4σ
(σ = sqrt(fit))

segments recorded on the same night). The overall chance probability is 1.71×10^{-9} when the Rayleigh vectors are added in phase; after allowing for degrees of freedom, this gives an overall 30% probability of this effect being spurious.

The entire file E020589A was tested for evidence of this particular frequency, with null results. Again the lack of a reliable known orbit acts as an argument against this periodicity as this frequency would be expected to shift between both segments (as orbital phase goes from 0.36 to 0.44). The overall conclusion is that the weak signal and the lack of a confirmed orbit for the neutron star (postulated as the TeV source) are major obstacles in finding a convincing candidate for a pulse period in Scorpius X-1.

5.3 PERIOD SEARCHES IN DATA FROM SUPERNOVA 1987A

5.3.1 Generalities

On February 23.316 UT 1987, the first supernova visible to the naked eye for this century appeared in the Large Magellanic Cloud (see Arnett *et al.*, 1989 for a review on Supernova 1987A). This rare occurrence has given astronomers from numerous fields a unique chance to construct or disqualify models and hypotheses. As supernovae are considered to be one of the most likely sources of cosmic rays, the detection of high energy gamma rays from Supernova 1987A (SN1987A), the first non solar neutrino source, would be of particular importance.

5.3.2 Early expectations

Shortly after the explosion there was the hope that a TeV signal might appear within few months once the column density had fallen to the appropriate value (Protheroe, 1987a). Some results of the DC analysis of the data of the Durham group were summarized in Chapter IV. No measurements were made in the chopping mode before the beginning of 1988 in the hope that a pulsar (at any wavelength) would appear shortly.

As the sub-millisecond pulsar reported in January 1989 has been rejected (Kristian *et al.*, 1989, 1991), the present expectation is that a pulsar, possibly in radio frequencies, with a period between 10 and 100 milliseconds and a strong magnetic field will eventually emerge. SN1987A is again a suitable target for period searches. In the last months a radio source with a flux above 4 mJy at 843 Hz (on August 1990), which increases with a (very large) rate of 45 $\mu Jy.day^{-1}$, has been reported (Turtle *et al.*, 1990). This discovery renews the hopes for the existence of a radio pulsar.

With the belief of the half millisecond pulsar it became clear that the search using FFTs of submillisecond signals in present TeV data is not practicable as the data become too sparse, and the segmented method turns out to be slower than the direct evaluation of the Rayleigh power; a supercomputer (Cray) is necessary to avoid segmentation. Also, the number of degrees of freedom which becomes enormous in the submillisecond range.

5.3.3 Count excess analysis results

There have been no reports of significant count excesses from SN1987A except for the report by the JANZOS collaboration, at an energy of 50 TeV (Bond *et al.*, 1988), who reported observing two 3σ excesses in consecutive nights, on January 14^{th} and 15^{th} 1988. Coincidentally, the most relevant result from the Durham database is a double 2σ excess on consecutive nights (210190 and 220190).

5.3.4 Period Searches & Results

(i) Individual nights

Data taken on January 1990, the two consecutive files each showing a moderate 2σ excess, were selected. These dataset were taken on the 21^{st} and 22^{nd} of January 1990. The first file, E210190A, was analysed down to 4.1 ms (Figure 5.7a); the second one, E220190AX, covering a larger time interval, was tested down to 6.058 ms (Figure 5.7b), with a total of $3 \times 2^{21} \approx 6.3 \times 10^6$ degrees of freedom (three trials per F.I.) on each case. The results are displayed in Table 5.6. The highest peak in the power spectrum was at (13.24029 ± .00002) ms, with a chance probability of 7.7×10^{-8}, or 38.5 % allowing for the number of trials.

The upper limits derived, corresponding to 4σ fluctuations, for the fluxes of periodic gamma rays are 7.13% and 5.46% of the cosmic ray background for the first and second night respectively. The corresponding limits in the flux for a 400 GeV threshold are 3.70×10^{-11} $cm^{-2}s^{-1}$ and 2.83×10^{-11} $cm^{-2}s^{-1}$.

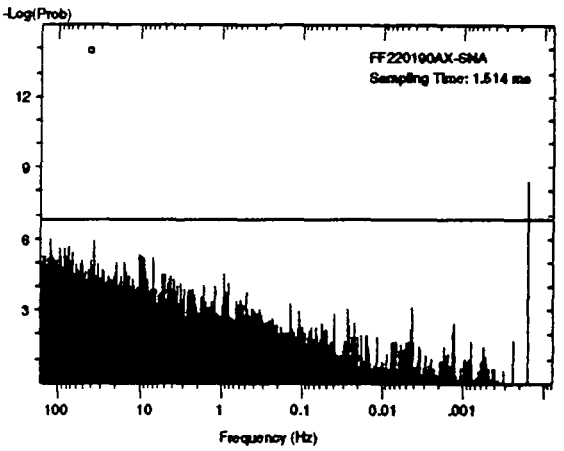

Figure 5.7b

FFT power spectrum of SN1987A data
Datafile 220190AX , event selection: CHOP
Minimum period searched is 6.1 milliseconds.

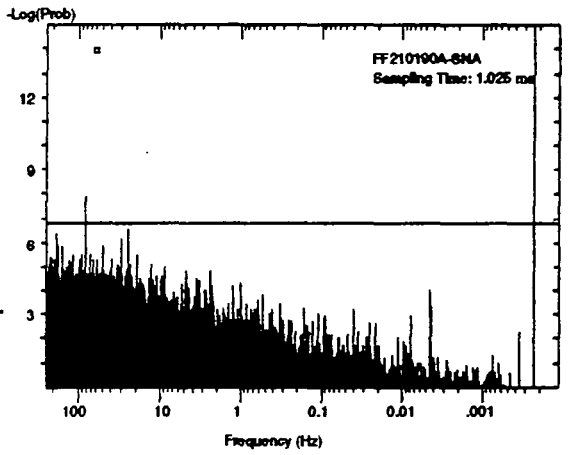

Figure 5.7a

FFT power spectrum of SN1987A data
Datafile 210190A , event selection: CHOP
The minimum period searched is 4.1 ms
The description of the construction of this particular power spectrum appears in Chapter IV.

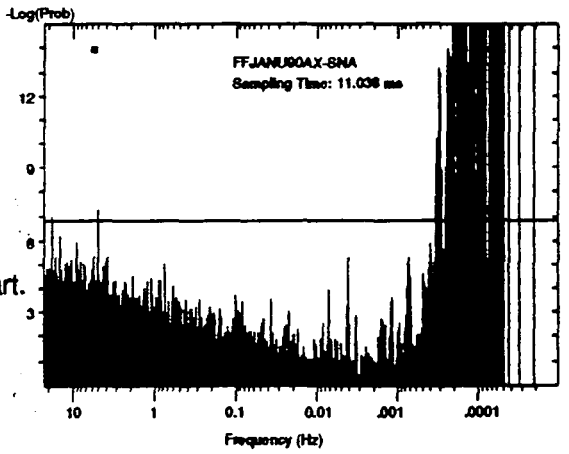

Figure 5.7c

Power spectrum of the two SN1987A datasets 210190A and 220190AX (Figures 5.7a & 5.7b) treated as a single 26 hour exposure.
Noise at low frequencies is due to the beating of the two "3 hour pulses" situated 20 hours apart.

(ii) Adding the two power spectra in phase

The two nights under consideration being consecutive, the 26 hours file (run + gap + run) was tested for periodicity. The resulting count rate had a profile looking schematically like:

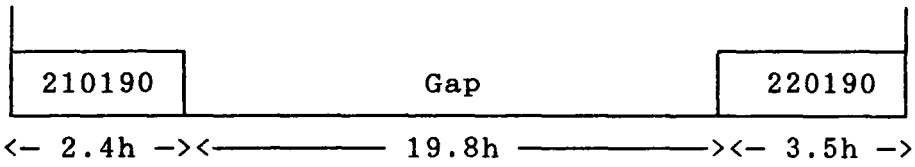

Due to the length of the file the period search was conducted down to just 44 ms. Figure 5.7c shows the corresponding power spectrum. Strong powers due to the "long term" time structure of the data are evident for frequencies below 1 mHz (duration of a run). The best candidate period is at (48.101684 ± .000001) ms with a chance probability of 1.36×10^{-7}, or 57% when allowing for the number of trials. The corresponding upper limit for the flux of periodic events (periods above 44 ms) is 4.32% of the cosmic ray background.

File	Period (ms)	Chance Probability	d.o.f. 3×2^{18}	Overall Prob.
E210190A	13.2402942	7.73×10^{-8}	8	0.38
E220190AX	117.226730	1.53×10^{-7}	8	0.62
E21&220190A	48.101684	1.36×10^{-7}	8	0.57

TABLE 5.6
Period Search Results for SN1987A
Individual Datafiles

5.4 COMPLETE POWER SPECTRA OF CYGNUS X-3 DURING BURSTS

In 1985 the Durham group reported finding a 12.59 ms periodicity in a seven minute segment of data from Cygnus X-3 recorded on the night of the 11th of September 1983 , after a period search down to 10 ms was carried out (Chadwick *et al.*, 1985). As described in Section 3.3.4, these data were chosen on the basis of a the count rate increase coinciding with the time of X-ray maximum at orbital phase 0.625. The same periodicity was observed again, with a weaker strength, in data taken on the 1st of October of the same year. Other groups (Whipple and Haleakala) did not confirm this finding (Resvanis *et al.*, 1986; Fegan *et al.*, 1986); however, the pulsar has been detected again by the Durham group using the Mark IV telescope at La Palma (Brazier *et al.*, 1990a), and a report of an independent detection by the Adelaide group was made early last year (Gregory *et al.*, 1990a & 1990b).

The power spectra of two sections of the data mentioned above, and of two more recent samples from the 1st and 7th of September 1989 where the pulsar reappeared with significant strength (Table 5.7), were computed. The minimum periods tested were around a few milliseconds, the value been dependent on the duration of the particular file ; the power spectra are shown in Figures 5.8a to 8d.

The peak on the first and third transforms appears slightly above the maximum power expected by pure chance and under expectation on the second file; in the most recent data it appears more clearly. No other frequency appears in two of the

power spectra with a probability better than 10^{-4}. The statistical behaviour of the power spectrum follows expectation (except for the 12.6 ms signal); the distribution of powers for the data taken the 7th of September 1989 is shown in Figure 5.8e. This control test is done simply to ensure that the data have the "correct" behaviour and it is evident that it does not degrade the original claim for the 12.6 ms pulsar as the pulse period had been extrapolated previously in 1985.

Datafile Segment	Range of Times (s from JD*.0)	T (s)	Number events	FFT nR^2	Exact nR^2	R (%)
C110983AX	148534 - 148948	414	447	14.7	14.6	18.1
C011083AX	146041 - 146378	337	70	11.2	12.2	41.8
E010989AX	129597 - 129991	395	242	14.6	13.3	23.5
E070989AW	129060 - 129364	304	218	21.8	18.6	29.2

TABLE 5.7

Segments of Cygnus X-3 data
shown in Figures 5.a to 5d.
T = duration of the segment of data.
R = ratio of pulsed to total events

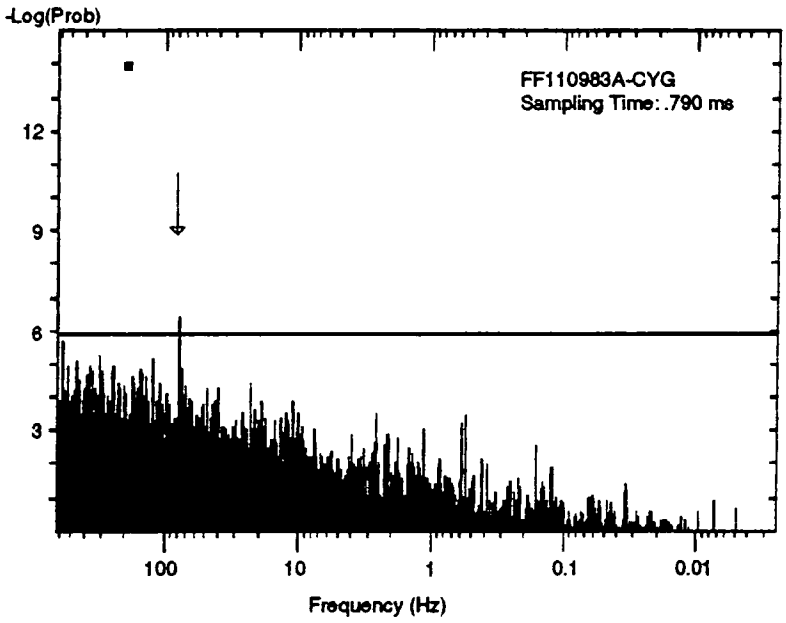

Figure 5.8a

Power spectrum of Cygnus X-3 data
400 second segment taken the 110983A
This is the segment where the 12.6 ms
periodicity was originally found

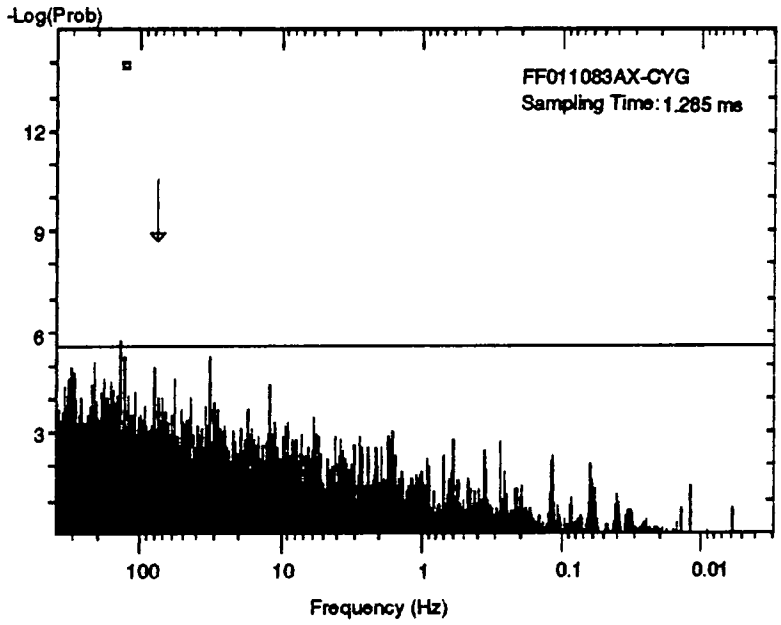

Figure 5.8b

Power spectrum of Cygnus X-3 data
Segment of datafile 011083A.
This was considered to confirm the
existence of a 12.6 ms pulsar

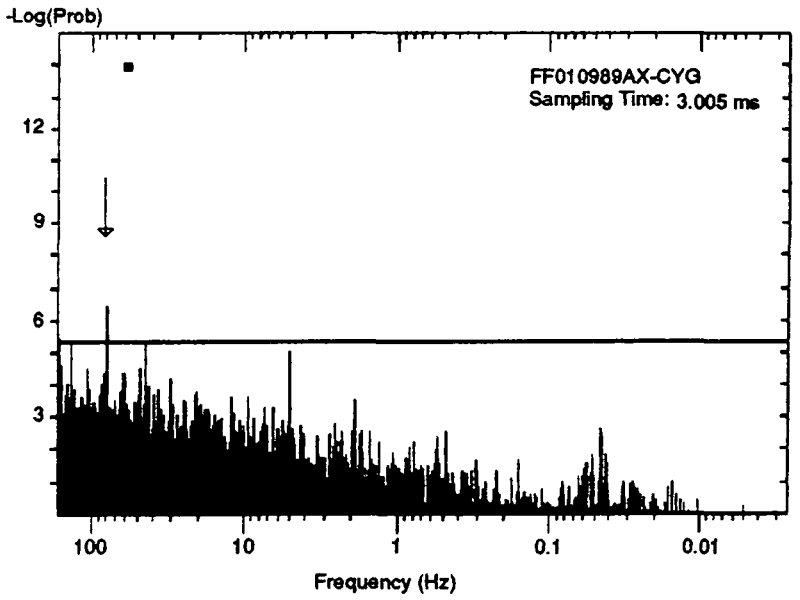

Figure 5.8c

Power spectrum of Cygnus X-3 data
taken the 010989 with the Mark IV telescope
at La Palma, Canary Islands

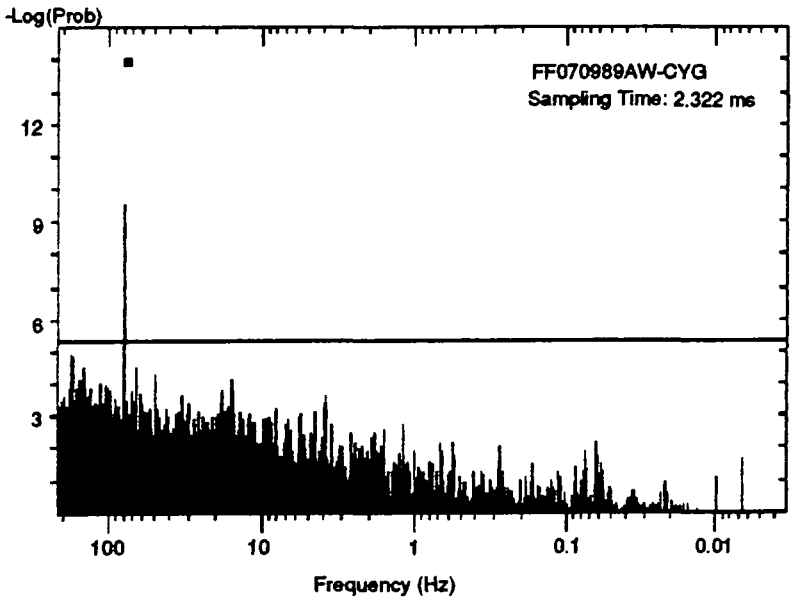

Figure 5.8d

Power spectrum of Cygnus X-3 data
taken the 7th of September 1989 with
the Mark IV telescope at La Palma
The power in the peak is in fact overestimated
by the FFT as 21.8 while the actual power is 18.8

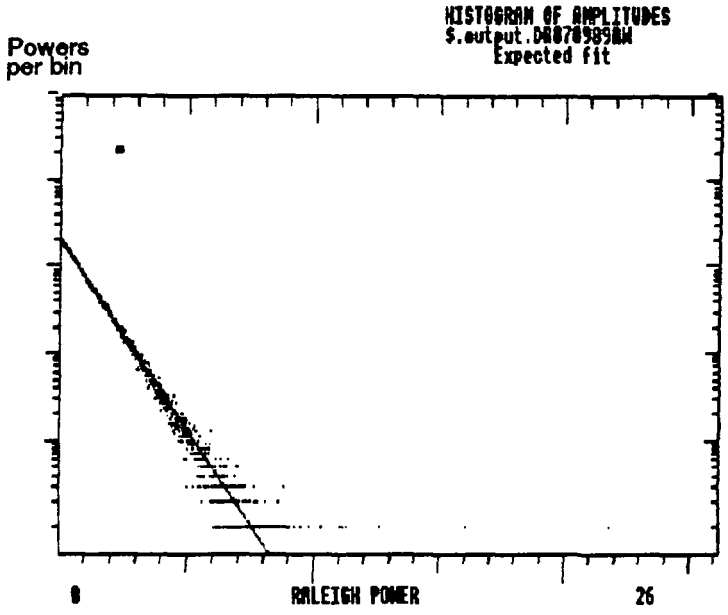

Figure 5.8e

Distribution of power in the spectrum shown in Figure 5.8d. Straight line represents the expected fit

5.5 A LOW MASS X-RAY BINARY QPO SOURCE: GX 5-1

5.5.1 Introduction

GX 5-1 is one of the brightests X-ray sources showing Quasi Periodic Oscillations (or QPO; van der Klis, 1989a); it is located in the "Normal" and "Horizontal" branches of the color - color X-ray diagrams. It shows broad peaks in the 20-36 Hz band, and the so-called "Low Frequency Noise" (LFN; or "Red Noise") was originally discovered in this object (van der Klis *et al.*, 1985). Alpar & Shaham (1985) suggested that a millisecond pulsar might exist in this system.

In July 1988 data from the direction of the LMXRB GX 5-1 were taken using the Mark III Cerenkov telescope in the tracking mode. These data could not be recorded in the chopping mode because the source passes within 5° of the Zenith and technical reasons forbid chopping at zenith angles below 10°. The sky conditions were described as "perfect" in four of the five nights. Three of these datasets, C140788A, C170788A and C190788A, were used for period searches; the fourth one could not be retrieved due to technical reasons. Unfortunately, no direct comparison between the source and background could be made, and no evidence in favor of γ-ray emission is available. Bursts significantly above Poissonian fluctuations were not observed. However, a steady emission cannot be ruled out. The period search itself can give upper limits only on the presence of coherent sinusoidal pulsations unaffected by the orbit within the duration of the considered files. How much the orbital corrections are required is unknown as the orbital parameters themselves have not been found; typical values for orbital periods in bright LMXRB are generally small enough to cause problems, as in Scorpius X-1.

The period search was divided in two parts: in the first instance the datafiles were considered entirely on their own, and in the second part they were cut into independent segments of duration 2500 seconds each.

5.5.2 Analysis of complete datafiles

The minimum periods tested were 25.2 ms, 20.2 ms and 14.0 ms for

C140788A, C170788A and C190788A respectively. Some 2^{20} independent periods were tested on each case, using three trials per F.I. (i.e. $3x2^{20}$ periods tested in total per file). The first file sets an upper limit of 2.76% pulsed events down to 25 ms while the last file indicates less than 3.66% pulsed events down to 14 ms. Best candidate periods appear in Table 5.8. Searching for periods reappearing (within eight Fouriers one of each other to account for possible redshifts) in any two of the datafiles with a probability below 10^{-4} gave the value of 24.57648 ms[1] as the least probable recurring fluctuation with an overall probability around 67.6% when all ($8 \times 3 \times 2^{20}$) degrees of freedom spent are considered. The implied upper limit for persistent coherent pulsations (100% of duty cycle) from GX 5-1 is around 1.06% of the cosmic ray background. The corresponding power spectra are shown in Figures 5.9a to 9c.

File	Period (ms)	Chance Probability	d.o.f. 3×2^{18}	Overall Prob.
C140788A	42.400600	1.37×10^{-6}	4	0.99
C170788A	41.473167	1.88×10^{-7}	4	0.45
C190788A	22.267521	4.37×10^{-7}	4	0.75
BEST	41.473167	1.88×10^{-7}	12	0.83

TABLE 5.8
Period search in GX 5-1 data. Complete datafiles

[1]The error on this being subjective, as one might allow for Doppler shifts.

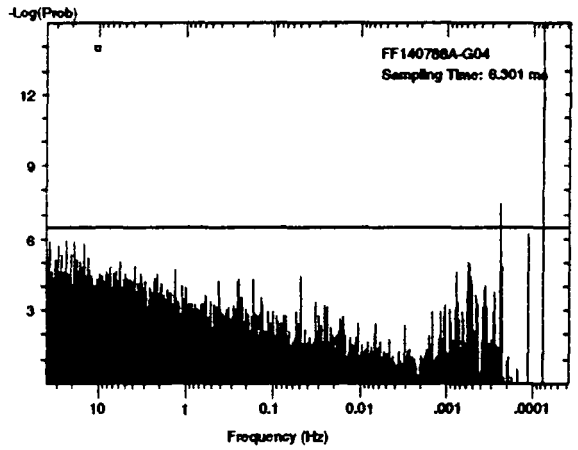

Figure 5.9a

Power spectrum of GX 5-1 data
File 140788A , CHOP events
Minimum period is 25 milliseconds

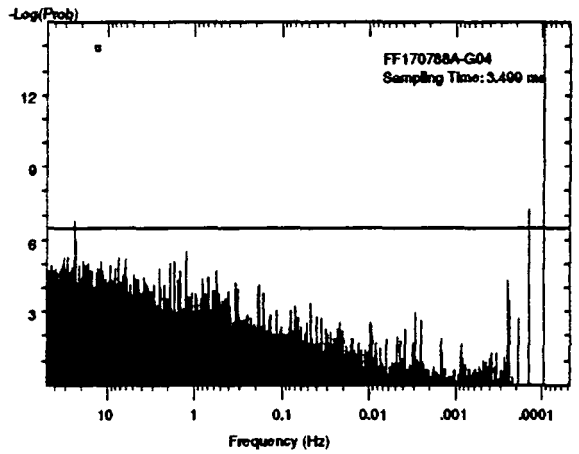

Figure 5.9b

Power spectrum of GX 5-1 data
File 170788A . CHOP events
Minimum period is 20 milliseconds

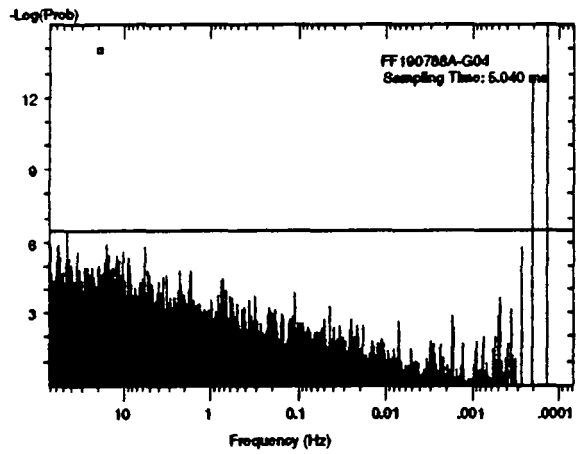

Figure 5.9c

Power spectrum of GX 5-1 data
File 190788A. . CHOP events
Minimum period is 14 milliseconds

5.5.3 Analysis of segments of data

As mentioned before the datafiles were cut into independent sections of 2500 seconds duraction. Although this would not improve the obtained limits, it can set bounds for pulsations remaining coherent only during short time intervals, because of either rapid orbital movements or transient activity. In total 21 of such sections were used for period searches down to 2.4 ms: 8 from C140788A, 8 from C170788A and 5 from C190788A. The ratio period/sampling rate was always above four. The highest power in any of the sections was at a frequency of (321.1448 ± .0004) Hz, i.e. (3.113861 ± .000005) ms, with a Rayleigh power $nR^2 \approx 17.2$, equivalent to a chance probability of 3.3×10^{-8}; when all the tries (21 files x 2^{20} independent periods x 3 trials per F.I.) were taken into account the significance was reduced to a 89% chance probability. This value for the frequency did not reappear with a power above 9.21 (prob $\leq 10^{-4}$) in any of the other files. This gives a 4σ upper limit of 9.26% pulsed events with a 4.76% duty cycle, periods above 2.4 ms appearing in "any" file.

Of more interest was the search for periodicities present with a significance better than a 10^{-4} chance probability in two or more sections. In order to allow for small orbital Doppler shifts, (very) small differences in frequency were permitted; these were below seven Fourier intervals, equivalent to a relative motion of 4 $km.s^{-1}$. A total of 80 repetitions were found. When the power contained in these repetitions is binned into bins of size 1 Hz, the distribution shown in Figure 5.9d is

obtained. Three "triple" coincidences within one hertz are found. One of them (at 163Hz) was rejected because two of the three pairs of periods were in the same file. The other two "persistent" repetitions were around 105 and 346 Hz; the second was considered to be more improbable, as all frequencies included in this bin can be accounted for with a redshift below ±.1%. Table 5.9 shows the exact values of the six frequencies involved. The total Rayleigh power in this six segments of data around this frequency is 62.05, giving a 9.38×10^{-21} chi square probability when using a χ^2 distribution with 12 degrees of freedom. The total number of trials made can be approximately estimated as follows:

File # 1: Frequencies tested in this file = 3×2^{20},

File # 2: Frequencies at ± 7 Fourier intervals from the one chosen from file # 1 = 3 x 14 ,

File # 3: Frequencies at ± 1 Hz from the one chosen from file 1 = 3 x 5000 as 1 Hz = 2500 Fourier intervals,

File # 4: Frequencies at ± 7 Fourier intervals from the one chosen from file # 3 = 3 x 14 ,

File # 5: Frequencies at ± 1 Hz from the one chosen from file # 4: 3 x 5000 ,

File # 6: Frequencies at ± 7 Fouriers from the one chosen from file # 5: 3 x 14

Total d.o.f.: $3 \times 2^{20} \times (3 \times 14)^3 \times (3 \times 5000)^2 \approx 5.24 \times 10^{19}$.

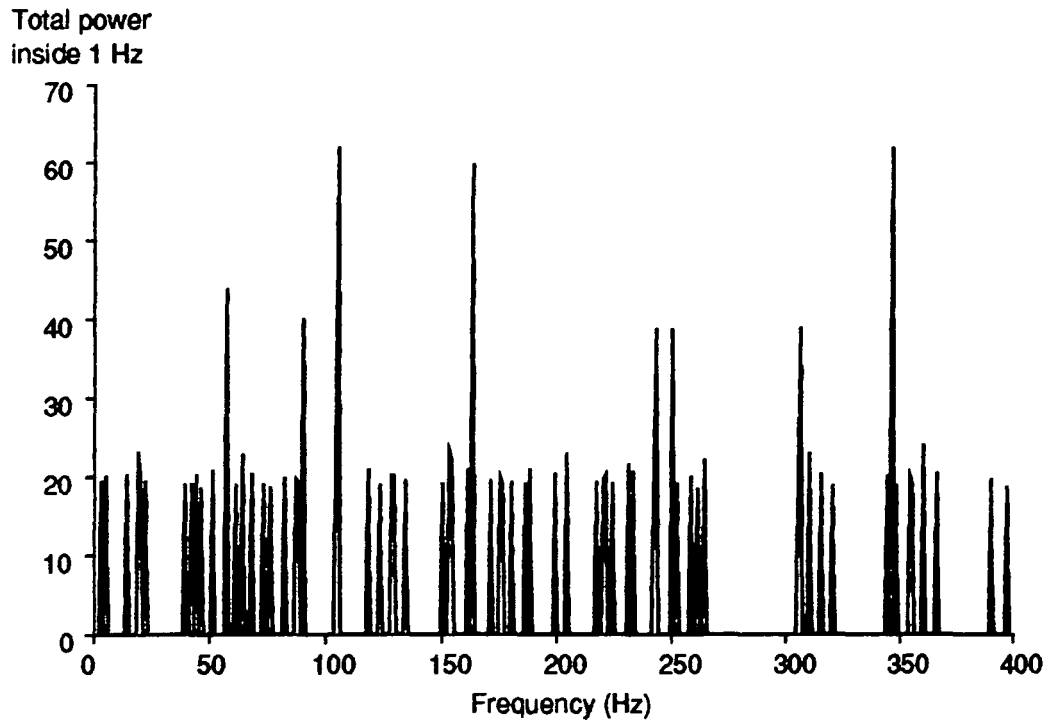

Figure 5.9d

Distribution of powers reappearing with probability better than 10^{-4} in segments of data from GX 5-1

The probability of this effect being due to chance once the number of degrees of freedom n_{dof} is taken into account is then $P_{adf} \approx 1 - \exp(- n_{dof} * Prob) \approx 0.39$. Even if this result were more significative, it is not possible to explain the different values of frequencies and times of observation in terms of the Doppler shift due to an orbital (circular) motion. Therefore, no claim for a 2.88 ms pulsar in GX 5-1 can be made here.

The overall conclusion is that there is no evidence for pulsations either steady or in short term (lasting around 2500s) in GX 5-1. A count excess analysis is desirable in future to investigate whether this is indeed a source of TeV γ-rays.

Section	Freq (Hz) ± .0004 Hz	Rayleigh Power	Centre of Segment - JD2447356.0 (s)
C140788A2	346.4025	13.50	84750
C140788A7	346.0354	9.58	97250
C140788A8	346.4036	9.68	99750
C170788A5	346.4325	9.28	351450
C190788A3	346.0353	10.58	525750
C190788A5	346.4340	9.43	530750

TABLE 5.9

Period Search in GX 5-1 data. Periodicity observed most frequently in the segments of data selected. t = 0 refers to the beginning of the first segment.

5.6 CONCLUSIONS FROM THE PERIOD SEARCHES

5.6.1. On the requirements of sensitivity

A comparison of the exact and FFT powers has been made for strong powers (probabilities better than 10^{-4} or 10^{-5}) using the observational data from the previous sections (simulations are not included). A plot of the ratio R_{period}/R_{fft}, the proportion of γ-rays found using both the direct evaluation and the FFT, against the ratio between the period and the sampling rate ($\geq$ 2) is shown in Figure 5.10. A straight conclusion is that sampling to one fourth of the minimum period in the test range appears to

be a good compromise between accuracy, errors below 30% in the estimation of the pulsed fraction, and speed.

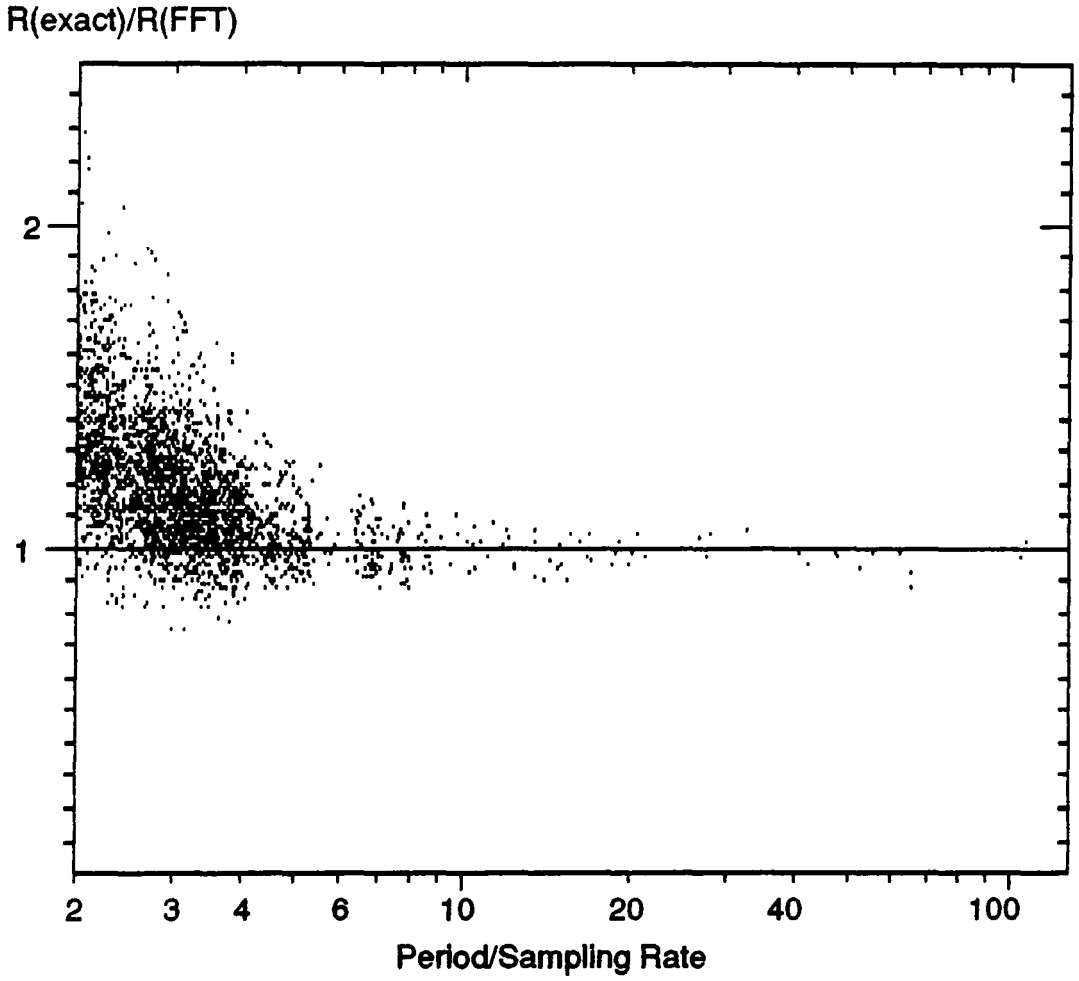

Figure 5.10

R(exact)/R(FFT) as a function of period/sampling rate
All points are from actual data as simulations were excluded.

5.6.2 On the period searches

At the present stage period searches with sparse and low signal to noise data from Cerenkov telescopes are likely to give negative results, but still deserve some attention. Future improvements in observational techniques point towards two directions, (i) increasing the present count rates (using an array of telescopes) to improve statistics, (ii) direct rejection of proton showers which would result in a high signal to noise with a low count rate. The second point is the most desirable but also technically more difficult. In this ideal case the count rate would be of the order of one count per minute, which would hamper the performance of a fast algorithm for period search relative to that of a direct evaluation of the Rayleigh vector (which is also more accurate). Using expression IV.3 one can estimate that segmented FFT algorithms are only worthwhile for:

$$T \geq \zeta \; p \; \mathrm{Log}_2(q) \; / \; \langle dn/dt \rangle \quad ,$$

where ζ is the minimum desirable "saving" ratio, defined (Chapter IV and expression IV.3) as the ratio of the time required by direct method / time required by fast algorithm. For a count rate of 1 s^{-1} and $\zeta = 5$, $q = 2^{17}$, segmented algorithms are only worth for:

$$T \geq 85 \text{ minutes} \; . \; p \quad ,$$

of data and, as a consequence, the sampling rate cannot be less

than 39 ms. Period searches in the millisecond range are not feasible either directly or with standard fast algorithms with such a low count rate. However, a sparse fast algorithm, avoiding the addition of empty bins and optimising the use of memory (information), is likely to be feasible and would be necessary in this case to take advantage of the noise-free data.

5.6.3 On the statistical behaviour of periodograms

Some small departures from the expected exponential shape were observed most of the times in the statistical distribution of both simulations and data. The plots of the residuals (observed distribution against expected fit) tend to show excesses at low powers, and a lack of medium powers. Appendix II gives the definition of "expected" and "best" fit to the distribution. Possible interpretation of this bias might be:

(a) non asymptotic behaviour. In principle this should not affect the slope in a sensible way due to the relatively large number of events and trials used. The first order corrections to the distribution is a factor of $k \approx 1 + (2x-x^2)/4N$ which, for $N \geq 3 \times 2^{16}$ and $x^2 \leq 10^3$, gives corrections well below 1% .

(b) oversampling. The trials in between and at the Nyquist frequencies have in principle the same distribution. Their mean value $\langle |J_{k \pm 1/3}|^2 \rangle$ can be estimated, accounting for approximations made when oversampling, and compared to the average power at Nyquist frequencies $\langle |J_k|^2 \rangle$. In other words how does the oversampling modify the overall mean. An artificially

large average power implies a larger slope β for the distribution. The parameter η, which in the ideal case is equal to 3, can be estimated in order to quantify the effect of oversampling in the distribution of powers:

$$\eta \equiv \frac{\langle |J_{k-1/3}|^2 \rangle + \langle |J_k|^2 \rangle + \langle |J_{k+1/3}|^2 \rangle}{\langle |J_k|^2 \rangle} \quad .$$

Using expressions IV.14 and IV.15, for the trials between Nyquist frequencies and the convolving function $H_1(\delta k)$:

$$\eta = 1 + 2 \sum_{l=-4}^{4} |H_l(1/3)|^2 \approx 1 + \frac{27}{2\pi^2} \sum_{l=-4}^{4} \frac{1}{(3l+1)^2} + 3/n^2$$

$$\eta \approx 2.9324 + 3/n^2 \quad .$$

where $n = T/\Delta$. This gives a value for β which is two percent larger than expected, but practically independent of the number of trials for $n \geq 10^4$.

(c) method - algorithm - of computing the histogram. It is relatively easy to construct a histogram so and explicit errors in the method are not likely. Also, the departures from the expected fit are related to the sampling rate (see below) and do not look like systematic errors.

(d) the sparse character of the data. The power spectrum of sparse data is made by the superposition of relatively few sine waves (thousands) beating at some particular frequencies and making the nearby Nyquist frequencies (millions) not completely

independent one from each other. In this case the departure from the expected exponential fit should increase with sparseness, measured either by the ratio between count rate/sampling rate or by count rate/mean period or frequency searched. Using both simulations and real data, the mean power and the value of β were both plotted against "frequency range" (Figures 5.11a and 5.11b), or the integer part of (Duration of Data/2^{17} sampling rate). Note that the number of segments used to construct the full FFT doubles each time that this "frequency range" is a power of two. While the mean power varies randomly, the value of β is related to the frequency range (steps in Figure 5.11b) or more precisely to the number of segments used in the FFT. The final result is that the slope of the distribution is sensitive to the sampling rate rather than to the range of the frequencies searched. This indicates a dependence, not on the intrinsic sparseness of the data but, with the method of segmentation or the algorithm.

Fortunately these departures are relatively small and might even be considered as a technical point. The segmentation algorithm, rather than a real feature of the periodogram, is likely to be the cause of this effect. Further work in terms of removing this departures might well deserve future attention although this is beyond the scope of the present work.

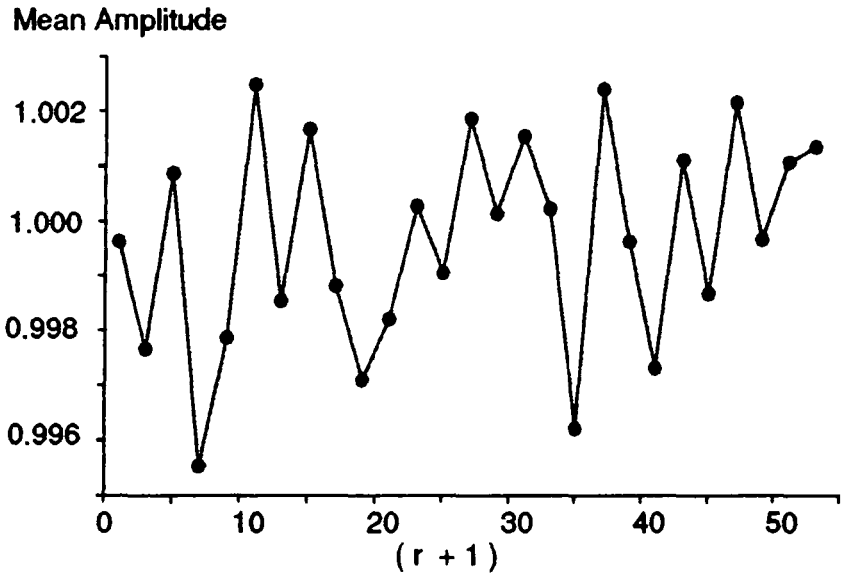

Figure 5.11a

Mean amplitude of powers relative to its expected vale, as a function of the frequency range r (see text), defined as the inte·ger part of period / ($2^{17}\Delta$) Δ being the sampling rate

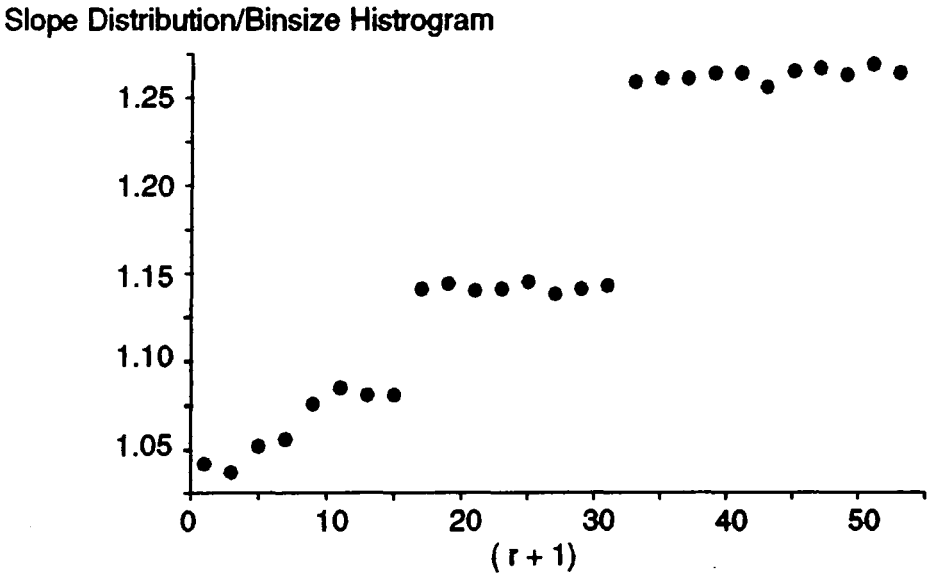

Figure 5.11b

Slope of the distribution of powers relative to its expected value, as a function of the frequency range. Each step coincides with a change in the sampling rate.

VI. PRODUCTION OF TeV γ-RAYS IN LMXRB

6.1 LOW MASS AND HIGH MASS X-RAY BINARIES

In both Low Mass and High Mass X-ray binary systems, the X-ray output energy comes from accretion of matter onto a neutron star. These systems form two versions of the same process, with the differences due to the distinct types of companion[1] star; in fact, the stellar evolution of its components may cause a binary system to pass through both stages of X-ray emission at different times. HMXRB are associated to young short lived objects, while LMXRB are old systems, frequently in a stage previous to that of millisecond radio pulsars. Neutron stars in LMXRB rotate rapidly (inferred rotational periods $P \sim 10$ ms), and possess weak magnetic fields ($B_* \sim 10^9$ Gauss), compared to massive systems where rotation is slower $P \sim 1$ s and $B_* \sim 10^{12}$ Gauss. This difference in the parameters of the compact object has consequences for the physical processes associated with the accretion flow. In Low Mass systems characteristic dimensions, like the light cylinder, the corotation and Alfven radii, are one or two orders of magnitude smaller; particles can therefore be deeper in the gravitational potential before magnetic effects can suppress particle acceleration, as it happens in HMXRB.

---

[1] The stars in the binary system are designated as the compact star (neutron star) and the companion (which can be either a Main Sequence or a late type star).

This chapter discusses the three stages involved in the production high energy γ-rays: (1) particle acceleration; (2) creation of neutral pions and photons through interaction with targets; (3) constraints caused by possible absorption of high energy γ-rays. This treatment will take into account the differences between the high mass systems, for which several models have been published, and low mass binaries, which, with the exception of Cyg X-3 and Her X-1, have not been considered in as much details. As mentioned in the Introduction, in terms of the discussion, Hercules X-1 is not included here as a LMXRB. Being in the high mass region of the LMXRB, has some properties of a HMXRB (namely high magnetic field, relatively slow rotation and coherent pulsations).

6.2 PARTICLE ACCELERATION

6.2.1 Dynamo models

As outlined by Chanmugam & Brecher (1985), and previously discussed by Lovelace (1976) in the context of AGNs, the differential rotation of an accretion disc threaded by magnetic field lines may induce voltage differences in the disc. For a dipolar magnetic field $B \sim \mu/r^3 = B_* (r_*/r)^3$ (where B_* is the magnetic field at the surface of the star, μ is magnetic dipole and r_* its radius) inside the Alfven radius, and a field frozen into the rotating plasma (implying B inversely proportional to the disc surface density which itself varies approximately as

$r^{1/2}$), the difference in the potential Ψ between the Alfven radius a and $r > a$ is:

$$\Psi(r) - \Psi(a) = \int_a^r - E.dr = - \frac{\mu\ (GM)^{1/2}}{c \cdot a^{5/2}} \ Ln(r/a) \quad ; \quad (VI.1)$$

M is the mass of the star, while G and c are the gravitational constant and the speed of light respectively. $\Delta\Psi$ increases when the Alfven radius decreases, and therefore voltages are likely to be larger in LMXRB ($a \sim r_*$) than in HMXRB ($a \sim 10^2\ r_*$). For spherically symmetric accretion, the Alfven radius is estimated to be (Appendix IV):

$$a_e = (2GM)^{-1/7}\ \dot{M}^{-2/7}\ \mu^{4/7} \qquad (VI.2)$$

$$a_e \approx 3.7 \times 10^6 \text{ cm } L_{38}^{-2/7} M_{1.44}^{1/7} R_6^{10/7} B_9^{4/7} \quad ;$$

where $\dot{M} = dM/dt$ is the mass accretion rate and L the luminosity (more convenient to use, as it is easier to measure and relates to the accretion rate by $L = G\dot{M}M/r_*$); the variables have been scaled to typical values $L_{38} = L/10^{38}$ erg.s^{-1}, $R_6 = r_*/10^6$ km, $B_9 = B_*/10^9$ G, and $M_{1.44} = M/1.44M_\odot$. The Alfven radius is expected to be smaller for a disc than in the spherically symmetric case. For a disc with $h/r \approx$ constant it can be shown that $a_{disc}/a_e = (36\alpha^2 h/r)^{4/7}$ or ≈ 0.56 for a thin disc (where $\alpha^2 h/r \approx 10^{-2}$). The substitution of a_e in expression (VI.1) gives

$\Delta\Psi \approx 5.2 \times 10^{15}$ Volts Ln(r/a) for $L_{38} = M_{1.44} = B_9 = R_6 = 1$, and $\Delta\Psi \approx 2.2 \times 10^{16}$ Volts when a_{disc} is used.

Voltage differences are not restricted to the disc. Cheng & Ruderman (1989) consider the motion of ions trapped in magnetic field lines crossing between separated regions of positive and negative charge density (depending on the sign of $\Omega \cdot B$); in this null surface "gaps" where $E \cdot B \neq 0$ exists where particles can be accelerated to energies of the order of $e\Delta\Psi$. An upper bound to the voltage that can be produced in these systems (when $a \approx r_*$) is given by:

$$\Delta\Psi_{lim} \approx (B_*/c)\,(GMr_*)^{1/2} \approx 1.38 \times 10^{17} \text{ Volts } B_9\, M_{1.44}^{1/2}\, R_6^{1/2} \qquad \text{(VI.3)}$$

However dynamo models give voltages which would occur only in a full vacuum, a situation which does not prevail even in isolated neutron stars. The highly conductive plasma present in accreting systems is very likely to short circuit any static electric field. As mentioned by Harding (1989) the actual voltage available for particle acceleration is likely to be much smaller due to the presence of matter.

6.2.2 Fermi shock Acceleration

Fermi (1949) proposed a mechanism for particle acceleration where a charged particle collides with a (moving) magnetic mirror, such as Alfven waves, or the field associated with a "clump" of plasma. Bell (1978) and Blandford & Ostriker (1978) showed, using

the Fermi mechanism, that astrophysical shocks related to supernovae explosions produce the observed cosmic ray power law spectrum. This process, known as Fermi shock acceleration, is the only one naturally predicting a power law spectrum. Suitable shocks might occur in various locations:

(i) shock acceleration in the base of accretion columns,

In the standard picture of a high mass systems, once it has penetrated the magnetosphere, the accretion flow is funnelled by magnetic field lines into a column (the accretion column) and then guided to the pole of the neutron star. There its velocity is abruptly brought from free fall speed (above c/2) to rest, in a collisionless shock (region size << dissipative length scales) with the surface of the compact object. Although no detailed calculations has yet been done, this shock has been considered as a suitable place for particle acceleration by Eichler & Vestrand (1985) and Kazanas & Ellison (1986). Eichler & Vestrand (1985) propose shock acceleration and disassociation of He^4 nuclei as a source of high energy neutrons.

Recently Hillas & Johnson (1990) have argued that a Fermi type acceleration mechanism, in which charges are scattered by moving magnetic mirrors, cannot work in this environment. They argue that the flow inside the column is subalfvenic (reason why it is contained by the column!), and therefore cannot excite Alfven waves, which normally would expected to be the scattering entities. In other words, there is no "alfvenic" shock. Magnetic

mirroring occurs for $(p^{\perp}/p)^2 \approx \delta B/B$ and, as Hillas & Johnson point out, the flow will have small magnetic perturbations, of the order of $\delta B/B \approx v/v_a << 1$, where $v_a = B\,(4\pi\rho)^{-1/2}$ is the Alfven velocity. Mirroring will occur only for particles with very low $p^{\perp}$, which will be sent back to the disc.

The accretion flow is stopped at the surface of the star, probably by radiation pressure (Davidson, 1973); the column emits hard X-rays (as its associated temperature is ~ 10^7 - 10^8 °K) and the formation of a jet is plausible, especially in a hollow column (Basko & Sunyaev, 1976). But in the case of HMXRB, because of the intense magnetic field and the dissipative processes associated (like synchrotron radiation and magnetic pair production), the shock itself does not appear likely to produce high energy particles other than neutrons.

In the case of LMXRB, due to the low value of $B_{\star}$, it is unclear whether an accretion column would form or not. If it does, fluctuations in the magnetic field will be of the order of $\delta B/B \sim v/v_a \sim 10^{-3}$, larger than in HMXRB but still too small to excite Alfven waves: a careful analysis is required to establish if (*some*) particle acceleration will occur in this shock. On the other hand, if the column does not form, the flow is likely to be stopped by an oblique shock with the equator of the neutron star. Drury (1990) has outlined this kind of shock as a promising source of high energy particles.

(ii) shock acceleration in semi-relativistic jets,

Both Sco X-1 and Cyg X-3 are associated with powerful jets.

where the bulk velocity is a sizeable fraction of c. Such jets manifest themselves at very large distance scales in radio emission (Achterberg, 1989 and Strom *et al.*, 1989). The symmetry of a disc gives a natural way to explain such jets. The plausible formation of jet in a hollow accretion column, which may allow super - Eddington luminosities, was postulated some fifteen years ago by Basko & Sunyaev (1976). The idea of particle acceleration in a jet, allusive to SS433, was mentioned by Grindlay (1982); more recently, Quenby & Lieu (1989) have studied particle acceleration in relativistic jets associated with AGNs. In these models, the acceleration is through scattering by clumps of material present in the jet. Observations suggest that jets in LMXRB do have an inhomogeneous nature (Achterberg, 1989).

(iii) particle acceleration in the shock of a jet with external material,

Kiraly & Meszaros (1988) also invoke a jet for the origin of high energy particles. They suggest that particle acceleration may occur where the jet encounters material present at a radius close to the Alfven radius (the "Alfven shell") to form a shock. They also consider the case of Her X-1 (and possibly LMC X-4), where the jet might interact with an accretion disc, in order to be consistent with a possible modulation by the precession of the disc, which has a 35 day period (30.5 days for LMC X-4). Note that when no magnetosphere is formed (i.e. $a \leq r_*$), an oblique shock with the equator of the star can also produce a jet of plasma perpendicular to the disc.

(iv) particle acceleration in an oblique shock,

When $B_* \leq 10^8 \text{Gauss}\ L_{38}^{1/2} M_{1.44}^{-1/4} R_6^{-3/4}$, the Alfven radius is smaller than the radius of the star, and magnetic effects can be neglected in the motion of the accretion flow, as a first approximation. The disc collides almost tangentially to the neutron star, forming a boundary layer where the flow is decelerated in a highly oblique shock. Gosh & Lamb (1979a) showed that the magnetic field will not be completely screened by the (practically) infinite conductivity of the plasma; processes like magnetic reconnection, turbulent diffusion and Kelvin Helmholtz instabilities allow the field to penetrate the disc, giving an effectively finite conductivity. Nevertheless there are some models where the conductivity is considered infinite (like in Anzer & Borner, 1983 and White & Stella, 1987) and the magnetic field is totally excluded from the disc. In this case, if a denotes the radius at which the energy density of the compressed magnetic field is larger than the kinetic pressure of the matter, it can be show that for h/r = constant[2]:

---

[2] Setting the condition:

$$\varepsilon_{cin}(a) = \varepsilon_{mag} \approx E_{Mag}\ \{r_* \leq r \leq a; |z| \leq h\} \ /\ VOL\{r_* \leq r \leq a; |z| \leq h\}$$

i.e.

$$\frac{1}{2} \rho(a) v^2(a) = \frac{B_*^2}{8\pi\ (a^3/r_*^3 - 1)}$$

$$\frac{(a/r_*)^3 - 1}{(a/r_*)^{5/2}} \approx \frac{3\alpha}{2}\left[\frac{h}{r}\right]^3 \frac{B_*^2 r_*^3}{\dot{M}(GMr_*)^{1/2}} \quad , \qquad (VI.4)$$

$$a/r_* \approx 1 + 1.4 \times 10^{-4}\ \alpha\ (100h/r)^3\ B_9^2\ L_{38}^{-1}\ M_{1.44}^{1/2}\ R_6^{3/2} \quad ,$$

the Alfven radius is only one metre above the surface of the star! The flow inside the disc cannot be contained by the magnetic pressure and an oblique shock does form at the stellar equator. Note the strong dependence of this result on $h/r \ll 1$.

Oblique shocks can be related both to the formation of jets (Canto *et al.*, 1988) and to particle acceleration (Kirk & Heavens, 1990). The latter authors take into account anisotropies in the particle distribution function to model the acceleration process in oblique shocks. This mechanism, unlikely to operate in massive binaries where the oblique shock is replaced by the accretion column, might deserve further attention in the context of Cyg X-3 and Sco X-1. As will be discussed in Section 6.2.4, charged particles with energies in the range 10^{13} to 10^{16} eV cannot escape from the field of a 10^9 Gauss neutron star. The same applies for 1 TeV photons, which undergo pair production with the virtual photons associated with the magnetic field at distances below $4r_*$. Therefore the only mechanism likely to produce TeV γ-rays starting from an oblique shock at the equator of the neutron star is the production of high energy neutrons, able to leave the vicinity of the star and produce high energy photons through strong interactions.

(v) particle acceleration in plasma turbulence,

In the paper where the α-disc solution to the structure of accretion discs was presented, Shakura & Sunyaev (1973) related the parameter α with the turbulent velocity v_t and the local magnetic field B associated with this turbulence:

$$\alpha = \frac{v_t}{c_s} + \frac{B^2}{4\pi\rho c_s^2} \quad ; \qquad \text{(VI.5)}$$

here c_s is the sound velocity. Although the Alfven velocity $B/(4\pi\rho)^{1/2}$ is subsonic, for $\alpha \approx 1$ one might expect non linear growth of Alfven waves. Wang (1986) and Katz & Smith (1988) considered the acceleration of particles through their scattering with Alfven waves induced by turbulence.

6.2.3 Particle acceleration in a pulsar wind

Newly born neutron stars, such as the Crab pulsar, are fast rotators with strong magnetic fields and a rapid spin down due to radiation losses. The rotational energy is lost at a rate:

$$dE/dt = I\,\Omega\,d\Omega/dt \quad ,$$

$$\approx 2 \times 10^{38}\ \text{erg.s}^{-1} \left[\frac{I}{10^{45}\ \text{g.cm}^2}\right]\left[\frac{P}{10\ \text{ms}}\right]^{-3}\left[\frac{\dot{P}}{10^{-14}}\right] ,$$

(VI.6)

where $I \sim Mr_*^2$ is the moment of inertia, P the spin period and $\dot{P}$

its time derivative. In the case of Cygnus X-3, the values reported by the Durham group (Chadwick *et al.*, 1985 and 1987), of $P \approx 12.59$ ms and $dP/dt \approx (2.8 \pm 0.4) \times 10^{-14}$ imply an output energy rate of $L_{rot} \approx 3 \times 10^{38}$ erg.s^{-1}. In models where the energy is supplied by rotation, a relativistic wind is generated by the rotation of the magnetic dipole and undergoes a shock with the ambient medium. High energy particles can be created in a shock with the matter near the neutron star. This idea has recently being developed in detail by Harding & Gaisser (1990), who envisage the shock between the pulsar wind and, the less powerful, wind of the companion star.

In HMXRB the loss of rotational energy does not provide enough energy to explain the observed emission, and accretion is the most likely source of energy of high energy photons. In the particular case of LMXRB the exact values of the rotational period and its time derivative are generally unknown but the present consensus is that $P \leq 10$ ms and $dP/dt \leq 10^{-15}$. For a rotating magnetic dipole forming an angle α with its spin axis the power loss is estimated to be:

$$dE/dt = 2\ \mu^2 \Omega^4 \sin^2\alpha\ /\ 3c^3 \quad . \qquad \text{(VI.7)}$$

For $\Omega = 2 \times 10^3$ Hz, $B_* = 10^9$ G and $r_* = 10$ km, plausible values for Sco X-1, a period derivative similar to that of millisecond pulsars (believed to originate from LMXRB), $dP/dt \approx 3 \times 10^{-16}$, and a rotational energy output $(dE/dt)_{rot} \approx 4 \times 10^{35}$ erg.s^{-1} are found. This latter value is an order of magnitude above the

TeV luminosity reported in Chapter III, and of the same order as the implied particle energy output. Therefore, a rotational origin for the TeV emission of Scorpius X-1 cannot be rejected.

An interesting point here is that neutron stars in LMXRB are thought to be spinning up, in contrast to the spin down observed in isolated pulsars. Therefore, although the system might be radiating (some of its) energy in the same way as an isolated pulsar, the neutron star is actually acquiring rotational energy from the accretion disc. This is an example of a pulsar powered by rotational energy, where the ultimate source of energy is in fact accretion.

6.2.4 Motion of charges in magnetic fields & Synchrotron emission

Charged particles in magnetic fields describe an helical motion with a field line as its axis (see Appendix III), the radius of gyration (Larmor radius) r_L being smaller for larger fields. As they are accelerated (instantaneous circular motion in the plane perpendicular to the line), particles radiate part of their energy, emitting what is known as synchrotron radiation. In strong magnetic fields, charged particles either can be forced to follow the lines, and therefore be effectively trapped by the field or, in the extreme case (only common for electrons), radiate practically all their (kinetic) energy in a very short time. In the case of highly magnetised neutron stars, $B_* \sim 10^{12}$ Gauss, magnetic effects are major obstacles to obtaining high energy electrons or free relativistic protons. The synchrotron

emission and the motion of charged particles, in the relatively weak fields of low mass systems, are quantified here.

The effect of a magnetic field is usually quantified by the Larmor radius, a; this is the radius of curvature of motion of the charge projected perpendicular to the magnetic field line. In the case of a LMXRB neutron star ($B_* \approx 10^9$ G), if $p^{\perp}$ denotes the component of the momentum perpendicular to the field line, then the Larmor radius is $a = (p^{\perp}c)/eB \approx 300$ cm $B_9^{-1}\ p^{\perp}_{14}$, where $p^{\perp}_{14}$ is in units of 10^{14} eV/c. Acceleration can occur only parallel to the field with motion relativistic, i.e in the direction of B. However, if $E \cdot B \neq 0$ acceleration along the magnetic field line can still occur and high energy protons can still be generated and collide with a targets permeated by the magnetic field (as in Cheng & Ruderman, 1989) to produce π^o which decay into γ-rays.

This small Larmor radius at the vicinity of the star indicates that charges get trapped by the lines in that region. As the magnetic field decays with radial distance, the Larmor radius increases and therefore there is a zone from where charges can escape from the system. For a dipolar magnetic field an "escape radius" can be defined by the condition:

$$r_e \approx E/eB(r_e) = (E/eB_*)\ (r_e/r_*)^3$$
$$r_e \approx 5.47 \times 10^7 \text{ cm}\ \ E_{14}^{-1/2}\ B_9^{1/2}\ R_6^{3/2} \quad . \qquad \text{(VI.8)}$$

This suggests that particles with 10^{14} eV might well escape from a region at 55 r_*, while 10^{16} eV protons can escape from 6

stellar radii. Computer simulations estimate that for a radius[3] $\approx$ 0.52 r_e particles escape with a somewhat diffusive motion, which is apparently chaotic, as trajectories with similar initial conditions separate with time. Some values found for this effective escape radius using $B_* = 10^9$ G are given in Table 6.1.

Energy (eV)	Distance/r_*	r_e/r_*
5×10^{13}	41	77.4
1×10^{14}	28	54.7
5×10^{14}	13	24.4
1×10^{15}	9	17.3
5×10^{15}	4	7.7

TABLE 6.1.

Distance for which most Charged Particles escape from the System as Function of their Energy. $B_* = 10^9$ Gauss.

Note that at a distance $r_{LC} = Pc/2\pi$ (the light cylinder radius) the field lines, if rigidly tied to the stars dipole would have to move faster than the speed of light. What actually occurs is that for $r \geq r_{LC} \approx 47.7\ r_*\ R_6\ (P/10ms)$ field lines are open and particles moving along these lines leave the system, forming a stellar wind. Therefore r_{LC} is an upper bound to the effective "escape" radius.

It is well known that electrons cannot be accelerated to

---

[3] the escape of a charge particle with fixed energy is sensible not only to its distance to the star but also to its initial conditions of motion (direction).

ultra-relativistic energies in the presence of high magnetic fields because of their energy losses due to synchrotron emission. A particle moving perpendicular to the magnetic field radiates energy at a rate:

$$\frac{d\gamma}{dt} = \frac{2e^2}{3mc^3}\,\gamma^4\,\omega_B{}^2 \quad . \qquad (VI.9)$$

Using $dt = dr/c$ and $\omega_B(r) = \omega_B(r_*)\,(r_*/r)^3$ the energy loss can be integrated over a radial straight path (therefore assuming that the magnetic field is weak and its effect on the motion can be neglected as a first approximation) to find:

$$\Delta\gamma/\gamma \approx (2e^2/15mc^3)\,\gamma^3\,w_B(r_*)^2\,(r_*/c)\,(r_*/r)^5 \quad , \qquad (VI.10)$$

which implies high energy losses $\Delta\gamma/\gamma \geq 1$ for:

$$r/r_* \leq 302\,E_{14}{}^{1/5}\,B_9{}^{2/5}\,R_6{}^{1/5} \quad . \qquad (VI.11)$$

Energy losses due to synchrotron emission are practically always negligible in the case of more massive particles, in particular protons, as $(r/r_*)_{prot} = (m_e/m_p)^{4/5}\,(r/r_*)_e < 1$ for typical values $E_{14} = B_9 = 1$.

To summarise this briefly, magnetic fields in low mass systems are likely to produce serious energy losses for electrons at distances below $300r_*$ and to trap protons, and other ions, at less than 30 or $20r_*$, depending on the energy. At this point it is worth mentioning again the mechanism proposed by Kazanas &

Ellision (1986) where Helium nuclei are accelerated and dissociated, providing high energy neutrons which are able to leave the system, interact with available targets and produce high energy radiation.

6.3 γ-RAY PRODUCTION BY NEUTRAL PION DECAY

High energy protons travelling through Hydrogen produce neutral pions when the column density is around $\kappa_o \approx 61.5$ g.cm^{-2} (Appendix III). These pions decay practically in situ into two γ-rays. If the medium traversed by the high energy protons is too thick, the γ-rays produced by the pions are absorbed and give a e^+e^- pair. A thick medium, of a few κ_o, would give rise to a cascade process developing in the same way as happens in the Earths atmosphere, where the average energy of electrons and photons is $E.\exp(-\kappa/\kappa_o)$. For a 10^{15} eV primary proton the mean photon energy will be below 1 TeV, on average, for a column density κ such that $\exp(-\kappa/\kappa_o) \sim 10^{-2}$ or 10^{-3}, or $\kappa \geq 5\ \kappa_o\ \mathrm{Ln}(E/10^{15}\mathrm{eV}) \approx 300$ g.cm^{-2}. Fortunately, a medium with the thickness of our atmosphere is not suitable for producing an appreciable flux of TeV γ-rays from high energy protons.

6.3.1 Interaction with the Companion star

Models where a beam of highly relativistic protons interacts with the limb of a companion star in a HMXRB system were developed

some years ago (Grindlay, 1982) and have had some popularity among TeV theoreticians. This sort of model clearly predict bursts, or at least enhancements, in the emission near eclipse ingress and egress, together with symmetric orbital light curves. As an example, a model including an isothermal atmosphere and wind for Vela X-1 gives bursts lasting 10^3 seconds (Figure 6.1); enhancements on the VHE γ-ray emission of Vela X-1 coincident with eclipse ingress and egress were reported to last three to four neutron star rotations, i.e. around 800 or 1000 seconds, by Raubenheimer *et al.* (1989). Of the HMXRB reported (or likely to be able to emit) as TeV γ-ray sources, Vela X-1 is the one where such an effect is most likely to be observable, as the duration of the enhacement has to be as long as possible in order to detect the burst above the noise (Table 6.2). Most of these models ignore magnetic steering of charged particles by the giant companion, which may be important in these systems (the magnetic dipole of the companion is not generally known). The effects of magnetic steering in HMXRB have recently been quantified by Mannings (1990). Magnetic steering allows to have emission during eclipse as observed in Her X-1 (Gorham & Learned, 1986), although it tends to give an asymmetric light curve.

In the case of LMXRB binaries the situation should be quite similar except that:

(i) the companion is smaller and therefore "eclipse - bursts" should be even closer to phase zero,

(ii) the accretion flow goes into a disc at proportionally (but not absolutely) larger radii (i.e. r_{out}/semiaxis is larger);

therefore there is less of a wake with which to interact,

(iii) the companion is of a later spectral type and winds as strong as those of early type O or B stars, the companions in high mass systems, are generally not expected.

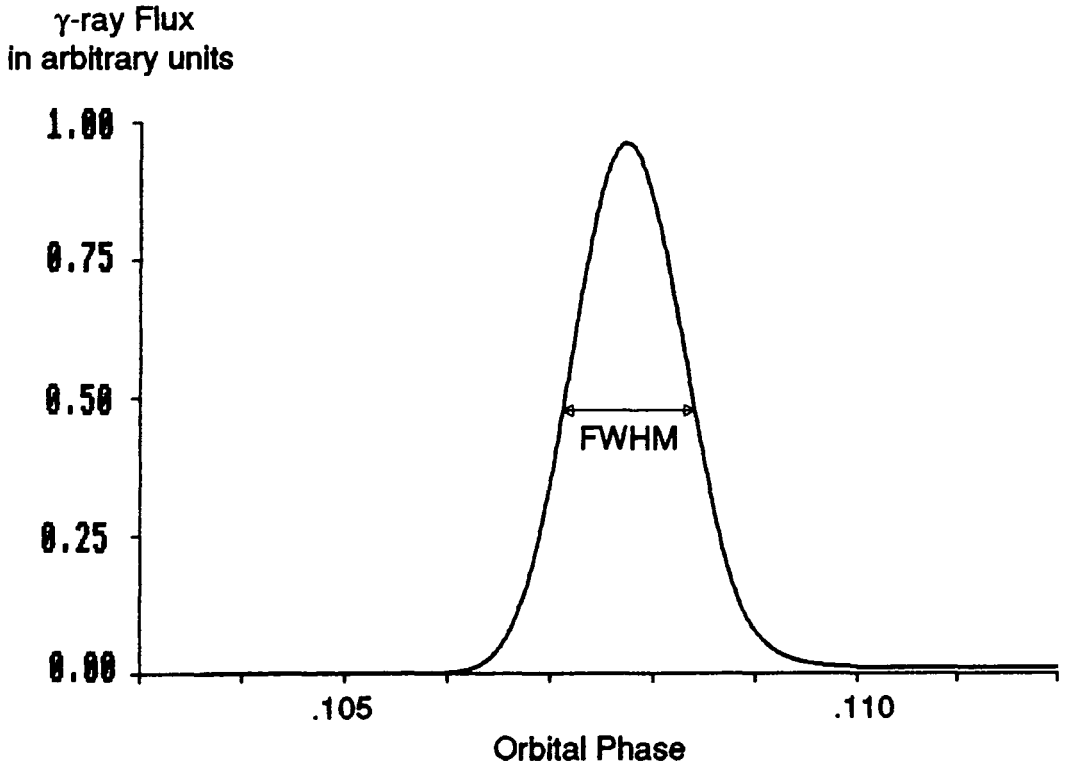

Figure 6.1

Orbital light curve predicted for Vela X-1
Particles emitted isotropically interact
with the atmosphere of the companion
FWHM is approximately 990 seconds

Object Name	LMC X-4	Cen X-3	SMC X-1	Vela X-1
Duration of Enhancement in seconds	46	101	207	1001

TABLE 6.2

FWHM Duration of Predicted Bursts in HMXRB using a Model with Isotheral Atmosphere and a Wind of Constant Velocity.

6.3.2 Interaction with the Accretion Disc

Accretion discs are usually dense enough to provide attractive targets for high energy γ-ray models. Two cases can be distinguished: (1) protons are trapped by the neutron star magnetic field, high energy neutrons are produced by ion - X-ray interaction and traverse the disc; (2) the target is matter related to the accretion flow outside the disc.

(i) interaction with the outer/middle disc and its atmosphere,

Cheng & Ruderman (1989) proposed a model for Hercules X-1, where protons are trapped in the dipolar field lines of a 10^{12} G neutron star magnetosphere and traverse the accretion disc. In this model, charged particles cross the surface of null charge

density (defined by $B.\Omega_* = 0$), are accelerated to energies of the order of 10^{14} eV, and sent to traverse the disc where they produce neutral pions. The direction of the emission follows the axis of the disc. The efficiency of this process relies on the thickness of the disc measured on a magnetic line (~ z axis) being less or of the same order as $\kappa_o \approx 61.5$ g.cm^{-2}. If the disc is thin, $\kappa < \kappa_o$, the proton would eventually interact after crossing the disc ~ κ_o/κ times. If $\kappa >> \kappa_o$, the particle would lose all its energy at the first crossing of the disc, with high energy photons also being absorbed (a proton cascade then forms).

The region where protons can interact adequately with the disc, that is where the column density Σ satisfies $\Sigma \leq \kappa_o$, is relatively far from the Alfven radius, which is equivalent to the corotation radius r_{co} for a system disc - star in equilibrium; $r_{co} \approx 1.69 \times 10^8$ cm $M_{1.44}^{1/3} P_s^{2/3}$. The standard α - disc model (Appendix IV) gives a column density of 10 κ_o at 10^8 cm (for an accretion rate of 10^{17} g.s^{-1} and a neutron star of 1.44 M_o) and $\Sigma \approx \kappa_o$ at $r \approx 5.1 \times 10^9$ cm $\alpha^{-4/3} \dot{M}_{17} M_{1.44}^{1/3}$, i.e. twenty times the Alfven/corotation radius. A low density fluctuation region moving through the disc might lead to a burst of observable γ-rays of duration ~ v_r/r. An attractive feature, briefly mentioned by Cheng & Ruderman, is the production of high energy neutrons by the interaction of relativistic ions, trapped in the field, with X-ray photons. Those neutrons, ejected in a direction tangential to the magnetic field line, will cross the disc at larger radii. In order to apply the same model to LMXRB it has to be taken into account that:

- as the Alfven radius is smaller, the disc is going to be even thicker at the point where the protons traverse it (of the order of 10^3 g.cm^{-2}). No high energy photons can therefore be expected to escape.

- on the other hand, as ions are trapped in a region where the radiation field is much more intense, more relativistic neutrons will be produced. Only those moving parallel to the disc surface would be expected to interact with an adequate amount of target material; therefore their emission would be confined to a narrow range of angles.

- motion at radii ~ r_e, where the Larmor radius begins to be large, will be rather chaotic. It is not possible to predict where charged particles will strike the disc.

Another way of modelling the production of high energy photons is using beams of ultra relativistic nucleons moving radially outward (either ions in magnetic fields weak enough to allow this motion for ions, or neutrons). The density at and near the disc, expressed in spherical coordinates (r,φ,θ), is approximately given by:

$$\rho(r,\theta) \approx \rho(r) \exp\{- 1/2 \, (r/h)^2 \cos^2\theta\} \quad , \qquad (VI.12)$$

while the column density for a given radial trajectory (θ fixed) for the particle beam is:

$$\kappa(\theta) = \int_{r*}^{r_{out}} \rho(r,\theta) \, dr \quad . \qquad (VI.13)$$

This sort of density profiles results in a strong dependence of $\kappa(\theta)$ with θ, leading to narrow beams of γ-rays, and only edge-on sources be; m detectable. The narrowest beam corresponds to the case h/r = constant, where the Gaussian dependence on $\cos\theta$ is preserved and the (radial) density is given by:

$$\rho = \frac{\dot{M}}{3\pi\alpha\ (h/r)^3\ (GM)^{1/2}}\ r^{-3/2} \quad , \qquad \text{(VI.14)}$$

from where the column density can be estimated to be:

$$\kappa_c = 8.033 \times 10^6\ \text{g.cm}^{-2}\ L_{38}\ M_{1.44}^{-3/2}\ R_{\alpha 6}^{1/2}$$

$$\kappa(\theta) = \kappa_c \exp\{-1/2\ (r/h)^2\ \cos^2\theta\} \quad . \qquad \text{(VI.15)}$$

The function $\Psi(\kappa) = \{1-\exp(-\kappa/\kappa_o)\} \exp(-\kappa/\kappa_g)$ is an indicator of the output flux of photons, for a given input flux of protons (Section 6.4.1). Setting $\Psi(\kappa) \geq \Psi_{max}/10$, equivalent to the requirement $1.6\ \text{g.cm}^{-2} \leq \kappa(\theta) \leq 225\ \text{g.cm}^{-2}$, implies:

$$5.555\ (h/r) \geq \cos\theta \geq 4.579\ (h/r) \quad ; \qquad \text{(VI.16)}$$

if $h/r \approx 0.01$, the beam is practically tangent to the plane of the disc ($\theta \approx 87^\circ$) and has a very small angular width, $\Delta\theta \approx 0.6^\circ$.

The beam for a convex or concave disc would be much wider. The α-disc model (Shakura & Sunyaev, 1973; Appendix IV) suggests that accretion discs are likely to be slightly concave in the outer ($h/r \sim \alpha^{1/10}\ r^{1/8}$) and middle ($h/r \sim \alpha^{-1/10}\ r^{1/20}$) zones, and flat ($h$ = constant) in the inner, radiation dominated, region. The beaming $\Psi\{\kappa(\theta)\}$ was computed for a disc with

constant α (= 1), outer radius of 10^{10} cm and a total luminosity of 10^{38} erg.s^{-1}; a much wider beam is effectively obtained, as shown in Figure 6.2. Maximum emission is at 69°, with an appreciable FWHM of 31° ($\Psi/\Psi_{max} \geq 0.10$ for $20° \leq \theta \leq 79°$). This suggests that, a relatively large proportion (~ 1/3) of the binaries producing high energy γ-rays through this process should be detectable. It also implies that, if the edge of the disc is not strictly symmetric relative to the φ axis, an orbitally modulated γ-ray signal can be produced. A precessing disc would also modulate the emission.

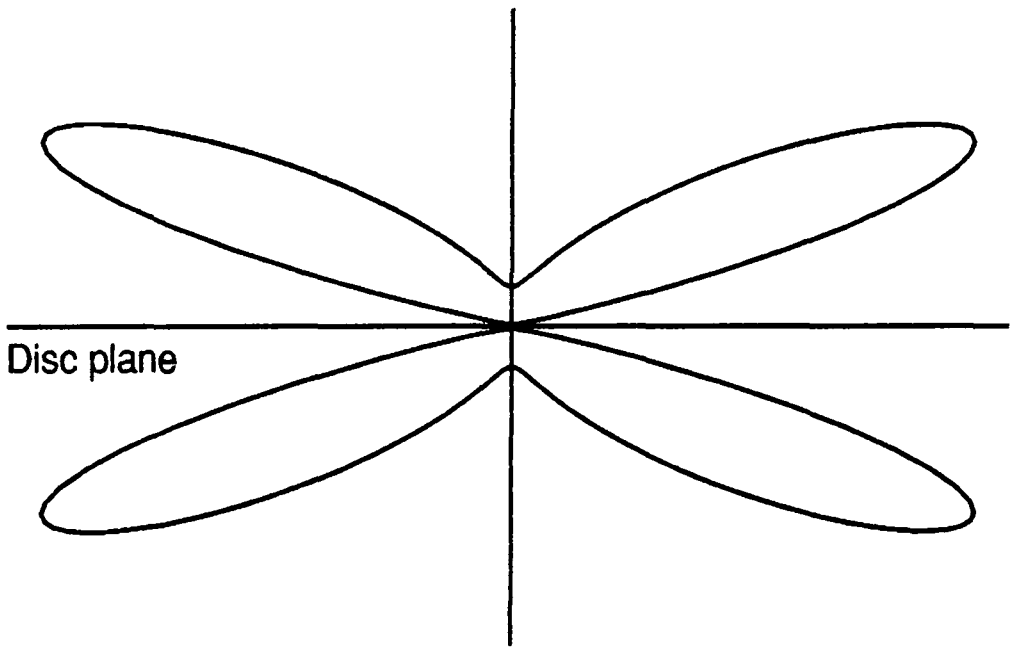

Figure 6.2

Output γray emission for an input isotropic particle emission traversing an α= constant accretion disc with luminosity 10^{38} erg.s^{-1}

(ii) interaction with matter in the inner (radiation dominated) regions,

As mentioned above, the thickness of an α disc in the inner region is too large for TeV γ-ray production ($\Sigma \sim 10^3$ gcm^{-2}). But an α - disc supported by radiation pressure is unstable under thermal instabilities (in the sense that thermal fluctuations grow with time) and the disc is most probably inflated by the radiation. This gives a suitable target for protons emitted with inclinations between $\sim 30^\circ$ to 90° located at around 10 stellar radii or less.

Another target can be a small magnetosphere forming a sort of shell of material. If most of the accretion flow goes into this shell of radius a , then a nucleon emitted radially from the surface of the star will pass through a column density given by:

$$\kappa \approx \frac{\dot{M}}{2\pi\,(GMa)^{1/2}} = 2.28\ \mathrm{g.cm^2}\ L_{38}\ M_{1.44}^{-3/2}\ r_6^{1/2}\ (a/7R_*)^{-1/2} \qquad (VI.17)$$

Although this value is relatively low, the shell of material can still work as a target (with an efficiency of $\Psi/\Psi_{max} \approx 0.14$). If this shell is like a "sandwich" of matter flowing between two magnetic lines, then there will be practically no material for angles θ below $\sin^{-1}\{(r_*/a)^{1/2}\}$, or 22° for $a/r_* \approx 7$ in the Scorpius X-1 system (as magnetic lines satisfy $r^{1/2} = A \sin\theta$).

Slane & Fry (1989) recently proposed a model where the target is made of density inhomogeneities which have been torn

out of the disc by instabilities near the inner magnetosphere. This was suggested in order to explain the anomalous periodicities reported in the TeV emission of Her X-1 (i.e. Gorham *et al.*, 1986; the Durham group has not seen these anomalous periods). As in LMXRB the inner edge of the disc will be much closer to the star, where instabilities are likely to be large, a similar model might applicable to Sco X-1. Typical densities near the neutron star can be $\sim 10^{-2}$ g.cm^{-3} and therefore clumps with diameters $\sim 10^{3}$ cm are suitable targets. The emission envisaged by this mechanism is likely to come in short bursts (10^{2} seconds) showing short term variability (possibly periodic or quasi periodic) in the millisecond range. The 1988 Scorpius X-1 data do show some enhancement in the count rate although the statistical significance is low, near to 3% (Chapter III). Its power spectrum does not show any highly significant feature although any pattern other than a high peak is not likely to be recognised due to the intrinsically poor signal to noise ratio of the data (and the large number of degrees of freedom; Chapter V).

6.3.3 Interaction with material in a jet

As it has been just mentioned, clumps of matter have already been proposed as a target for TeV production (Slane & Fry, 1989). Fermi acceleration of particles by plasma inhomogeneities moving upwards in an accretion column might give high energy nucleons (Section 6.2.2). In a picture where the scatterer and the target

are the same, particles can then be accelerated by, and collide with, clumps of plasma thereby producing high energy photons. The emission is most likely to come out parallel to the jet and therefore this mechanism might be explain emission if seen face on. Again jets are associated with both Cyg X-3 and Sco X-1. Future TeV observations of this kind of objects with more sensitive telescopes may give clues about any possible link between the ejection of relativistic jets of matter and particle acceleration.

6.4 ABSORPTION OF γ-RAYS BY PAIR PRODUCTION

For photon energies above 1 GeV absorption processes other than pair production, like inverse Compton scattering are negligible. Pair production can occur either in electromagnetic or radiation fields, i.e. by interaction with virtual or real photons. The first case covers absorption by matter (virtual photons from the electric field of nuclei) and by magnetic fields (large scale electrostatic fields are very rare), while in the second case pair production by interaction with the photons emitted by the accretion disc is considered. As virtual photons introduce a term in the cross section of the order of the fine structure constant, $\alpha \approx 1/137$, the radiation field of the disc, constituted of real photons, is a more likely absorber of high energy photons.

6.4.1 Pair production through interaction with matter

γ-rays interact weakly with matter and are absorbed when they produce an e^+e^- pair upon interacting with the virtual photons associated with the electric field of a charge (electron or nucleus). This process has in fact been included in the context of π^o production by high energy protons interacting with matter. A finely tuned column depth of material ($\kappa \approx \kappa_o \approx 61.5$ g.cm^{-2}) is necessary in order to allow most of the protons to produce neutral pions and, therefore, γ-rays while preventing the latter from interacting with matter (γ-rays are absorbed with e-folding depth $\kappa_g \approx 62.8$ g.cm^{-2} in the case of Hydrogen). A rough estimate of the adequate value of κ can be found neglecting energy dependences and imagine a beam of protons traversing a medium of thickness κ. The number of protons that have not interacted after depth $N_p(\kappa) = No\ \exp(-\kappa/\kappa_o)$, while the number of γ-rays at κ (considering production and absorption):

$$N_g(\kappa) = A\ N_o\ \{1-\exp(-\kappa/\kappa o)\}\ \exp(-\kappa/\kappa g) \equiv A\ N_o\ \Psi(\kappa) \quad , \qquad (VI.18)$$

where A is the number of photons created per proton. It is easy to see that the number of γ-rays is maximised for:

$$\kappa = \kappa_o\ \ Ln(1 + \kappa_g/\kappa_o) \approx \kappa_o\ Ln2 \approx 43\ g.cm^{-2} \quad , \qquad (IV.19)$$

where, $\Psi_{max} \approx 1/4$. If $\kappa_o = \kappa_g$ then it is possible to find

analytically the interval $(\kappa_{min}, \kappa_{max})$ where the emission of photons is above a ratio ε of its maximum, i.e. $\Psi(\kappa) \geq \varepsilon \cdot \Psi_{max}$:

$$\kappa_{min,max} = \kappa_o \, Ln \left\{ \frac{2}{1 \pm (1-\varepsilon)^{1/2}} \right\} \quad ; \quad (IV.20)$$

As an example, if $\varepsilon = 1/2$ then $9.7 \; g.cm^{-2} \leq \kappa \leq 118 \; g.cm^{-2}$ while for $\varepsilon = 0.1$, $1.6 \; g.cm^{-2} \leq \kappa \leq 225 \; g.cm^{-2}$. As mentioned in Section 6.2, a thick target will hold a cascade with roughly κ/κ_o "steps", where the mean photon energy is $\leq E_o \exp(-\kappa/\kappa_o)$, E_o being the energy of the incident proton; in other words, there is still an outgoing γ-ray flux but the mean photon energy is too low. The absorption of γ-rays by matter is implicitely included considered in the requirement $\kappa \leq 300 \; g.cm^{-2}$.

One point worth mentioning is that a medium with thickness a few times κ_o is likely to modify the shape of the particle energy spectrum. Hillas (1984b) showed that a monoenergetic particle spectrum $f_p(E) = \delta(E-E_o)$ subject to a process of cascades would give a γ-ray power law spectrum $f_f(E) = E^{-k}$ at the output.

6.4.2 Pair production in the magnetic field of the neutron star

High magnetic fields are common in the vicinity of neutron stars and pair annihilation of high energy γ-rays with virtual photons associated with the field can occur. Although this process is likely to cause severe absorption near a young and highly magnetised neutron star (high mass system), it is not obvious that the same should happen in low mass systems where typical

magnetic fields at the surfaces of neutron stars are of the order of 10^8 or 10^9 Gauss. This absorption mechanism can be described in terms of an absorption coefficient k, the inverse of the mean free path, given by (Erber 1966; Appendix III):

$$k \approx (\alpha/2\lambda_c)\ (B_{\perp}/Bc)\ T(\chi) \quad , \qquad (A4.23)$$

where $B_{\perp}$ is the component of the magnetic field perpendicular to the motion of the photon, $Bc = m^2c^4/eh \approx 7.02 \times 10^{12}$ G is the critical field, $\lambda_c = h/mc \approx 2.43 \times 10^{-10}$ cm is the Compton wavelength and the parameter $\chi = 1/4\pi\ (E/mc^2)\ (B_{\perp}/Bc)$, where E is the energy of the photon, is an indicator of the strength of the absorption given by the function:

$$T(\chi) \approx 0.46\ \chi^{-1}\ K^2_{1/3}(2/3\chi)\ ; \qquad (A4.24)$$

$K_{1/3}$ is the modified Bessel function of order 1/3. Although the absorption coefficient is an increasing function of the magnetic field, as one would expect, it does not have the same behaviour with energy when the magnetic field is fixed: initially the value of k increases rapidly with χ to reach a maximum for $\chi \approx 6.52$; afterwards it decreases slowly although k^{-1} is still typically below 10^6 cm. In practice once the photon has an energy above a threshold value ($\sim mc^2\ Bc/B_{\perp}$) it is absorbed (Figure A3.2).

Given the strength of the magnetic field at the surface of the neutron star, the radius from which γ-rays can escape, i.e. the value r such that:

$$\int_{r}^{\infty} k(E;B_{\perp}(r',\theta)) \cdot dr' = 1 \quad ; \quad \text{(VI.22)}$$

can be estimated. As indicated in the formula, the magnetic field is a function of the angle θ (between magnetic axis and photon propagation): $B_{\perp} = B_{*} (R_{*}/r)^3 \sin\theta$. Figures 6.3 (a to c) show the probability of escaping from a 10^9 G neutron star as a function of radius for different emission angles θ and for γ-ray energies of 0.1, 1 and 10 TeV.

B_{*} (G)	10^{13}	10^{12}	10^{11}	10^{10}	10^{9}	10^{8}	10^{7}	10^{6}
R/R_{*}	117	53	24	10.94	4.95	2.24	1.01	≤ 1

TABLE 6.3

Radius of Escape for Photons as a Function of Stellar Magnetic Field. γ-Ray Energy is 1 TeV Emission Angle is 60 degrees

Table 6.3 shows the value of r at which photons with an energy of 1 TeV and emitted with an angle of 60° relative to the

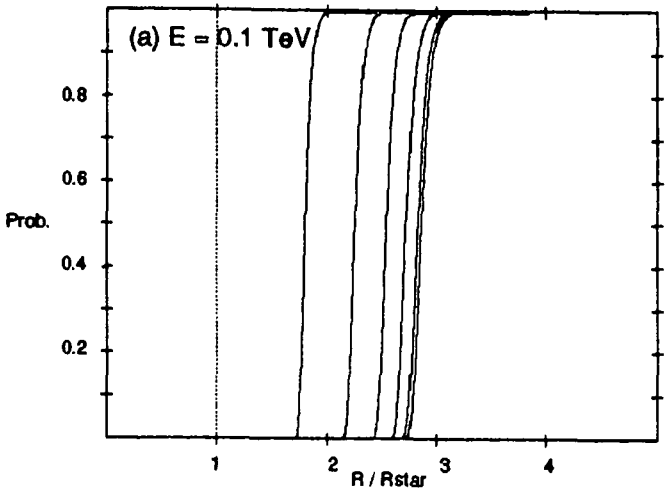

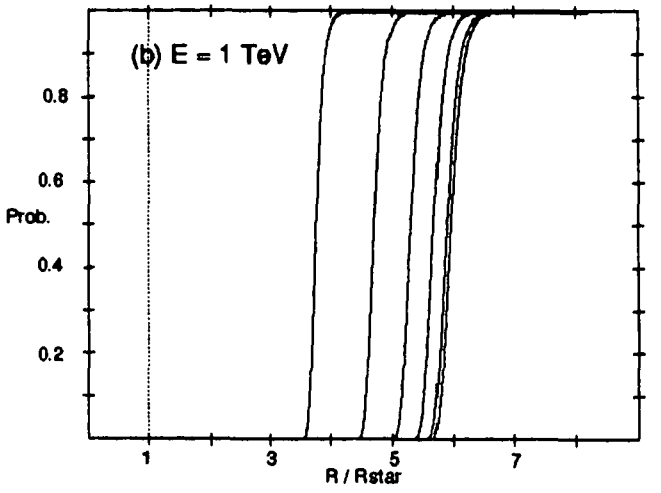

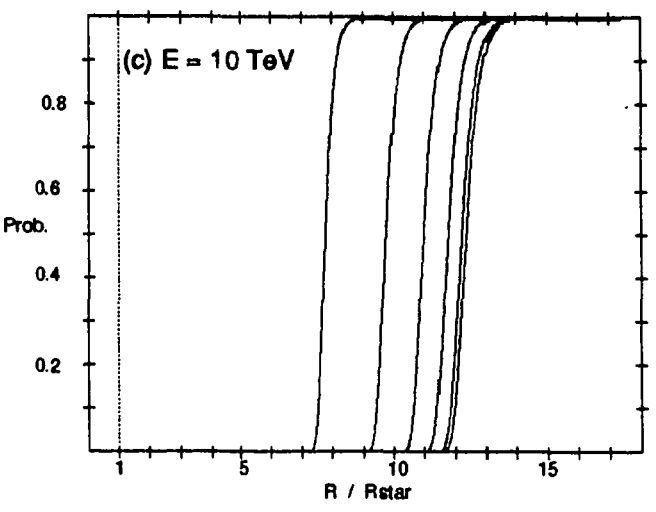

Figures 6.3a,b,c

Probability as a function of radial distance to the star of a high energy photon escaping from the magnetic field of a 10^9 Gauss neutron star. Curves from left to right represent different angles of emission from 0° (equator) to 75° in steps of 15°. The free parameter is the energy of the photon: (a) 0.1 TeV, (b) 1 TeV, (c) 10 TeV

magnetic axis can escape, as a function of magnetic field at the surface of the star. For stellar fields of the order of 10^9 Gauss or less most TeV photons produced in the vicinity of the neutron star can escape. Photons with higher energies are likely to trigger cascade processes (pair production - Compton or synchrotron) down to lower energies such as 1 TeV, at which γ-rays will escape.

6.4.3 Pair production in the radiation field of the disc

A γ-ray is likely to have encounters with other photons while it propagates above the accretion disc. If N_{enc} is the number of such encounters then the flux of γ-rays will be attenuated by a factor $\exp(-N_{enc})$, due to pair production with disc photons. Let a photon move in the direction of the unitary vector $\bar{k}$. Its position (using Cylindrical coordinates (R,φ,z) is given by:

$$\bar{r}(t) = \bar{r}(0) + \bar{k}\, ct = R(t)\,\bar{R} + z(t)\,\bar{z} \quad .$$

Now consider a point in the disc with coordinates

$$\bar{r}' = R'\,(\cos\varphi'\,\bar{R} + \sin\varphi'\,\bar{\varphi}) \ ,$$

their distance between these two points is then:

$$|\bar{r}(t) - \bar{r}'|^2 = R^2(t) + z^2(t) - 2R(t)R'\cos\varphi' + R'^2 \quad .$$

The solid angle covered by the cross section at the position of the TeV photon seen from the disc is $\sigma/|\bar{r}(t)-\bar{r}'|^2$, and for a disc emitting with an intensity $I(\nu)$, the expected number of

encounters N_{enc} that the γ-ray will have is:

$$N_{enc} = \int_0^{\infty} \int_{\nu_m}^{\infty} \int_0^{2\pi} \int_{R_{in}}^{R_{out}} \frac{\sigma\{h\nu, E, \theta(r(t), r')\}}{|\, r(t) - r' \,|^2} \cdot \frac{I\{\nu, T(R')\}}{h\nu} \cdot R' dR' d\varphi' d\nu \, dt \; ; \qquad (VI.23)$$

where prime quantities refer to points of the disc. σ is the pair production cross section, which depends on the γ-ray and disc photon energies, E and $h\nu$ respectively, and θ, their incidence angle given by:

$$\cos\theta = \{ k_R (R - R'\cos\varphi') + k_z z \} / |r - r'| \quad ,$$

with $k_R = \bar{k}\cdot\bar{R}$, $k_z = \bar{k}\cdot\bar{z}$; $\nu_m = m^2c^4/Eh$ is the threshold energy to produce a pair while the emission of the disc, neglecting its atmosphere (likely to introduce lines in the spectrum), is given by a local black body expression:

$$I(\nu; T(R)) = \frac{2h\nu^3}{c^2 \{\exp(h\nu/kT) - 1\}} \qquad (IV.24)$$

$$T(R') = T_* (R_*/R')^{3/4} [\, 1 - (R_*/R')^{1/2} \,]^{1/4}$$

$$T_* = (3GM\dot{M}/8\pi\sigma_s R_*^3)^{1/4} \quad .$$

The initial conditions for the gamma ray are $\{E, r(0), \bar{k}\}$, and the disc parameters $\{T_*, R_{in}/R_*, R_{out}/R_*\}$ are also required. Evaluation

of this integral is not feasible in the practise even numerically, and some simplification is necessary.

If photons are assumed to propagate perpendicular to the disc (i.e. along the z axis) $|r(t)-r'|^2$ is cancelled out with the disc area differential and, the integral becomes:

$$N_{enc} = \int_0^{\infty} \int_0^{\infty} \sigma(E;h\nu)\ (4\pi I(\nu)/h\nu)\ d\nu\ dt \quad ; \qquad (IV.25)$$

The details of its computation are given in Appendix III. The final result depends only on the parameter x_{min}:

$$x_{min} \approx 1.190 \times 10^{-4}\ E_{Tev}^{-1}\ L_{38}^{-1/4}\ R_6^{1/2}\ (R_{min}/R_*)^{3/4}\ (1-\cos i)^{-1}$$

$$N_{enc} \approx 1.3348 \times 10^{-2}\ E_{Tev}^{-5/3}\ L_{38}^{1/3}\ R_6^{1/3}\ \frac{H(x_{min})}{\sin i\ (1-\cos i)^{5/3}}$$

(IV.26)

Where i is the inclination of the binary to the plane of the sky. The function H(x) in (IV.26) is an integral expression, defined in Appendix III, that can be well approximated for $x \leq 10^{-2}$ by a power law $H(x) \approx 9.798\ x^{-0.75}$ and decays rapidly to zero (almost as a cutoff) for $x \geq 1$. The condition $N_{enc} \leq 1$, related to the escape of high energy γ-rays gives a restriction on the energy, disc luminosity, minimum radius R_{min} and inclination i at which γ-rays can be seen (using a power law index equal to -0.75 and assuming $R_6 = 1$)):

$$N_{enc} \approx 114.8 \frac{E_{tev}^{-11/12} (R_{min}/R_*)^{-9/16} L_{38}^{25/48} R_6^{-1/24}}{\sin i \, (1 - \cos i)^{11/12}}$$

(IV.27)

This approximation holds for small x_{min} or large energies. The net effect of the γ-ray absorption by the disc is to produce a gap in the spectrum, as shown in Figure 6.4, where high energy photons are assumed to be produced at $r - a \approx 3.46\ R_*$. The start of the gap corresponds to the energy where γ-rays and the hardest of the X-rays from the disc begin to annihilate, i.e. $x_{min} \geq 1$. The end of the gap occurs when the cross section of the high energy photon becomes small enough to allow it to survive. This is found by setting $N_{enc} \leq 1$ with the power law approximation for H(x). These conditions give:

$$E_{min} = 119 \text{ MeV } L_{38}^{-1/4} R_6^{1/2} (R_{min}/R_*)^{3/4} (1-\sin i)^{-1}$$

$$E_{max} = 176 \text{ TeV } L_{38}^{25/48} R_6^{-1/22} (R_{min}/R_*)^{-27/44} \cos i^{-12/11} (1-\sin i)^{-1}$$

(IV.28)

Using the same parameters as in Figure 6.4 these approximations give $E_{min} \approx 226$ MeV and $E_{max} \approx 141$ TeV while the computer model gave 332 MeV and 793 TeV as the values at which the photon flux is halved. This model predicts a total absorption of the photon emission of Scorpius X-1 at energies below 800 TeV, unless:

(i) the inclination is (*very*) small, so that the observed

photons travel perpendicular to the disc and have an incidence angle of 180° with disc photons, for which the pair production cross section tends to zero,

(ii) γ-rays are produced far from the stellar surface. For a luminosity $L_{38} \approx 0.2$ and $i \approx 30°$ then if photons are produced at $R_{min} = R_*$ then $E_{max} \approx 81$ TeV ; in order to have $E_{max} = 5$ TeV γ-rays have to be produced at $R_{min} \approx 94\ R_*$.

Optical observations are not consistent with a small inclination (as the amplitude of the velocity curve for the He II line is relatively large); on the other hand, emission with orbital modulation (Scorpius X-1 showing such a effect at the 3% confidence level) is more likely to be produced far from the neutron star as this modulation can be attributed to a disc with an asymmetric edge (as far as the shape is time independent).

It is worth mentioning the case of younger and more massive systems, where the emission site seems to correspond to the corotation radius, where the disc rotates with the same angular velocity as the star, and $R_{min}/R_* \approx 10^2$. In a system like Hercules X-1 the dip in the spectrum predicted by this model, shown in Figure 6.5, ranges from 3 GeV up to 4.3 TeV. If this is the case, the existing discrepancies between imaging and non imaging ground based Cerenkov observations of Her X-1 (and probably 4U0115+63) may be explained if the imaging cuts are sensitive to the energy of the γ-rays. A more energetic photon has a cascade with more Cerenkov photons that develops deeper into the atmosphere. As mentioned by Hillas & Patterson (1986b) it is desirable to select cascades developing high in the

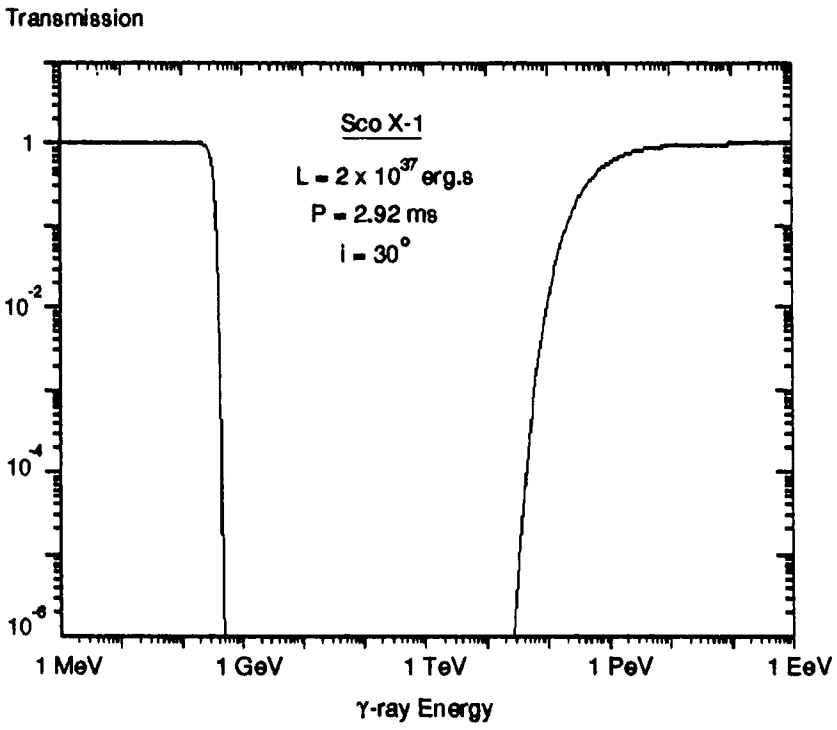

Figure 6.4a

Transmission coefficient for γ-rays
Pair production with photons from the accretion disc
Disc extends down to corotation radius r_{co}= 3.46 r_{star}

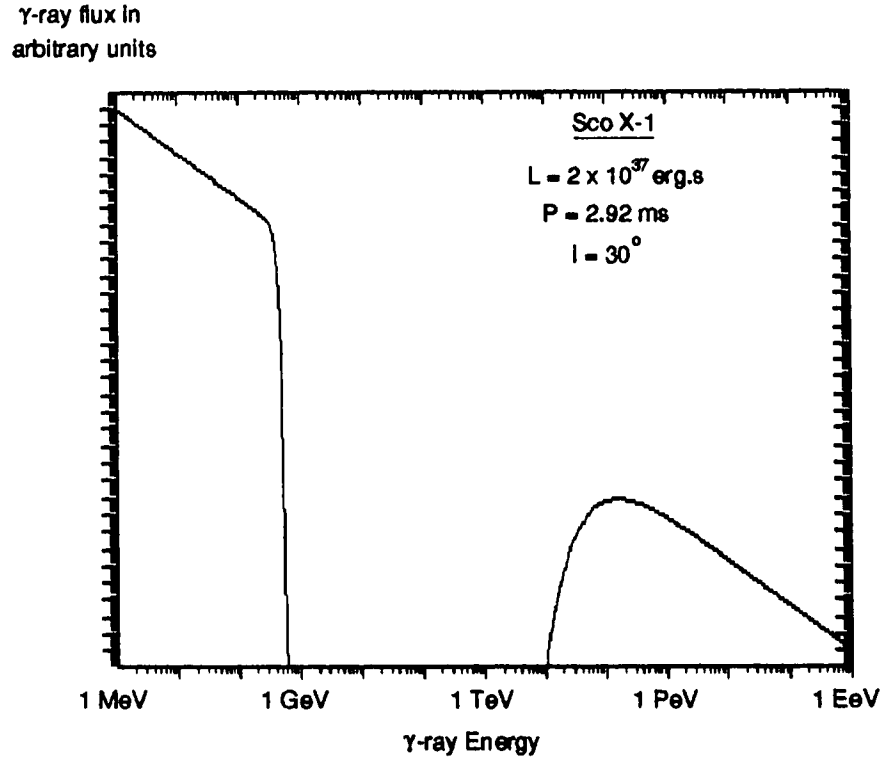

Figure 6.4b

Power law spectrum (index=-2.65) modified by
Pair production with photons from the accretion disc
Disc extends down to corotation radius r_{co}= 3.46 r_{star}

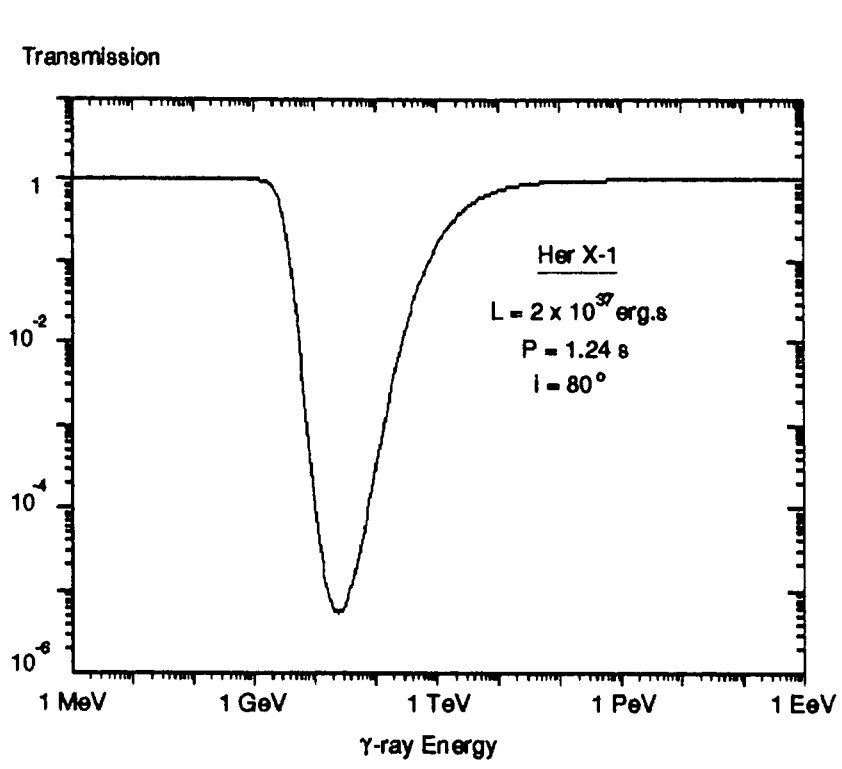

Figure 6.5a

Transmission coefficient for γ-rays
Pair production with photons from the accretion disc
Disc extends down to corotation radius r_{co}= 195 r_{star}

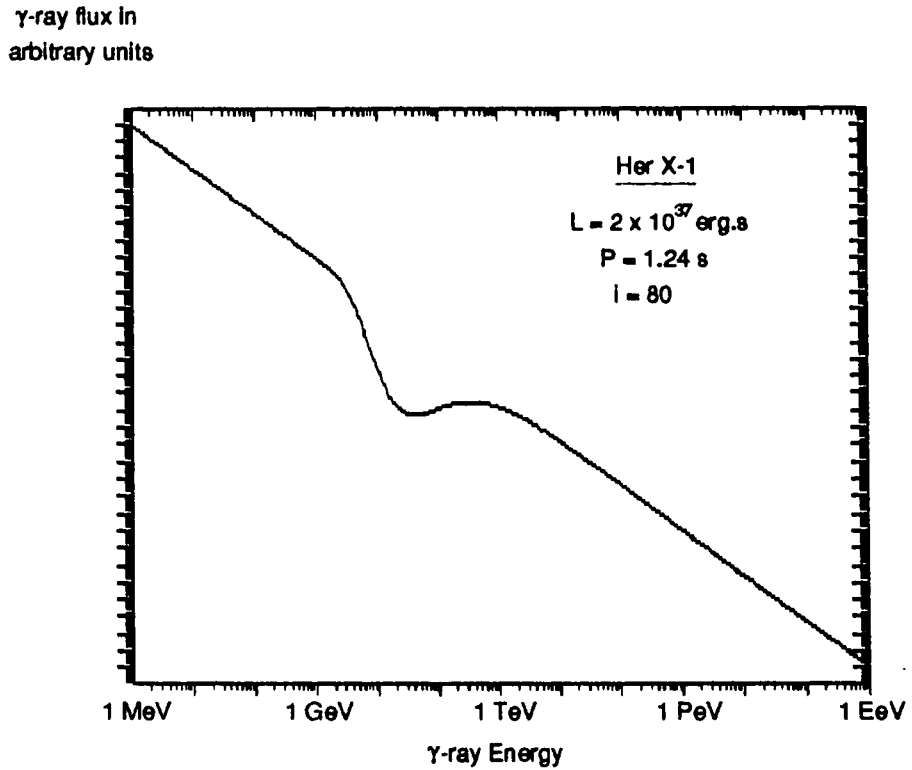

Figure 6.5b

Power law spectrum (index=-2.65) modified by
Pair production with photons from the accretion disc
Disc extends down to corotation radius r_{co}= 195 r_{star}

atmosphere in order to accentuate the differences between p and γ showers. This topic might deserve future attention.

6.5 CAN THERE BE A TeV PULSAR? CONCLUSIONS

In the case of both Cygnus X-3 and Scorpius X-1 rotation cannot be ruled out as the source of energy. In fact it is interesting to note the case of Sco X-1 where, while accretion supplies - 10^{37} - 10^{38} erg.s^{-1} in X-rays, the TeV γ-ray luminosity is of the same order as the rotational power of 10^{35} erg.s^{-1} inferred by its (order of magnitude) period and magnetic field. Such an origin for the high energy radiation makes the presence of a pulsar more likely although, to be fair, the case of the Crab pulsar appears to be at odds with this point.

For an accretion powered source the presence of a pulsed signal is far from obvious and it is in fact model dependent. For example plasma turbulence would not be as likely to give a pulsar as a shock at the surface of the neutron star. Also the creation of gamma rays in a localised site near the star would result in a periodic signature.

As discussed in this chapter, many models in which these binary systems can produce 10^{12} eV photons have been found. Most models have barely been more than sketched and all have their "weak" and "strong" points. Two severe restrictions are the magnetic confinement of charged particles near the neutron star and the absorption of high energy photons through pair production

with the radiation field of the accretion disc. While the first point can be avoided by producing photons in situ the second one requires photons to be produced far away in order to escape; the production of high energy neutrons appears to be necessary to open this deadlock. Anyhow it is unlikely that models will cease to have some speculative character before detectors become more sensitive and more information about this high energy γ-ray emission can be extracted.

VII. CONCLUSIONS

Very high energy γ-ray astronomy has meet various successes in the last decade: an increasing understanding of the atmospheric cascades and the experimental methods required has led to reports of statistically significant signals from compact objects, mainly neutron stars. But in the last two or three years, the observational technique established in the field, rejection of protons by selection of the aperture (like the ring guard technique), and the recent imaging technique appear in conflict as recent observations with the latter, in principle more sensitive, have failed to confirm some sources previously reported. At this point, the field requires non statistical detections in order to establish as a branch of astronomy. An increase in sensitivity in the more "traditional" aperture rejection techniques, which can be achieved with the construction of arrays of several telescopes, is essential in order to obtain consistency in the results with both techniques. The development of new observational methods may also reconcile the present results.

Cerenkov data on the brightest low mass X-ray binary, Scorpius X-1, taken during 1988 and 1989 with the Mark III γ-ray telescope showed a positive signal. In here these data were re-analysed in order to investigate the presence of any orbital modulation; a weak effect, at the 3% significance level, or 1.8σ, was found; but more recent data failed to show a signal and support this result, leaving the question still open.

A method to perform large FFT on microcomputers with a limited (4 Mby) memory, but relatively high speed, was developed and implemented. Using BBC workstation microcomputers (up to half a dozen simultaneously) period searches down to few milliseconds were carried out in some of the Scorpius X-1 Cerenkov data. No periodicity was found at significant level in these Scorpius X-1 data, nor in those from the low mass binary GX 5-1 and SN1987A, where the finding of a pulse signal would be of major interest.

In the last section of this work, previous theoretical models relying on the accretion of matter as the source of energy, and developed in the context of more massive systems - like Hercules X-1, Centaurus X-3 and Vela X-1 - were reviewed in the context of low mass objects, primarily Scorpius X-1. Some of these reviews may also apply to the case of Cygnus X-3. The rapid rotation induced by the mass accretion and the decay of the magnetic field of the neutron star is a viable source of energy in these low mass systems. The signals reported from Cygnus X-3 and Scorpius X-1 are of the same order of magnitude as implied by their rotation and magnetic field, the maximum luminosity predicted by pulsar mechanism being $dE/dt \sim \mu^2 \Omega^4 / c^3$. The finding of pulsations in Cerenkov data not reported in other energy bands, would bring support to a pulsar origin for the high energy emission. In other LMXRB pulsar models predict fluxes below present detectability levels and only the direct feeding by accretion would give detectable sources. As a consequence, further positive results from non pulsating LMXRB might probably have to wait a next generation of instruments.

Finally, the absorption of high energy photons by pair production in the radiation field of the accretion disc points towards a strong suppression of γ-rays. This provides the tightest constraint on the site of production of these photons. On the other hand, in the case of Hercules X-1, alterations in the energy spectrum caused by this process may well be behind the "imaging dilemma". Further investigation on this subject, namely adapting the same model to objects like 4U0115+63 may deserve future attention.

APPENDIX I

ABOUT TIMES AND FILES

A1.1 CONVENTIONS

(i) Datafile names have the form [1]ddmmyy[12]-[123] where:

- The first letter [1] denotes the kind of dataset:

[1] = C is for datafiles containing event records ≡ {time, fire pattern, 7qts} with 22 bytes per event (used until 1988).

[1] = E is for datafiles containing event records ≡ {time, fire pattern, 21 qts} with 36 bytes per event (1989 & 1990).

[1] = F is for datafiles containing one header record of 1024 bytes and event records ≡ {time, fire pattern, 21 qts, telescope number and spare byte} with 35 bytes per event (since mid 1990).

- The string "ddmmyy" indicates the day of observation.

- The second set of characters [12] indicates about processes done to the original file: the original dataset has [12] = A while subsections are identified by [12] = AX where "X" is dummy ("X" can be 1 and 2 for first and second segments or A, B and C for the first, second and third ones of a new selection). Distinct datasets do not have the same characters [12].

- The last set of characters [123] corresponds to a three codename for each source. Examples are SCO ≡ Scorpius X-1, SNA ≡ SN1987A, G04 ≡ GX 5-1 and CYG ≡ Cygnus X-3.

(ii) Time assigned to an event

A time t from a datafile CddmmyyA corresponds to the UTtime:

$$UTtime = INTEGER\{JD(ddmmyy)\} + t$$

Therefore, frequently times have values above 86400s. For example, the "burst" in E070989AX-CYG started near t = 129060. As JD(070989; 0 UT) = 2447776.5, the UTtime of the burst is = JD24447776 + 129060/86400 = JD2447777.4938

A1.2. THE DATA

For each datafile we display the following information:

FILENAME: "Day", Site, telescope, Mode, Tstart, Tend, Duration, Number of events (All, Chplus, Cplus, Chop, Conly), ¿Zenith Angle, culmination time?

SEGMENTS: Tstart, Tend, Duration, ALL events, CONLY, (CHOP).

And we use the following abbreviations and definitions:

"Day": Integer of {Julian Day - 2440000}

Telescopes: Mk3 refers to Mark 3

Operating Modes: Tr = Tracking, Ch = Chopping

Categories of events defined by firing pattern (chapter 3):

ALL: any channel is triggered

Ch+: channel #1 or #3 is required

Chop: (channel #1 on source only) or
(channel #3 on source only)

Cplus: Channel #1 on source is required

Conly: Channel #1 on source only

C290387A: 6883, Narrabri, Mk3, Ch, 103314 s, 110938 s, 7624 s,
All: 22066, Ch+: 11869, Chop: 4239, Conly: 2371

C010487A: 6886, Narrabri, Mk3, Ch, 103449 s, 111026 s, 7576 s,
All: 29216, Ch+: 16637, Chop: 5942, Conly: 2842

C020487A: 6887, Narrabri, Mk3, Ch, 103116 s, 111397 s, 8280 s,
All: 31876, Ch+: 17461, Chop: 6237, Conly: 2985

C100588A: 7291, Narrabri, Mk3, Ch, 88533 s, 100092 s, 11558 s,
All = Ch+: 27568, Chop: 11193, Conly: 4753

C110588A: 7292, Narrabri, Mk 3, Ch, 88578 s, 103153 s, 14575 s,
All = Ch+: 28492, Chop: 10598, Conly: 5326

A2: 95340s,103141s, 7800s, All=Ch+:16495, Chop:6101, Conly:3076

C120588A: 7293, Narrabri, Mk 3, Ch, 87959 s, 107333 s, 19373 s,
All = Ch+: 47376, Chop: 19407, Conly: 7271

A1: 87960s, 97140s, 9180s, All=Ch+:22534, Chop:9297, Conly:3566
A2: 93903s,100439s, 6536s, All=Ch+:17614, Chop:7112, Conly:2709
AA: 88622s, 90783s, 2160s, All=Ch+: 4756, Chop:2082, Conly: 811
AB: 96782s, 97263s, 480s, All=Ch+: 1277, Chop: 540, Conly: 143

C130588A: 7294, Narrabri, Mk 3, Ch, 88072 s, 112750 s, 24677 s,
All = Ch+: 55269, Chop: 22853, Conly: 8651

A3: 99781s,106020s, 6239s, All=Ch+:15455, Chop:6456, Conly:2445
A4: 105905s,112742s, 6836s, All=Ch+: 9278, Chop:4040, Conly:1676

C140588A: 7295, Narrabri, Mk 3, Ch, 87867 s, 97744 s, 9876 s,
All = Ch+: 23450, Chop: 9461, Conly: 3507

C060688A: 7318, Narrabri, Mk 3, Ch, 85645 s, 91517 s, 5871 s,
All = Ch+: 14420, Chop: 5689, Conly: 2506

C070688A: 7319, Narrabri, Mk 3, Ch, 90073 s, 95250 s, 5176 s,
All = Ch+: 12779, Chop: 5045, Conly: 2224

C120688A: 7324, Narrabri, Mk 3, Ch, 85617 s, 101386 s, 15769 s,
All = Ch+: 14420, Chop: 5689, Conly: 2506

C150688A: 7327, Narrabri, Mk 3, Ch, 92823 s, 99713 s, 6890 s,
All = Ch+: 14985, Chop: 6177, Conly: 2468

C160688A: 7328, Narrabri, Mk 3, Ch, 85464 s, 101386 s, 15769 s,
All = Ch+: 35955, Chop: 14622, Conly: 5874

C180688A: 7330, Narrabri, Mk 3, Ch, 81141 s, 96463 s, 15321 s,
All = Ch+: 33143, Chop: 13484, Conly: 5312

C190688A: 7331, Narrabri, Mk 3, Ch, 84142 s, 100379 s, 16236 s,
All = Ch+: 37526, Chop: 15343, Conly: 6122

E020589A: 7648, Narrabri, Mk 3, Ch, 93554 s, 107332 s, 13777 s,
All = Ch+: 43196, Chop: 14251, Conly: 6995

A1: 94713s,103892s, 9177s, All=Ch+:29887, Chop:9786, Conly:4766
A2: 100653s,107188s, 6535s, All=Ch+:20169, Chop:6684, Conly:3362
AA: 94854s, 96874s, 2020s, All=Ch+: 6244, Chop:2129, Conly:1084
AB: 98796s,100235s, 1439s, All=Ch+: 4902, Chop:1622, Conly: 761
AC: 103354s,104074s, 720s, All=Ch+: 2338, Chop: 846, Conly: 434

E060589A: 7652, Narrabri, Mk 3, Ch, 95638 s, 104947 s, 9308 s,
All = Ch+: 24669, Chop: 7909, Conly: 3927

E080589A: 7654, Narrabri, Mk 3, Ch, 93246 s, 98027 s, 4781 s,
All = Ch+: 13234, Chop: 3995, Conly: 1930

MK3.F230490A: 8004, Narrabri, Mk 3, Ch, 92296 s, 109575 s, 17279 s,
All: 107910, Ch+: 41851, Chop: 14332, Conly: 5570

MK3.F240490A: 8005, Narrabri, Mk 3, Ch, 94446 s, 101699 s, 7253 s,
All: 38883, Ch+: 15021, Chop: 4977, Conly: 1882

MK3.F260490A: 8007, Narrabri, Mk 3, Ch, 99126 s, 101430 s, 2304 s,
All: 38799, Ch+: 15251, Chop: 5046, Conly: 1958

MK3.F270490A: 8008, Narrabri, Mk 3, Ch, 91552 s, 103981 s, 12429 s,
All: 74108, Ch+: 28258, Chop: 9528, Conly: 3588

MK3.F280490A: 8009,Narrabri, Mk 3, Ch, 91925 s, 104913 s, 12988 s,
All: 75308, Ch+: 28388, Chop: 9462, Conly: 3457

MK3.F290490A: 8010, Narrabri, Mk 3, Ch, 92046 s, 104298 s, 12252 s,
All: 100642, Ch+: 38446, Chop: 13107, Conly: 5033

MK4.F290490A: 8010, Narrabri, Mk 4, Ch, 98251 s, 103706 s, 5454 s,
All = Ch+: 10672, Chop: 3943, Conly: 2200

MK3.F300490A: 8011, Narrabri, Mk 3, Ch, 96863 s, 104028 s, 7165 s,
All: 58884, Ch+: 22822, Chop: 7398, Conly: 2702

MK4.F300490A: 8011, Narrabri, Mk 4, Ch, 97564 s, 105389 s, 8275 s,
All = Ch+: 16615, Chop: 6273, Conly: 3789

MK3.F010590A: 8012, Narrabri, Mk 3, Ch, 94209 s, 101322 s, 7113 s,
All: 59115, Ch+: 22366, Chop: 7604, Conly: 2617

MK4.F010590A: 8012, Narrabri, Mk 4, Ch, 95626 s, 102633 s, 7007 s,
All = Ch+: 15309, Chop: 5916, Conly: 3569

MK3.F020590A: 8013, Narrabri, Mk 3, Ch, 95991 s, 103164 s, 7173 s,
All: 57171, Ch+: 21143, Chop: 7014, Conly: 2439

MK3.F210690A: 8063, Narrabri, Mk 3, Ch, 77592 s, 94129 s, 16537 s,
All: 124710, Ch+: 46538, Chop: 15301, Conly: 5625

MK4.F210690A: 8063, Narrabri, Mk 4, Ch, 83132 s, 95511 s, 12378 s,
All = Ch+: 20551, Chop: 8026, Conly: 4822

MK3.F190790A: 8091, Narrabri, Mk 3, Ch, 76996 s, 86863 s, 9867 s,
All: 63853, Ch+: 25279, Chop: 8327, Conly: 2970

MK3.F210790A: 8093, Narrabri, Mk 3, Ch, 74782 s, 76988 s, 2205 s,
All: 17109, Ch+: 6655, Chop: 2197, Conly: 846

MK3.F210790B: 8093, Narrabri, Mk 3, Ch, 78846 s, 86997 s, 8150 s,
All: 66615, Ch+: 26206, Chop: 8711, Conly: 3252

MK4.F210790A: 8093, Narrabri, Mk 4, Ch, 75667 s, 82839 s, 7172 s,
All: 23339, Ch+: 13880, Chop: 5412, Conly: 2675

SN1987A

—

E210190A: 7912, Narrabri, Mk 3, Ch, 88662 s, 97263 s, 8601 s,
All = Ch+: 14397, Chop: 3224, Conly: 1501

E220190A: 7913, Narrabri, Mk 3, Ch, 82141 s, 97240 s, 15099 s,
All: 26781, Ch+: 14961, Chop: 5670, Conly: 2734

AX: 82141s, 94846s, 12704s, All:24798, Ch+: 13581, Chop:5268,
Conly:2530

CYGNUS X-3

—

C110983A: 5589, Dugway, Mk 2, Tr, 143429 s, 171311 s, 27880 s,
All: 16646, C+: 4534, Conly: 1045

AX: 148534s, 148949s, 415s, All: 448, C+: 112, Conly: 45

C011083A: 5609, Dugway, Mk 2, Tr, 138636 s, 156977 s, 18340 s,
All: 5092, C+: 1281, Conly: 519

AX: 145910s, 146403s, 494s, All: 115, C+: 21, Conly: 16
AL: 146041s, 146379s, 340s, All: 70, C+: 13, Conly: 11

E010989A: 7770, La Palma, Mk 4, Tr, 126184 s, 131704 s, 5520 s,
All: 15492, C+: 5594, Conly: 3414

AX: 129597s, 129992s, 295s, All:1128, C+: 414, Conly: 242

E070989A: 7776, La Palma, Mk 4, Tr, 127714 s, 136520 s, 8806 s,
All: 22127, C+: 7846, Conly: 5075

AW: 129060s, 129365s, 305s, All: 875, C+: 325, Conly: 217

GX 5-1

C140788A: 7356, Narrabri, Mk 3, Tr, 74896 s, 101325 s, 26428 s
All = C+: 28374, Conly: 17722

A1: 81000 s, 83500 s, 2500 s, All=C+: 7632, Conly: 1880
A2: 83500 s, 86000 s, 2500 s, All=C+: 10854, Conly: 1933
A3: 86000 s, 88500 s, 2500 s, All=C+: 14174, Conly: 1919
A4: 88500 s, 91000 s, 2500 s, All=C+: 17487, Conly: 1925
A5: 91000 s, 93500 s, 2500 s, All=C+: 20747, Conly: 1933
A6: 93500 s, 96000 s, 2500 s, All=C+: 23614, Conly: 1762
A7: 96000 s, 98500 s, 2500 s, All=C+: 26092, Conly: 1586
A8: 98500 s,101000 s, 2500 s, All=C+: 28143, Conly: 1395

C170788A: 7359, Narrabri, Mk 3, Tr, 80167 s, 101309 s, 21141 s
All = C+: 24755, Conly: 15745

A1: 81000 s, 83500 s, 2500 s, All=C+: 4118, Conly: 1973
A2: 83500 s, 86000 s, 2500 s, All=C+: 7488, Conly: 1996
A3: 86000 s, 88500 s, 2500 s, All=C+: 10799, Conly: 2013
A4: 88500 s, 91000 s, 2500 s, All=C+: 14128, Conly: 1997
A5: 91000 s, 93500 s, 2500 s, All=C+: 17319, Conly: 2012
A6: 93500 s, 96000 s, 2500 s, All=C+: 20170, Conly: 1848
A7: 96000 s, 98500 s, 2500 s, All=C+: 22647, Conly: 1701
A8: 98500 s,101000 s, 2500 s, All=C+: 24572, Conly: 1405

C190788A: 7361, Narrabri, Mk 3, Tr, 87159 s, 101837 s, 14678 s
All = C+: 15955, Conly: 10945

A1: 87500 s, 90000 s, 2500 s, All=C+: 3935, Conly: 2144
A2: 90000 s, 92500 s, 2500 s, All=C+: 7306, Conly: 2174
A3: 92500 s, 95000 s, 2500 s, All=C+: 10248, Conly: 1981
A4: 95000 s, 97500 s, 2500 s, All=C+: 12750, Conly: 1846
A5: 97500 s,100000 s, 2500 s, All=C+: 14860, Conly: 1584

APPENDIX II

ON DATA ANALYSIS

A2.1 WHIPPLE ACCEPTANCE OF γ AND REJECTION OF p SHOWERS

The numbers given by the Whipple group in relation to their two initial detections of the Crab (Lang et al., 1990; Weekes et al., 1989) are given in the following table:

Selection	CRAB89	CRAB90
ALLON	652974	403379
ALLOFF	651801	398563
AZON	9092	12352
AZOFF	7929	10065

TABLE A2.1

Whipple Counts on the Crab

These numbers are estimators of more relevant quantities like $N(\gamma) \equiv$ number of γ-rays, $N(p) \equiv$ number of protons, $N(e) \equiv$ number of electrons, and α and β, the respective acceptances of γ-rays and protons (it is assumed here that electrons cannot be distinguished from photons by imaging cuts):

$$\begin{aligned} x_o &\equiv \text{ALLON} = N(\gamma) + N(p) + N(e) \\ y_o &\equiv \text{ALLOFF} = N(p) + N(e) \\ x_c &\equiv \text{AZON} = \alpha\, N(\gamma) + \beta\, N(p) + \alpha\, N(e) \\ y_c &\equiv \text{AZOFF} = \beta\, N(p) + \alpha\, N(e) \quad . \end{aligned} \tag{A2.1}$$

Four of the five unknowns {N(γ), N(p), N(e), α, β} can be deduced. Assuming the ratio N(e)/N(p) as a known parameter:

$$N(\gamma) = x_o - y_o \quad , \quad N(p) = \frac{y_o}{1 + N(e)/N(p)}$$

$$\alpha = \frac{x_c - y_c}{x_o - y_o} \tag{A2.2}$$

$$\beta = \frac{y_c}{y_o \{1 + N(e)/N(p)\}} - \left\{ \frac{x_c - y_c}{x_o - y_o} \right\} \left\{ \frac{N(e)}{N(p)} \right\} .$$

Considering all errors (or deviations) as Poissonian (except for N(e)/N(p) which is assumed to be error free) the errors associated to the unknowns can be found:

$$\Delta N(\gamma) = \Delta\{x_o + y_o\} = x_o^{1/2} + y_o^{1/2}$$

$$\Delta N(p) = \frac{\Delta y_o}{1 + N(e)/N(p)} = \frac{y_o^{1/2}}{1 + N(e)/N(p)}$$

$$\Delta\alpha = \left\{ \frac{x_c - y_c}{x_o - y_o} \right\} \left\{ \frac{\Delta\{x_o - y_o\}}{x_o - y_o} + \frac{\Delta\{x_c - y_c\}}{x_c - y_c} \right\}$$

$$= \left\{ \frac{x_c - y_c}{x_o - y_o} \right\} \left\{ \frac{1}{x_o^{1/2} - y_o^{1/2}} + \frac{1}{x_c^{1/2} - y_c^{1/2}} \right\} \tag{A2.3}$$

$$\Delta\beta = \frac{\Delta\{y_c/y_o\}}{1 + N(e)/N(p)} - \left\{ \frac{N(e)}{N(p)} \right\} \Delta\alpha$$

$$= \frac{y_c}{y_o \{1 + N(e)/N(p)\}} \left\{ \frac{1}{y_c^{1/2}} + \frac{1}{y_o^{1/2}} \right\} + \Delta\alpha \left\{ \frac{N(e)}{N(p)} \right\}$$

The value $N(e)/N(p) \approx 5.8 \times 10^{-3}$ (Lang, 1986) can be substituted, together with the values of Table A2.1, to obtain:

	CRAB1	CRAB2
$N(\gamma)$	1173 ± 1615	4816 ± 1266
α	0.991 ± 1.523	0.475 ± 0.169
$N(p)$	648042 ± 803	396264 ± 627
β	$(0.634 \pm 0.898) \times 10^{-2}$	$(2.235 \pm 0.127) \times 10^{-2}$
$N(p)^*$	651801 ± 807	398563 ± 631
β^*	$(1.216 \pm 0.015) \times 10^{-2}$	$(2.525 \pm 0.029) \times 10^{-2}$

TABLE A2.2

Acceptances of γ-rays and Protons from Whipple Data

(* = value obtained assuming N(e) = 0)

The original "detection" is in fact compatible with a null acceptance of γ-ray events ($\alpha = 0$) - note that the number of photons is in fact estimated from the raw counts (it is only because (ALLON-ALLOFF) and (AZON-AZOFF) differ by less than 1% of the error on the first quantity that α is so close to 1; a 2σ fluctuation would have given $\alpha < 1/3$). It is the second observation that points toward an effective discrimination between photons and protons. Note that, as the acceptance of γ-rays is just under 50%, the flux measured might require a correction to account for photons rejected and correspond with

the actual flux. These results are likely to be energy dependent; the latter measurements were made at a lower threshold energy, where the method appears to be more efficient.

A2.2 THE RAYLEIGH TEST AS A LEAST SQUARES SINUSOIDAL FIT

The data consist in series of time events:

$$x(t) = \sum_j \delta(t-t_j) \quad . \qquad (A2.4)$$

The Rayleigh test fits the function f(t) to the data x(t):

$$f(t) = a \cos(2\pi t/P) + b \sin(2\pi t/P) \quad . \qquad (A2.5)$$

To obtain the best fit (best a and b, once P is set), the deviation between data and fit given by $\Delta = \langle \{ x - f(t) \}^2 \rangle$, is to be minimised with respect to a and b. The resulting conditions are $\partial\Delta/\partial a = \partial\Delta/\partial b = 0$ which give the system of algebraic equations ($\omega = 2\pi/P$):

$$\begin{bmatrix} \langle x \cdot \cos\omega t \rangle \\ \langle x \cdot \sin\omega t \rangle \end{bmatrix} = \begin{bmatrix} \langle \cos^2\omega t \rangle & \langle \sin\omega t \cdot \cos\omega t \rangle \\ \langle \sin\omega t \cdot \cos\omega t \rangle & \langle \sin^2\omega t \rangle \end{bmatrix} \begin{bmatrix} a \\ b \end{bmatrix} \quad , \quad (A2.6)$$

whose solution is given by :

$$a = \frac{\langle x \cdot \cos\omega t \rangle \langle \sin^2\omega t \rangle - \langle x \cdot \sin\omega t \rangle \langle \sin\omega t \cdot \cos\omega t \rangle}{\langle \cos^2\omega t \rangle \langle \sin^2\omega t \rangle - \langle \sin\omega t \cdot \cos\omega t \rangle^2} \qquad (A2.7)$$

$$b = \frac{\langle x \cdot \sin\omega t \rangle \langle \cos^2\omega t \rangle - \langle x \cdot \cos\omega t \rangle \langle \sin\omega t \cdot \cos\omega t \rangle}{\langle \cos^2\omega t \rangle \langle \sin^2\omega t \rangle - \langle \sin\omega t \cdot \cos\omega t \rangle^2} \quad .$$

Some of the averages are independent of the data x(t) and, for times in the interval (0,T), they are given by:

$$\langle \cos^2 \omega t \rangle = \frac{1}{T} \int_0^T \cos^2(\omega t) \cdot dt = \frac{1}{2} + \frac{1}{2\omega T} \sin(\omega T) \cos(\omega T)$$

$$\langle \sin^2 \omega t \rangle = \frac{1}{2} - \frac{1}{2\omega T} \sin(\omega T) \cos(\omega T)$$

$$\langle \sin\omega t \cdot \cos\omega t \rangle = \frac{1}{2\omega T} \sin^2(\omega T) \qquad \text{(A2.8)}$$

$$\langle \cos^2 \omega t \rangle \langle \sin^2 \omega t \rangle - \langle \sin\omega t \cdot \cos\omega t \rangle^2 = \frac{1}{4} - \frac{1}{4\omega^2 T^2} \sin^2(\omega T) \; .$$

These expressions simplify considerably at the Nyquist frequencies, where by definition $\sin(\omega T) = 0$. Note that for a Poissonian time series:

$$\langle Tx \rangle = n_e \qquad \text{and} \qquad \langle T^2 x^2 \rangle = 2n_e$$

A2.3 EXPECTED AND BEST EXPONENTIAL FITS TO DISTRIBUTIONS

In the asymptotic case, the number n of powers contained in an interval dx around x is given by the distribution:

$$dn = N e^{-x} dx \qquad ; \qquad \text{(A2.9)}$$

where N is the total number of trials. Performing a sample of powers using a "power width" ξ gives n(j), the number of powers inside the bin number j (all powers between $j\xi$ and $(j+1)\xi$; the value j = 0 included), as:

$$n(j) = N \int_{j\xi}^{(j+1)\xi} e^{-x}\, dx = N\,\{1-\exp(-\xi)\}\cdot\exp(-j\xi) \qquad . \quad (A2.10)$$

The parameters A and β of an exponential fit to the distribution, $A.\exp(-\beta x)$, relate to the step and total number of points by:

$$\begin{aligned} A &= N\,\{1-\exp(-\xi)\} \\ \beta &= \xi \qquad . \end{aligned} \qquad (A2.11)$$

The constrictions $\partial\Gamma/\partial A = \partial\Gamma/\partial\beta = 0$ derived by minimizing the deviation between data and fit $\Gamma = \langle\{\, n(j) - A\cdot\exp(-\beta j)\,\}^2\rangle_j$ with respect to the parameters A and β give:

$$A = \frac{\langle\, n(j)\cdot\exp(-\beta j)\,\rangle}{\langle\, \exp(-2\beta j)\,\rangle} = \frac{\langle\, n(j)\cdot j\cdot\exp(-\beta j)\,\rangle}{\langle\, j\cdot\exp(-2\beta j)\,\rangle} \qquad . \quad (A2.12)$$

β is calculated by a numerical iteration of expression A2.12 (using Newton's method) with A being derived straightforwardly.

A2.4 COUNT RATES AND FITS

The count rate x(t) - events per unit time - for a dataset of duration T can be well fitted by a parabola with its parameters being uniquely defined by the time series $\{t_j\}$:

$$x(t) = \sum_{j=0}^{ne-1} \delta(t-t_j) = a\,(t/T)^2 + b\,(t/T) + c \quad . \qquad (A2.13)$$

Least squares minimisation arguments give:

$$\begin{bmatrix} \langle x \rangle \\ \langle xt/T \rangle \\ \langle xt^2/T^2 \rangle \end{bmatrix} = \begin{bmatrix} \langle t^2/T^2 \rangle & \langle t/T \rangle & 1 \\ \langle t^3/T^3 \rangle & \langle t^2/T^2 \rangle & \langle t/T \rangle \\ \langle t^4/T^4 \rangle & \langle t^3/T^3 \rangle & \langle t^2/T^2 \rangle \end{bmatrix} \begin{bmatrix} a \\ b \\ c \end{bmatrix} \quad . \qquad (A2.14)$$

The matrix elements are independent of x(t) and can be calculated directly: $\langle t^n/T^n \rangle = 1/(n+1)$. The matrix is then a constant:

$$\begin{bmatrix} \langle t^2/T^2 \rangle & \langle t/T \rangle & 1 \\ \langle t^3/T^3 \rangle & \langle t^2/T^2 \rangle & \langle t/T \rangle \\ \langle t^4/T^4 \rangle & \langle t^3/T^3 \rangle & \langle t^2/T^2 \rangle \end{bmatrix} = \begin{bmatrix} 1/3 & 1/2 & 1 \\ 1/4 & 1/3 & 1/2 \\ 1/5 & 1/4 & 1/3 \end{bmatrix} ,$$

and can easily be inverted to give the parabolic fit:

$$\begin{bmatrix} a \\ b \\ c \end{bmatrix} = \begin{bmatrix} 30 & -180 & 180 \\ -36 & 192 & -180 \\ 9 & -36 & 30 \end{bmatrix} \begin{bmatrix} \langle x \rangle \\ \langle xt/T \rangle \\ \langle xt^2/T^2 \rangle \end{bmatrix} \quad . \qquad (A2.15)$$

The count rate fit can be expressed in a more descriptive way:

$$x = x_c \left[1 - \frac{1}{2} \left[\frac{t - t_c}{\tau} \right]^2 \right] \quad ; \qquad (A2.16)$$

the curvature is expected to be negative (i.e. $a < 0$) for a "good" dataset (defined by good observing conditions and a duration long enough to be sensible to count rate variations, i.e. a few hours). This second order fit can also be described in terms of other more meaningful parameters, namely: the count rate at culmination $x_c \equiv c + b^2/4(-a)$, the extrapolated time of culmination $t_c \equiv T(b/2(-a))$, and the characteristic time for count rate variations $\tau \equiv T\sqrt{-x_c/2a}$; the latter was found to be between two and three hours in good agreement with the following estimation.

The zenith angle z is expressed in terms of the latitude l, declination δ and hour angle $H_o + \Omega t$ (where $2\pi/\Omega$ = 1 day) as:

$$\begin{aligned} \cos z &= \sin l \sin\delta + \cos l \cos\delta \cos(H_o + \Omega t) \\ &= A + B \cos(H_o + \Omega t) \quad , \end{aligned} \qquad (A2.17)$$

and, using the empirical relation between the count rate x(t) and the zenith angle of the source:

$$x(t) = \cos^k z \quad ; \qquad (A2.18)$$

a Taylor expansion of x(t) around $t = 0$ can be made in order to find a polynomial fit to the count rate near the time of

culmination ($\sin H_o = 0$). The expansion is relatively simple up to the third order as:

$$x(0) = (A + B)^k$$

$$dx / dt\ (0) = - (A + B)^{k-1}\ B\ k\ \Omega \sin H_o = 0$$

$$d^2x/dt^2\ (0) = - (A + B)^{k-1}\ B\ k\ \Omega^2$$

$$d^3x/dt^3\ (0) = 0$$

The expression (A2.16) can be recovered where:

$$\tau_o = \frac{1}{\Omega} \left\{ \frac{A + B}{k\ B} \right\}^{1/2} \approx 3.82 \text{ hrs } \{(A+B)/kB\}^{1/2} . \qquad (A2.19)$$

Substituting $k \approx 2.5$ for Cygnus X-3 ($\delta \approx 41^\circ$) observed from La Palma ($l \approx 29^\circ$) on the 7th of September 1989 (when $z \approx 12^\circ$) in A2.19 gives $\tau \approx 2.94$ hours compared to the value found using the parabolic fit to our data (all events), $\tau \approx 2.45$ hours. Fourth order corrections become important for t - 6.56 hours.

Finally, the effect of the count rate variation due to the change in the Zenith angle (which negligible below 0.1 Hz) can be removed by giving a weight $w(t_j) = 1 - 1/2\ (t_j - t_c)/\tau^2$ to an events occuring a $t=t_j$.

APPENDIX III

PRODUCTION AND ABSORPTION OF γ-RAYS

A3.1. PRODUCTION PROCESSES

A3.1.1 Low Energy γ-rays by Nuclear Transitions

γ-rays were originally found as an unknown kind of radiation produced by the decay radioactive nuclei. Typical energies of photons emitted in nuclear transitions are in the MeV range. Examples are the ^{56}Ni and ^{56}Co transitions to ^{56}Fe lines (at 0.812 MeV and 0.847 Mev) observed in SN1987A. The Crab nebula might be emitting gamma ray lines around 0.4 MeV due to the decay of ^{249}Cf (Hillier, 1984).

A3.1.2. Particle - Antiparticle annihilation

The annihilation of pairs particle - antiparticle produces two γ-rays with energy given by the rest mass of the particles in the rest frame. Electron (and positrons) are the lightest (non massless) particles (rest mass $\approx$ 0.511 MeV) and theirs is the most common annihilation process. High energy photons can be produced by highly relativistic particles (Lorentz factors above 10^6). A continuous annihilation of nucleons and antinucleons would require a source of antimatter (an ambient with continuous high energy particle interactions) in order to achieve a significant output of high energy photons.

A3.1.3. Inverse Compton Scattering

Compton scattering describes the interaction of a charged particle of energy $E = \gamma mc^2$ with a (low energy) photon of energy $h\nu$ where $\gamma mc^2 \gg h\nu$. Two cases can be distinguished depending whether quantum effects are important or not:

(i) $\gamma h\nu \ll mc^2$ or $h\nu \ll 0.26\ \text{eV}\ (E/\text{TeV})^{-1}$:

A low energy (infrared or radio) photon interacts with a highly energetic charged particle. The cross section for this process is constant and given by:

$$\sigma_c \longrightarrow \sigma_T = 8\pi/3\ (e^2/mc^2)^2 \quad , \quad (A3.1)$$

numerically $\sigma_c \approx 6.652 \times 10^{-25}\ \text{cm}^2$ for electrons and a lower value of $1.97 \times 10^{-31}\ \text{cm}^2$ for protons. The mean energy of the photon produced is:

$$E_{comp} \approx (4/3)\ \gamma^2 h\nu \quad , \quad (A3.2)$$

which from the condition $\gamma h\nu \ll mc^2$ and energy conservation arguments E_{comp} is clearly below γmc^2.

(ii) $\gamma h\nu \gg mc^2$:

When, for example, the energy of a photon interacting with a charged particle of energy 1 TeV is above 1 eV (optical light or X-rays for example) the cross section has to include quantum effects; the exact expression is given by the Klein - Nishima formula (Rybicki, Lightman; 1979):

$$\sigma = \sigma_T \frac{3}{4}\left[\frac{1+x}{x^3}\left\{\frac{2x(1+x)}{1+2x} - \mathrm{Ln}(1+2x)\right\} + \frac{\mathrm{Ln}(1+2x)}{2x} - \frac{1+3x}{(1+2x)^2}\right] ,$$

(A3.3)

where $x \equiv h\nu/mc^2 < 1$. Compton scattering is relevant mainly when the charged particle is an electron, as the cross section has a m^{-2} dependence which makes the process irrelevant for the production of γ-rays by protons generally. It might still be worth noticing that a proton crossing the radiation field of a accretion disc with luminosity 10^{38} erg.s^{-1} has a probability above 1% of having a Compton interaction.

A3.1.4. Synchrotron

An electron moving with velocity βc in an electromagnetic field (E,B) experiences the Lorentz (four vector) force given by:

$$d(\gamma mc)/dt = e\,\beta\cdot E$$
$$d(\gamma m\beta c)/dt = e\,(E + \beta \times B) . \qquad (A3.4)$$

The electric field is not usually included in the context of synchrotron radiation, although it can be seen as a source or well of energy. When $E = 0$ the path of the charge is described by an helix with a magnetic field line as the axis; the particle rotates around the line with a frequency $\omega_c = eB/\gamma mc$ and radiates pulses of (temporal) width $\Delta t \approx mc/\gamma^2 eB$ with a characteristic separation $\Delta T = 2\pi / \omega_c \approx \gamma^3 \Delta t$ (Rybicki, Lightman, 1979). The

range of the spectrum is given by these two times and the maximum energy of the photons emitted is (Ginzburg, 1979):

$$E_{sync} \approx (3/4\pi)\ \gamma^2\ (eBh/mc) \quad , \qquad (A3.5)$$

analogue to expression (A3.2) for Compton scattering. The resemblance is not a coincidence as synchrotron radiation can be described as scattering of charges by virtual quanta associated to the magnetic field. A particle moving perpendicular to magnetic field radiates energy at a rate:

$$\frac{d\gamma}{dt} = \frac{2e^2}{3mc^3}\ \gamma^4\ \omega_B{}^2 \quad . \qquad (A3.6)$$

Relativistic electrons in high magnetic fields suffer large energy looses due to synchrotron emission.

A3.1.5. Bremsstrahlung

Bremsstrahlung consists in the deflection of a moving charge by the (electric) field of another charge, generally an atomic nucleus at rest. This process can also be described as the scattering of particles by virtual photons associated to the electric field of the nucleus. The cross section for a particle with charge e and energy γmc^2 in the non relativistic regime (defined by $\gamma << \alpha^{-1}\ Z^{-1/3}$) to produce a photon of energy hν in the field of a nucleus of charge Ze is (Stecker, 1974):

$$\sigma_b = (4\alpha Z^2/\pi)\ \sigma_T\ Ln(2\gamma - 1/3)\ (\gamma mc^2/h\nu) \quad ; \qquad (A3.7)$$

for ultrarelativistic particles, $\gamma \gg \alpha^{-1}Z^{-1/3}$, the screening of the nucleus by electron gives the expression:

$$\sigma_b = (4\alpha Z^2/\pi)\,\sigma_T\,\mathrm{Ln}(183\cdot Z^{-1/3} + 1/18)\,(\gamma mc^2/h\nu) \quad , \quad (A3.8)$$

where α is the fine structure constant. The dependence of these cross sections with γ is practically linear which makes more useful the description of this absorption mechanism in terms of a radiation length X and the mean mass of target atoms M:

$$\sigma_b \approx (M/X)\cdot(\gamma mc^2/h\nu) \quad ,$$
$$X^{-1} = 4\alpha Z^2\,(e^2/mc^2)^2\,N_A\,A^{-1}\,\mathrm{Ln}(183Z^{-1/3}) \quad , \quad (A3.9)$$

where A is the mass number and $N_A \approx 6.022 \times 10^{23}$ mole^{-1} is the Avogadro number; $X \approx 62.8$ g.cm^{-2} in hydrogen and 38.6 g.cm^{-2} in nitrogen (Lang 1986). Bremsstrahlung and synchrotron are usually negligible compared to inverse compton scattering in relation to the production of high energy γ-rays. On the other hand bremsstrahlung is, together with pair production, the basic process involved in the electromagnetic air shower cascades.

A3.1.6 The decay of neutral pions

High energy particles colliding with matter produce secondary particles of short lifetime. The most relevant for the production of high energy γ-rays is the π^o (for other secondary processes see Stecker 1970,1973) with a mean life of 0.84×10^{-16} s. Observed reactions (with their relative recurrences) are:

$$\pi^{o} \longrightarrow \begin{cases} 2\gamma & (0.9884) \ , \\ \gamma + e^{+} + e^{-} & (0.0116) \ , \\ 2e^{+} + 2\,e^{-} & (3.47 \times 10^{-5}) \ , \\ 3\gamma & (< 5 \times 10^{-6}) \ . \end{cases} \qquad (A3.10)$$

As the rest mass of the neutral pion is 134.97 MeV its decay occurs before its has travelled more than one or two centimetres, even at TeV energies, and the reaction can be regarded as instantaneous. π^{o} are produced in proton - proton interactions like $p + p \longrightarrow p + p + \pi^{o}$ (section A3.3), for which the threshold kinetic energy E_{th} for the production of a particle of mass m given by:

$$E_{th} = 2mc^{2} \ (1 + m/4M_{p}) \qquad ; \qquad (A3.11)$$

therefore the production of a neutral pion (mass 135 MeV) at rest requires a minimum kinetic energy of 280 MeV. γ-rays produced by the π^{o} decay have an energy of 67.5 MeV in the rest frame of the pion, but pions are seldom produced at rest. The energy of the gamma rays seen by an external observer is given by the Doppler relation:

$$E = h\nu \cdot \gamma \ (1 \pm \beta \cos\theta) \qquad , \qquad (A3.12)$$

where θ is the angle between the γ-ray and the axis of the transformation in the pion rest frame (β is the relative speed between both frames).

A3.2. ABSORPTION PROCESSES

A3.2.1. Direct Interaction with Matter

For photon energies above a few MeV the interaction of γ-rays with matter is negligible. In the specific example of Compton scattering (section A3.1.3), $e^- + \gamma \longrightarrow e^- + \gamma$, for TeV photons the Klein-Nishima expression (A3.3) has to be generally used as $\gamma h\nu \gg mc^2$. For very high energy photons the asymptotic expression is:

$$\sigma \approx \frac{3\sigma_T}{8x}\left[\frac{1}{2} + \mathrm{Ln}(2x)\right] \quad , \qquad (A3.14)$$

which for 250 GeV photons ($x \approx 5 \times 10^5$) gives a cross section of the order 10^{-30} cm^2, thus negligible.

A3.2.2. Interaction with Radiation: Pair Production

For energies above a few MeV pair production $\gamma+\gamma \longrightarrow e^-+e^+$, becomes the dominant process for photon absorption. Isolated photons cannot produce particle pairs by themselves and conserve energy momentum, as it would require $\gamma_1 + \gamma_2 = \gamma_1\beta_1 \cdot x + \gamma_2\beta_2 \cdot x$ where x is the direction of the photon and (γ_i, β_i) the Lorentz factor and velocity of the i-th particle. Interaction with other photons allows the conservation of both quantities.

(i) direct interaction with another photon,

In the centre of momentum system, particle and antiparticle have the same energy γmc^2; using the invariance of the four momentum:

$$(\gamma mc^2)^2 = E\ h\nu\ (1-\cos\theta)/2 \quad , \qquad (A3.15)$$

where E and $h\nu$ are the respective energies of the high energy γ-ray and low energy photon with θ being the angle of incidence. The minimum energy $h\nu$ required to produce a pair corresponds to a head-on collision ($\cos\theta = -1$) for which $h\nu_{min} = (mc^2)^2/E$. A well known example is the attenuation of UHE radiation on intergalactic distances by the 2.7° K (0.232 meV) microwave background for which $(mc^2)^2/h\nu \approx 1.12 \times 10^{15}$ eV. As the background actually corresponds to a Planck distribution photons with higher "temperatures" are present and γ-rays with energies below 1 PeV are absorbed.

The pair production cross section, also related to the Thompson cross section (A3.1), is given by (Lang 1986):

$$\sigma = (\pi/2)\ (e^2/mc^2)^2\ f(\beta)$$

$$f(\beta) = (1-\beta^2)\left[\ 2\beta(\beta^2-2) + (3-\beta^4)\ \mathrm{Ln}\{(1+\beta)/(1-\beta)\}\right] \quad , \qquad (A3.16)$$

where βc is the speed of the e^- (and e^+) in the rest frame:

$$\beta^2 = 1 - m^2c^4\ /\ Eh\nu \quad . \qquad (A3.17)$$

The adimensional function $f(\beta)$, shown in figure A3.1, has its maximun value $f(\beta) \approx 3/2$ at $\beta \approx 0.657$, when $Ehv \approx 1.84\ (mc^2)^2$. For high energies the approximation $f(1-\varepsilon/2) \approx 4\varepsilon Ln(2/\varepsilon)$ holds, while for small β, $f(\beta) \approx 2\beta$. Note that (A3.17) has to actually include the incidence angle θ, through the factor $(1-\cos\theta)$.

(ii) Pair production in electrostatic field (atomic nuclei):

This interaction, $\gamma + CF \longrightarrow e^+ + e^- + CF$, is equivalent to pair production with a virtual photon of the charged field. As in the case of bremsstrahlung two cases are distinguished (Lang 1986):

- when screening of the nucleus by electrons is negligible $(1 \leq E/mc^2 \ll \alpha^{-1}Z^{-1/3})$:

$$\sigma = 4\alpha Z^2\ (e^2/mc^2)^2 \left[\frac{7}{9} Ln(2E/mc^2) - \frac{109}{54} \right] \quad ; \quad (A3.18)$$

when screening has to be taken into account the cross section is independent on the energy E of the photon $(E/mc^2 \gg \alpha^{-1}Z^{-1/3})$:

$$\sigma = 4\alpha Z^2\ (e^2/mc^2)^2 \left[\frac{7}{9} Ln(191\ Z^{-1/3}) - \frac{1}{54} \right] \quad . \quad (A3.19)$$

The introduction of the fine structure constant $\alpha \approx 1/137$ indicates that the cross section for this process is small. Pair production can also occur in the electrostatic field of an electron. For $E \geq 200$ MeV this process has an approximately constant cross section of 1.8×10^{-26} cm^2 (Stecker, 1974).

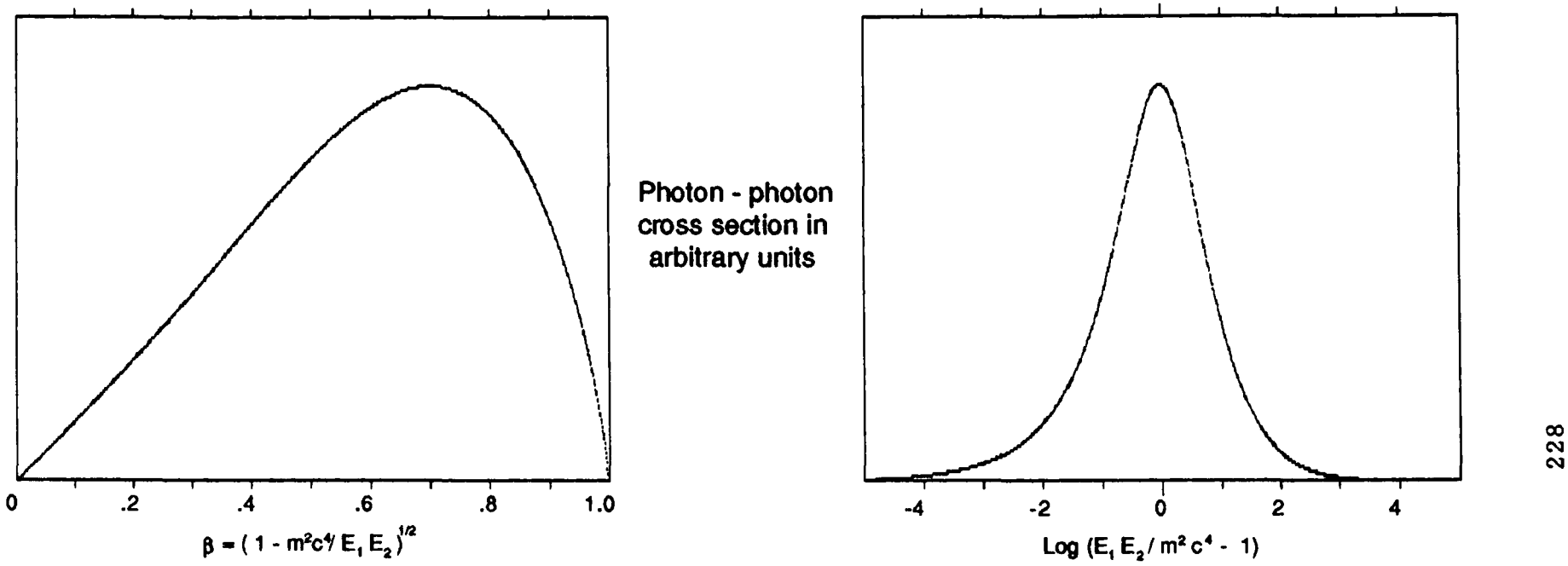

Figure A3.1

Photon - photon cross section in arbitrary units:

(a) as a function of $\beta = (1 - m^2c^4/ E_1 E_2)^{1/2}$

(b) as a function of $\text{Log} (E_1 E_2 / m^2 c^4 - 1)$

E is the energy of the (respective) photon

m is the mass of the particle to be created.

(iii) pair production in a Magnetic field:

This process, represented by $\gamma + BF \longrightarrow e^+ + e^- + BF$, is equivalent to pair production by a virtual quanta of the field. As in the previous case a factor α appears and therefore this process is important only for high magnetic fields, above or of the order of 10^8 G. Young neutron stars have frequently a superficial field of 10^{12} G and this process becomes important within 2×10^7 cm $\approx$ 20 R* of their surface.

In an attempt to estimate the absorption coeficient k (the inverse of the mean free path) for this process, the energy density of the magnetic field B is described as a photon bath:

$$u = B^2/8\pi = \int n(h\nu)\, h\nu\, d(h\nu) \quad , \qquad (A3.20)$$

where $n(h\nu)$ - in units of $erg^{-1} \cdot cm^{-3}$ - is the density of virtual photons per volume and energy (or frequency) $h\nu$. The absorption coefficient for a γ-ray of energy E is given by:

$$k(E) \equiv \int_0^\infty n(h\nu)\, \sigma(E,h\nu)\, d(h\nu) \quad . \qquad (A3.21)$$

Using the pair production cross section (A3.16) and a Bose Einstein distribution with typical frequency (energy) $\nu_c = eB/mc$ for the virtual photons gives:

$$n(\nu) = \frac{1}{8\pi\eta} \left[\frac{mc}{eh} \right]^2 \frac{1}{\exp(\nu/\nu_c) - 1} \quad , \qquad (A3.22)$$

with the numerical factor η deduced from (A3.20):

$$\eta = \int_0^{\infty} \frac{x\,dx}{e^x - 1} = \sum_{j=1}^{\infty} 1/j^2 \approx 1.644934 \quad .$$

Following Erber (1966), suitable dimension are introduced by using $B_c = m^2c^3/eh$, the critical magnetic field, $\lambda_c = h/mc$, the Compton wavelength, and $\chi \equiv 1/4\pi\ (E/mc^2)(B/B_c)$, dimensionless variable of the form {field*energy} (note the use of rationalized units in Erbers paper):

$$k \approx (\alpha/2\lambda_c)\ (B/Bc)\ T(\chi) \quad , \qquad (A3.23)$$

where the adimensional function $T(\chi)$ derived is:

$$T(\chi) = \frac{1}{16\pi\eta\chi} \int_0^1 \frac{(3-\beta^4)\mathrm{Ln}\{(1+\beta)/(1-\beta)\} - 2\beta(2-\beta^2)}{\exp(1/4\pi\chi(1-\beta^2))-1}\,\beta\,d\beta \quad .$$

The actual form of this function $T(\chi)$ was deduced with more rigour by Erber (1966); it is also an integral expression which can be well approximated by the analytic function:

$$T(\chi) \approx 0.46\ \chi^{-1}\ K^2_{1/3}(2/3\chi) \quad , \qquad (A3.24)$$

where $K_{1/3}$ is the modified Bessel function of order 1/3. When $2/3\chi$ is small compared to the order of the modified Bessel function, i.e $\chi \gg 2$, then $K_n(x) \approx \Gamma(n)/2\ (x/2)^{-n}$ while for large arguments $K_n(x)$ decays as $x^{-1/2}\exp(-x)$. Most of the times

energies above 1 TeV $\approx 10^6$ mc^2 will be considered and large magnetic fields, $B_{\perp} \geq 10^6$ G, and therefore $\chi \gg 1$. A plot indicating the mean free path k for different energies using (A3.23) and (A3.24) appears in figure A3.2.

A3.3. NEUTRAL PIONS FROM HIGH ENERGY NUCLEON INTERACTIONS

The decay of π^o into photons -section A3.1.7- is thought to be the most important process for the production of γ-rays from high energy nucleons, mostly protons (and quite probably neutrons). Interactions between energetic protons have different outcomes but they result in the emission of neutral and/or charged pions:

$$p + p \longrightarrow \begin{cases} p + p + n_1 (\pi^+ + \pi^-) + n_2 \pi^o \\ p + n + (n_3+1) \pi^+ + n_3 \pi^- + n_4 \pi^o \\ n + n + (n_5+2) \pi^+ + n_5 \pi^- + n_6 \pi^o \\ D + (n_7+1) \pi^+ + n_7 \pi^- + n_8 \pi^o \end{cases} ,$$

where n_1 to n_8 denote integer numbers (energy dependent). While π^o decay into gamma rays charged pions produce muons and neutrinos. Experimental results indicate that the cross section for production of pions by proton with energies E above 2 Gev is approximately constant, $\sigma(E) \approx 2.7 \times 10^{-26}$ cm^2 , with the multiplicity, or number of pions produced, given by (Lang 1986):

$$m_+ = m_- = 2 \, (E/2 \text{ GeV})^{0.25}$$
$$m_o = 0.5 \, m_+ \quad . \qquad \text{(A3.25)}$$

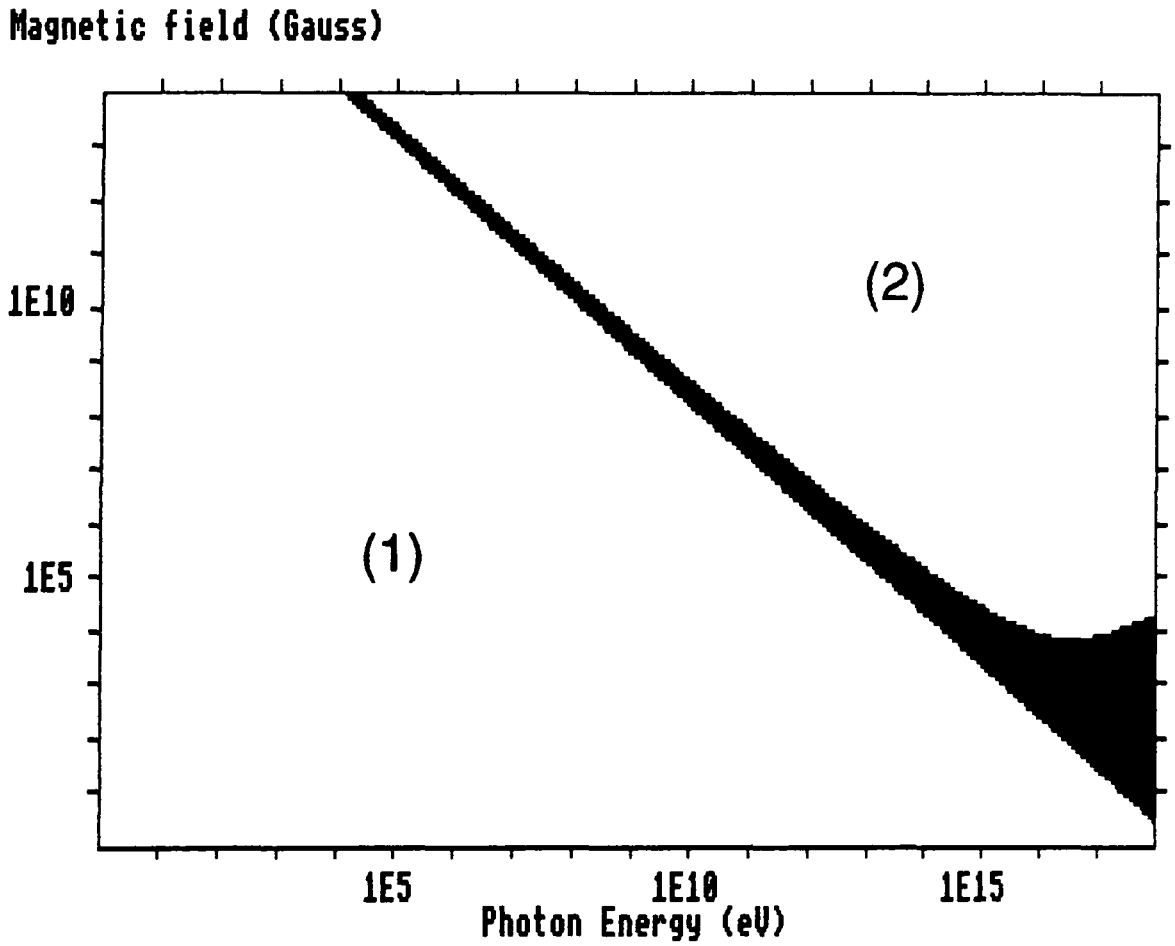

Figure A3.2

Absorption of photons by pair production in magnetic fields
In region (1) photons are not absorbed
In region (2) photons are absorbed
In the black region the m.f.p. for a photon ranges from 10^2 cm to 10^{16}cm and absorption depends on the size of the system considered

The cross section is equivalent to an absorption coefficient in hydrogen of $m_p/\sigma \approx 61.5$ g.cm^{-2}.

A3.4 THE ABSORPTION OF TeV γ-RAYS BY DISC PHOTONS: DETAILS

The integral to calculate gives the expected number of pair interactions N_{enc} a γ-ray of energy E is expected to undergo:

$$N_{enc} = \int_0^{\infty} \int_0^{\infty} \sigma(E;h\nu)\ (4\pi I(\nu)/h\nu)\ d\nu\ dt \qquad ; \text{(IV.25)}$$

in other words the fraction of the γ-rays produced that will escape from the system is $\exp(-N_{enc})$. In the case of a geometrically thin and optically thick accretion disc, each surface element emits as a black body with temperature T(R):

$$I(\nu,T) = 2h\nu^3/c^2\ \{\exp(h\nu/kT)-1\}^{-1} \quad , \quad \text{erg.cm}^{-2}.\text{s}^{-1}.\text{Hz}^{-1}.\text{sr}^{-1}$$

$$T(R) = T_* \ (R_*/R)^{3/4}\ \{1 - (R_*/R)^{1/2}\}^{1/4} \qquad \text{(A3.26)}$$

$$T_* = (3G\dot{M}M/8\pi\sigma_s R_*^3)^{1/4} \ .$$

$R_c = t \sin i$ and $T(R) = T_* \ (R_*/R)^{3/4}$ (good approximation for $R \gg R_*$) can be used to change variables. Noticing that the angle of incidence for γ-rays and disc photons (assumed to propagate following the normal to the disc plane) is equal to the inclination of the object with respect to the observer, $\theta = i$, (the γ-ray moves towards the observer) and using the cross

section for pair production given by (A3.16) and (A3.17):

$$N_{enc} = \frac{A}{\sin i\ (1-\cos i)^{5/3}} \int_{x_{min}}^{x_{max}} x^{1/3} \int_0^1 \frac{g(\beta)}{\exp\{x/(1-\beta^2)\} - 1}\, d\beta\, dx \qquad (A3.27)$$

where $g(\beta) = \beta\, f(\beta) / (1-\beta^2)^4$, and the integration variables are:

$$\beta^2 = 1 - \frac{m^2c^4}{E\ h\nu\ (1-\cos i)}\ , \quad x = \frac{m^2c^4\ (R/R_*)^{3/4}}{E\ kT_*\ (1-\cos i)}\ , \qquad (A3.28$$

$$x \approx 1.19 \times 10^{-4}\ E_{Tev}^{-1}\ L_{38}^{-1/4}\ R_6^{1/2}\ (R/R_*)^{3/4}\ (1-\cos i)^{-1}\ .$$

The constant A introduced in (A3.27) is expressed in terms of the Compton wavelength $\lambda_c = h/mc \approx 2.4 \times 10^{-10}$ cm and the fine structure constant $\alpha \approx 1/137$, together with the black body temperature of the disc $T_*^4 = 3L/4\pi\sigma_b R_*^2$ to get:

$$A = \frac{4\alpha^2}{\pi^2} \left[\frac{E}{mc^2}\right]^{-5/3} \left[\frac{5\ LR_*}{3\ mc^3}\right]^{1/3}\ , \qquad (A3.29)$$

$$A \approx 1.3348 \times 10^{-2}\ E_{Tev}^{-5/3}\ L_{38}^{1/3}\ R_6^{1/3}$$

N_{enc} is relatively easy to compute taking advantage of the finite limits on β to define the function:

$$\Phi(x) = \int_0^1 \frac{g(\beta)}{\exp\{x/(1-\beta^2)\} - 1}\, d\beta\ , \qquad (A3.30)$$

which is well fitted by a power law, $\Phi(x) \approx 8.300\ x^{-2.074}$, for $x \leq 10^{-2}$, and decays rapidly afterwards (mainly for $x \geq 0.1$) due to the exponential factor. Typical outer radius for accretion discs are $\geq 10^{11}$ cm implying x_{max} of the order of 1 or 0.1 and its contribution can be neglected. The final expression depends practically only on x_{min} and with the definition:

$$H(x) = \int_x^{\infty} u^{1/3}\ \Phi(u)\ du \quad , \qquad (A3.31)$$

the final solution can be written as:

$$x_{min} \approx 1.19 \times 10^{-4}\ E_{TeV}^{-1}\ L_{38}^{-1/4}\ R_6^{1/2}\ (R_{min}/R_{\odot})^{3/4}\ (1-\cos i)^{-1}$$

$$N_{enc} \approx 0.01333\ E_{TeV}^{-5/3}\ L_{38}^{1/3}\ R_6^{1/3}\ \frac{H(x_{min})}{\sin i\ (1-\cos i)^{5/3}}$$

$$(A3.32) \quad .$$

H(x) can (as one would expect) also be approximated by a power law, $H(x) \approx 9.798\ x^{-0.75}$, in the same range ($x \leq 10^{-2}$) and decays rapidly to zero (cutoff) for $x \geq 1$. Setting the condition $N_{enc} \leq 1$ for the escape of high energy γ-rays a restriction on the energy, disc luminosity, minimum radius R_{min} and angle α at which γ-rays can be emitted (using 0.8 for the power law index) is obtained:

$$N_{enc} \leq 114.6\ \frac{E_{tev}^{-11/12}\,(R_{min}/R_{\odot})^{-9/16}\,L_{38}^{25/48}\,R_6^{-1/24}}{\sin i\ \ (1-\cos i)^{11/12}} \quad .$$

$$(A3.33)$$

N_{enc} is in fact overestimated as the actual T(R) given by (A3.26) is below the value used by a factor $(1-(R/R_*)^{1/2})^{1/4}$ which is noticeable only for R/R_* close to one. Although the use of this extra term complicates sensibly the substitutions, it might be worth to include it in future computations, to see if it does make any significant difference in the final result.

APPENDIX IV

ACCRETION DISCS

A4.1 EQUATIONS AND ALPHA DISCS

Accretion like most of the astrophysical processes where matter flows are involved (winds, stellar structure, interstellar medium, ...) is described with the hydrodynamic equations. The equations that are used to construct disc models are:

(1) Conservation of Mass or Continuity equation:

$$\partial\rho/\partial t + \nabla\cdot(\rho v) = 0 \quad ,$$

(2) Conservation of Momemtum or Euler equation:

$$\rho\ \partial v/\partial t + \rho\ (v\cdot\nabla)v = -\nabla P + f \ ,$$

The forces included are gravity (from a point mass as self gravity of disc is negligible) and a dissipative force which is necessary in order to have accretion from a rotating disc:

$$f = \rho\ g + \rho\ \Gamma$$

where $g = -\bar{r}\ GM/r^2$ and $\Gamma = \Gamma\ \bar{\varphi}$. If Γ is modelled as a viscous force (torque) then:

$$\Gamma = \frac{1}{\rho}\ \frac{1}{r^3}\ \frac{\partial}{\partial r}\ (r^3\ \pi_{13})$$

the component 13 (i.e. $r\varphi$) of the stress tensor π given by:

$$\pi_{13} = \rho\nu\, r \frac{\partial}{\partial r}\left[\frac{v\varphi}{r}\right]$$

This defines a viscosity coefficient ν associated to the dissipative process.

(3) Conservation of energy:

$$\partial\{\rho(\varepsilon+v^2/2)\}/\partial t + \nabla\cdot\{\rho v(\varepsilon+v^2/2+P/\rho)\} = f\cdot v - \nabla\cdot F_r - \nabla\cdot q - \nabla\cdot F_c$$

(4) the equation of state (including radiation pressure):

$$P = \rho kT/\mu m_h + 4\sigma T^4/3c = \rho c_s^2 = 2\varepsilon/3\rho \quad ;$$

(5) Energy dissipation is assumed to occur by radiative looses only (not by conduction or convection) and the disc is optically thick (local thermal equilibrium):

$$F_{rad} = -\frac{4\,\nabla(\sigma T^4)}{3\rho\kappa}$$

(6) a description of the opacity or scattering processes; physical conditions expected bremsstrahlung + Compton scattering:

$$\kappa = \kappa_T + (6.6 \times 10^{22}\ g^{-1}cm^2)\ \rho T^{-7/2}$$

Six equations are given for seven unknowns $\{P,\rho,T,v,F,\kappa,\nu\}$; turbulence is likely to be the mechanism for energy dissipation and from physical arguments one expects $\nu \leq hc_s$. The equation that permits to close this system was introduced by Shakura & Sunyaev (1973) as $\nu = \alpha\, h\, c_s$, where α is unknown but ≤ 1. A self consistent solution is found for a steady state ($\partial/\partial t=0$), with

axial symmetry ($\partial/\partial\varphi=0$), and assuming a thin (i.e. Keplerian) disc. The differential equations can be simplified to a system of algebraic equations soluble analytically. Suitable units are introduced by the following notation: $\dot{M}_{17}$ is the accretion rate in 10^{17} g.s^{-1}, M_1 is the mass of the accreting star in solar units and r_x is the distance in 10^x cm. For a neutron star (radius $\approx$ 10 km) the critical luminosity and accretion rate are:

$$\dot{M}_{crit} = 9.5 \times 10^{17}\ \mathrm{g.s^{-1}}\ r_6$$

$$L_{38} = 0.133\ \dot{M}_{17}\ M_1\ r_6^{-1} \quad .$$

Note that the factor $f \equiv 1 - (r_*/r)^{1/2}$ has been omitted and $\dot{M}$ has to be multiplied by it everywhere except in v_r. The parameters are given for three different regions depending on opacity and pressure.

OUTER ZONE: opacity = bremsstrahlung; pressure = thermal. Solution in terms of r_9 (where $f \approx 0.97$):

h/r	$= 1.35 \times 10^{-2}$		$\alpha^{-1/10}$	$\dot{M}_{17}^{3/20}$	$M_1^{-3/8}$	$r_9^{1/8}$
ρ	$= 1.19 \times 10^{-5}$	g cm^{-3}	$\alpha^{-7/10}$	$\dot{M}_{17}^{11/20}$	$M_1^{5/8}$	$r_9^{-15/8}$
Σ	$= 1.60 \times 10^{2}$	g cm^{-2}	$\alpha^{-4/5}$	$\dot{M}_{17}^{7/10}$	$M_1^{1/4}$	$r_9^{-3/4}$
T_c	$= 1.80 \times 10^{5}$	°K	$\alpha^{-1/5}$	$\dot{M}_{17}^{3/10}$	$M_1^{1/4}$	$r_9^{-3/4}$
v_φ	$= 3.65 \times 10^{8}$	cm s^{-1}			$M_1^{1/2}$	$r_9^{-1/2}$
c_s	$= 4.92 \times 10^{6}$	cm s^{-1}	$\alpha^{-1/10}$	$\dot{M}_{17}^{3/20}$	$M_1^{1/8}$	$r_9^{-3/8}$
v_r	$=-9.94 \times 10^{4}$	cm s^{-1}	$\alpha^{4/5}$	$\dot{M}_{17}^{3/10}$	$M_1^{-1/4}$	$r_9^{-1/4}$

The boundary between the outer and middle zones is at:

$$r_{o-m} = 1.38 \times 10^{9}\ \mathrm{cm}\ \dot{M}_{17}^{2/3}\ M_1^{1/3}$$

MIDDLE ZONE: opacity = e^- scattering; pressure = thermal. Solution in terms of r_8 is (where $f \approx 0.9$):

h/r	$= 1.23 \times 10^{-2}$		$\alpha^{-1/10}$	$\dot{M}_{17}^{1/5}$	$M_1^{-7/20}$	$r_8^{1/20}$
ρ	$= 4.94 \times 10^{-4}$	g cm^{-3}	$\alpha^{-7/10}$	$\dot{M}_{17}^{2/5}$	$M_1^{11/20}$	$r_8^{-33/20}$
Σ	$= 6.07 \times 10^{2}$	g cm^{-2}	$\alpha^{-4/5}$	$\dot{M}_{17}^{3/5}$	$M_1^{1/5}$	$r_8^{-3/5}$
T_c	$= 1.50 \times 10^{6}$	°K	$\alpha^{-1/5}$	$\dot{M}_{17}^{2/5}$	$M_1^{3/10}$	$r_8^{-9/10}$
$v\varphi$	$= 1.16 \times 10^{9}$	cm s^{-1}			$M_1^{1/2}$	$r_8^{-1/2}$
c_s	$= 1.42 \times 10^{7}$	cm s^{-1}	$\alpha^{-1/10}$	$\dot{M}_{17}^{1/5}$	$M_1^{3/20}$	$r_8^{-9/20}$
v_r	$=-2.62 \times 10^{5}$	cm s^{-1}	$\alpha^{4/5}$	$\dot{M}_{17}^{2/5}$	$M_1^{-1/5}$	$r_8^{-3/5}$

The boundary between the middle and inner zones is at:

$$r_{m-i} = 1.42 \times 10^{7} \text{ cm } \alpha^{2/21} \dot{M}_{17}^{16/21} M_1^{1/3}$$

INNER ZONE: opacity = e^- scattering; pressure = radiation. Solution is in terms of r_7 (where $f \approx 0.68$):

h	$= 1.59 \times 10^{5}$	cm		$\dot{M}_{17}$		
ρ	$= 7.19 \times 10^{-3}$	g cm^{-3}	α^{-1}	$\dot{M}_{17}^{-2}$	$M_1^{-1/2}$	$r_7^{3/2}$
Σ	$= 1.15 \times 10^{3}$	g cm^{-2}	α^{-1}	$\dot{M}_{17}^{-1}$	$M_1^{-1/2}$	$r_7^{3/2}$
T_c	$= 7.43 \times 10^{6}$	°K	$\alpha^{-1/4}$		$M_1^{1/8}$	$r_7^{-3/8}$
$v\varphi$	$= 3.66 \times 10^{9}$	cm s^{-1}			$M_1^{1/2}$	$r_7^{-1/2}$
c_s	$= 5.82 \times 10^{7}$	cm s^{-1}		$\dot{M}_{17}$	$M_1^{1/2}$	$r_7^{-3/2}$
v_r	$=-1.39 \times 10^{6}$	cm s^{-1}	α	$\dot{M}_{17}^{2}$	$M_1^{1/2}$	$r_7^{-5/2}$

It is relevant to outline that α is most probably dependent on the physical conditions of the disc (like density and temperature), and only a self similar dissipative process

produces $\alpha \approx$ constant. The success of the model resides in that α is (in principle) less or equal to one. As the solution does not depend strongly on α, the values are expected to be representative of the physical conditions prevailing in the disc, even if the actual mechanism for dissipating angular momentum remains unknown. The model is self consistent although in some regions it is unstable to density or thermal perturbations.

A4.2. ACCRETION ONTO MAGNETIC STARS & RELATED QUANTITIES

The effects of magnetic fields on the motion of the plasma have been ignored. When dominant magnetic torques force the fluid to corotate with the field lines whilst following a free fall motion along them. The case of disc accretion onto neutron stars was developed in detail by Gosh, Lamb & Pethick (1977) and Gosh & Lamb (1979a, 1979b) who reproduced the empirical relation between luminosity, rotational period and its derivative found in pulsating X-ray binaries, $dP/dt = f(PL^{3/7})$. The Alfven radius a is defined by the equilibrium between magnetic and kinetic pressures:

$$\frac{1}{2}\,\rho(a)\,v^2(a) = \frac{B^2(a)}{8\pi} \quad ;$$

in the case of spherically symmetric accretion and assuming a dipolar magnetic field $B \sim r^{-3}$, the Alfven radius is given by:

$$a_e = (2GM)^{-1/7}\,\dot{M}^{-2/7}\,\mu^{4/7}$$

$$a_e \approx 3.70 \times 10^6 \text{ cm } \mu_{27}^{4/7} L_{38}^{-2/7} M_{1.44}^{1/7} R_6^{-2/7}$$

$$\approx 1.92 \times 10^8 \text{ cm } \mu_{30}^{4/7} L_{38}^{-2/7} M_{1.44}^{1/7} R_6^{-2/7} .$$

As the density of an accretion disc can be written as:

$$\rho = \frac{\dot{M}}{3\pi\alpha\ (h/r)^3\ r^2 v_\varphi} = \frac{\dot{M}}{3\pi\alpha\ (h/r)^3\ (GM)^{1/2}}\ r^{-3/2} ,$$

one finds for a $\alpha^2 h/r \approx 10^{-2}$, $a_{disc}/a_e = (36\alpha^2\ h/r)^{4/7} \approx 0.56$.

Other useful distances related to accretion are:

- the Corotation radius: where $\Omega_k = (GM/r^3)^{1/2} = \Omega_*$,

$$r_{co} \approx 1.63 \times 10^7 \text{ cm } (P/3ms)^{2/3} M_{1.44}^{1/3}$$

$$\approx 1.69 \times 10^8 \text{ cm } (P/1s)^{2/3} M_{1.44}^{1/3} .$$

Most of the X-ray pulsars have reached an equilibrium state in the exchange of angular momentum between the disc and the neutron star, and Alfven radius ≈ corotation radius (accretion torques are the cause of changes in angular momentum of the neutron star).

- Radius of Light Cylinder: where $r\Omega_* = c$,

$$r_{LC} \approx 10^8 \text{ cm } (P/3ms) \approx 3 \times 10^{10} \text{ cm } (P/1s)$$

- Larmor radius: defined by $r = \omega_b/c = pc/eB$,

$$r_L \approx 300 \text{ cm } B_9^{-1} p_{14} \approx 0.3 \text{ cm } B_{12}^{-1} p_{14}$$

- Escape radius: defined by $r_e \approx E/eB(r_e) = (E/eB_*)\ (r_e/r_*)^3$,

$$r_e \approx 5.47 \times 10^7 \text{ cm } B_9^{1/2} p_{14}^{-1/2} R_6^{3/2}$$

$$\approx 1.73 \times 10^9 \text{ cm } B_{12}^{1/2} p_{14}^{-1/2} R_6^{3/2} .$$

REFERENCES

Achterberg, A., *Nature*, **342**, 51 (1989)

Akerlof, C., DiMarco, J., Levy, H., MacCallum, C., Meyer, D., Radusewicz, P., Tschirhart, R., Yama, Z., *"Proc. 21st Int. Cosmic Ray Conf."*, ed. Protheroe, R.J., p. 135, vol. 4, Adelaide, Australia, Jan 6-19, 1990

Alpar, A., & Shaham, J., *Nature*, **316**, 239 (1985)

Anzer, U, Borner, G., *Astron. & Ap.*, **122**, 73 (1983)

Arnett, W.D., Bahcall, J.N., Kishner, R.P., Woosley, R.P., *Ann. Rev. Astron. Ap.*, **27**, 629 (1989)

Ashworth, M., & Lyne, A.G., *Parallel Computing*, **6**, 217-225 (1987)

Baltrusaitis, R.M. *et al.*, *Nucl. Instr. & Meth.*, **A240**, 410 (1985)

Basko, M.M., & Sunyaev, R.A., *M.N.R.A.S.*, **175**, 395 (1976)

Battistoni, G., *et al.*, *Nucl. Instr. & Meth.*, **A245**, 277 (1986)

Bell, A.R., *M.N.R.A.S.*, **182**, 443 (1978)

Bertsch, D.L., Fitchtel, C.E., Trombka, J.I., *"Instrumentation for Gamma-Ray Astronomy"*, Preprint to appear in *Space Science Rev.* (1988)

Birnklow, A., *"Searches for Millisecond Pulsars"*, Ph D. Thesis, University of Manchester (1989)

Blanford, R.D., & Ostriker, J.P., *Ap. J.*, **221**, L29 (1978)

Bloomfield, P., *"Fourier Analysis of Time Series: An Introduction"*, ed. John Wiley & Sons (1976)

Bond, I.A., *et al.*, *Phys. Rev.*, **61**, 2292 (1988)

Bonnet-Bidaud, J.M., & Chardin, G., *Phys. Rep.*, **170**, 325 (1988)

Bowen, T., & Halverson, P.G., *Nucl. Phys. B (Proc. Suppl.)*, **14A**, 340 (1990)

Brazier, K.T.S., Ph. D. Thesis, University of Durham, in preparation (1991)

Brazier, K.T.S., Carramiñana, A., Chadwick, P.M., Currel, T.R., Dipper, N.A., Lincoln, E.W., Mannings, V.G., McComb, T.J.L.,

Orford, K.J., Rayner, S.M. & Turver, K.E., *Experimental Astron.*, 1, 77 (1989a)

Brazier, K.T.S., Carramiñana, A., Chadwick, P.M., Dipper, N.A., Lincoln, E.W., McComb, T.J.L., Orford, K.J., Rayner, S.M., Turver, K.E., *"Proc. 23rd ESLAB Symp.: X-Ray Binaries"*, ed. Hunt, J., & Battrick, B., p. 311, Bologna, Italy, Sept. 13-20, 1989b

Brazier, K.T.S., Carramiñana, A., Chadwick, P.M., Dipper, N.A., Lincoln, E.W., McComb, T.J.L., Orford, K.J., Rayner, S.M., Turver, K.E., *"Proc. 23rd ESLAB Symp.: X-Ray Binaries"*, ed. Hunt, J., & Battrick, B., p. 325, Bologna, Italy, Sept. 13-20, 1989c

Brazier, K.T.S., Carramiñana, A., Chadwick, P.M., Dipper, N.A., Lincoln, E.W., Mackie, P.C., Mannings, V.G, McComb, T.J.L., Orford, K.J., Rayner, S.M., Turver, J.H. & Turver, K.E., *Ap. J.*, 350, 745 (1990a)

Brazier, K.T.S, Carramiñana, A., Chadwick, P.M., Dipper, N.A. Lincoln, E.W., Mannings, V.G, McComb, T.J.L., Orford, K.J., Rayner, S.M, Turver K.E., *Astron. & Ap.*, 232, 383 (1990b)

Browing, R., & Turver, K.E., *Nuovo Cimento*, 38A, 223 (1977)

Cantó, J., Tenorio-Tagle, G., Rozyczka, M., *Astron. & Ap.*, 192, 287 (1988)

Cassiday, G.L., *et al, Phys. Rev. Lett.*, 62, 383 (1989)

Cawley, M.F., Fegan, D.J., Harris, K., Hillas, A.M., Kwok, P.W., Lamb, R.C., Lang, D., Lewis, D.A., Macomb, D., Reynolds, P.T., Schmid, D.J., Vacanti, G., Weekes, T.C., *Experimental. Astron.*, 3, 173 (1990)

Cawley, M.F., Fegan, D.J., Hillas, A.M., Kwok, P.W., Lamb, R.C., Lang, M.J., Lewis, D.A., Macomb, D., Reynolds, P.T., Vacanti, G., Weekes, T.C., *Astron. & Ap.*, Accepted for publication (1991)

Cerenkov, P.A., *Dokl. Akad. Nauk.*, 2, 451 (1934)

Chadwick, P.M., *"Very High Energy Gamma-Rays from Radio and X-Ray Pulsars"*, Ph.D. Thesis, University of Durham (1987)

Chadwick, P.M., Dipper, N., Dowthwaite, J.C, Gibson, A.I., Harrison, A.B., Kirkman, I.W., Lotts, A.P., Macrae, J.H., McComb, T.J.L., Orford, K.J., Turver, K.E., Walmsley M., *Nature*, 318, 642 (1985)

Chadwick, P.M., Dipper, N.A., Dowthwaite, J.C., McComb, T.J.L., Orford, K.J., Turver, K.E., *"Proc. of the NATO workshop on Very High Energy Gamma Ray Astronomy"*, ed. Turver, K.E., p. 115, Durham, U.K., Aug. 11-15, 1986 (1987)

Chanmungam, G., & Brecher, K., *Nature*, 313, 767 (1985)

Cheng, K.S., & Ruderman, M., *Ap.J.*, 337, L77 (1989)

Cooley, J.W., & Tuckey, J.W., *Math. Comput.*, 19, 297 (1965)

Cooley, J.W., Lewis, P.A.W. , & Welch, P.D., *I.I.I.E. Trans. Audio Electroacoust.*, AU-15, 76 (1967)

Crampton, D., Cowley, A.P., Hutchings, J.B., Kaat, C., *Ap.J.*, 207, 907 (1976)

Davidson, K., *Nat. Phys. Sci.*, 245, 1 (1973)

de Jager, O.C., Swanepoel, J.W.H., Raubenheimer, B.C., *Astron. & Ap.*, 221, 180 (1989)

de Jager, H.I., de Jager, O.C., North, A.R., Raubenheimer, B.C., van der Walt, D.J., van Urk G., *S. Afr. J. Phys.*, 9, 107 (1986)

Dipper, N.A., *"X-Ray Astronomy"*, Ph. D. Thesis, University of Southampton (1980)

Drury, L.O'C., "Shock Acceleration of Cosmic Rays", talk given at the *7th Int. School of Cosmic Ray Astrop.*, Erice, Sicily, July 27 August 5, 1990

Eichler, D. & Vestrand, W.T., *Nature* 318, 345 (1985)

Erber, T., *Rev. Mod. Phys.*, 38, 626 (1966)

Fegan, D.J., Cawley, M.F., Gibbs, K., Gorham, P.W., Lamb, R.C, Porter, N.A., Reynolds, P.T., Stenger, V.J., Weekes, T.C., *"Proc. of NATO Advanced Research workshop on VHE Astronomy"*, ed. Turver, K.E., P. 111, Durham U.K., Aug. 11-15, 1986 (1987)

Fermi, E., *Phys. Rev.*, 75, 1169 (1949)

Fisher, R.A., *"Statistical Methods for Research Workers"*, 12th Edition, Ed. Oliver & Boyd, Edinburg (1954)

Frank, I.M., & Tamm, Ig., *Dokl. Akad. Nauk.*, 14, 109 (1937)

Galbraith, W. & Jelley, J.V., *Nature*, 171, 349 (1953)

Gentleman, W.M., & Sande, G., *Fall Joint Comput. Conf.*, AFIPS *Conf. Proc.*, 29, 563 (1966)

Ginzburg, V.L., *"Theoretical Physics and Astrophysics"*, Ed. Pergamon Press, (1979)

Good, I.J., *J. R. Stat Soc., Ser B.*, 20, 361-372 (1958)

Good, I.J., *I.I.I.E. Trans. Comput.* C-20, 310-317 (1971)

Gorham, P.W., *et al.*, *Ap.J.*, **309**, 114 (1986)

Gorham, P.W., & Learned, J.G., *Nature*, **323**, 422 (1986)

Gosh, P., Lamb, F.K., & Pethick, C.J., *Ap.J.*, **217**, 578 (1977)

Gosh, P., & Lamb, F.K., *Ap.J.*, **232**, 259 (1979a)

Gosh, P., & Lamb, F.K., *Ap.J.*, **234**, 296 (1979b)

Gottlieb, E.W., Wright, E.L., Liller, W., *Ap.J.*, **195**, L33 (1975)

Gregory, A.A., Patterson, J.R., Roberts, M.D., Smith, N.I., Thornton, G.J., *Astron. & Ap.*, **237**, L5 (1990a)

Gregory, A.A., Patterson, J.R., Roberts, M.D., Smith, N.I., Thornton, G.J., *"Proc. 21st Int. Cosmic Ray Conf."*, ed. Protheroe, R.J., p. 279, vol 2.,Adelaide, Australia, Jan. 6-19, 1990, (1990b)

Grindlay, J.E., *"Proc. Int. Workshop VHE Gamma Ray Astronomy"*, Ed. Ramana Murthy, P.V., & Weekes, T.C., p. 178, Ootacamund, India, Sept. 20-25, 1982

Harding, A., *"Proc. of Workshop on Physics and Experimental Techniques of High Energy Neutrinos and VHE and UHE Gamma-Ray Astronomy"*, ed. Yodh, G.B., & Wold, D.C., to be published, Little Rock, Arkansas, May 11-13, 1989

Harding, A., & Gaisser, T.K., *Ap.J.*, **358**, 561 (1990)

Hartman, R.C., Preprint to appear in *"Proc. of the Int. Worshop on High Resolution Gamma Ray Cosmology"*, Los Angeles, California, Nov. 2-5, 1988

Heaviside, O., *Electrical Papers*, **2**, 494 (1890)

Hillas, A.M., *Ann. Rev. Astron. Astrophys.*, **22**, 425 (1984a)

Hillas, A.M., *Nature*, **312**, 50 (1984b)

Hillas, A.M., *"Proc. 19th Int. Cosmic Ray Conf."*, p. 445, La Jolla, California, USA, Aug. 23, 1985

Hillas, A.M., & Patterson, J.R., *"Proc. of the NATO Advanced Workshop on Very High Energy Gamma Ray Astronomy"*, ed. Turver, K.E., p. 243, Durham U.K., August 11-15, 1986 (1986a)

Hillas, A.M., & Patterson, J.R., *"Proc. of the NATO Advanced Workshop on Very High Energy Gamma Ray Astronomy"*, ed. Turver, K.E., p. 249, Durham U.K., August 11-15, 1986 (1986b)

Hillas, A.M., & Johnson, P.A., *"Proc. 21st Int. Cosmic Ray Conf."*, ed. Protheroe, R.J., p. 19, vol 4., Adelaide, Australia,

Jan. 6-19, 1990

Hillier, R., *"Gamma-Ray Astronomy"*, ed. Oxford Science Publications, (1984)

Jackson, J.D., "*Classical Electrodynamics*", ed John Wiley (1975)

James, F., *Rep. Prog. Phys.*, **43**, 1145 (1980)

Jelley J.V., *"Proc. of the INt. Workshop on High Energy Gamma Ray Astronomy"*, ed. Ramana Murthy, P.V., & Weekes, T.C., p. 3, Ootacamund, India Sept. 20-25, 1982

Jelley, J.V., *"Proc. of the NATO Advanced Workshop on Very High Energy Gamma Ray Astronomy"*, ed. Turver, K.E., p. 27, Durham U.K., August 11-15, 1986

Katz, J.I., & Smith, I.A., *Ap. J.* **326**, 733 (1988)

Kazanas, D., & Ellison, D.C., *Nature*, **319**, 380 (1986)

Kiraly, P., & Meszaros, P., *Ap. J.* **333**, 719 (1988)

Kirk, J.G., Heavens, A.F., *"Proc. 21st Int. Cosmic Ray Conf."*, ed. Protheroe, R.J., p. 93, vol 4., Adelaide, Australia, Jan. 6-19, 1990

Kniffen, D., Kurfess, J., Schonfelder, V., Fitchtel, C., Hofstadter, R., Pinkau, G. "*The Gamma Ray Observatory Science Plan*", by the Gamma Ray Observatory Team (1988)

Kristian, J., Pennypacker, C.R, Middleditch, J., Hamuy, M.A., Imamura, J.N., Kunkel, W.E., Lucinio, R., Morris, D.E., Muller, R.A., Perimutter, S., Rawlings, S.J., Sasseen, T.P., Shelton, I.K., Steinman-Cameron, T.Y., & Tuohy, I.R., *Nature*, 338, 234 (1989)

Kristian, J., Pennypacker, C.R, Middleditch, J., Hamuy, M.A., Heathcote, J.N., Imamura, J.N., Kunkel, W.E., Lucinio, R., Morris, D.E., Muller, R.A., Perimutter, S., Rawlings, S.J., Sasseen, T.P., Shelton, I.K., Steinman-Cameron, T.Y., & Tuohy, I.R., *Nature*, **349**, 747 (1991)

Lamb, R.C., Lewis, D.A., Akerlof, C.W., Meyer, D.I., Weekes, T.C., Hillas, A.M., Cawley, M.F., Fegan, D.J., *"Proc. of the. Int. workshop on Very High Energy Gamma Ray Astronomy"*, Ed. Stepanian, A.A., Fegan, D.J., Cawley, M.F., p. 30, Crimea, USSR, April 17-21, 1989

Lang, K.R., "*Astrophysical Formulae*", ed. Springer-Verlag, Berlin, Heidelberg. New York (1986)

Lang, M.J., Cawley, M.F., Fegan, D.J., Hillas, A.M., Kwok, P.W., Lamb, R.C., Lewis, D.A., Macomb, D., Reynolds, P.T., Vacanti, G.,

Weekes, T.C., *"Proc. 21st International Cosmic Ray Conf."*, ed. Protheroe, R.J., p. 139, vol. 2, Adelaide, Australia, Jan 6-19, 1990

LaSala, J., Thorstensen, J.R., *Astron. J.*, **90**, 2007 (1985)

Lena, P., *"Observational Astrophysics"*, ed. Springer-Verlag, Berlin Heidelberg (1988)

Lindley, D., *Nature*, **340**, 503 (1989)

Loh, E.C., *et al.*, *Nucl. Phys. B (Proc. Suppl.)*, **14A**, 256 (1990)

Longair, M.S., *"High Energy Astrophysics"*, ed. Cambridge University Press, Cambridge UK (1981)

Lovelace, R.V.E., *Nature*, **262**, 649 (1976)

Macrae, J.H.K., *"The Detection of Very High Energy Gamma Rays using the Atmospheric Cerenkov Technique"*, Ph.d Thesis, University of Durham (1985)

Macomb, D.J, Cawley, M.F., Fegan, D.J., Hillas, A.M., Kwok, P.W., Lamb, R.C., Lewis, D.A., Reynolds, P.T., Vacanti, G., Weekes, T.C., *"Proc. of Int. Conf. on High Energy Gamma Ray Astronomy"*, to be published, Ann Arbor, Michigan, Oct 2-5, 1990

Mannings, V.G., *"TeV Gamma Rays from Accreting Binary Pulsars"*, Ph.d Thesis, University of Durham (1990)

Mampe, W., *et al.*, *Phys. Rev. Lett.*, **63**, 593 (1989)

Mardia, K.V., *"Statistics of Directional Data"*, ed. Academic Press, New York (1972)

Matsuno, S., *et al.*, *Nucl. Instr. & Meth.*, **A276**, 359 (1989)

Middleditch, J., Priedhorsky, W., *I.A.U. Circ.*, **4060** (1985)

Middleditch, J., Priedhorsky, W., *Ap.J.*, **306**, 230 (1986)

Mihara, T., Makishima, K., Ohashi, T., Sakao, T., Tashiro, M., Nagase, F., Tanaka, Y., Kitamoto, S., Miyamoto, S., Deeter, J.E., Boynton, P.E., *Nature*, **346**, 250 (1990)

Priedhorsky, W.C, & Holt, S.S., *Ap.J.*, **312**, 743 (1987)

Protheroe, R.J., *Astron. Exp.*, **1**, 137 (1985)

Protheroe, R.J., *Nature*, **329**, 135 (1987a)

Protheroe, R.J., *Proc. Astron. Soc. Austr.*, (1987b)

Protheroe, R.J., & Clay, R.W., *Nature*, **315**, 205 (1985)

Quenby, J.J., & Lieu, R., *Nature*, 342, 654 (1989)

Ramana Murthy, P.V., & Wolfendale, A.W., *"Gamma-ray astronomy"*, ed. Cambridge University Press, (1986)

Rao, MVS, & Sinha, S.J., *Phys. G: Nucl. Phys.*, 14, 811-827, (1988)

Raubenheimer, B.C., North, A.R., de Jager, O.C., Nel, H.I., *Ap.J.*, 336, 394 (1989)

Resvanis, L., Learned, J., Stenger, V., Weeks, D., Gaidos, J., Loeffer, F., Olson, J., Palfrey, T., Sembrosky, G., Wilson, C., Camerini, U., Finley, F., Fry, W., Jaworsky, M., Jennings, J., Kenter, A., Koepsel, R., Lomperski, M., Loveless, R., March, R., Matthews, J., Morse, R., Reeder, D., Sandler, P., Slane, P. & Szentgyorgyi, A., *"Proc. of NATO Advanced Research workshop on VHE Astronomy"*, ed Turver, K.E., p. 105, Durham U.K., Aug. 11-15, 1986

Rossi, B., & Greisen, K., *Rev. Mod. Phys.*, 13, 240 (1941)

Rybicki, G.B., & Lightman, A.P., *"Radiative Processes in Astrophysics"*, Ed. John Wiley & Sons, (1979)

Scargle, J.D., *Ap. J.*, 263, 835 (1982)

Shakura, N.I., & Sunyaev, R.A., *Astron. Ap.*, 24, 337 (1973)

Slane, P., & Fry, W.F., *Ap.J.*, 342, 1129 (1989)

Smith, N.J.T., *et al.*, *N.I.M.*, A276, 622 (1989)

Stecker, F.W., *Astrophys. & Space Sci.*, 6, 377 (1970)

Stecker, F.W., *Ap. J.*, 185, 499 (1973)

Stecker, F.W., *"Proc. of NATO Advanced Workshop on Origin of Cosmic Rays"*, p. 267, ed. J.L. Osborne & A.W. Wolfendale; D. Reidel Publ., Durham, UK, Aug. 26 -Sept. 6 , 1974

Stepanian, A.A., Fomin, V.P., Vladimirsky, B.M., *Izv. Crimean Astrofiz. Obs.*, 66, 234 (1983)

Strom, R.G., van Paradijs, J., & van der Klis, M., *Nature*, 337, 234 (1989)

Tumer, O.T., Hammond, J.S., White, R.S., Zych, A.D., *"Proc. 21st International Cosmic Ray Conf."*, ed. Protheroe, R.J., p. 155, vol. 2, Adelaide, Australia, Jan 6-19, 1990

Turtle, A.J., Campbell - Wilson, D., Manchester, R.N., Staveley - Smith, L., Kesteven, M., *IAU Circ.* 5086 (1990)

Vladimirsky, B.M, Zyskin, Yu.L., Neshpor, Yu.I., Stepanian, A.A, Fomin, V.P., Shitov, V.G., *"Proc. of the Int. Worshop on Very High Energy Gamma Ray Astronomy"*, p. 21, Ed. Stepanian, A.A., Fegan, D.J., Cawley, M.F., Crimea, USSR, April 17 - 21, 1989

van der Klis, M., Jansen, F., van Paradijs, J., Lewin, W.H.G., van den Heuvel, E.P.J., Trümper, J.E., Sztajno, M., *Nature*, **316**, 225 (1985)

van der Klis, M., *Ann. Rev. Astron. Ap.*, **27**, 517 (1989a)

van der Klis, M., *"Proc. of the NATO Advanced Study Inst. on Timing neutron stars"*, ed. Ögelman, H. & van den Heuvel, E.P.J., p. 27, Cesme, Izmir, Turkey, April 4-15, 1988 (1989b)

Wang, Y.M., *Ap. Spa. Sci.*, **121**, 193 (1986)

Weekes, T.C., & Turver, K.E., *"Proc. of the 12th ESLAB Symp."*, E.S.R.O., Frascati (1977)

Weekes, T.C., Cawley, M.F., Fegan, D.J., Gibbs, K.G., Hillas, A.M., Kwok, P.W., Lamb, R.C., Lewis, D.A., Macomb, D., Porter, N.A., Reynolds, P.T., Vacanti, G., *Ap. J.*, **342**, 379 (1989)

White, N.E., & Stella, L., *M.N.R.A.S.*, **231**, 325 (1987)

Zatsepin, G.T., & Chudakov, A.E, *Zh. Etsp. Teor. Fiz.*, **41**, 655 (1961)